Layered Double Hydroxides and their Derived Nanomaterials for Efficient Electrochemical Water Splitting

Doctor of Philosophy

By

Arslan Hameed

Inorganic/Analytical Chemistry

Catalysis and Materials Lab 22 & 27,

Department of Chemistry,

Quaid-i-Azam University Islamabad, 45320

Pakistan.

2024

Layered Double Hydroxides and their Derived Nanomaterials for Efficient Electrochemical Water Splitting

This dissertation is submitted to the Department of Chemistry, Quaid-i-Azam University, Islamabad, in partial fulfilment of the requirements for the degree of "Doctor of Philosophy" in Inorganic/Analytical Chemistry

Submitted By:

Arslan Hameed

Inorganic/Analytical Chemistry

Supervised By:

Prof. Dr. M. Arif Nadeem

Catalysis and Materials Lab 22 & 27,

Department of Chemistry,

Quaid-i-Azam University Islamabad, 45320

Pakistan.

2024

"In the name of Almighty Allah, the most merciful and the most beneficent"

Dedication

This dissertation is wholeheartedly dedicated to,

My beloved parents,

"Their unwavering support and selfless sacrifices have been the cornerstone of my academic journey, enabling me to pursue my dreams and aspirations. From the earliest stages of my education to the completion of this doctoral research, their boundless love and encouragement have provided me with the strength and determination to overcome challenges and persevere in the pursuit of knowledge. Their belief in my abilities has been a guiding light, illuminating my path and inspiring me to reach new heights. This dissertation stands as a testament to the profound impact of their efforts, and it is with profound respect and love that I offer this work as a tribute to their unyielding belief in me."

Acknowledgements

I express deep gratitude to **Almighty Allah**, the Compassionate and Merciful, for granting me the capacity to add to the vast sea of knowledge. I hold immense reverence for the **Holy Prophet Hazrat Muhammad (PBUH)**, a timeless source of enlightenment and direction for all of humanity.

I am deeply grateful to my honorable supervisor, **Prof. Dr. Muhammad Arif Nadeem**, Department of Chemistry, Quaid-i-Azam University, Islamabad, for his invaluable guidance, knowledgeable recommendations, and constant encouragement throughout my research work. His expertise and support have been instrumental in shaping the direction and quality of my research. I will forever cherish the lessons learned and the inspiration gained under his mentorship. Words cannot adequately express my gratitude for his unwavering belief in my abilities and the profound impact he has had on my academic and personal growth.

Furthermore, I extend my heartfelt appreciation to **Prof. Dr. Zareen Akhtar**, Head of the Inorganic/Analytical section, and **Prof. Dr. Aamer Saeed Bhatti**, Chairman of the Department of Chemistry, for their generous support in providing the essential facilities that were crucial for the successful undertaking of my research work. Their assistance and resources have been instrumental in enabling me to carry out my studies effectively, and I am truly thankful for their unwavering commitment to fostering a conducive research environment.

I would like to express my inmost obligation to my Ph.D. colleagues **Waheed Iqbal, Mariam Batool, Fatima Naseem, Muhammad Sofian, and M. Phil colleagues Arooj Nisar**, **Nimra Nisar**, **Shayan Gul**, **Maham Tariq** and **Hira Malik** for their moral support, fruitful suggestions and discussion and untearable cooperation during my research work. I am also sincerely grateful for the firm support and encouragement of my dear friend, **Aqsa Mansoor Khan**, throughout my research journey. I deeply appreciate her true friendship and the positive impact she has had on my research work.

I would like to express my deepest gratitude to my wife **Sanaa Javed** for her unwavering support, patience, and understanding throughout this journey. Her encouragement, love, and belief in me have been the pillars that sustained me during the challenging moments of this endeavor. Her sacrifices and constant encouragement

have been invaluable, and I am forever indebted to her for her unwavering belief in my abilities. Thank you for being my rock and my source of inspiration.

Eventually, I extend my heartfelt thanks to my family, especially my parents - Father **Abdul Hameed** and Brothers **Farhan Hameed and Rayyan Dilawar**, for their unwavering support, prayers, and immense pride in my accomplishments. I am truly grateful for their love and encouragement throughout my dissertation journey. This work stands as a testament to their affection and the strong bond we share. I am forever indebted to them for being my pillars of strength and motivation.

Arslan Hameed

Dated: 26-02-2024

Department of chemistry, Quaid-i-Azam university, Islamabad, Pakistan, 45320.

Table of Contents

List of Figures

List of Figures

List of Tables

List of Abbreviations

BDC	Benzene dicarboxylate
BTC	Benzene tricarboxylic acid
B.E	Binding energy
CNTs	Carbon nanotubes
Rct	Charge transfer resistance
CO_2	Carbon dioxide
CVD	Chemical vapor deposition
CA	Chronoamperometry
CPE	Controlled potential electrolysis technique
Cs	Specific capacitance.
CV	Cyclic voltammetry
DI	Deionized water
DFT	Density functional theory
DOS	Density of states
DO	Dissolved oxygen
Cdl	Double layer capacitance
DMF	Dimethylformamide
EPR	Electron paramagnetic resonance
ECSA	Electrochemical active surface area
EIS	Electrochemical impedance spectroscopy
EELS	Electron energy loss spectroscopy
EDX	Energy-dispersive X-ray spectroscopy
FE	Faradaic efficiency
FWHM	Full width at half maximum
GC	Glassy carbon
GO	Graphene oxide
GPPY	Graphene/polypyrrole
HRTEM	High resolution transmission electron microscopy
HER	Hydrogen evolution reaction
IRCE	Ionic-resin complexation extraction
JCPDS	Joint Committee on Powder Diffraction Standards

List of Abbreviations

LDHs	Layered double hydroxides
LA	Ligand-Assisted
LSV	Linear sweep voltammetry
MA	Mass activity
MOFs	Metal organic frameworks
MMNs	Mixed-metal nitrides
MWCNTs	Multi-walled carbon nanotubes
NSA	Nanosheets array
NWs	Nanowires
NCP	Nickel carbonyl powder
NF	Nickel foam
NCNTs	Nitrogen-doped carbon nanotubes
OER	Oxygen evolution reaction
PEC	Photoelectrochemical
PANI	Polyaniline
PEM	Proton exchange membrane
PCET	Proton-coupled electron transfer
PLAL	Pulsed laser ablation in liquids
RHE	Reference hydrogen electrode
SEM	Scanning electron microscopy
SAED	Selected area electron diffraction
TMSs	Transition metal sulfides
TMSes	Transition Metal-based selenides
TMPs	Transmission metal phosphides
TEM	Transmission electron microscopy
TBP	Tributylphosphine
TOF	Turnover frequency
XAS	X-ray Absorption spectroscopy
XRD	X-ray diffraction
XPS	X-ray photoelectron spectroscopy
ZIFs	Zeolitic imidazole framework

List of Symbols

pKa	Acid dissociation constant
Vo	Oxygen vacancy
η	Overpotential
λ	Wavelength
K	Sherrer constant
D	Crystallite size
b	Tafel slope
R	General gas constant
T	Temperature
n	Number of electrons
F	Faraday constant
$\mathbf{j_0}$	Exchange current density
$\mathbf{i_{eq}}$	Current at equilibrium,
$\mathbf{\eta_{eq}}$	Equilibrium potential
I	Current
ω	Angular frequency
J	Current density
Q	Charge
t	Time
E	Applied potential
$\mathbf{E_{eq}}$	Equilibrium potential
B	Full width half maximum
θ	Bragg angle
ΔG	Gibbs free energy

List of Publications

Below is the list of publications derived from the thesis.

- **Hameed, A.**; Batool, M.; Liu, Z.; Nadeem, M. A.; Jin, R., Layered double hydroxide-derived nanomaterials for efficient electrocatalytic water splitting: Recent progress and future perspective. *ACS Energy Lett.* **2022,** *7* (10), 3311-3328.
- **Hameed, A.**; Nasim, F.; Nisar, N.; Ali, H.; Qurashi, A.; Anjum, D. H.; Sohail, M.; Nadeem, M. A., Heterostructure NiCo-Alloy Nanosheet Embedded Ceria Nanorods: A Highly Efficient Bifunctional Electrocatalyst toward Oxygen Evolution Reaction and Oxygen Reduction Reaction. *Energy & Fuels* **2023,** *37* (22), 17605-17615.
- **Hameed, A**.; Nisar, A.; Nasim, F.; Nadeem, M. A.; Nadeem, M. A., CoOx-NCNT-Supported NiFe-Selenide Nanosheets as an Efficient Bifunctional Electrocatalyst for Water Splitting. *Energy & Fuels* **2023,** *38* (1), 586-597.
- **Hameed, A.**; Zulfiqar, F.; Iqbal, W.; Ali, H.; Shah, S. S. A.; Nadeem, M. A., Electrocatalytic water oxidation on CuO–Cu_2O modulated cobalt-manganese layered double hydroxide. *RSC Adv.* **2022,** *12* (45), 28954-28960.

Abstract

The electrochemical water splitting is an efficient and environment-friendly path-way to produce hydrogen which is a clean fuel. This PhD dissertation presents a comprehensive exploration of novel electrocatalytic materials tailored for efficient water splitting. The study focuses on the synthesis, characterization, and evaluation of three distinct materials, each demonstrating remarkable electrocatalytic properties for oxygen evolution reaction (OER) and hydrogen evolution reaction (HER) in alkaline electrolytes. The first type of material is based upon deposition of bimetallic (CoMn) layered double hydroxide (LDH) over the surface of highly crystalline copper oxide to form a composite material, CoMn-LDH@CuO/Cu_2O. One electrocatalyst out of this class of materials exhibits remarkable OER performance, necessitating only an additional 297 mV potential to achieve a catalytic current density of 10 mA/cm^2, with a minimal Tafel slope of 89 mV/dec. The synergistic interaction of CoMn-LDH and CuO/Cu_2O contributes to an increased electrochemical active surface area (ECSA), enabling efficient OER processes with least charge transfer resistance (Rct). The second type of material, NiCo-alloy@CeO_2, introduces a bifunctional electrode catalyst with superior performance for both OER and HER in alkaline environments. The integration of bimetallic (NiCo) alloy with cerium oxide (CeO_2) nanorods leads toward significantly reduced overpotential of 170 mV at 20 mA/cm^2 for OER and 221 mV for HER. The synergistic interface between alloy and CeO_2, oxygen vacancies in CeO_2 facilitate the ionic conductivity, are the main factors which are thought to uplift the water splitting efficiency. The third type of materials composed of bimetallic (NiFe) selenide which were derived from their parent LDH and supported over cobalt containing N-doped carbon nanomaterials (CoOx-NCNTs). The optimized electrocatalyst (NiFeSe@CoOx-NCNTs) exhibits exceptional performance towards OER and HER under alkaline electrolyte conditions. Notably, it achieves a small overpotential of 240 mV at 20 mA/cm^2 for OER, a reduced Tafel slope of 59.2 mV/dec. For HER, it attains 20 mA/cm^2 at just 145 mV overpotential, exhibiting a small Tafel slope of 169 mV/dec. The catalyst also demonstrates a small Rct, a large ECSA, and exceptional stability over a continuous 15 h experimental period. The exceptional efficiency of NiFeSe@CoOx-NCNTs in both reactions holds significant promise for designing efficient water electrolyzer. Collectively, this thesis underscores the significance of tailored electrocatalytic materials in advancing the realm of renewable energy conversion. This research paves the way for future investigations into

optimizing synthesis processes, uncovering underlying mechanisms, and broadening the applications of electrocatalysts, thus contributing to the ongoing global efforts to achieve a more sustainable energy future.

Introduction

1 Introduction

As humanity endeavors towards achieving cleaner and more sustainable energy resources, hydrogen is emerging as a promising alternative.[1, 2] Hydrogen, as a clean and highly favorable energy carrier possess unrivaled advantages including high energy density and zero greenhouse gas emissions, considered as a potential substitute for conventional fossil fuels.[3-6] Sustainable hydrogen production through electrochemical water splitting has been a mounting concern within the scientific community.[7] Electrolysis of water is a process that can be used to produce hydrogen; however, it is currently hindered by its inefficiency and high costs, attributable to the significant energy input required.[8-10] Consequently, to unlock the potential of electrocatalytic water splitting for hydrogen production, it is essential to design efficient and cost-effective catalysts that can drive the reaction.[11] The objective of this dissertation is to explore the principle of electrocatalytic water splitting, its application in hydrogen production, and the current state of research on the development of catalysts capable of enhancing the efficiency and reducing the cost of the process.

1.1 Principle of Electrocatalytic Water Splitting

Electrocatalytic water splitting is a process that comprises of the splitting of water molecules into hydrogen and oxygen gases by using an electric current.[12] This process takes place in an electrolytic cell, which consists of two electrodes (cathode and anode) separated by an electrolyte.[13] On the surface of anode, oxidation reaction takes place while a reduction occurs on cathode surface. When an electric current is passed through the cell, water molecules are oxidized at the anode, releasing oxygen gas, and reduced at the cathode, releasing hydrogen gas.[14] Figure 1.1 illustrates an electrocatalytic cell designed for water electrolysis.

The overall reaction is represented as follows:

$$2H_2O_{(l)} \rightarrow 2H_{2(g)} + O_{2(g)}$$

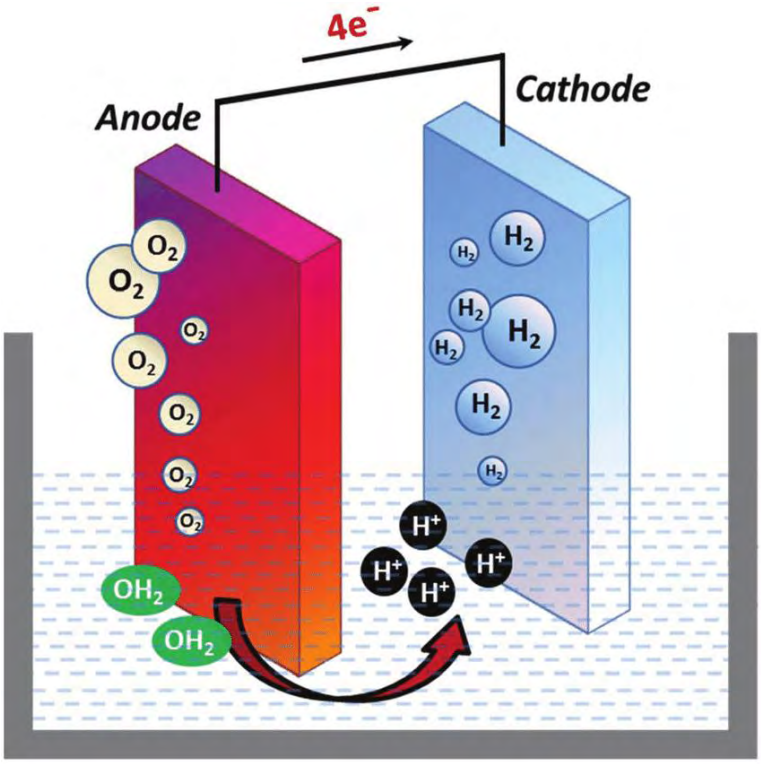

Figure 1.1: Electrocatalytic water splitting cell. Modified from ref.[15]

The effectiveness of the reaction relies on the catalyst used, as well as the operating conditions such as temperature, pressure, and electrolyte composition. Therefore, the advancement of efficient catalysts is crucial for the commercialization of the process.

1.2 Application of Hydrogen Fuel

Hydrogen has many applications, including fuel for transportation and power generation.[16, 17] Hydrogen presents a viable avenue for large-scale clean energy, but producing reliable, cost effective, and clean hydrogen suffers numerous limitations such as 95% of H_2 is produced by steam reforming of coal and natural gas while only 4% of the hydrogen is produced from water splitting.[18, 19] Water splitting using sustainable sources such as wind and solar power is a sustainable and clean method to produce hydrogen.[20] Direct electrocatalytic splitting of water into O_2 and H_2 has fascinated notable attention due to its better efficiency for producing clean and sustainable hydrogen and ability to hasten the development of low-carbon economies.[21]

Electrolysis of water can be performed using two different technologies, namely alkaline electrolysis,[22] and proton exchange membrane (PEM) electrolysis.[23] Alkaline

electrolysis is the most commonly used method for the generation of hydrogen from water. In this method, the electrolyte is an alkaline solution of potassium hydroxide or sodium hydroxide. Alkaline electrolysis requires a high current density and a large amount of electrical energy, which makes the process inefficient and costly. However, Currently available commercial water-splitting catalysts are based on precious metals belonging to the platinum group, with ruthenium, iridium, and their oxides being used for the OER, while platinum (Pt) is considered as the standard electrode material for the HER.[24, 25] Other than noble metals wide range of materials have also been reported with their some limitation.

1.3 Classes of Materials Reported for Electrocatalytic Water Splitting

The catalytic activity of noble metals-based Pt and oxides (RuO_2/IrO_2) has been found to be most effective in facilitating OER and HER.[25] Nevertheless, due to high cost and terrestrial scarcity, their utilization as an electrode material is restricted for global-scale production of hydrogen.[26, 27] Therefore, there is an urgent need to design electroactive materials that are cheap, efficient, and durable for large-scale applications. Transition metal-based compounds have gained substantial attention for electrocatalytic water hydrolysis due to their low cost and high abundance. Metal oxides , hydroxides, sulfides ,phosphides, nitrides, and other metal chalcogenides such as selenides and tellurides have been employed as potential contender for HER and OER under alkaline and acidic cicumstances.[28, 29]

Recently, LDH based on transition metals and their derivatives have gained considerable attention owing to cheap, high reservoirs of transition metals, and high activities as compared to noble metals for OER/HER.[30-32] Designing the LDHs with different modification represents an alternative and beneficial route for replacing the state-of-the-art electrocatalysts.

1.4 Layered Double Hydroxides (LDHs)

LDHs are a class of anionic clays that consist of positively charged layers of metal hydroxides with interlayer anions. LDHs have a layered morphology that offers a large surface area for electrocatalytic activity and tunable interlayer spacing that can accommodate a variety of anions. LDHs have gained attention as promising catalysts

for electrocatalytic water splitting due to their high catalytic activity and stability. The general formula of LDHs is $[M(II)_{1-x}M(III)_x(OH)_2]^{x+}[A^{n-}_{x/n}\cdot mH_2O]^{x-}$, where M(II) and M(III) are divalent and trivalent metal cations, respectively, while A^{n-} is the intercalated anion.[8, 18, 33] The M(II) and M(III) cations occupy octahedral sites of metal hydroxide layers, and the interlayer anions are located between the metal hydroxide layers. LDHs have a layered structure that consists of positively charged metal hydroxide layers and interlayer anions (Figure 1.2).[34] The metal hydroxide layers are composed of octahedrally coordinated metal cations surrounded by hydroxide ions. The interlayer anions are located between the metal hydroxide layers and are balanced by the positively charged metal cations. The interlayer spacing of LDHs can be modified by changing the size and charge of the interlayer anions.[18, 35, 36] This distinct morphology of LDHs provides several advantages including tuneable metal cations ratio, [35] ability to tune catalytic activity by changing interlayer anions,[37] and ability to exfoliate the layered structure into ultrathin nanosheets by etching or applying external force.[38]

LDHs exhibit a 2D layered structure, providing several merits over other materials.[18] These advantages include the ability to tune metal cations in the hydroxide layers,[35] the ability to tune catalytic activity by changing interlayer anions,[37] and the ability to exfoliate the layered structure into ultrathin nanosheets by etching or applying external force.[38] Mostly, LDH-based materials have shown overpotentials (~200 mV) for reaching a benchmarking 10 mA/cm^2 current density, while RuO_2 and IrO_2 possess overpotentials around ~250 mV.[39, 40] Recently, significant research has been devoted on the application of LDHs based material in the area of electrochemical water splitting, particularly for boosting torpid OER process. LDHs based on transition metals, particularly Ni, Co, and Fe, are increasingly reported to show excellent activity towards OER and HER. These materials gain a high catalytic current density of 1000 mA/cm^2 and display exceptional stability up to 1000 hours. Moreover, low cost and high abundance on earth underscore their remarkable potential to replace precious metal-based catalysts.[41] Recent studies reported that the catalyst activity towards OER depends on availability of the electrons in e_g orbital, hance cobalt with a +2 oxidation state demonstrate ideal OER activity as a single electron in e_g orbital ($t_{2g}^6e_g^1$).[42] Yu Pei et al. documented a one-step electrodeposition synthesis of CoFe-LDH deposited on nickel foam. This material demonstrated bifunctional activity, achieving a catalytic

current density of 10 mA/cm^2 at overpotentials of 250 mV and 58 mV for OER and HER, respectively.[43] Yanping Ye et al., introduce Co doped into NiFe-LDH creates dislocation in lattice which significantly improved the catalytic performance with low overpotential of 280 mV@ 50 mA/cm^2 for OER and 170 mV@10mA/cm^2 for HER.[44] Subbaraman et al. presented a report that outlined the reactivity order as Ni > Co > Fe > Mn. This order corresponds with the energy strength order of OHad–M2+ as Ni < Co < Fe < Mn.[45] Numerous studies have indicated that incorporating different transition metals (Mo, Fe, Co, Mn and V) into the Ni-based materials significantly enhanced the electrocatalytic performance.[46-48] Zhao et al., reported that vanadium dopant into $Ni(OH)_2$ modulate the electronic state of Ni^{+2}, enhanced active sites and kinetics of catalytic reaction. The composite V–$Ni(OH)_2$/NF represents high potential towards OER and HER executed η = 275 mV (OER) and 254 mV (HER) at 100 mA/cm^2.[49] The impact of iron contaminations in $Ni(OH)_2$ electrode was first noticed by Edison and Junger, both capacity and life span of alkaline batteries have aroused by iron contamination.[50]

Harnessing the advantages of incorporating iron into nickel-based electrodes, a multitude of studies on NiFe-LDH as an electrocatalyst have emerged over the past several decades.[51-55] Gultom et al., created a bifunctional catalyst NiFe-LDH/$Ni(OH)_2$ synthesized via electrodeposition method. The composite achieved current density of 10 and 100 mA/cm^2 at a cell voltage of 1.6 and 1.8 V vs RHE, respectively for overall water splitting.[56] Research has revealed that the inclusion of third element to the bimetallic LDHs tunes the electronic configuration and enhanced catalytic behavior.[57-59] The introduction of third elements into NiFe oxide/hydroxide forming ternary composite NiFeM (where M = Cr, V, Mn , Co, and Al) significantly boost OER process.

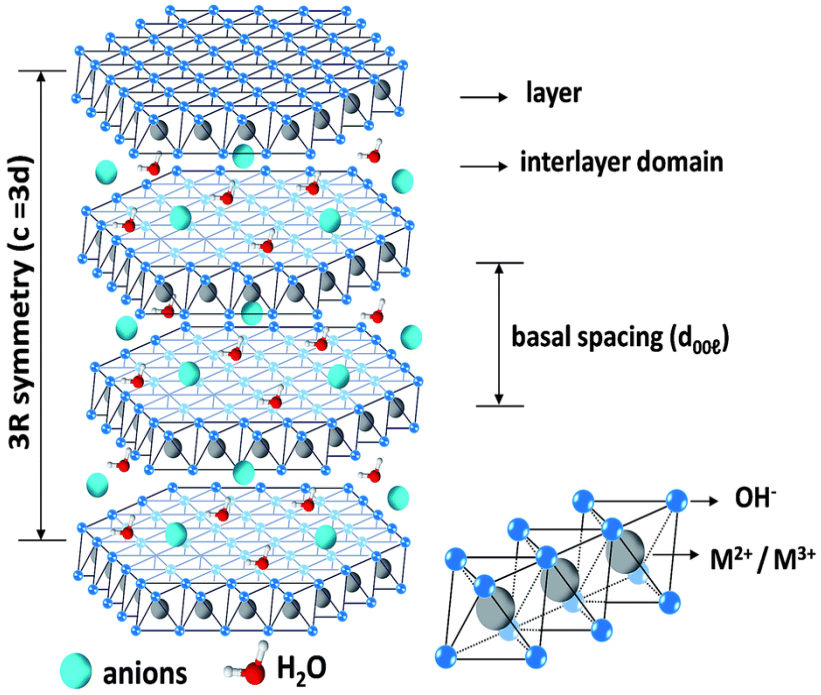

Figure 1.2: Schematic structure of LDHs. Modified from ref.[60]

Mukerjee et al. conducted research exploring the influence of cobalt ion incorporation on the charge transfer behavior of the Ni-Fe oxide lattice for applications in OER.[61] The inclusions of cobalt ion stabilized the oxidation state (Ni^{3+}) while Fe impurity stabilized oxidation state (Ni^{2+})as investigated by in-situ X-ray Absorption spectroscopy (XAS). The improved activity of $Ni(OH)_2$ framework can be attributed to the stabilized Ni^{3+} by Co^{2+} impurity and structure dislocations in host lattice resulting from cobalt doping. Yang et al., found that by adjusting the cobalt content in NiFe-LDH forms crystalline-amorphous interface sites. The composite $Co_{1.98}$-NiFe LDH demonstrate incredible OER activities with an overpotential of 236 mV at 10 mA/cm^2 and a high durability of 96 h in 1M KOH.[62] Yangping et al., also supported the studies that by inclusion of Co in NiFe-LDH created stacking faults which enhance catalytic activity towards OER and HER. The as-prepared electrode $Co_{0.03}$-$NiFe_{0.97}$ LDH showed a low overpotential 280 mV@50 mA/cm^2 for OER and 170 mV@10 mA/cm^2 for HER. Jiang et al., explained the impact of doping the vanadium into NiFe-LDH for OER process. DFT analysis showed that addition of V^{4+} in NiFe-oxide crystal facilitates the charge transfer because of symmetry overlap among the orbitals.[63] Jin et al., synthesized V-doped NiFe-LDH exhibits potential OER and HER performance with overpotential of 195 and 120mV at 10 mA/cm^2, respectively. Understanding the electronic structure of material provides

insight into the strategies to improve catalytic activity. Ultimately, this knowledge can enable the development of environmentally benign methods for commercial scale applicability of the synthesized cheap electrocatalyst in the future.[64]

1.5 Properties of LDHs

1.5.1 High Surface Area

The property of high surface area in LDHs provides a large area for catalytic activity, as it allows for many active sites for catalysis, leading to high catalytic activity.[65] The large surface area of LDHs is due to their layered structure, which provides a large number of exposed surfaces for catalysis.[66] The high surface area of LDHs also provides ample opportunities for interaction with surrounding molecules or ions, which can enhance the catalytic efficiency of the material. The interaction of the molecules or ions with the surface of LDHs can result in changes to the electronic properties of the catalyst, which can lead to an increase in catalytic activity.[67] Furthermore, the extensive area of LDHs allows for the accommodation of a variety of anions in the interlayer space, which can modify the electronic configuration of the catalyst and enhance its catalytic activity. This tunable property allows for the optimization of the catalytic behavior of LDHs for specific utilization.

1.5.2 Tunable Properties

The property of tunable chemical composition and morphology in LDHs is a highly desirable trait that makes them an attractive candidate for electrocatalytic water splitting.[68-70] Numerous host-guest assemblies and nanoarchitectures can help in the creation of materials with desirable physical and chemical characteristics because of the tunability of the metal cations, a regulated M^{2+}/M^{3+} molar ratio, and exchangeable charge-compensating anions. The tunable properties of LDHs can modulate the catalyst's efficiency and durability, leading to more efficient electrocatalytic water splitting.[71-73] Overall, tunable properties in LDHs makes them a highly promising catalyst for electrocatalytic water splitting, with the potential to improve the sustainability and affordability of hydrogen fuel production.

1.5.3 Stability

One of the key properties of LDHs is their stability in an alkaline media, which refers to their ability to maintain their structure and catalytic activity under harsh conditions.[74, 75] This stability is attributed to their layered structure, which provides a strong interlayer interaction among the metal hydroxide layers and the anions.[76] The stability of LDHs is important for electrocatalytic water splitting, as it ensures that the catalyst remains active and effective under the operating conditions. LDHs' stability also makes them a promising candidate for use in industrial applications, where harsh conditions are common.[77, 78] Thus, the stability of LDHs is a desirable property for electrocatalytic water splitting and other applications, as it guarantees the long-term effectiveness of the catalyst.

1.5.4 Catalytic Activity

LDHs exhibit high catalytic activity, which is a crucial property for their use as electrocatalysts for water splitting.[30, 78] This high activity is due to the large surface area of LDHs that provides ample active sites for catalysis. The tunable interlayer spacing of LDHs also allows for the accommodation of a variety of anions, which can modify the electronic configuration of the material and enhance its catalytic activity.[38, 79] In addition, the high catalytic activity of LDHs is beneficial for electrocatalytic water splitting, as it helps to boost the overall productivity of the process. The catalytic activity of LDHs for both the HER and OER has been extensively studied, and LDHs have shown promising results in both cases.[80-85] Overall, the high catalytic activity of LDHs is a desirable property for electrocatalytic water splitting and other applications, as it enables the efficient production of clean and sustainable hydrogen fuel.

1.5.5 Ion Exchange Properties

LDHs exhibit ion exchange properties due to the presence of interlayer anions, which can be exchanged with other anions.[86, 87] This property allows for the modification of the electronic environment of the catalyst particularly crucial for electrocatalytic water splitting, as they enable the optimization of the catalyst's activity for a specific application. By exchanging the interlayer anions, the electronic structure of LDHs can be modified, leading to enhanced catalytic activity.[88, 89] Additionally, the ion exchange

properties of LDHs can be used to introduce new anions that can act as redox-active species, further improving their catalytic activity.[90-92] Overall, the ion exchange property of LDHs is a desirable trait for electrocatalytic water splitting and other applications, as it enables the modification of the catalyst's electronic structure, leading to improved catalytic activity.

1.5.6 Low Cost and Abundance

LDHs are composed of abundant and low-cost metal cations and anions, making them a potential catalyst for commercial applications.[93] This property of LDHs is important for electrocatalytic water splitting, as it offers a cost-effective and sustainable substitute to noble metal-based catalysts.[65, 72, 94] The low-cost and abundance of LDHs make them an attractive option for large-scale production of hydrogen fuel, as they offer a more economically feasible solution than other catalysts. Additionally, the low-cost of LDHs make them utilizable in various applications, from laboratory research to industrial-scale applications.[95] Overall, the low cost and abundance of LDHs is a desirable property for electrocatalytic water splitting and other applications, as it provides a economical and sustainable substitute to noble metal-based catalysts.

1.5.7 Biocompatibility

LDHs exhibit biocompatibility, which is a desirable property utilized biomedical field.[96, 97] The low toxicity of LDHs makes them a potential candidate for drug delivery and other biomedical utilization.[97-99] The tunable properties of LDHs also enable the optimization of their catalytic activity for specific biomedical applications, such as the detection of biomolecules or the degradation of pollutants in biological systems.[100] The biocompatibility of LDHs is attributed to their low toxicity, high biodegradability, and low immunogenicity. The biocompatibility of LDHs makes them a promising material for use in a several biomedical applications including cancer therapy, gene therapy, and imaging.

1.5.8 Environmental Friendliness

LDHs are composed of low-cost and abundant metal cations and anions, making them an environmentally friendly alternative to noble metal-based catalysts.[101] Additionally, the low energy input required for the synthesis of LDHs makes them an attractive option

for green chemistry and sustainable manufacturing.[102] The use of LDHs in electrocatalytic water splitting can facilitate to reduce the carbon footprint of hydrogen production, making it a more environmentally friendly process.[103] The environmental friendliness of LDHs makes them a promising candidate for use in various applications, from energy storage to water treatment.

1.5.9 Selectivity

LDHs exhibit selectivity for specific electrochemical reactions, such as the HER or OER.[104-106] This selectivity is due to the electronic configuration of LDHs, which can be altered by changing the metal cation composition and interlayer anion.[71, 107] The selectivity of LDHs is important for electrocatalytic water splitting, as it can improve efficiency and reduce the energy input required for the process.[108]

1.5.10 Durability

LDHs exhibit high durability under harsh conditions, such as prolonged exposure to electrochemical reactions.[109] This durability is due to the stability of the layered structure of LDHs and their ability to maintain their catalytic activity under harsh conditions.[65] The durability of LDHs is important for electrocatalytic water splitting, as it ensures the long-term effectiveness of the catalyst and reduces the need for frequent replacements. The durability of LDHs also makes them suitable for use in industrial applications, where prolonged exposure to harsh conditions is common.[110] Overall, the durability of LDHs is a desirable property for electrocatalytic water splitting and other applications, as it ensures the prolonged effectiveness of the catalyst.

1.6 Mechanism of OER

The OER mechanism in LDHs typically involves four proton-coupled electron transfer (PCET) steps.[83, 111] Here, we outline a generalized OER mechanism for LDHs as electrocatalysts, assuming M as a representative transition metal:

1. **Initial state:** The metal ions (M) in the LDHs are surrounded by hydroxide (OH^-) ions in their octahedral coordination sites.[112-114]

2. **First PCET step:** One electron is transferred from the metal center (M) to the electrode, and one hydroxide (OH^-) ion loses a proton to form a metal-oxo species (M=O).[115] This step is typically the rate-determining step for the overall OER process.

$$M\text{-}OH \rightarrow M{=}O + e^- + H^+$$

3. **Second PCET step:** Another electron is transferred from the metal center (M) to the electrode, and a water molecule binds to the metal-oxo species (M=O).

$$M{=}O + H_2O \rightarrow M(OH)_2 + e^-$$

4. **Third PCET step:** The metal-dihydroxo species ($M(OH)_2$) transfers one electron to the electrode and loses one proton, forming a metal-hydroperoxo species (M-OOH).

$$M(OH)_2 \rightarrow M\text{-}OOH + e^- + H^+$$

5. **Fourth PCET step:** The metal-hydroperoxo species (M-OOH) transfers one electron to the electrode and loses one proton, forming an oxygen molecule (O_2) and regenerating the initial metal-hydroxo species (M-OH). [116-119]

$$M\text{-}OOH \rightarrow M\text{-}OH + e^- + H^+ + \tfrac{1}{2}O_2$$

The overall OER reaction can be summarized as follows:

$$2H_2O \rightarrow O_2 + 4H^+ + 4e^-$$

The activity and efficiency of LDHs as OER electrocatalysts can be enhanced by optimizing their composition, structure, and morphology to facilitate electron transfer, improves the number of active hotspots, and stabilize the reaction intermediates.[120-123]

1.6.1 Mechanism of OER in term of Gibbs Free Energy

When discussing the OER mechanism in terms of Gibbs free energy, we consider the thermodynamic aspects of the reaction steps. The OER involves four PCET steps, each

with its own associated shifts in Gibbs free energy (ΔG).[124] To evaluate the OER performance of a catalyst, one crucial parameter is the overpotential (η), which is the difference of the potential applied to equilibrium potential of the OER.[125] The overpotential indicates the additional energy required to drive the reaction, mainly due to kinetic barriers associated with each elementary step.

In an ideal catalyst, the four PCET steps of the OER mechanism would have equal and minimal overpotentials, which means that the variation in Gibbs free energy (ΔG) should be the same for each step. The overall OER reaction has a standard change in Gibbs free energy (ΔG°) of 4 x 1.23 eV = 4.92 eV (where 1.23 eV is the standard potential for water splitting). Ideally, each step should have a ΔG of 4.92 eV / 4 = 1.23 eV. [126, 127] In practice, however, catalysts have different energy barriers for each step due to the nature of the reaction intermediates and the electronic configuration of the electrode material. Therefore, the Gibbs free energy for every step is typically different, and one or more steps might have higher energy barriers, which result in larger overpotentials.[128]

The activity and efficiency of LDHs as OER electrocatalysts can be improved by minimizing the ΔG for each step and lowering the overpotentials.[129] This can be achieved by modifying the electronic structure, optimizing the composition and coordination environment, and enhancing the number of active sites. [130] A catalyst with a lower overpotential and a more balanced distribution of ΔG across the steps will have better OER performance, as it can drive the reaction with less energy input.[131]

1.7 Mechanism of HER

LDHs have also been explored as electrocatalysts for the HER in water splitting.[132] The HER mechanism generally involves two PCET steps, known as the Volmer step and the Heyrovsky or Tafel step.[133] Here, we outline a generalized HER mechanism for LDHs as electrocatalysts, assuming M as a representative transition metal:

1. **Volmer step (electrochemical adsorption):** In this step, a proton from the electrolyte accepts an electron from the electrode and binds to the metal center (M) in the LDH, forming a metal-hydride species (M-H).

$$H^+ + e^- + M \rightarrow M\text{-}H$$

2. **Heyrovsky step (electrochemical desorption):** In this step, a second proton from the electrolyte accepts an electron from the electrode and reacts with the metal-hydride species (M-H), forming a hydrogen molecule (H_2) and regenerating the initial metal site (M).

$$M\text{-}H + H^+ + e^- \rightarrow M + H_2$$

Alternatively, the Tafel step (recombination) may occur, where two adjacent metal-hydride species (M-H) recombine to form a hydrogen molecule (H_2) and regenerate the initial metal sites (M). [134-137]

$$2\ M\text{-}H \rightarrow 2\ M + H_2$$

The overall HER reaction can be summarized as follows:

$$2\ H^+ + 2\ e^- \rightarrow H_2$$

The activity and efficiency of LDHs as HER electrocatalysts can be enhanced by optimizing their composition, structure, and morphology to facilitate electron transfer, and stabilize the reaction intermediates.[138-140] Additionally, the presence of suitable transition metals and optimized local environments in the LDH can improve the binding strength of the hydrogen intermediates, leading to improve HER performance.[141]

1.7.1 Mechanism of HER in term of Gibbs Free Energy

When discussing the HER mechanism in terms of Gibbs free energy, we consider the thermodynamic aspects of the reaction steps. The HER involves two PCET steps, each with its associated ΔG. The Gibbs free energy of adsorption (ΔG_{ads}) for the hydrogen intermediates (H*) on the catalyst surface is a critical parameter to evaluate the performance of HER electrocatalysts.[142] A good catalyst should have an optimal ΔG_{ads} for hydrogen, which is neither too strong nor too weak. Ideally, the hydrogen binding should be close to the thermoneutral point, where $\Delta G_{ads} \approx 0$ eV. This implies that the adsorption and desorption of hydrogen intermediates are equally favorable.

If the hydrogen binding is too strong ($\Delta G_{ads} << 0$ eV), the Volmer step (formation of metal-hydride species, M-H) will be favored, but the Heyrovsky or Tafel step (release of hydrogen molecules, H_2) will be hindered.[143, 144] Conversely, if the hydrogen binding is too weak ($\Delta G_{ads} >> 0$ eV), the Volmer step will be hindered, and the HER will be slow.[145] In practice, the optimal ΔG_{ads} for hydrogen on the LDH catalyst surface can be achieved by modification of the electronic configuration, optimizing the composition and coordination environment, and enhancing catalytic activity. A catalyst with an optimal ΔG_{ads} for hydrogen will have better HER performance, as it can facilitate both the adsorption/desorption of hydrogen intermediates with minimal energy input.[146, 147] Overall, understanding and optimizing the ΔG_{ads} for hydrogen intermediates on the LDH catalyst surface is essential for enhancing the activity and performance of LDHs as HER electrocatalysts.[148]

1.8 Synthetic Protocols of LDHs

There are several methods for the synthesis of LDHs. Below is a comprehensive explanation of only co-precipitation and hydrothermal synthesis.

1.8.1 Co-Precipitation

In co-precipitation, divalent and trivalent metal cations are simultaneously precipitated from their aqueous solutions.[149] The process begins by dissolving the metal salts (such as nitrates or chlorides) in water to form a clear solution. Then, a strong base like sodium hydroxide (NaOH) or ammonium hydroxide (NH_4OH) is added slowly to the solution under constant stirring. The pH is carefully controlled (usually between 8 and 11) to favor the formation of LDHs.[150] The precipitation process can be carried out either under constant pH or constant rate of base addition. During the reaction, the metal cations form hydroxide complexes that combine to form the LDH structure. After precipitation, the resulting slurry is aged, usually at ambient temperature or slightly high temperatures (e.g., 60-80°C) for several hours to enhance the crystallinity of the LDHs. Finally, the precipitate is washed, filtered, and dried to obtain the desired LDH product.[151-153]

Ariel et al., constructed NiCoFe-LDHs with different ratio of Co/Ni by a co-precipitation process. The designed catalysts are evaluated for OER demonstrate a modest overpotential around 265 mV with a low Tafel value of 65 mV/dec, the sample

$Ni_3Co_3Fe_3$ manifest a lowest value of overpotential 250 mV. [154] Ultrathin nanosheets of iron-cobalt oxide (Fe_xCo_y-ONSs) with profuse oxygen vacancies synthesized via a feasible solution reduction method by Zhuang et al., The mass activity of Fe_1Co_1-ONS as assessed demonstrated a remarkable activity with 350 mV of overpotential acquired at 54.9 A g^{-1}, with a reduced Tafel slope of 36.8 mV/dec. Because of the distinct structural characteristics such as ultrathin nanosheets which facilitates mass diffusion of OH- ions and presence of oxygen vacancies enhance electrical conductivity, the catalyst Fe_1Co_1-ONS depicted a exceptional catalytic activity. [155]

1.8.2 Hydrothermal Synthesis

Hydrothermal synthesis involves the reaction of metal salts and a hydroxide source in a sealed autoclave under high temperatures and pressures.[156] Initially, the metal salts (such as nitrates, chlorides, or sulfates) are dissolved in water along with a base like sodium hydroxide (NaOH) or ammonium hydroxide (NH_4OH). The mixture is then moved to a Teflon-lined autoclave, which is sealed and heated to temperatures typically ranging from 100-200°C for several hour or even days.[157, 158] The elevated temperature and pressure cause the metal cations to form hydroxide complexes that combine to form the LDH structure. The hydrothermal conditions promote the growth of LDH crystals with higher crystallinity and purity than those obtained through co-precipitation.[159] Yang Hou group carried out a hydrothermal synthesis of 3D hierarchical hybridized compound (EG/$Co_{0.85}$Se/NiFe-LDH). The fabricated catalyst was investigated for OER, displayed a high OER activity attained a current density of 150 and 250 mA/cm^2 with an overpotential of 1.50 and 1.51 mV respectively. Additionally, the hybrid also demonstrated a proficient HER activity demanding -0.26 V to gain catalytic current of 10 mA/cm^2.[160] Lei Zhao et al. integrated a bifunctional electrocatalyst (NiAl-LDH/Ni_3S_2) for water splitting onto a Ni-foam substrate by employing a subsequent hydrothermal processes. As-designed electrode NiAl-LDH/Ni_3S_2/NF displayed a phenomenal electrochemical performance for both OER and HER, demanded a 350 mV overpotential to derive 100 mA/cm^2 current density for OER, and similarly for HER, needs overvoltage of 53.6, 90.2, and 209.2 mV to reach a 10 ,20, and 100 mA/cm^2 current density.[161]

1.9 Limitations of LDHs

Over the past three decades, there has been significant research on using LDH materials for electrocatalytic water splitting. LDH materials are composed of positively charged metal hydroxide layers and negatively charged interlayer anions.[162, 163] These materials have gained popularity because of extensive area and tunable composition, which allows for the incorporation of various transition metal ions to enhance their electrocatalytic properties.[164, 165] Despite the development of many LDH based materials using various synthetic protocols, there exist constraints that hinders their commercial utilization. One of the primary limitations is the inadequate disclosure of surface-active sites.[166] The surface of LDH materials is often covered by hydrophobic organic molecules or water molecules that hinder the interaction between the active sites and reactant molecules. Therefore, it is essential to develop synthetic strategies to expose active centers and boost the electrocatalytic performance of the materials.[167, 168]

Another limitation of LDH materials is the difficulty in the passage of ions through the structured layers in some cases.[169] The layered structure of LDHs is beneficial for incorporating multiple metal ions and enhancing the catalytic activity, but it can also inhibit the diffusion of ions through the layers. This limitation affects the performance of the materials as it restricts the transport of reactants to the active centers and the removal of reaction biproducts.[170] Therefore, it is necessary to explore ways to improve the ion transport through the layered morphology of LDH materials to enhance their electrocatalytic properties. Overall, the advancement of LDH-based materials for electrocatalytic hydrolysis is an encouraging area of research, but there are still challenges that need to be addressed to facilitate their commercial application. Overcoming these limitations and enhancing the electrocatalytic efficiency of LDH-based materials could potentially be achieved by escalating the disclosure of active surface sites and boosting charge flow through the structured layers.[171]

1.10 Strategies to Enhance its Electrocatalytic Performance

To overcome the limitations of LDHs in water electrolysis, several promising strategies have emerged. These include designing nanostructures to enhance surface properties,[172] achieved through particle size reduction to increase surface area and expose active centers; incorporating alternative cations to expand interlayer spacing,[173, 174] promoting

ion transmission and electronic conductivity; enhancing LDH catalytic traits with conductive substances to overcome low bulk conductivity, [175] crucial for efficient electrocatalysis; exploring advanced derivatives of LDHs like metal oxides,[176] hydroxides, oxyhydroxides,[177] phosphides,[178] bimetal nitrides,[179] sulfides, [180] and selenides,[181] leveraging their unique structures and properties to greatly enhance electrocatalytic performance,[171, 182] tuning interlayer spacing through anion replacement to optimize ion transport and catalytic efficiency, [183-185] and inducing vacancy formation within LDH structures to augment active site density and ultimately enhance electrocatalytic activity.[186] Following are some strategies to overcome limitations of LDHs:

1.10.1 Enhancing Surface Properties Through Nano-structuring

Nano structuring is a technique to significantly enhance the surface area of LDHs based materials which is essential for its catalytic activity since an elevated surface area manifests more active hotspot, resulting in higher catalytic activity.[187-189] For instance, Tanmay et al. conducted a study in which they synthesized CoFe-LDH on Graphitic Carbon Nitrides (gCNx) exploited as a substrate and compared its performance to $Co(OH)_2$/g-CNx and FeO(OH)/g-CNx catalysts. The CoFe-LDH/gCNx materials gain a current density (10 mA/cm^2) at η of 0.28 V, accompanied by a Tafel slope of 29 mV/dec. The observed overpotential was notably lower compared to the requirements for the other two materials, implying that the introduction of graphene moiety and nitrogen into graphene resulted in an augmentation of ECSA and the generation of defects.

This combined effect led to a surface modification a 2D sheet-like structure, facilitated efficient mass and charge transfer within the LDH materials.[190] Liu and co., synthesized $NiCo_2S_4$-integrated NiFe-LDH on a nickel foam using a straightforward hydrothermal synthesis method. The resultant heterostructures, comprising of $NiCo_2S_4$@NiFe LDH, NiFe-LDH nanosheets, and $NiCo_2S_4$ nanotubes depicted an overpotential of 201 mV, 260 mV, and 306 mV at 60 mA/cm^2. Blending $NiCo_2S_4$ with LDH materials led to an enhancement in surface properties through a reduction in energy of chemisorption contrast to pristine NiFe-LDH.[191] Yang et al. employed electrodeposition techniques at a constant potential (-1.0 V) vs Ag/AgCl for varying durations to couple a CoFe-LDH

and NiFe-LDH nanosheet on a nickel foam substrate. This coupling strategy resulted in improved electrocatalytic activity compared to individual CoFe-LDH and NiFe-LDH configurations, attributed to the synergistic interaction between the two LDH materials and surface modifications. Notably, among the four tested materials, the CoFe@NiFe-200/NF configuration exhibited the highest activity, demanding an overpotential of 0.19 V to achieve a current density of 10 mA/cm^2 in the OER, whereas the stand alone NiFe-LDH and CoFe-LDH necessitated η of 0.27 V and 0.24 V, respectively, to attain the similar current density.[172] In contrast to bulk LDHs, ultrathin LDH nanosheets exhibit enhanced catalytic activity due to their ability to offer a larger surface area to the electrolyte and expose numerous active sites, a characteristic that becomes particularly pronounced during the exfoliation process.[192, 193]

1.10.2 LDH-Heterostructures with Different Conductive Substrates

Carbon Nanotubes: Carbon nanotubes (CNTs) consist of tubular structures that have a nano-meter scale diameter and micro-meter scale length.[194] CNTs are fundamentally made up of pure carbon atoms that are set out and interconnected by the strong sp^2 carbon-carbon bond and give a distinctive geometrical structure.[195] CNTs have captivated substantial attention as a highly conductive substrate due to their unique morphology and fascinating features such as high electrical conductivity, high thermal conductivity, exceptional optical properties, high mechanical strength, and large surface area.[196] Extensive studies have been focused on modulating the electronic structure of LDH-based materials to elevate the intrinsic catalytic activities while retaining the structural integrity of the LDHs. One of the interesting approaches to overcoming the conductivity issues of the LDHs is to make a composite with conductive substrates like carbon black, graphene, and carbon nanotubes (CNTs). Out of these, MOFs derived carbon emerged as an amazing support material attributable to the features, organic ligands transformed into carbon support while those containing the nitrogen modulate into nitrogen-doped CNTs, immensely boosting the carbon's conductivity.[197,198] Moreover, the metal center contained in the MOFs, during the synthetic condition forms coordinated metals while enhancing the graphitization process of carbon. One category of cobalt-containing MOFs (ZIF-67) based CNTs has been thoroughly investigated as a remarkable substrate material for improving OER/HER kinetics. Kang et al., reported the synthesis of NiFe-LDH supported on Co/Ni-CNTs (CNT-D@LDH), by the

hydrothermal method. The as-prepared material when deployed as an anode exhibits an impressive OER catalytic performance by overpotential (η=267 mV) to generate a current density (10 mA/cm^2), in 1M KOH. The CNTs remarkably increase the electrical conductivity and remove the accumulation of NiFe-LDH, while the bimetallic (Co/Ni) serves as a bridge to transfer charges thus making NiFe-LDH electrons rich.[199]

Wang et al., synthesized the defect-rich heterostructure containing ultrathin CoNi-LDH with oxygen vacancies decorated on a network of CNTs by the one-pot (Absorption-Alkalization-Reduction) synthetic method. The designed electrode demonstrates an efficient OER activity in basic electrolyte (1M KOH), derives a 10 mA/cm^2 catalytic current density at an overpotential (257 mV), along with a small Tafel value (51 mV/dec). Additionally, it exhibits a cell potential of 1.54 V @10 mA/cm^2 for overall water electrolysis. DFT studies indicate that the presence of oxygen vacancies and (CNT) significantly narrow the band gap of the catalyst, enhancing its conductivity. Additionally, the computed value for ($\Delta G_O - \Delta G_{OH}$) in CNT@NiCo LDH-OV is near 1.23 eV, making it more favorable for OER.[200]

Aulia et al., designed a ZIF-67 derived bifunctional electrode (Co_3O_4@NiCo-LDH/N-CNTs) for the oxygen conversion reactions via a step by step transformation reactions. The resulting electrode display enhanced catalytic performance for the OER (η= 355 mV@ 10mA/cm^2), under alkaline reaction conditions. The improved performance is attributed to the synergistic effect caused by ZIF-67 derived Co_3O_4 and NiCo-LDH nanocomposites.[201] The addition of the CNTs to the active LDHs components beneficially increases the electronic conductivity and ultimately optimizes the electrocatalytic performance of actual LDHs composite, which otherwise suffers low conductivity and agglomeration of the active centers. Dinari et al., documented the synthesis of a highly active OER electrode comprising of Ce-doped NiCo-LDH deposited on the conductive CNTs via a solvothermal self-assisted methods. The composite has shown remarkable OER performance by overpotential (η=236 mV) at 10mA/cm^2 catalytic current density, as well as a small Tafel value (b=56 mV/dec) and high stability of 16 h. The high OER performance is explained by the bolstered charge transfer, high surface area, and creation of crystal defects by Ce^{3+} doping.[202] Hengjie liu et al., developed straightforward hydrothermal process to combine NiFe-LDH with single-walled CNTs (SWNT) film. This results in a flexible electrode that is tailor-made

for OER. The integrated electrode (NiFe-LDH@SWNT), attained a current density of 10 mA/cm^2 in 1M KOH at an overpotential of only 250 mV, accompanied by a Tafel slope (35 mV/dec) evident fast reaction kinetics. Advanced soft X-ray absorption near-edge structure tests effectively highlight a robust electron interaction at the interface of LDH and SWNT. This interaction is key to its exceptional OER capabilities. This study provides a new alternative approach for creating flexible and binder-free electrodes suitable for commercial utilizations.[203] Rong Chen et al., reported an easy and economical approach to create stable colloidal nanoparticles (NiFe-LDH), by the co-precipitation of Ni^{2+} and Fe^{3+} ions accompanied by the sonication at standard temperature. The synthesized NiFe-LDH are integrated into orderly structured MWCNTs creating a binder free hybrid microfibre electrode (NiFe-LDH@MWCNT). The as-prepared electrode displayed an excellent OER activity deliver a current density of 180 m A/cm^2 at an overpotential (255 mV). The electrode also exhibits a small Tafel slope (33.3 mV/dec) and a high durability for a period of 24 h under continuous electrolysis. This research offers a universal approach for integrating active electrocatalysts with flexible, porous, and conductive CNTs suitable for an extensive array of electrochemical and catalytic uses.[204]

Gan Jia et al., reported a simple chemical bath deposition (CBD) technique to fabricate bimetallic nanoplates (NiMn-LDH and CoMn-LDH) onto a conductive MWCNTs framework resulted in a highly efficient composites (NiMn-LDH/MWCNT and CoMn-LDH/MWCNT), respectively. Taking the advantage of catalytically active bimetallic hydroxides and optimal conductivity of MWCNTs, both Ni_5Mn-LDH/MWCNT and Co_5Mn-LDH/MWCNT were able to show acceptable OER activity produce 10 mA/cm^2 (current density) at overpotential of 350 and 300 mV, respectively.[205] The development of economical HER electrocatalyst that work in broad pH range have been a tedious task, hindering the overall efficiency of water splitting process, particularly in lack of sufficient proton sources. Lin Wang et al., reported a hybrid electrocatalyst relying on 3D carbon nanostructure that combines CoP nanoparticles (CoP NPs) within N-doped CNTs framework (NCNT). These NCNTs, averaging around 20 nm in diameter and containing CoP NPs, were anchored onto carbon polyhedrons by an average size of approximately 500 nm. This hybrid catalyst, known as CoP/NCNT-CP, was derived from the pyrolysis of the ZIF-67 precursor using a continuous H_2 flow and was

subsequently treated with NaH_2PO_2 for phosphatization. When deployed as cathode, CoP/NCNT-CP depicts a notable HER activity in a basic environment, delivers a current density (10 mA/cm^2) at an overpotential of only 165 mV. Moreover, the CoP/NCNT-CP needed overpotentials (η=203 mV) in a neutral environment and 305 mV in an acidic conditions to reach the same current density for HER.[206]

The advancement of water splitting process also relies on the development of non-noble based bifunctional electrocatalyst, which display high activity and stability towards both OER/HER, simplifying the electrolyzer design and optimal choice for practical implementations. Xin Q. Shen et al., integrated a CNTs supported iron/nickel-alloy as a high-performance bifunctional electrode for water electrolysis. The Fe–Ni/CNT electrocatalyst displays remarkable activities, exhibits an overpotential (221 mV) to produce 10 mA/cm^2, along with a high stability of 150 h at 0.48 V. Furthermore, it accelerates complete water hydrolysis, reaching 10 mA/cm^2 at 1.50 V and maintaining remarkable stability for 65 h at 20 mA/cm^2. This represents its significant potential for large-scale use.[207] Gao et al., synthesized unique carbon-based carrier using a carbonization of ferrocene on CNT by a rapid microwave-assisted approach, which takes approximately 3 minutes, benefiting from the high microwave thermal effects. This Fe/C@CNT features a distinctive heterogeneous iron-carbon structure where numerous carbon-wrapped Fe/Fe_3C nanoparticles are dispersed on the CNT surface. The distinct heterostructure enhances the dispersion and durability of Ni and Ru-based compounds forming an efficient (Ni-Ru@Fe/C@CNT) electrode, which endure robust bifunctional activity and stability by an overvoltage of 32 mV (HER) and 246 mV (OER) at 10 mA/cm^2, as well as a lowest Tafel slope value (54 mV/dec) for HER and 31 mV/dec for OER dictates the faster reaction kinetics of the catalyst.[208]

Ceria as a Conductive Substrate: CeO_2, a crucial rare-earth oxide, has demonstrated significant potential in catalytic applications due to its amazing attributes such as excellent redox properties, substantial oxygen storage capability, plentiful surface oxygen disorders, and stable structure.[209] Materials based on ceria are extensively sought after for their applications in three-way catalysts, de-NOx catalysts, water-gas shift catalysts, oxygen sensors, fuel cells, and ultraviolet absorbers. Additionally, they have notable uses in biotechnology, environmental science, and medical fields. The electron arrangement for Cerium (Ce) is [Xe] $4f^2$ $6s^2$, and it typically exists in the Ce^{3+}

and Ce^{4+} valence states. Cerium oxide (CeO_2) adopts a fluorite structure characterized by a face-centered cubic (fcc) lattice.[210] CeO_2 presents a high density of oxygen vacancies via a fast exchangeable electronic configuration Ce^{4+} to Ce^{3+}, exhibits a strong coupling tendency and easily hybridized with different components.[211-213] Duet to its distinct features, researchers have documented CeO_2/metal alloys,[214] CeO_2/metal oxides,[215] CeO_2/metal sulfides,[216] and CeO_2/metal hydroxides[217] catalysts for HER and OER.

XiXi Wang et al., exploited the electrodeposition methods to incorporate CeOx nanoparticles into NiFe LDH nanosheets, creating a balance number of oxygen defects in resultant three-dimensional electrode (NF@NiFe LDH/CeOx). In alkaline solutions, the NF@NiFe LDH/CeOx electrode shows an overpotential of only 154 mV for a current density of 10 mA/cm^2 and 267 mV for 20 mA/cm^2 for HER. Additionally, this electrode serves as an effective bifunctional electrocatalyst for complete water splitting, attaining cell potential of 1.51 V for 10 mA/cm^2 in 1M KOH solution, outperforming benchmark catalyst (Pt/C and RuO_2). The high performance is explained by DFT analysis which demonstrated that the oxygen vacancies are created by accumulation of positive charges due to the potential difference between NiFe LDH and CeOx.[218] Ceria itself has weak ionic conductivity but the hybrid of it with metals substantially increases the charge transfer between metal and CeO_2 interface. Thus, the addition of ceria to a metal catalyst beneficially tune the electronic structure of actual catalyst, which as a result enhance the adsorption/desorption of reactants and products significantly enhance the electrocatalytic activity.[219,220] Yiming Hu et al., introduced the heterostructure approch to decorate CeO_{2-x} onto a active OER catalyst (CoFe LDH), grown on nickel form. The resulting electrode labbled as CeO_{2-x}@CoFe LDH/NF display efficient OER efficacy with a remarkably low overpotential (η=204 mV@ 100 mA/cm^2), accompanied by a long-term stability of 30 h under the alkaline seawater conditions. In the heterostructure composite, CoFe LDH supplies the active sites for OER activities, while the CeO_{2-x} nanoparticles contribute additional oxygen vacancies, working in harmony with the LDH framework to elevate the OER catalytic efficiency.[221]

Bingkai Wang et al., reported a unique in-situ approach leading to a direct growth of ceria on cerium-nitrogen-carbon abbreviated as CeO_2@CeNC, which is exploited as a

support to OER active NiFe-LDH catalyst. The resultant hybrid structure abbreviated as NiFe-LDH/CeO_2@CeNC have been tested for OER under an alkaline solution, represents a decent electrocatalytic activity by an overpotential (235 mV@ 10 mA/cm^2 and 430 mV @ 100 mA/cm^2), surpassing benchmark Ir/C (20%) electrocatalyst.[222] Interface engineering has garnered substantial attention as a promising approach to produce efficient and cost-effective electrocatalysts for water oxidation. Designing the heterostructures with two different active sites provide additional advantage of effective charge transfer and enhanced activity compared to single components. Zhang et al., successfully synthesized a unique flower-like (NNO/CeO_2/NF) by integrating the $Ni_3(NO_3)_2(OH)_4$ nanosheets on CeO_2 nanoparticles deposited on three-dimensional nickel foam through a single step hydrothermal method. When deployed as anode, NNO/CeO_2/NF only demands 330 mV to generate 50 mA/cm^2 current density, as well as remarkable stability for a duration of 40 h. For HER, it display a overpotential of 120 mV @ 10 mA/cm^2. The anion substitution in nickel hydroxide, coupled with the synergistic effect of ceria, enhances the active site and boosts the reaction's electron transport capability, leading to a notable increase in electrocatalytic performance.[223] Zhao et al., reported a class of electrocatalyst comprising of numerous vulnerable hydroxide heterostrucutures with ceria ($Ni(OH)_2$)–oxide (CeO_2), anchored on the carbon paper (CP) labeled as Ni_xCe_y@CP. The as-prepared electrode represents high performance towards OER (η= 220 mV@ 10 mA/cm^2), along with a low Tafel slope (b= 81.9 mV/dec). Moreover, the catalyst display a negligible decline in potential under constant chronoamperometry test for 20 h, which is evidence of the high durability of intimate interfaces. High effectiveness of the catalyst is ascribes to synergistic interactions of exposed interfaces ($Ni(OH)_2$ and CeO_2), which improves the binding energy of intermediates on surface of catalyst.[224]

Furthermore, the HER activities of CoS_2,[225] Cu_3P,[226] Mo_2N,[227] NiO,[228] and V-CoP [229] have been enhanced by coupling with CeO_2 under the alkaline electrolyte. The easily transformable oxidation states Ce^{4+} to Ce^{3+} creates oxygen vacancies, particularly beneficial for oxidation reactions as the binding energy of water is stronger particularly beneficial for oxidation of water during Volmer step of HER.[228, 230] Sinan Li et al., reported porous CeO_2/Ni-Cu, which serve as a cathodic material achieve a catalytic current density of 10 mA/cm^2 with remarkably low overpotential (η=72 mV), and a

high durability of more than 24 h.[231]Sun et al., deployed electrodeposition route to fabricate NiCo–CeO_2 onto a graphene plate (NiCo–CeO_2/GP). The resulting electrode displayed phenomenal HER performance in alkaline media, with a low overpotentials of 34 mV and 140 mV at 10 mA/cm^2 and 500 mA/cm^2, respectively.[232]

1.10.3 Advance LDHs Derivatives

LDHs have shown great potential in various applications due to their unique properties. By transforming LDHs into derived materials with altered structures, compositions, or morphologies, researchers can further enhance their properties and create advanced materials with improved catalytic, electronic, or optical properties. These derived materials include mixed metal oxides, hydroxides, oxyhydroxides, bimetallic phosphides, bimetallic nitrides, bimetallic selenides, bimetallic alloy, bimetallic sulfides and LDH derived MOFs. These materials have the potential to revolutionize areas of catalysis, energy storage, and environmental remediation. With their unique properties and versatile synthesis methods, LDH-derived materials are promising candidates for the development of advanced materials for various applications.

Metal Oxides, Hydroxides and Oxyhydroxides as Electrocatalysts

The 3d transition metal oxides, oxyhydroxides, and hydroxides have shown decent electrochemical performance. However, due to the availability of limited active sites and thus low catalytic performance, their OER properties are often unsatisfactory. The oxides, hydroxide and oxyhydroxides obtained from LDHs are of two-dimensional (2D) layered structures with large specific surface area, more vulnerable to surface atoms, tunability of electronic structure, and innately high dynamic activity that exhibits increased performance in the OER.[233]

Li et al. recently designed nickel foam (NF) assisted porous nickel oxide nanosheets co-doped with phosphorus and aluminum (PA-NiO, Figure 1.3(a)). PA-NiO was deployed as a bifunctional electrocatalyst for water electrolysis. The overpotential needed for the OER in alkaline medium is 310 mV at 100 mA/cm^2 (Figure 1.3(b,c)). Whilst in a two electrode water splitting system, potential of 1.56 V was attained at current density of 10 mA/cm^2 .[218] The fast kinetics of OER is depicted through the smallest Tafel slope value (Figure 1.3(d)). This study pointed out that the enhanced

efficiency of PA-NiO was owing to the co-doping of Al and P, which not only improved the material's intrinsic electron transmission and durability but also provided a porous structure for the exposure of active hotspots for better mass transfer. As illustrated in (Figure 1.3(e-g)), it also exhibits superior electrochemical performance towards HER exhibits 138 mV overpotential at 10 mA/cm^2 in alkaline medium. Initially, hydrothermal technique was employed to synthesize AlNi-LDH@NF as a precursor which was then phosphidized in the presence of $NaH_2PO_2.H_2O$ under N_2 to produce NF-supported PA-NiO (Figure 1.3(a)). The catalyst's morphology was investigated by SEM and TEM, which revealed a layered structure of PA-NiO, like the AlNi-LDH precursor which was developed vertically on the surface of nickel foam.

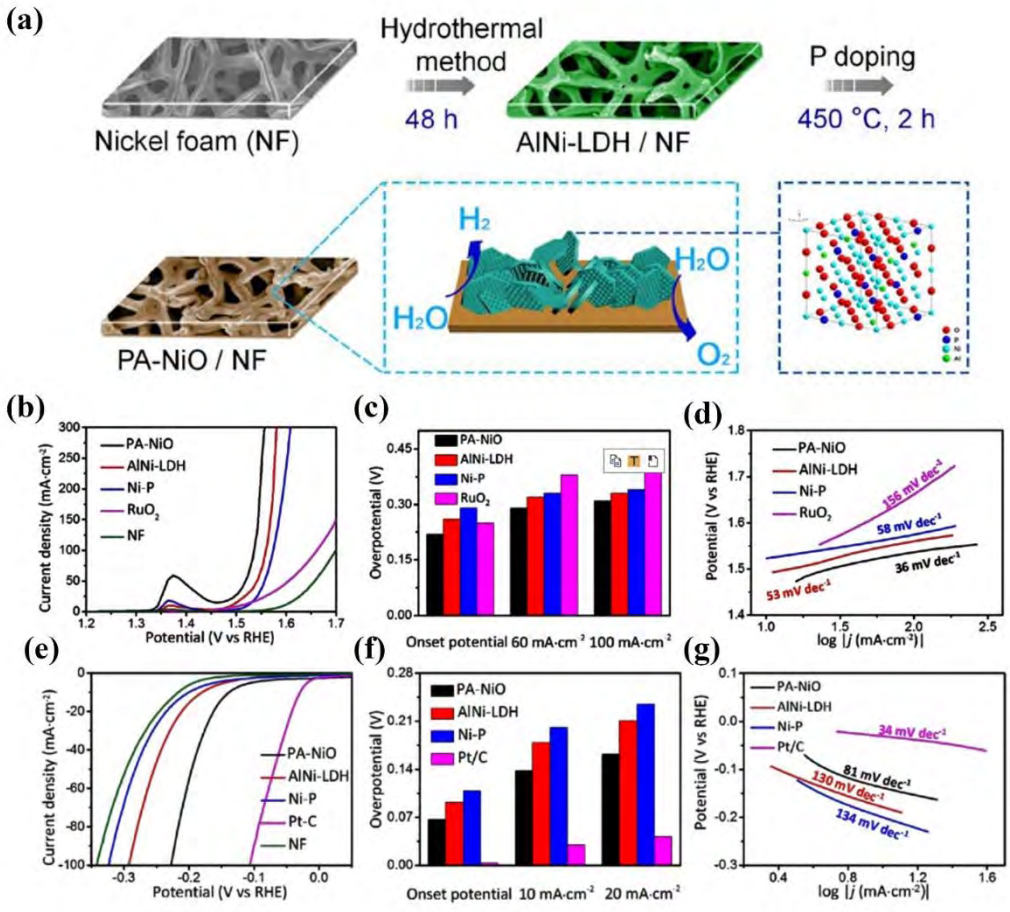

Figure 1.3: (a) Schematics for the synthesis of PA-NiO, (b) LSV curves of PA-NiO, AlNi-LDH, Ni-P, and RuO2 for OER, (c) corresponding onset potentials, overpotentials, (d)Tafel plots, (e) LSV curves of PA-NiO, AlNi-LDH, Ni-P, and RuO2

for HER, (f) corresponding onset potentials and overpotentials, (g) Tafel plots. Copyright The American Chemical Society, 2018.[218]

Shi et al. reported a NiFe-$NiCoO_2$ composite which was synthesized by selecting NiCo-$NiFe(CN)_6$ as the substrate to pyrolyze at 350 °C under an Ar/H_2 environment.[234] The NiFe-$NiCoO_2$ nanomaterial exhibited a notably low overpotential (102 mV) for HER and (286 mV) for OER, accompanied by low Tafel slopes, as depicted in figure 1.4(b-e). The dodecahedral ZIF-67 crystals were employed as a sacrificial template. NiCo-LDH was grown on the surface of ZIF-67 and heated at temperature of 90 °C in water to form hollow NiCo-LDH dodecahedrons (Figure 1.4(a)) followed by intercalation of $K[NiFe(CN)_6]$ to form NiCo-$NiFe(CN)_6$. The NiCo-$NiFe(CN)_6$ was calcined at 350 °C to produce the NiFe-$NiCoO_2$ composite. The NiCo-LDHs have a distinctive hollow shape that allows exposure to active sites, as revealed by SEM and TEM images (Figure 1.4(f-h)). Besides, the as-synthesized composite retained its primary hollow polyhedron structure after the carbonization, which offers good mass transport thus enlarging the contact area with the electrolyte.

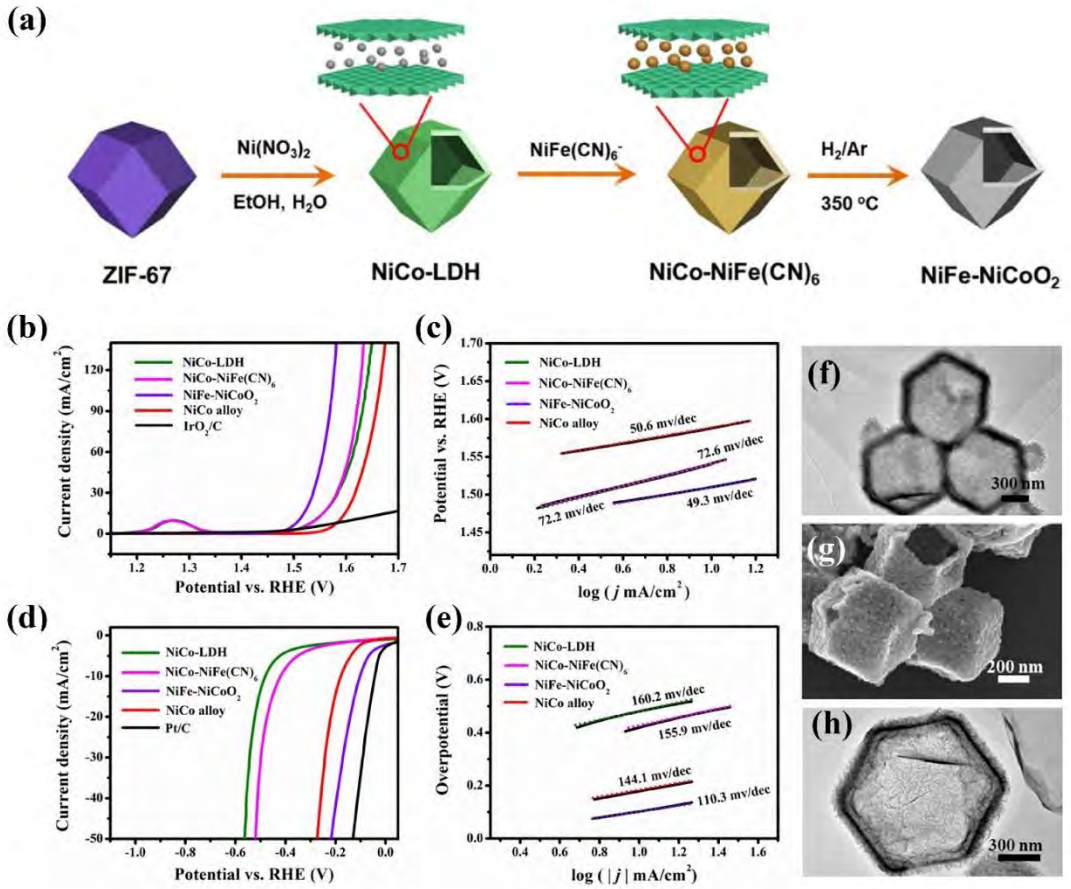

Figure 1.4: (a) Schematically depicted fabrication process of the NiFe-$NiCoO_2$, The LSV curves of the electrocatalysts for OER (b) and HER (d) corresponding Tafel slopes for OER (c) and HER (e) SEM and TEM images of NiCo-LDH and NiFe-$NiCoO_2$ (f-h). Journal of Energy Chemistry, 2018.[234]

Bimetallic Phosphides

Transition metal phosphides (TMPs) are being exploited as a class of potent bifunctional electrocatalysts on account of their high abundance, low cost, electrical conductivity, and durability over a range of pH. Despite abundant active sites, the electrocatalytic behavior is relatively low due to intrinsic strong H-bonding ability, low specific capacity and low catalytic rate of TMPs.[235] Therefore, the atomic and electronic structures should be modulated by manipulating the morphology/particle size, creating defects, doping extrinsic atoms or forming heterojunctions to increase the catalytic properties. The LDH-derived TMPs are a good choice due to thin-layered structure,

tunable cations and intercalated anions and good adsorption capability. The resultant topological TMPs with modulated structure and electronic distribution provide ample active sites and rapid mass transport for achieving outstanding catalytic activity.

Li et al. carried out a simple, in-situ phosphidization for the fabrication of a Mo-CoP composite for total water splitting (Figure 1.5(a)).[236] The synthesized CoMo-LDH was employed directly as a precursor. The cations in the precursor were phosphidized to generate ultra-even Mo dispersion in the CoP structure to produce a superior bifunctional electrocatalyst. By increasing the Mo doping, both HER and OER activities first increase and then decrease. With a 1:2.3 molar ratio of Mo to Co, the composite exhibits the best HER activity and high durability in acidic medium (0.5 M H_2SO_4), have η = 116 mV at 10 mA/cm^2 as correlated to the pure CoP at 160 mV (Figure 1.5(b-c)). The composite also performs well in alkaline medium by generating catalytic 10 mA/cm^2 current density at 118 mV and 317 mV overpotential for HER and OER, respectively, with good stability and durability being superior to most of the reported catalysts (Figure 1.5(d-g)). The lower R_{ct} of Mo-CoP as compared to pure CoP in both acidic and alkaline solution confirms the Mo doping effect in improving charge transfer properties and hydrogen and hydroxide adsorption for HER and OER, respectively, to boost the overall water electrolysis.

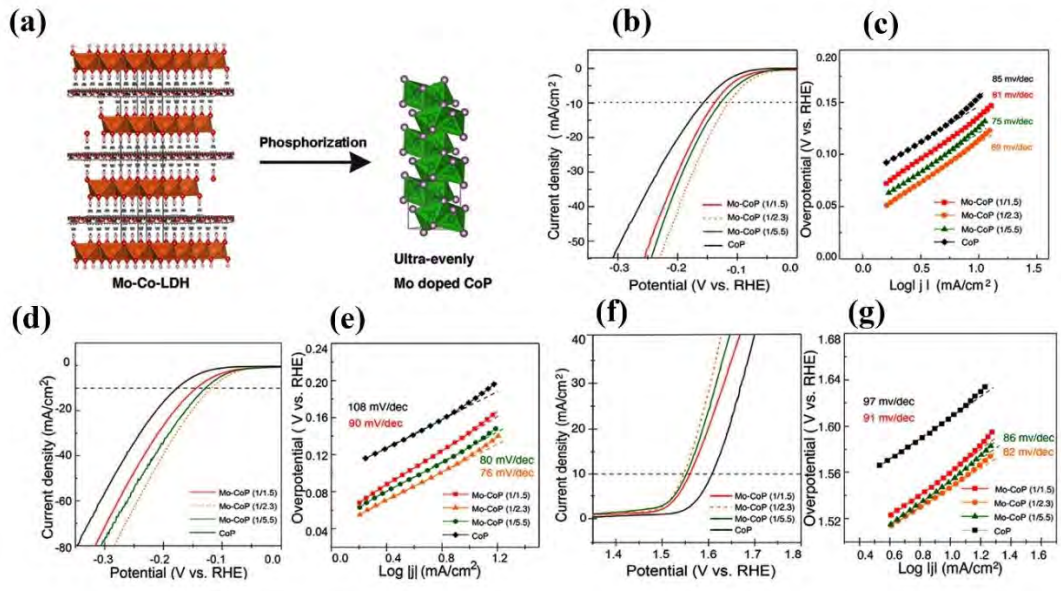

Figure 1.5: a) Schematics of ultra-even Mo-doped CoP composite, (b) Linear sweep voltammogram of individual CoP and Mo-CoP with various molar ratios in 0.5 M

H_2SO_4, (c) Calculated Tafel slopes, (d) Linear sweep voltammograms of individual CoP and Mo-CoP with various molar ratios in 1M KOH, (e) corresponding Tafel slopes, (f) Polarization curves for OER of individual CoP and Mo-CoP with various ratios, (g) Tafel slopes. Copyright 2018 The Royal Society of Chemistry.[236]

Bimetallic Nitrides

The 3d-transition metal nitrides exhibit excellent performance in water splitting owing to their distinctive features including low resistance to charge transfer, enhanced active sites, excellent mechanical strength, high resistance to corrosion, ease of conversion to catalytically more active species, and noble-metal like behavior. In comparison to monometallic nitrides, bimetallic and ternary nitrides show remarkable activity since the mixing of elements can modulate the electronic structure and valence state of the metals. Temperature programmed ammonolysis of LDH nanosheets results in the nanostructured mixed-metal nitrides (MMNs) that outperformed the benchmark catalysts for OER.

Li et al. recently employed a two-step facile hydrothermal and successive ammonia annealing method to grow nanosheet arrays of $CoFeN_x$ over Ni foam at different temperatures ranging from 300 ℃ to 600 ℃ (Figure 1.6(a)).[179] Among all the materials prepared, $CoFeN_x$-500 HNA/NF demonstrated outstanding OER kinetics with low Tafel slope of 57.6 mV/dec. To achieve the electrocatalytic current density of 50 mA/cm^2, the nanostructure needed an overpotential value of 259 mV, that is lower than the 292 mV, 274 mV and 289 mV of the materials synthesized at 300 ℃, 400 ℃ and 600 ℃, respectively (Figure 1.6(b-c)). The CoFeNx-500 HNA/NF composite also demonstrated remarkable catalytic efficacy for HER, showing a minimal overpotential of 200 mV versus RHE to obtain 10 mA/cm^2, accompanied by a minor Tafel slope, as illustrated in figure 1.6(d-e).

Jia et al. synthesized Ni_3FeN-NPs of 100 nm size by temperature-controlled ammonolysis of extremely thin Ni_3Fe-LDH nanosheets developed by reverse microemulsion (Figure 1.6(f)).[237] For comparison, Ni_3FeN-bulk and Ni_3N were also fabricated and evaluated for electrocatalytic HER and OER (Figure 1.6(g-h)). Among these materials, Ni_3FeN-NPs manifested excellent performance with 158 mV and 280 mV overpotential to acquire the catalytic current density of 10 mA/cm^2 for HER and

OER, respectively. Similarly, the low Tafel slope for HER and OER verified the fast kinetics with 42 mV/dec and 46 mV/dec, respectively (Figure 1.6(i-j)). The increased conductivity is attributed towards low intrinsic charge transfer resistance (R_{ct}) of the material. DFT pointed the root cause of enhanced electrochemical performance of nanoparticles to metallic character discovered through density of states (DOS) and band structure, which in-turn is responsible for accelerated electrical conductivity and electron transfer. Furthermore, the higher adsorption energy for water in Ni_3FeN-NPs also aids in extending electronic DOS and consequently improved water splitting efficiency.

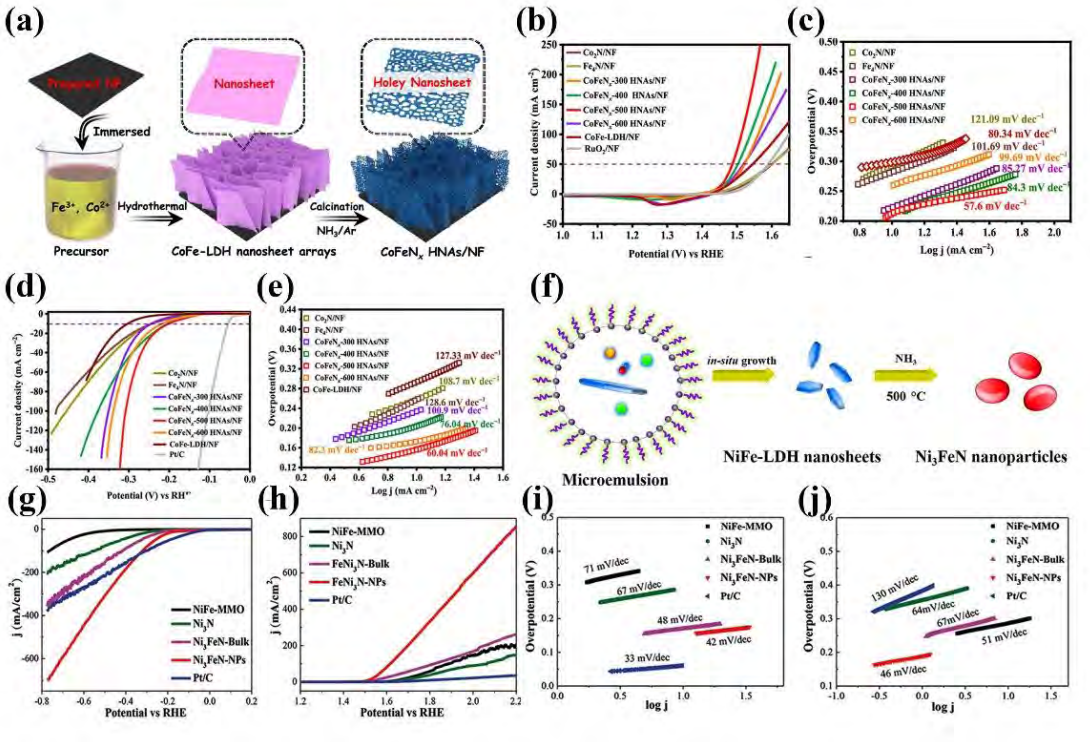

Figure 1.6: (a) Schematic illustration for synthesis of $CoFeN_x$ HNAs/NF. OER activity of a series of CoFe-LDH/NF, Co_2N/NF, and Fe_4N/NF catalysts; (b) Linear sweep voltammograms; (c) corresponding Tafel slope plots. HER performance tests of CoFe-LDH/NF, Fe4N/NF, Co_2N/NF and series of bimetal nitride $CoFeN_x$ HNAs/NF catalysts; (d) Linear sweep voltammograms; (e) corresponding Tafel slope plots; (f) Schematics for the fabrication of Ni_3FeN nanoparticles; (g) LSV curves for HER at a scan rate of 5 mV/s; (h) Linear sweep voltammograms at scan rate of 5 mV/s for OER; (i) Tafel plots for HER; (j) Tafel plots for OER kinetics. Copyright 2020 American Chemical

Society.[179] © 2016 WILEY-VCH Verlag GmbH & Co. KGaA, Weinheim holds the copyright for this material.[237]

Bimetallic Selenides

Transition metal selenides emerged as another class of active electrocatalysts for water splitting. During HER reaction, metal selenides provide very good activity, however, certain limitations are associated i.e., metal leaching under acidic condition whilst they can be converted into hydroxides under basic conditions. To resolve this, converting LDHs into different forms, such as sulfides or selenides, has been examined and has been regarded as a highly significant approach. The benefits of this strategy include: (1) modification of the electronic structure of the original materials by transitioning to sulfide, selenide, or phosphide; (2) enhanced conductivity; (3) maintaining a 2D sheet-like shape. Xiao et al. reported bifunctional $(Ni,Co)_{0.85}Se$ nanosheets array (NSA) which was fabricated via hydrothermal treatment of NiCo-LDHs precursor deposited on nickel foam (Figure 1.7(a)).[238] The as-synthesized hierarchical $(NiCo)_{0.85}Se$ NSAs catalyst displayed good catalytic efficiency for both HER and OER by requiring overpotential of 287 mV @ 20 mA/cm^2 for OER and 169 mV @ 10 mA/cm^2 for HER, respectively (Figure 1.7(a-c,e)). The Tafel slope value 86.75 mV/dec was calculated from the data. In addition, selenization was carried out for various time periods ranging from 1 h to 24 h (Figure 1.7(d)). It was reported that under alkaline conditions, $(NiCo)_{0.85}Se$-8h showed better activity for OER compared to other samples. The water electrolyzer consumes just 1.65 V at 10 mA/cm^2 and shows stability in a 50 h test. The presence of vacancies in the crystal structure created due to Jahn-Teller distortion enhances the electrochemical activity. The hierarchical porous structure of $(Ni,Co)_{0.85}Se$ NSAs vertically grown on NF reduces the pathway for the mass transfer, limits the aggregation of active hotspot leading towards high activity and stability.

Du et al. reported nanosheets of $(Ni,Fe)_3Se_4$ via solvothermal synthesis of NiFe-LDH followed by hydrothermal selenization.[239] The as-synthesized ultrathin $(Ni,Fe)_3Se_4$ nanosheets exhibit numerous catalytically accessible active sites, high specific area and fast charge transfer for water splitting. The nanostructures anchored on Ni foam exhibited remarkable performance in both OER and HER, showcasing a minimal overpotential of 173 mV and 225 mV for HER and OER, respectively at 10 mA/cm^2.

Additionally, a Tafel slope of 41 mV/dec was measured for OER in relation to this material. Ultrathin porous nanosheets and mixed transition metal structure enhances the charge transfer that results in fast diffusion and reaction on electrode-electrolyte interface.

Considering the significance of LDH derivatization, Karmakar et al., presents a successful selenization of the flower-like NiFe-LDH material under solvothermal conditions. This selenization process resulted in 2D Fe-doped Ni_3Se_4 hierarchical nanostructure with altered coordination surroundings at the active Ni sites. The conversion from hydroxide to selenide increased the material's porosity, which allowed the Fe-doped Ni_3Se_4 (Fe@Ni_3Se_4) a superior charge and mass transport at the electrode–electrolyte junction. The catalyst (Fe@Ni_3Se_4) utilized as a bifunctional electrode, depicts a small overpotential (η=185 mV) for OER and (η= 33 mV) for HER at 10 mA/cm^2. Moreover, a tenfold surge in turnover frequency (TOF) was observed in Fe@Ni_3Se_4 relative to the unaltered NiFe-LDH, highlighting a significant enhancement in specific activity due to the selenization process.[240] Recent research has also been devoted to the construction of heterostructures which abundantly create heterointerfaces, that result in the more vulnerable active hotspot, increased electron transfer, and consequently boost the catalytic activity and stability. Zhao et al., exploited a two-step hydrothermal technique to construct a heterostructure CoSe/Ni_3Se_4 by utilizing LDH- based template containing NiCo LDH nanosheets decorated on stainless steel meshes (SS), which serve as a superior bifunctional electrocatalyst towards both OER/HER. The as-prepared catalyst This SS@CoSe/Ni_3Se_4 blend represents remarkable electrocatalytic performance, demanding minimal overpotentials (η=97 mV) for HER and (η=230 mV) for OER to produce a catalytic 10 mA/cm^2 current density. The superior functionality of SS@CoSe/Ni_3Se_4 is due to the combined efficiency of the SS mesh's vulnerable active hotspot and faster charge transfer at the heterointerface (CoSe/Ni_3Se_4), which emerges from the in-situ transformation of NiCo LDH nanosheets. Analyses of the electrochemical impedance spectrum and active surface area and suggest the anchored CoSe/Ni_3Se_4 on stainless steel meshes possesses the highest number of electroactive sites and the least electrochemical resistance. This configuration, in turn, reveals more active regions and boosts charge movement, thereby elevating its catalytic efficiency. Moreover, when SS@CoSe/Ni_3Se_4 deployed

as both anode and cathode, the built electrolyzer needs just 1.55 V to attain 10 mA/cm^2 for full water electrolysis.[241] One of the important considerations to boost the catalytic efficiency is the electrical conductivity of the material during the OER/HER process. The enhanced electronic conductivity can significantly boost energy conversion efficiency by speeding up the electron-transfer process and minimizing the overpotential due to Schottky barriers at the catalyst-electrode interfaces and catalyst-electrolyte junction. The various structural modifications of the TMSe, and tunable band gaps from insulating to metallic states can be realized, enhancing OER performance. For instance, Zhao et al., reported a feasible approach to produce Mn-modified cobalt selenide nanosheets labeled as (CoMn)Se_2. For the synthesis, first a LDH template (Co_4Mn_1 LDH nanosheets) was prepared by a one-pot coprecipitation method, subsequently followed by selenation process to produce CoMn)Se_2. The (CoMn)Se_2 catalysts required an overpotential (270 mV@ 10mA/cm^2), notably lowered than the CoSe2 electrocatalyst and the benchmark IrO_2. By incorporating Mn, specific atomic disorders are induced, adjusted electronic structure, and simultaneously optimize the electrical conductivity of the CoMn selenide. These modifications in morphology and electrical properties are key to raising the creation of active species and speeding up the OER process, resulting in higher catalytic activity.[242] Zhang et al. studied the effects of molybdenum doping on LDH-derived NiFe-Se and found significant structural and electronic modulation to improve bifunctional activities toward water electrolysis. The NF decorated Mo-doped Nickel-iron selenide catalyst represented as Mo-NiFe-Se/NF, was formed by a two-step process, firstly NiFe-LDH/NF prepared by hydrothermal method, which is subsequently treated with molybdenum source ($Na_2MoO_4 \cdot 2H_2O$) and selenized for 12 h at 180 °C. When employed in overall water splitting electrolyzer, the catalyst demands a mere voltage (1.51 V) at 10 mA/cm^2 in alkaline conditions. Incorporating Mo results in the formation of nanospheres with an extensive active surface area and refines the electronic configuraton of NiFe-Se. As a result, Mo-NiFe-Se/NF exhibits superior bifunctional performance.[243] Huang et al., reported a high performance electrocatalyst P-$Ni_{0.75}Fe_{0.25}Se_2$, fabricated on nickel foam for OER and complete water electrolysis . The catalyst was derived from NiFe-LDH/NF synthesized by facile hydrothermal process, transformed by a selenation process under hydrothermal reaction for 20 h at 180 °C. The P-doping of $Ni_{0.75}Fe_{0.25}Se_2$ is carried out to produce optimized P-

$Ni_{0.75}Fe_{0.25}Se_2$, which demonstrates an impressive OER performance at (η= 156 mV@ 10 mA/cm^2) and (η= 226 mV@ 300 mA/cm^2). Through a combination of theoretical and empirical analyses, it is evident that phosphorus doping can individually fine-tune the electronic configuration of Fe without impacting Ni. This modulation optimizes the binding of OER intermediates at the active centers, thus enhancing its kinetics. Moreover, the catalyst display high stability exhibits negligible loss in current density (300 mA/cm^2) for a duration of 1000 h under multi-chronoamperometry test in the alkaline electrolyte.[244]

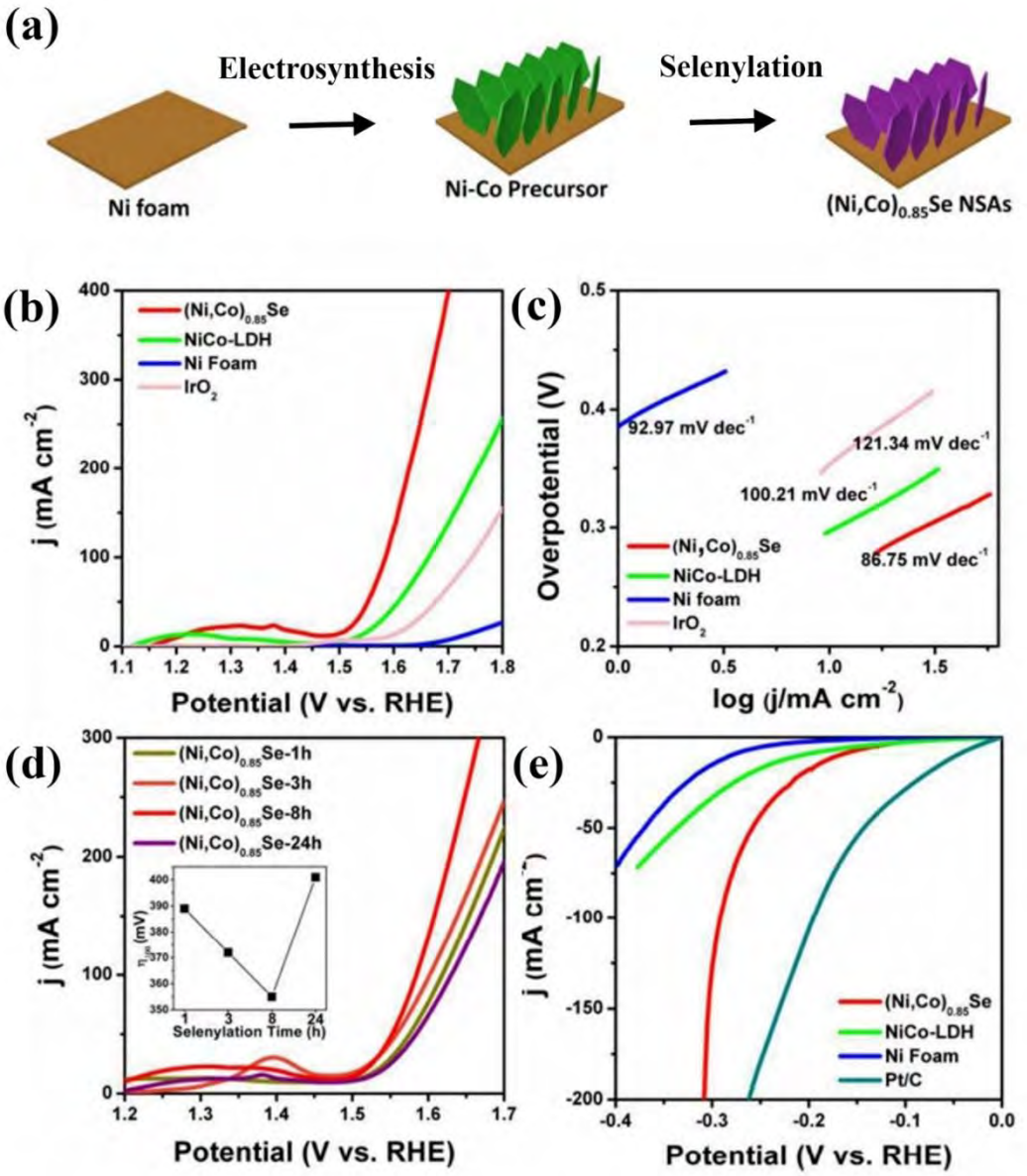

Figure 1.7: (a) Schematic illustration of $(NiCo)_{0.85}Se$ NSAs, (b) Linear sweep voltammogram of $(Ni,Co)_{0.85}Se$ for OER, (c) Tafel slopes of NiCo-LDH, bare Ni foam, $(Ni,Co)_{0.85}Se$ and IrO_2 for OER, (d) LSV of $(Ni,Co)_{0.85}Se$ with different times of selenization for OER (inset: overpotential volcano plot at 100 mA/cm^2), (e) LSV curves for HER. Copyright 2018 The Royal society of Chemistry.[238]

Bimetallic Alloy

LDH derived bimetallic alloys have emerged as potent material for electrocatalytic water splitting attributable to their unique structural and electronic properties. These materials have a high catalytic activity towards water splitting, owing to the presence of two different metal species in their structure. The layered structure of LDH provides high stability and prevents agglomeration of the nanoparticles, resulting in long-term durability. Additionally, the composition of these alloys can be easily modulated by changing the ratio of the metal precursors, allowing for the optimization of their electronic structure and catalytic activity towards water splitting. The electronic interactions between the two metal species lead to enhanced charge transfer between the catalyst and the reactants, resulting in increased catalytic activity. Furthermore, the precursors employed for their fabrication are economical and readily available, presenting a promising substitute for costly and scarce noble metal catalysts. Overall, LDH derived bimetallic alloys hold great potential for efficient and economical electrocatalysts for hydrogen generation through water splitting.

In recent times, the utilization of alloy catalysts has garnered significant interest from researchers, mainly due to the synergistic interplay exhibited by the constituent metals, coupled with their enhanced conductivity in processes like HER, OER, and ORR.[245] Notably, the NiCo alloy has emerged as a particularly appealing electrocatalyst for water splitting, attributed to the efficacious active sites provided by its Ni and Co components. This characteristic facilitates efficient electron and mass transfer, thereby bolstering electrolytic performance. Nonetheless, a considerable drawback of numerous NiCo alloy catalysts has been their tendency to obscure active sites due to aggregation and larger particle sizes. In this context, alloys characterized by a nanosheet structure hold the advantage of more readily exposing these pivotal active sites.

Yuanting Lei et al. have successfully fabricated a novel architecture of 3D interconnected NiO/CoFe alloy nanosheets using an electrochemical activation technique involving a NiO/CoFe-LDH pre-catalyst.[246] This intricate nanosheet arrangement not only maximizes the exposure of active sites but also facilitates rapid electrical conductivity, culminating in exceptional performance during both the HER and OER. The harmonious integration of NiO and CoFe alloy within this design yields remarkable electrocatalytic proficiency, as evidenced by notably low overpotentials of 218 mV at 10 mA cm^{-2} and 280 mV at 30 mA cm^{-2}, alongside commendable Tafel slopes. Impressively, the durability of these catalysts is also noteworthy, as they maintain their prowess for 27 h during HER and 42 hours during OER. This study showcases a promising avenue for crafting cost-effective, high efficiency electrocatalysts boasting a distinct structure, holding substantial promise for applications encompassing comprehensive water splitting and beyond.

Rahul Patil et al. conducted a study in which they synthesized bimetallic NiCo alloys supported on nitrogen-doped carbon derived from LDH precursors, resulting in NiCo@LDH-NC.[247] Through comprehensive structural and compositional analysis, the authors confirmed the formation of NiCo alloy particles with a unique arrangement. The alloy particles exhibited a coherent substitution of Co within the Ni lattice, aligning strongly with the (111) plane of Ni particles. This arrangement introduced strain to the face-centered cubic (fcc) lattice of the NiCo alloy, resulting in a robust interaction between the pure Ni and Co metals. The electronic structure of the NiCo@LDH-NC monolayer electrode displayed characteristics reminiscent of free atoms, contrasting with the host Ni lattice. Remarkably, in the OER during water electrolysis, the NiCo@LDH-NC electrode demonstrated minimal overpotentials of 330 mV and 346 mV at 10 and 20 mA cm^{-2}, respectively. This was accompanied by an improved electrokinetic-driven Tafel slope of 36.4 mV dec^{-1}, evident from the Tafel plot. The low Rct value of 2.48 Ω indicated swift charge transfer kinetics across the electrode-electrolyte interface, a key factor influencing the OER activity. This study's insights into the behavior of NiCo alloy and associated electronic structure hold promise for enhancing the characteristics of bimetallic alloy nanoarchitectures, potentially advancing various electrochemical processes.

Indeed, bimetallic alloy catalysts derived from LDHs have demonstrated their potential beyond water splitting and have exhibited remarkable results in various electrocatalytic applications. These catalysts benefit from their unique structure and composition, which offer synergistic effects between the constituent metals, enhanced surface area, and improved electronic properties. This versatility extends their usefulness to a wide range of electrochemical reactions, each benefiting from the tailored properties of these bimetallic alloy catalysts. For instance, Gao et al. devised a facile two-step process to synthesize core-shell structured Cu@(CuCo-alloy) nanocatalysts embedded within an Al_2O_3 matrix.[248] The method involved first growing a CuCoAl-LDH precursor onto an aluminum substrate, followed by a subsequent calcination and reduction step. HRTEM and high-angle annular dark-field scanning transmission electron microscopy (HAADDF-STEM) images revealed that the resultant CuCo-alloy catalysts, with nanoparticles measuring 15–20 nm in diameter, exhibited a core-shell arrangement. This structure exhibited a uniform and even distribution of Cu and Co, with Cu forming the core and a CuCo-alloy constituting the outer shell. In contrast to powdered-CuCo/Al2O3, Co/Al2O3, and Cu/Al2O3 catalysts, the core-shell Cu@(CuCo-alloy)/Al_2O_3 catalysts demonstrated markedly superior catalytic activity in the hydrogenation of CO into higher alcohols. The most optimal catalyst (Cu/Co = 1/2) achieved a 48.9% selectivity for C_{6+} 1-alcohols at a CO conversion of 21.5%. XPS revealed electron transfer from Cu to Co, signifying a robust electronic interaction between the two metallic components. Importantly, Cu-rich catalysts displaying predominantly bridge-type CO adsorption favored hydrocarbon selectivity, whereas Co-rich catalysts promoted oxygenated compound formation. The researchers proposed a reaction mechanism wherein negatively charged Co sites facilitated the dissociative adsorption of CO, leading to chain growth and the creation of C_nH_z groups, while electron-deficient Cu sites acted as active sites for associative CO adsorption, generating CO species. This study underscored the potential of constructing core-shell structures through LDH precursor calcination and reduction as a promising approach to enhance synergistic effects in bimetallic alloy catalysts.

Bimetallic Sulfides

Transition metal sulfides (TMSs) on account of exposed edge sites, low cost and high catalytic performance have been thoroughly studied as electrocatalysts for HER and

OER. However, aggregation and low conductivity are serious problems, along with instability under operating conditions that hinder its practical utility. TMSs are thus integrated with other nanomaterials to enhance charge mobility by preventing re-stacking and aggregation or doped with other metals to boost the catalytic performance.

Liu and coworkers described a facile approach for preparing the polymetallic sulfides of NiFeMoS by sulfurization of a NiFe-MoO_4-LDH precursor prepared by one pot solvothermal process (Figure 1.8(a)).[249] Using the LDH template, microspheres were formed by cross linking nanoplates embedded in metal sulfide nanoparticles. However, the confinement effect imposed by LDH inhibits the formation of metal sulfides, resulting in the MoS_2 and $(NiFe)S_x$ nanoparticles with abundant exposed edge sites. NiFeMoS-400 displays superior performance for HER in basic electrolyte by an overpotential of 210 mV to generate a catalytic current density of 10 mA/cm^2 (Figure 1.8(b)) and small value of Tafel slope of 88 mV/dec (Figure 1.8(c)). Additionally, the charge transfer resistance of the catalyst was measured by electron impedance spectroscopy (EIS), Nyquist plot shows NiFeMoS-400 has low charge transfer resistance (Figure 1.8(d)), the material exhibited its durability for continuous 15 h of activity in 1M alkaline solution of KOH (Figure 1.8(e)). The accelerated efficiency is mainly attributed to unique morphology derived from LDH nanosheets and large surface area of Mo/Ni/Fe-S nanoparticles with copious exposed edge sites. Moreover, abundant nanointerfaces also form structural defects between multi-metal sulfides to optimize Gibbs free energy facilitating water splitting.

Topotactic sulfidation of FeNi LDH was done by Long et al. to produce ultrathin β-INS nanosheets which exhibit high HER performance and stability in acidic conditions.[250] The annealing of β-INS was done to transform into metallic ultrathin α-INS, which results in enhanced activity. To gain a 10mA/cm^2 catalytic current density α-INS necessitates a 105 mV overpotential (as depicted in Figure 1.8(f)), exhibiting a negligible Tafel slope (40 mV/dec) (as illustrated in Figure 1.8(h)), minimal charge transfer resistance (as shown in Figure 1.8(i)), and long-lasting stability. To calculate the charge storage capability of the catalyst, cyclic voltammetry was executed in non-faradaic region at different scan rates (Figure 1.8(g)). To understand the better catalytic efficiency due to the Fe incorporation, DFT calculations were also carried out on α-INS and α-NiS. (Figure 1.8(j)). According to DFT calculations, the H^+ (H_{ad}) to already

absorbed proton (H^+) to form adsorbed H_2. The formation of H_2 on NiS catalyst occurs on Ni site while it prefers Fe site for INS catalyst. This infers that the introduction of Fe alters the electronic configuration of the active sites that assists HER process. The coherent migration of H_2 leaves the active center for the next cycle, enhancing the overall performance as is believed in the case of metal complexes and hydrogenase reactions. The dangling bases S near to the active metal site of Ni and Fe in INS nanosheets have same structural and chemical composition as that of $NiFeS_2$(μ-H) core in NiFe thiolato hydride complex.[251] It is thus rational to relate the mechanism of catalysis to metal complexes and hydrogenases towards HER.

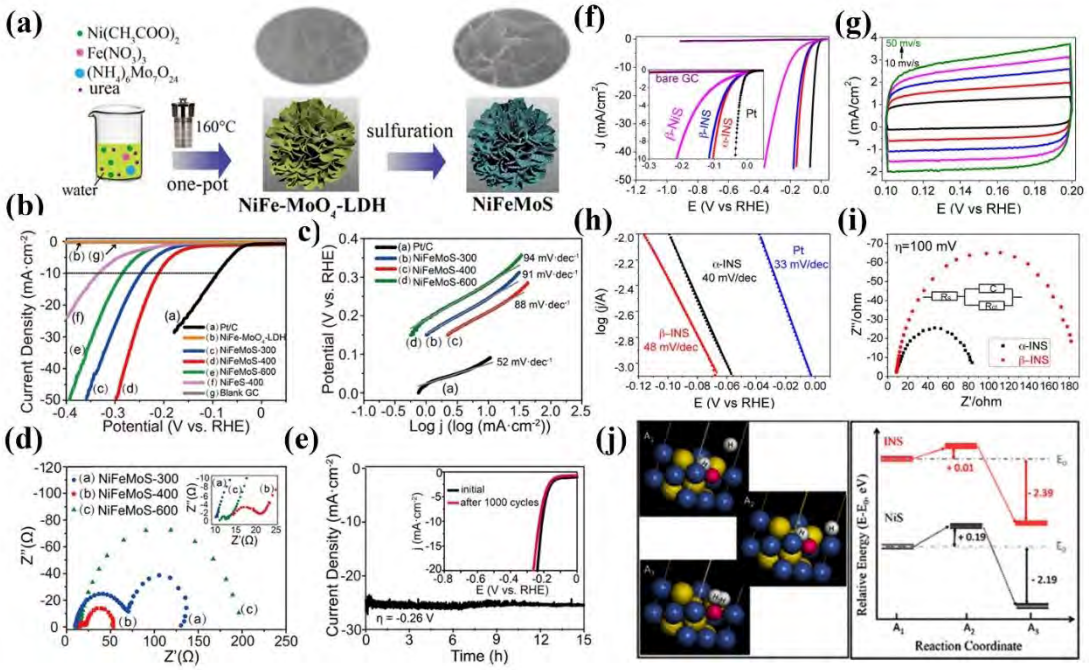

Figure 1.8: (a) Synthetic route of NiFeMoS-T, (b) LSV curves of Pt/C, NiFeMoS at different temperatures, and blank GC, (c) corresponding Tafel slopes, (d) Nyquist plots, (e) CPE data of the NiFeMoS-400 hybrid (inset: LSV recorded before and after 1000 CV cycles), (f) Linear sweep voltammograms for HER of β-INS, β-Ni-Sulfide and α-INS, (g) Cyclic voltammograms of β-NiS, β-INS nanosheets at different scan rates from 5-50 mV/s, (h) Tafel slope data plots of Pt, α-INS and β-INS, (i) EIS of β-INS and α-INS NS, (j) Schematics for HER pathway of α-INS nanosheets in acidic environment and kinetic barrier profiles of α-INS and α-NiS nanosheets. Yellow, blue, and red spheres in A_1-A_3 symbolize S, Ni and Fe, respectively. Copyright 2015 American Chemical Society.[250] Copyright 2019 IOP Publishing Ltd.[249]

Bimetallic Organic Frameworks (B-MOFs)

Metal-organic frameworks (MOFs) exhibits decent electrocatalytic performance owing to their perfect periodicity, porous structure, versatile topology, tunable functionalities, and abundant active sites.[252] However, due to the low conductance and mass permeation as well as insufficient stability, they are not actively employed as electrocatalysts for water splitting. To make MOFs effective electrocatalysts, the development of 2D MOFs with the nanosheet structures is considered a suitable approach for enhancing their conductivity, mass transport and exposed active sites i.e., the coordination-unsaturated metal sites.

Recently, LDHs have been utilized as a fruitful precursor of metal-oxide building block of MOFs. Since the space between the LDH 2D layers can adjusted and thus the ligands can target the inner Fe and Co from the interlayer, so LDHs are the excellent candidates for synthesis of 2D MOFs. For instance, Cai et al. demonstrated ligand-assisted synthesis of 2D MOFs from 2D LDHs and utilized them as electrocatalysts for water oxidation (Figure 1.9(a)).[253] The process involved the mixing of organic linker (benzene dicarboxylate; BDC) with the CoFe-LDH in DMF and kept at various temperatures and time duration. The resulting 2D CoFe MOF exhibits an overvoltage of 274 mV at 10 mA/cm^2 in 1 M KOH with 46.7 mV/dec Tafel slope. The catalyst shows stability for 70 h at 271 mV overpotential deposited over Ni foam (Figure 1.9(b-e)). The outstanding performance is because of unique 2D structure and coupling effect of Fe and Co, which assists charge transfer and ion diffusion.

Yang et al. used NiFe-LDH nanoarray on NF (NiFe-LDH/NF) as a template and precursor to fabricate highly ordered layered MOF ($Fe_{0.1}$–Ni–MOF/NF) (Figure 1.9(f)).[254] The Fe^{3+} and Ni^{2+} ions in the solution initially replaced proton positions that were uniformly distributed across either sides of NiFe-LDH layers. These cations then act as anchor points to form the MOF self-assembly. The $Fe_{0.1}$-Ni-MOF demonstrated exceptional activity, with overpotential values of 243 mV and 263 mV at 50 mA/cm^2 and 100 mA/cm^2, respectively, in an alkaline solution. Additionally, it exhibited a Tafel value of 69.8 mV/dec for OER. The multi-step chronopotentiometry curves suggest excellent mass transport and good conductivity with superior stability for 20 h (Figure 1.9(g-j)).

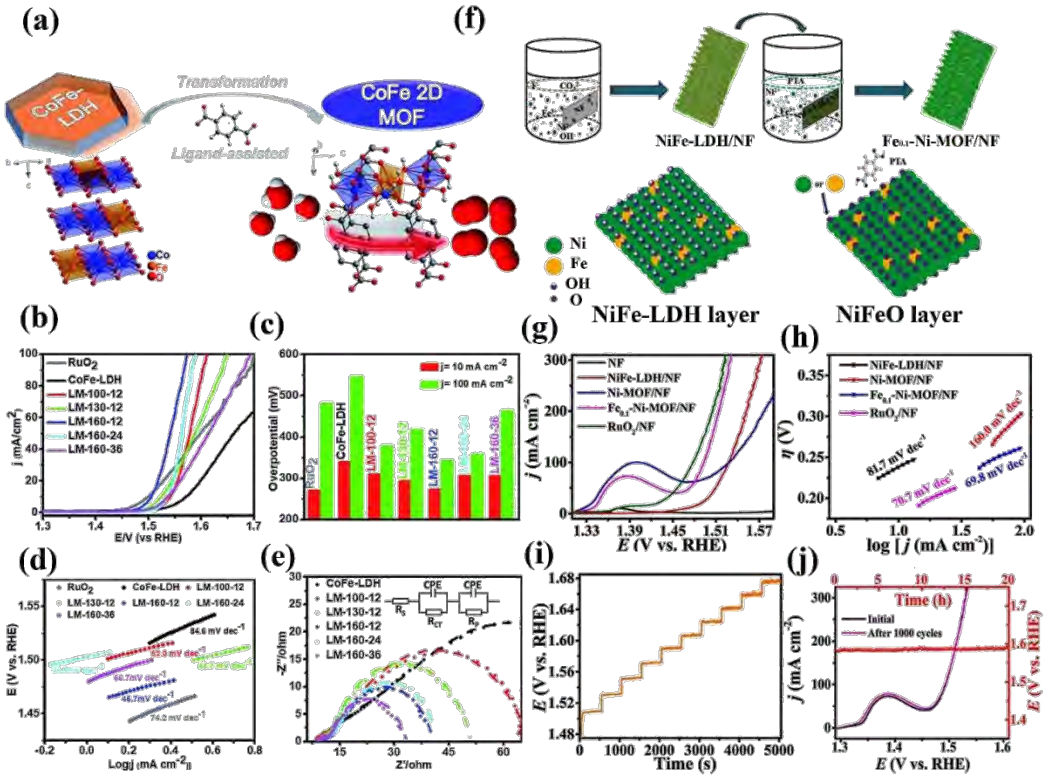

Figure 1.9: (a) Schematic representation of ligand-Assisted (LA) transformation to two dimensional–MOF, (b) LSV potential curves for OER, (c) OER overpotential at 10 and 100 mA/cm^2 is compared, (d) Tafel plots, (e) EIS curves, (f) Schematic of the fabrication process for $Fe_{0.1}$-Ni-MOF/NF, (g) Comparison of OER activity with sweep rate of 2 mV/s, (h) corresponding Tafel plots, (i) Multiple current approach for $Fe_{0.1}$-Ni-MOF/NF, (j) LSV curves for pristine and post 100 CV cycles of $Fe_{0.1}$-Ni-MOF/NF and CPE data for 20 h. Copyright 2019 The Royal Society of Chemistry.[253, 254]

Table 1.1: A comparison of recently reported LDH-derived materials for OER and HER.

S. No	Materials	Overpotential @ 10 mA/cm^2 (OER) (mV)	Overpotential @ higher j (OER) (mV)	Overpotential @ 10 mA/cm^2 (HER) (mV)	Ref.
1	PA-NiO/NF	-	330@100	138	255
2	β-$Ni(OH)_2$	-	500@ 250	-	256
3	β-$Ni(OH)_2$	415	-	-	257
4	FeNi-O nanosheet	213	-	-	258
5	NiFe-$NiCoO_2$	286	-	102	234

6	Mono-NiTi-MMO	320	-	-	[259]
7	NiFe-MMO/CNTs	-	-	-	[260]
8	Fe-CoOOH/G	330	-	-	[261]
9	$CoFeN_x$-500 HNAs/NF	-	259@50	200	[179]
10	Ni_3N-V_2O_3	-	-	57	[262]
11	Ni_3FeN-NPs	280	-	158	[237]
12	NSP-Ni_3FeN/NF	223	-	45	[263]
13	Mo-doped CoP	317	-	118	[236]
14	Hollow CoP/FeP_4@CNT	301	-	-	[264]
15	$(Fe_{0.2}Co_{0.8})_2P$@C	290	-	130	[265]
16	$(Ni_{0.2}Co_{0.8})_2P$@C	280	-	110	[265]
17	CoP@FeNiP/NF	-	283@100	-	[266]
18	CoNiP-NiFeLDH@NF	216	-	83	[267]
19	FeNi-LDH/CoP/CC	-	231@20	-	[268]
20	Fe-doped CoP nanoarray	230	-	78	[269]
21	$(Fe_xNi_{(1-x)})_2P$ nanosheets	156	255@500	-	[270]
22	NiCoP(PH_3 plasma-assisted)	280	-	32	[271]
23	Fe-CoP/CoO	219	-	-	[271]
24	Fe–NiP nanocomposite	233	-	-	[272]
25	Fe-Ni_2P/CC	-	215@50	-	[273]
26	Mn-doped CoP nanosheets	-	-	108	[274]
27	FeCoP UNSAs	-	330@100	160@100	[275]
28	α -INS ultrathin nanosheets	-	-	105	[250]
29	NiFeMoS-400	-	-	210	[276]
30	$FeCo_2S_4$-$NiCo_2S_4$/Ti	230	-	150	[277]
31	40% MoS_2/$NiCo_2S_4$	-	-	94	[278]

32	FeS–NiS/Ti	260	-	-	[279]
33	H-3DRG@NiCoLDH	289	-	-	[280]
34	H-3DRG@$NiCo_2S_4$	264	-	-	[280]
35	PA-$CoS_x(OH)_y$/NF	261	-	-	[281]
36	(NiCo)0.85Se NSAs@NF	-	287@20	169	[282]
37	$(Ni,Fe)_3Se_4$ nanasheets	225	-	173	[283]
38	$Ni_xFe_{1-x}Se_2$	195	-	-	[284]
39	$(Ni_{0.75}Fe_{0.25})Se_2$	-	225@35	-	[285]
40	$Ni_{0.76}Fe_{0.24}Se$ microspheres	197	-	-	[286]
41	CoFe 2D MOF	274	-	-	[253]
42	$Fe_{0.1}$-Ni-MOF/NF	-	243@50	-	[287]
43	Ni_xV_{1-x}-MOF	-	290@150	-	[288]

1.11 Electrochemical Evaluating Parameters

Electrochemical evaluation is a critical tool for studying the catalytic properties of LDHs and their derived materials. Electrochemical techniques can provide information on kinetics, thermodynamics, and mechanisms of various electrochemical reactions, such as OER, HER, or CO_2 reduction. Here are some commonly deployed electrochemical parameters for evaluation of catalytic performance of LDHs:

1.11.1 Overpotential (η)

An electrocatalytic reaction is most efficient if the applied voltage aligns with the equilibrium potential. Nevertheless, practical electrocatalysis demands a higher applied potential than the equilibrium potential to surmount the energy hinderance inherent in the reaction. The Nernst equation presents the relationship for an electrocatalytic redox reaction: [289]

$$E = E^0 + RT/nF \ln(C_{ox}/ C_{red})$$

In this equation, E signifies the actual applied potential, E^0 stands for the standard potential, R represents the universal gas constant, T is the absolute temperature, n corresponds to the quantity of electrons transferred, F denotes Faraday's constant, and Cred plus Cox denote concentrations of the reduced and oxidized reactants, respectively. To drive the reaction effectively, a surplus potential called overpotential (η) is necessary, calculated by the formula:

$$\eta = -(E - E_{eq})$$

Here, E_{eq} signifies the equilibrium potential. Researchers commonly report overpotential data at 10 mA/cm^2 current density.

1.11.2 Tafel Slope (b)

Tafel slope is a measure of the reaction kinetics and can be computed from the slope of the linear region of the polarization curve. It reflects the rate-determining step of the electrochemical reaction and is inversely proportional to the catalytic activity.[290] The Tafel slope can be estimated using the following formula:

$$\eta = \beta \log(i / i_0)$$

where β is the Tafel slope, η is the overpotential, i is the current density and i_0 is the exchange current density.

1.11.3 Exchange Current Density (j_0)

Exchange current density is an extent of the rate of the electrochemical reaction at equilibrium and can be determined from the intercept of the Tafel plot. It is associated to the catalytic activity and the electron transfer rate of LDHs. The exchange current density can be calculated using the following formula:

$$i = i_0 \cdot \exp (\alpha \cdot F \cdot \eta / RT)$$

where i is the current density, α is the current transfer coefficient , η is the over potential, and F is the faraday constant, R is the gas constant and T is the temperature.[291]

1.11.4 Turnover Frequency

Turnover Frequency provides a valuable measurement of how frequently catalytic cycles take place at the active sites of a catalyst within a given time. This parameter offers insights into the inherent efficiency of a catalyst and can be calculated using the formula provided:

$$TOF = J \times A / n \times N \times F$$

Here, 'j' represents the current density, 'N' stands for the number of moles corresponding to active sites, A denotes the surface area of the working electrode, 'F' is the Faraday constant, and n signifies the number of electrons needed to produce the target product (where n = 4 specifically for the OER).[292]

1.11.5 Double-Layer Capacitance (C_{dl})

Double-layer capacitance is a measure of the electrochemical surface area and can be determined from the impedance spectrum. It reflects the availability of active hotspots for the electrochemical reaction and can be deployed to calculate the catalytic activity and stability of LDHs.[293] The double-layer capacitance can be computed using the following formula:

$$C_{dl} = (1/i\omega)^{-1}$$

where C_{dl} is double-layer capacitance, i is the current, ω is the angular frequency, and the other symbols have the same meaning as in the impedance formula.

1.11.6 Electrochemical Active Surface Area (ECSA)

Electrochemical active surface area holds significant importance as a catalyst attribute ensuring the vulnerability of active sites. The assessment of ECSA involves the evaluation of C_{dl} exhibited by the catalyst within the non-faradaic region.[32] This is accomplished by plotting scan rates against current density at a constant potential,

wherein the slope of the resulting straight line corresponds to C_{dl}. The determination of ECSA is achieved using the subsequent equation:

$$ECSA = Cdl / Cs$$

Here, Cs represents the specific capacitance. For OER, the specific capacitance value (Cs) is reported to be 0.04 mF/cm² in 1 M KOH.[294]

1.11.7 Faradaic Efficiency (FE)

Faradaic efficiency is a measure of the selectivity and efficiency of the electrochemical reaction and can be determined from the current ratio of the desired product and the total current. It reflects the ability of LDHs to selectively catalyze the desired reaction and can be used to optimize the catalytic performance. The Faradaic efficiency is calculated by using the following formula:

$$FE = (nF \times \text{moles of desired product}) / (Q \times 100\%)$$

where FE is the Faradaic efficiency, n is the number of electrons transferred in the reaction, F is the Faraday constant, Q is the total charge passed, and moles of desired product is the amount of desired product formed during the reaction.[295]

1.11.8 Mass Activity

The mass activity parameter is an essential metric used to access the intrinsic activity of a catalyst, particularly in the context of electrocatalysis. It quantifies the efficiency of the catalyst in producing the desired product per unit mass of the active material over a specific period. The mass activity (M.A) is measured as the ratio of the current density (j) to the active material loading (m):

$$\text{Mass activity (M.A)} = j / m$$

In this equation, the current density (j) represents the current produced during the catalytic reaction, while the active material loading (m) is the mass of the catalytic material per unit geometric surface area of the electrode. By dividing the current density

by the active material loading, the mass activity parameter normalizes the catalytic performance with respect to the catalyst's mass, allowing for a good comparison of different catalysts and providing insights into their intrinsic activity. Mass activity parameter often use to assess and compare the efficiency of different catalysts for electrochemical reactions, such as fuel cells, water electrolysis, and other energy conversion technologies, where maximizing the catalytic activity is important for enhancement of the overall efficiency of the system.

1.11.9 Chronoamperometry (CA)

Chronoamperometry is a time-based electrochemical technique that gives information on the reaction kinetics and stability of LDHs. It involves application of constant potential to the electrode and measuring the resulting current over time. The decay of the current can indicate the stability and activity of the catalyst. The current can be computed using the following formula:

$$i = (Q/t)$$

where i is the current, Q is the total charge passed, and t is the time. The decay of the current can be analyzed to determine the stability and activity of the catalyst.[296]

By evaluating these electrochemical parameters, researchers can gain insights into the catalytic properties of LDHs and their derived materials and optimize their performance for various electrochemical applications. The overpotential, Tafel slope, and exchange current density can provide information on the kinetics and thermodynamics of the electrochemical reaction, while the double-layer capacitance and Faradaic efficiency can give information on the surface area and selectivity of the catalyst. Chronoamperometry can be used to access the stability and activity of the catalyst over time. Together, these electrochemical techniques can provide a comprehensive understanding of the catalytic performance of LDHs and their derived materials and guide the design of advanced materials for various electrochemical applications.

1.12 Aims and Objectives of the Research

The aims and objectives of this work are to:

1. Create and characterize diverse compositions and structures of LDHs and their derived nanomaterials.
2. Explore the electrocatalytic abilities of LDHs and their derived nanomaterials towards OER and HER.
3. Enhance the synthesis procedures and electrochemical performance of LDHs and their derived nanomaterials to maximize efficiency in these reactions.
4. Compare the electrocatalytic efficacy of synthesized nanocomposites with previously reported catalysts.
5. Investigate the stability and durability of LDHs and their derived nanomaterials during extended electrocatalytic reactions.
6. Develop a holistic comprehensive understanding between the structure and function of LDHs and their derived nanomaterials within the realm of electrocatalysis.
7. Propose potential applications of LDHs and their derived nanomaterials within renewable energy technologies, particularly in energy conversion.
8. Contribute to the advancement of superior and more sustainable electrocatalysts for electrolysis processes, thus fostering the transition toward a low-carbon economy.

Experimental

2 Experimental

2.1 Synthesized Materials and their Composition

In this section, we aimed to synthesize three distinct materials with varying molar ratios and subsequently determine the optimized ratio for each material. The synthesized materials were then utilized to fabricate composites with a chosen substrate, employing the respective optimized ratios. To begin, the synthesis process involved meticulous control over the molar ratios of the constituent elements. By carefully adjusting these ratios, we aimed to achieve materials with enhanced properties and performance characteristics. The three materials under investigation were selected based on their potential applicability toward electrocatalytic water splitting. The detailed composition of synthesized materials is summarized in the table below:

Table 2.1: Composition of synthesized materials

Materials	Materials with different ratio	Optimized ratio	Composite	Application
Material-I	CoMn-LDH (1:1)	CoMn-LDH (1:1)	CoMn-LDH@CuO/Cu_2O Heterostructure of hexagonal sheets of CoMn-LDH over HKUST-1 derived CuO/Cu_2O	Electrocatalytic OER
	CoMn-LDH (1:3)			
	CoMn-LDH (1:5)			
Material -II	NiCo-LDH (1:1)	NiCo-LDH (2:1)	NiCo-Alloy@CeO_2 Hetero-interface between LDH-derived bimetallic alloy over the surface of Ceria-nanorods	Electrocatalytic OER and HER
	NiCo-LDH (2:1)			
	NiCo-LDH (3:1)			
Material -III	NiFe-LDH (1:1)	NiFe-LDH (3:1)	NiFeSe@CoOx-NCNTs LDH-derived bimetallic nickle iron selenides sheets embedded ZIF-12 derived Co-based Carbon nanotubes	Electrocatalytic OER and HER
	NiFe-LDH (2:1)			
	NiFe-LDH (3:1)			

2.2 Synthesis of Material-I (CoMn-LDH@CuO/Cu_2O)

2.2.1 Materials

All the chemicals were used without any further purification, including sodium carbonate (Na_2CO_3, ≥ 99.0%, Sigma Aldrich), manganese (II) nitrate tetrahydrate (Mn $(NO_3)_2$. $4H_2O$, ≥ 99% trace metal basis, Sigma Aldrich), cobalt (II) nitrate hexahydrate (Co $(NO_3)_2$. $6H_2O$, 99%, Merck), copper (II) nitrate hexahydrate (Cu $(NO_3)_2$. $6H_2O$, 99.5%, Merck) and BTC ($C_9H_6O_6$, 98%, Sigma Aldrich).

2.2.2 Synthesis of HKUST-1 Derived CuO/Cu_2O

The synthesis of HKUST-1 involved a modified technique previously described by Wang et al. [297] This material has promising applications in various fields due to its unique properties. The process began by preparing two solutions: Solution A and Solution B. In Solution A, benzene tricarboxylic acid (BTC) was dissolved in ethanol. BTC serves as a crucial component for forming the final product. In Solution B, copper nitrate ($Cu(NO_3).6H_2O$), was dissolved in deionized water. This solution was mixed with strong agitation to ensure thorough mixing of the components. After preparing Solutions A and B, they were combined and transferred to a Teflon-lined stainless-steel autoclave. An autoclave is a high-pressure vessel used to carry out chemical reactions at elevated temperatures and pressures. The mixture was then subjected to a controlled temperature of 120 °C for a duration of 12 h. This controlled heating process is essential for the formation and growth of the desired HKUST-1 crystals. After this heating period, the autoclave was allowed to cool naturally to room temperature. The outcome of this process was the formation of blue-colored crystals known as HKUST-1. These crystals were separated from the remaining liquid through a filtration process. To ensure purity, the crystals were thoroughly washed using ethanol and deionized water. After washing, any remaining liquid was removed by carefully drying the crystals at a relatively low temperature of 80 °C overnight. To take the process further, the synthesized HKUST-1 crystals were subjected to calcination. Calcination involves exposing a substance to high temperatures in the presence of air or oxygen. In this case, the HKUST-1 crystals were heated at a significantly higher temperature of 900 °C for 3 h in an oxygen-rich environment. This process led to a transformation of the HKUST-1 crystals into CuO/Cu_2O particles. These particles are composed of copper (II) oxide

and copper (I) oxide, and they possess distinct properties that are useful for various applications. The entire process was carefully controlled and designed to produce the desired material, CuO/Cu_2O particles, by going through specific chemical transformations under controlled conditions. The figure 2.1 illustrates the different stages of the process, providing a visual representation of the transformations that occur.

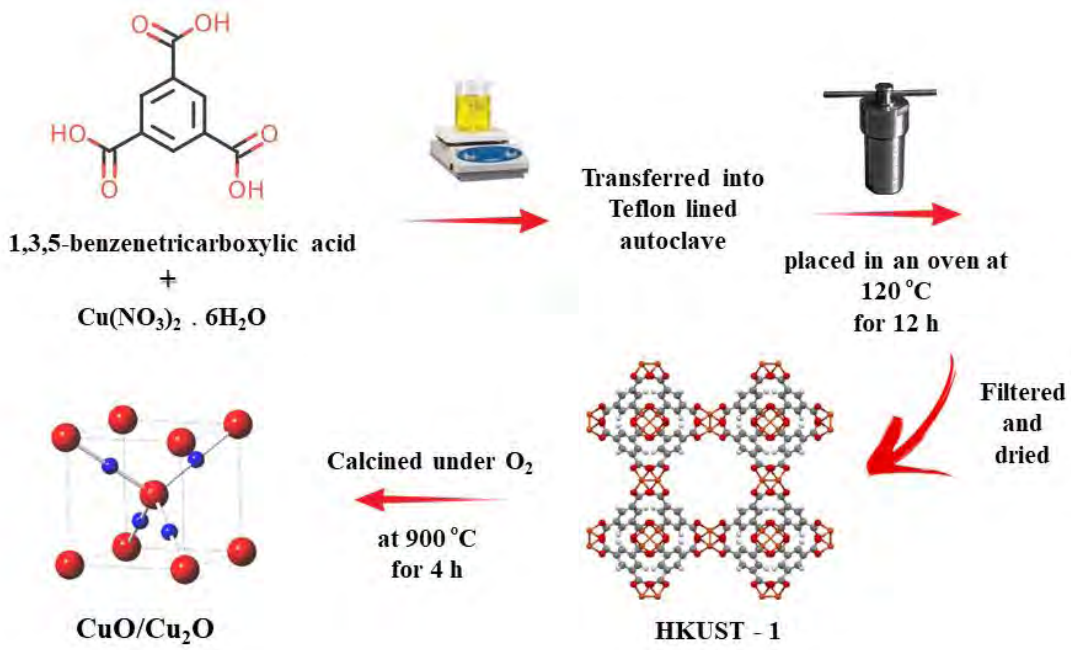

Figure 2.1: Schematic illustration for the synthesis of HKUST-1 derived CuO/Cu_2O.

2.2.3 Synthesis of Composite (CoMn-LDH@CuO/Cu₂O)

The fabrication process of the CoMn-LDH@CuO/Cu_2O composite involved a hydrothermal synthesis technique, as depicted in figure 2.2. This method enables the controlled growth of complex materials by exploiting the interactions between precursor components in a high-temperature aqueous environment. To initiate the process, 100 mg of the previously prepared CuO/Cu_2O particles were meticulously dispersed in 15 mL of deionized water. This dispersion is crucial to ensure uniform distribution and interaction of the components. The precursor compounds for CoMn-LDH, comprising 218 mg of cobalt nitrate hexahydrate ($Co(NO_3)_2.6H_2O$), 297 mg of manganese chloride tetrahydrate ($MnCl_4.4H_2O$), and 180 mg of urea, were

methodically introduced into the CuO/Cu_2O dispersion. Urea, in this context, plays a vital role as a complexing agent that facilitates the controlled formation of LDHs. The mixture was continuously stirred for a period of 3 h to ensure thorough mixing and interaction of the precursors. Subsequently, the homogenized mixture was carefully transferred into a specialized autoclave designed with a Teflon lining, which maintains a sealed environment conducive to the hydrothermal reaction. The autoclave was then subjected to a relatively high temperature of 130 °C for an extended duration of 24 h. During this hydrothermal treatment, the combined influence of heat and pressure enabled the conversion of the precursor materials into the desired composite structure. This process encourages the growth of CoMn-LDH and facilitates its integration with the CuO/Cu_2O particles. Following the hydrothermal treatment, the resulting solid precipitates were isolated from the liquid phase using a centrifugation process. This step helped to separate the composite particles from the residual solution. To ensure the removal of any residual impurities or unreacted materials, the obtained precipitates underwent a thorough washing procedure using deionized water. Finally, to eliminate excess moisture and achieve optimal particle stability, the composite material was subjected to a controlled drying process at a moderate temperature of 60 °C within a drying oven.

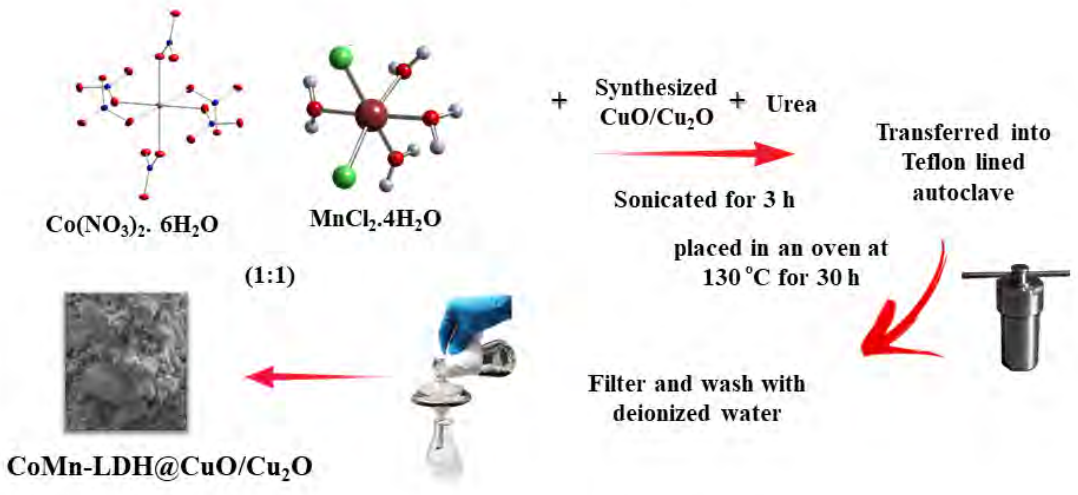

Figure 2.2: Schematic illustration for the synthesis of composite CoMn-LDH@CuO/Cu_2O.

In essence, the hydrothermal synthesis method employed here allowed for the controlled assembly of the CoMn-LDH@CuO/Cu_2O composite by guiding the transformation of precursor substances into a composite material with tailored properties. This process exploits the unique characteristics of each component to yield a synergistic material capable of serving various functional applications.

2.3 Synthesis of Material-II (NiCo-Alloy@CeO_2)

2.3.1 Materials

All the chemicals were used without any further purification, including potassium carbonate (K_2CO_3, ≥ 99.0%, Sigma Aldrich), Cerium nitrate hexahydrate (Ce $(NO)_3.6H_2O$, ≥ 99% trace metal basis, Sigma Aldrich), Cobalt (II) nitrate hexahydrate ($Co(NO_3)_3.6H_2O$, 99%, Merck), Nickel(II) nitrate hexahydrate ($Ni(NO_3)_2.6H_2O$, 99.5%, Merck) and Urea (CH_4N_2O, 98%, Sigma Aldrich).

2.3.2 Synthesis of CeO_2-nanorods

A reported synthetic approach was followed for the synthesis of ceria nanorods.[298] This approach is designed to systematically create nanoscale cerium dioxide (CeO_2) structures with specific properties. The process commenced by gradually adding a 0.03 M solution of K_2CO_3 drop by drop into a solution containing 0.02 M of $Ce(NO)_3.6H_2O$, corresponding to 4 mmol of cerium. This controlled addition was critical to achieving the desired pH of around 8, which triggered the onset of precipitation. The formation of a precipitate marks the initial stage of ceria nanorod synthesis. After allowing the reaction to proceed for 3 h under gentle agitation at room temperature, the formed solid was separated from the liquid phase using a centrifugation process. This step effectively isolated the evolving ceria nanorod material from the remaining solution. To ensure purity and remove any residual reaction components, the collected solid residues were subjected to thorough rinsing with deionized water. The next phase involved preparing the solid residues for further transformation. They were carefully placed within a ceramic crucible, a heat-resistant container suitable for thermal treatments. The residues were subjected to a prolonged drying process, spanning 10 h, at a moderate temperature of 70 °C. This step aimed to remove any remaining moisture, ensuring a stable starting material for subsequent processing. To achieve the final desired product, the dried

granules underwent a fundamental carbonization process. This was carried out within an electric furnace, with temperatures elevated to 650 °C. Maintaining this temperature for a duration of 5 h induced a controlled chemical transformation within the granules. This thermal treatment led to the conversion of the granular material into well-defined cerium dioxide nanorods, with their distinctive properties attributed to their nanoscale size and unique crystalline structure. The entirety of this sequential process, from controlled precipitation to purification and final thermal conversion, constitutes a highly controlled and structured approach to producing ceria nanorods. Each step is meticulously designed to ensure the formation of nanorods with specific characteristics and properties. The accompanying figure 2.3 likely provides a visual representation of the stages involved, further aiding in understanding the transformation of precursor solutions into the desired nanorod structure.

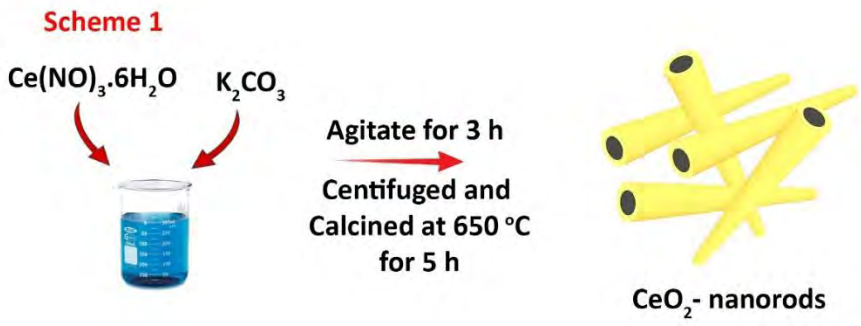

Figure 2.3: A schematic representation can visually demonstrate the synthesis of CeO_2 nanorods.

2.3.3 Synthesis of NiCo-Alloy@CeO_2

The synthesis of NiCo-Alloy@CeO_2 followed a systematic procedure, starting with the preparation of NiCo-LDH. Initially, 180 mg of urea was dissolved in an aqueous solution containing $Co(NO_3)_2.6H_2O$ and $Ni(NO_3)_2.6H_2O$ in a molar ratio of 1:2. This mixture was then stirred for a period of 3 h to ensure proper mixing and interaction of the components. Subsequently, the resulting solution was transferred to a Teflon-lined autoclave and exposed to a temperature of 130 °C for a duration of 24 h. This controlled thermal treatment facilitated the formation of solid precipitates. The obtained precipitates were subjected to several washings using deionized water to remove any residual impurities. Following this purification step, the solid material was carefully

dried within a desiccator, ensuring the removal of moisture, and achieving a stable material. The next step involved the annealing of the NiCo-LDH at 850 °C for a duration of 4 h under an Ar/H_2 atmosphere. This high-temperature treatment induced a chemical transformation, resulting in the formation of NiCo-alloy nanosheets. This annealing process is crucial for creating the desired alloy structure and enhancing material properties. Once the NiCo-alloy nanosheets were successfully synthesized, a previously reported impregnation method was employed to create NiCo-Alloy@CeO_2, a composite material. This method involves introducing CeO_2 onto the surface of the NiCo-alloy nanosheets to achieve the desired composite structure. The detailed protocol for this impregnation process is likely elaborated in reported article. [299] For a visual representation of the synthesis steps, Figure 2.4 illustrates the synthetic protocol of NiCo-Alloy@CeO_2, providing a clear overview of the sequence of processes involved in transforming precursor solutions into the final composite material. This systematic approach ensures the controlled creation of NiCo-Alloy@CeO_2, a material with tailored properties suitable for its intended application, likely as an electrode material.

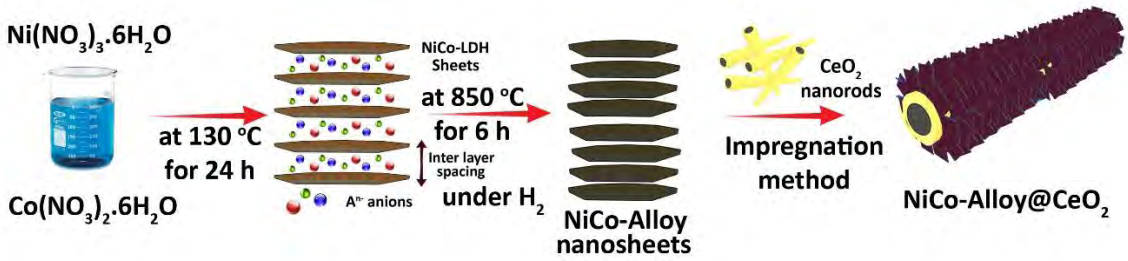

Figure 2.4: Schematic representation for the synthesis of NiCo-Alloy@CeO_2

2.4 Synthesis of Material-III (NiFeSe@CoOx-NCNTs)

2.4.1 Materials

All the chemicals used in the experiment were of high purity and obtained from reputable suppliers, including potassium carbonate (K_2CO_3) sourced from Sigma Aldrich, which had a purity level of 99.0%. Iron nitrate nonahydrate ($Fe(NO_3)_3.9H_2O$) was also employed, acquired from Sigma Aldrich, with a purity of 99% and trace metals, nickel nitrate hexahydrate ($Ni(NO_3)_2.6H_2O$) from Merck was incorporated, possessing a purity of 99.5%, urea (CH_4N_2O, 98% purity, from Sigma Aldrich), and

cobalt nitrate hexahydrate ($Co(NO_3)_2.6H_2O$, 99% purity, from Merck). The experiment also utilized benzimidazole ($C_7H_6N_2$, 98% purity, from Sigma Aldrich).

2.4.2 Synthesis of ZIF-12

The synthesis of ZIF-12 commenced with the dissolution of cobalt nitrate hexahydrate and benzimidazole in dimethylformamide solvent, as illustrated in figure 2.5. By mixing these solutions, precursor compounds were homogeneously blended. This mixture was then carefully transferred into a specialized Teflon-lined autoclave, providing a controlled environment for subsequent processes. Within the autoclave, a solvothermal reaction occurred at 150°C for 48 h, facilitating the gradual formation of ZIF-12 crystals through intricate chemical interactions.[300] After the solvothermal reaction, the solution was filtered, yielding shiny, purple-colored ZIF-12 crystals. Rigorous washing with excess DMF followed to ensure purity. Subsequently, the crystals were dried at 70°C to eliminate residual solvent. This systematic approach involved controlled dissolution, reaction, and purification steps, ultimately leading to the successful synthesis of visually distinctive ZIF-12 crystals. The accompanying figure 2.5 likely depicted the procedure's key stages, enhancing the understanding of the precursor-to-crystal transformation.

Figure 2.5: Illustration showing the formation of ZIF-12 through a solvothermal method.

2.4.3 Carbonization of ZIF-12

To obtain cobalt oxide encapsulated nitrogen-doped carbon nanotubes (CoOx/N-CNT), the synthesized ZIF-12 underwent a carbonization process. This involved placing the ZIF-12 sample in a ceramic boat and putting it into a quartz tube within a tube furnace

(Nabertherm B 180). Initially, the air within the tube was evacuated by continuous argon flow for 2 h, ensuring an inert atmosphere conducive to the subsequent steps. Subsequently, the sample was subjected to a calcination process at 950°C for 6 h. This thermal treatment facilitated the transformation of the ZIF-12 into cobalt oxide-encapsulated nitrogen-doped carbon nanotubes (CoOx/N-CNT), resulting in approximately 83% yield of the target CoOx/N-CNT material, as depicted in figure 2.6. This transformation involves the carbonization of the organic components of ZIF-12 and the controlled formation of cobalt oxide nanoparticles encapsulated within a nitrogen-doped carbon nanotube matrix. It is important to note that prior research conducted by our research group has reported the comprehensive synthesis and characterization of these nanotubes, highlighting the previous scientific contributions in this area of study. [301]

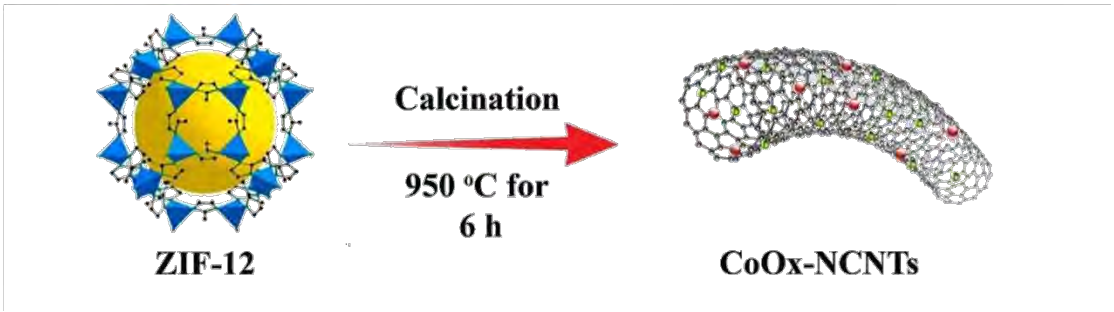

Figure 2.6: Schematic depiction of the carbonization route used for the synthesis of CoOx-NCNTs from ZIF-12 precursor.

2.4.4 Synthesis of NiFeSe@CoOx-NCNTs

The synthesis of NiFeSe@CoOx-NCNTs involved a two-step process, with the initial phase centered on the synthesis of NiFe-LDH@CoOx-NCNTs, as illustrated in figure 2.7. This process began by mixing the precursors $Ni(NO_3)_2.6H_2O$ and $Fe(NO_3)_3.9H_2O$ in a 3:1 ratio, along with 180 mg of urea and the synthesized CoOx-NCNTs (100mg). The resulting mixture underwent sonication for 3 h to ensure thorough mixing and uniform dispersion of the components. Subsequently, the solution was transferred into a Teflon-lined autoclave, where it underwent treatment at a temperature of 130°C for 30 hours. This controlled thermal treatment led to the formation of precipitates within the solution. The resulting precipitates were separated from the liquid phase through centrifugation and underwent washing with deionized water to remove any residual

impurities. The obtained NiFe-LDH@CoOx-NCNTs were subjected to a drying process at 60°C, followed by annealing at a temperature of 850°C for a duration of 4 hours under an Ar/H_2 atmosphere. During this annealing process, an additional component, Se powder, was strategically positioned upstream. This arrangement facilitated the interaction of Se with the precursor materials, resulting in the transformation into the final product, NiFeSe@Co-NCNTs. This synthesis process results in the synthesis of NiFeSe@Co-NCNTs, a material with a tailored composition and properties. The utilization of a two-step approach, starting with the formation of NiFe-LDH@CoOx-NCNTs, followed by annealing in the presence of Se, enables the controlled incorporation of Se into the composite structure. This synthesis method offers precise control over the composite's characteristics, making it suitable for specific applications. The presented figure 2.7 likely offers a visual representation of the synthesis process, aiding in understanding the transformation of precursor components into the final NiFeSe@Co-NCNTs product.

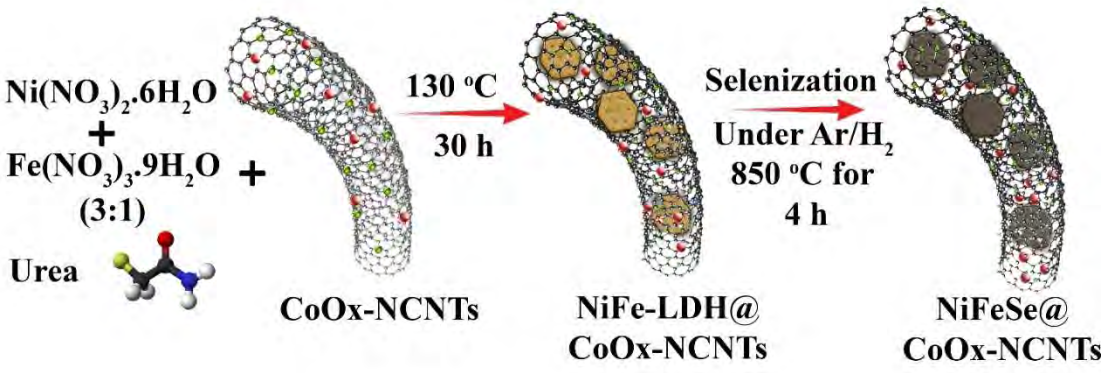

Figure 2.7: Step-by-step illustration for the synthesis of NiFeSe@CoOx-NCNTs .

2.5 Fabrication of Working Electrode

The fabrication of the working electrode entailed the choice of a glassy carbon substrate possessing a specific surface area of 0.1962 cm^2. Ensuring the substrate's cleanliness and purity, an exhaustive cleaning procedure was implemented to eliminate any potential contaminants that could influence the subsequent electrochemical measurements. To prepare the catalyst dispersion, a precisely measured mass of 2 mg of the catalyst material was dispersed within 1 mL of ethanol. This solvent not only facilitates the dispersion process but also ensures compatibility with subsequent

electrode coating. To enhance both the stability and the adherence of the catalyst on the electrode surface, a strategic addition of 5 µL of Nafion solution was incorporated into the catalyst dispersion. Nafion serves to create a stable interface between the catalyst and the electrode, promoting better performance and more consistent results. The catalyst dispersion underwent a 3 h sonication period.

Figure 2.8: Schematic representation of the fabrication of a working electrode using the drop casting method.

This ultrasonic treatment promotes effective mixing and distribution of the catalyst within the solvent, yielding a well-homogenized ink with uniform particle distribution. This ink was meticulously applied onto the pristine glassy carbon electrode. During this process, careful attention was paid to ensure a consistent and even spread of the catalyst ink on the electrode's surface. This uniformity is pivotal for obtaining reproducible and reliable electrochemical measurements. Following the ink application, the coated electrode was subjected to a drying process within an oven. This drying phase facilitated the removal of the ethanol solvent, leaving behind a firmly attached and well-adhered catalyst film on the electrode surface. This film forms a crucial component of the working electrode, as it provides the active sites for catalytic reactions during electrochemical studies. In essence, this well-orchestrated procedure guarantees the preparation of a functional working electrode that boasts a consistent and uniformly distributed catalyst layer. The meticulous steps taken in cleaning, catalyst dispersion,

application, and drying ensure accurate and reproducible electrochemical analyses, making the electrode a reliable tool for investigating catalytic processes. The process is depicted in figure 2.8, likely offering a visual representation of the steps involved in the creation of the working electrode.

2.6 Electrochemical Evaluation

Throughout the entirety of the electrochemical experiments, a conventional three-electrode system was employed, facilitated by a Gamry Interface 5000E potentiostat and a rotating disk electrode assembly. The experimental setup consisted of a single compartment, wherein a glassy carbon electrode possessing a surface area measuring 0.1962 cm^2 was designated as the working electrode. Concurrently, a Hg/HgO electrode as reference electrode, while a graphite rod was employed as the counter electrode. To facilitate the measurements, a 1M KOH electrolyte was consistently utilized, and prior to the commencement of electrochemical evaluations, the electrolyte was calibrated by purging N_2 gas for a duration of 30 minutes to ensure optimal experimental conditions. A comprehensive assessment of electrochemical performance was executed employing a variety of techniques. Linear sweep voltammetry was conducted, maintaining a scan rate of 10 mV/s while the working electrode was rotated at a speed of 1600 rpm. Impedance assessment encompassed a wide-ranging frequency spectrum spanning from 0.01 Hz to 100 kHz. Chronoamperometry tests were performed to evaluate the catalyst's stability under varying conditions. Additionally, cyclic voltammetry recorded cyclic voltammograms within a specified narrow potential window of 1-1.3 V vs RHE, across a range of scan rates spanning from 5 mV/s to 50 mV/s, thereby facilitating the determination of double-layer capacitance. To ensure a consistent basis for comparison and analysis, all potential values were transformed into the RHE scale by using the Nernst equation. This conversion accounted for any variations in reference electrode potentials, ultimately rendering the data more reliable for thorough interpretation and cross-comparison.

2.7 Characterization Techniques

The synthesized materials were subjected to different characterization techniques to investigate their chemical structure and morphology. These techniques included powder X-ray diffraction (PXRD), scanning electron microscopy (SEM), transmission electron

microscopy (TEM), X-ray photoelectron spectroscopy (XPS), energy-dispersive X-ray spectroscopy (EDX), selected area electron diffraction (SAED), and electron energy loss spectroscopy (EELS) mapping. These analyses were carried out to gain a comprehensive understanding of the synthesized materials' properties and to obtain valuable insights into their composition and structural features.

2.7.1 Powder X-ray Diffraction (PXRD)

XRD data was acquired using a Bruker D8 diffractometer equipped with a sealed copper (Cu) tube with a wavelength (λ) of 1.54178 Å. The XRD data was collected over a range of 10-80° with a scanning rate of 2° per minute.

Working Principle: This technique operates on the fundamental concept of X-ray scattering through a powdered sample. When X-ray radiation interacts with a polycrystalline substance, it undergoes diffraction at distinct angles upon encountering the atoms in the crystal lattice. Through the measurement of both the intensity and angle of these diffracted X-rays, it becomes possible to deduce the interatomic distances existing within the crystal lattice. Consequently, this methodology facilitates the recognition of crystal structure of the material, phase composition, and lattice parameters.

2.7.2 Scanning Electron Microscopy (SEM)

The SEM images were captured using a Hitachi S4800 microscope operating at an accelerating potential of 10 kV.

Working principle: The principle involves directing a primary electron beam onto the sample's surface, which results in the ejection of secondary electrons and backscattered electrons. These emitted electrons are then detected, and their signals are converted into an image. The primary electron beam scans across the sample in a raster pattern, allowing for the collection of data point by point. By controlling the intensity of the primary electron beam and detecting the emitted electrons, SEM produces high-resolution, detailed images of the sample's surface, providing information about its morphology, topography, and elemental composition.

2.7.3 High Resolution Transmission Electron Microscopy (HR-TEM)

HRTEM images were captured using a JEOL 2100 Cryo TEM instrument equipped with an X emitter, operating at an accelerating voltage of 200 kV. This instrument allows for imaging samples with high spatial resolution and enables detailed examination of the atomic structure and morphology of materials.

Working Principle: TEM is an advanced imaging technique that allows for high-resolution examination of the internal structure of thin specimens. The working principle of TEM involves a beam of electrons being transmitted through a thin sample. The electron beam is generated and accelerated, and then passes through the specimen, interacting with its atoms along the way. As the electrons pass through the specimen, they undergo scattering, diffraction, and absorption, forming an image on a fluorescent screen or a detector. By manipulating the electron beam, adjusting the lens system, and collecting the transmitted electrons, TEM produces detailed images that reveal the specimen's atomic structure, crystal defects, and fine details.

2.7.4 Selected area Electron Diffraction (SAED)

The acquired HR-TEM images were further analyzed using SAED technique, which involves selecting a specific area of the sample and obtaining a diffraction pattern by interacting it with a focused electron beam. The SAED analysis provides valuable information about the crystallographic structure and orientation of the sample.

Working Principle: It works on the principle of electron diffraction, where a selected area of the sample is exposed to a highly focused electron beam. As the electrons interact with the crystal lattice, they are diffracted by the atomic planes and produce a diffraction pattern. This pattern is recorded on a detector and represents the arrangement of atoms within the crystal lattice. By analyzing the intensity and distribution of the diffraction spots, valuable information about crystal symmetry, lattice parameters, and crystal orientation can be obtained.

2.7.5 Electron Energy Loss Spectroscopy (EELS)

EELS mapping was performed using the same instrument utilized for TEM analysis. The EELS measurements were performed with a probe size of approximately 1 nm and a beam energy of 200 keV. The spectrometer was set to collect energy-loss spectra in

the range of 0-2000 eV, with a dispersion of 0.1 eV per channel. The EELS mapping was carried out by scanning the electron probe over the sample area of interest and acquiring spectra at each pixel to generate a spatial distribution map of the elemental composition and chemical bonding information within the sample.

Working Principle: EELS operation is based on the principle of inelastic scattering of electrons. In EELS mapping, a focused electron beam is directed onto the sample surface, and as the electrons interact with the atoms in the sample, some of them lose energy through inelastic scattering processes. By measuring the energy loss of the scattered electrons, valuable information about the material's electronic structure, elemental composition, and chemical bonding can be obtained. The collected data is then used to generate maps that provide spatially resolved information about the distribution of specific elements, chemical states, and their variations across the sample.

2.7.6 X-ray Photoelectron Spectroscopy (XPS)

XPS analysis was performed using the Kratos AXIS Ultra DLD instrument. The XPS measurements utilized monochromatic Al Kα radiation at an operating voltage of 15 kV. The photoelectrons were emitted at a detection angle of 90°. The peak positions in the XPS spectra were calibrated using the C 1s peak at 284.4 eV as a reference, and other peaks were adjusted accordingly. The peak fitting analysis was carried out using Casa XPS software, allowing for accurate determination of the chemical states and composition of the analyzed samples.

Working Principle: XPS operates based on the principle of photoelectric effect. In XPS, a material sample is bombarded with X-ray photons, typically from a monochromatic X-ray source. When the X-ray photons interact with the sample's surface, they eject photoelectrons from the atomic orbitals of the constituent atoms. These photoelectrons are then energy-analyzed and detected to generate a spectrum. By measuring the kinetic energy and intensity of the emitted photoelectrons, XPS provides valuable information about the elemental composition, chemical states, and electronic structure of the surface region of the material.

2.7.7 Energy dispersive X-ray Spectroscopy (EDX)

EDX data was collected using a Shimadzu EDX-700 spectrometer equipped with Rhodium (Rh) X-rays as the excitation source. To prepare the samples for analysis, powder samples were loaded onto a polypropylene cup with an ultralene film placed at the bottom.

Working Principle: Energy-dispersive X-ray spectroscopy (EDX) operates on the principle of X-ray fluorescence. When a sample is bombarded with high-energy X-rays, the atoms within the sample are excited and subsequently emit characteristic X-rays that are specific to each element. In EDX, a detector measures the energies of these emitted X-rays, allowing for the identification and quantification of the elements present in the sample. The detected X-ray energies are then converted into a spectrum, which represents the elemental composition of the sample.

Results and Discussion

3 Results and Discussions

3.1 Material-I (CoMn-LDH@CuO/Cu_2O)

The novel CoMn-LDH@CuO/Cu_2O was successfully fabricated by a simple and facile process. CuO/Cu_2O nanoparticles produced by the calcination of HKUST-1 were added during the growth of CoMn-LDH nanosheets and their integration is proved using PXRD, SEM, TEM, EDX and XPS techniques. Complete characterization is discussed in detail in this section. The desired electrocatalyst exhibits High performance OER activity. The optimized electrode required just 297 mV overpotential to attain catalytic current density of 10mA/cm^2 along with the Tafel slope value (89 mV/dec^1) which is remarkably lower than the individual CoMn-LDH and CuO/Cu_2O. Figure 3.1 illustrates the graphical representation of OER catalysis using CoMn-LDH@CuO/Cu_2O composite material. The incorporation of cobalt manganese layered double hydroxide (CoMn-LDH) with HKUST-1 derived CuO/Cu_2O results in enhanced catalytic activity and stability, leading to the production of oxygen gas from water electrolysis.

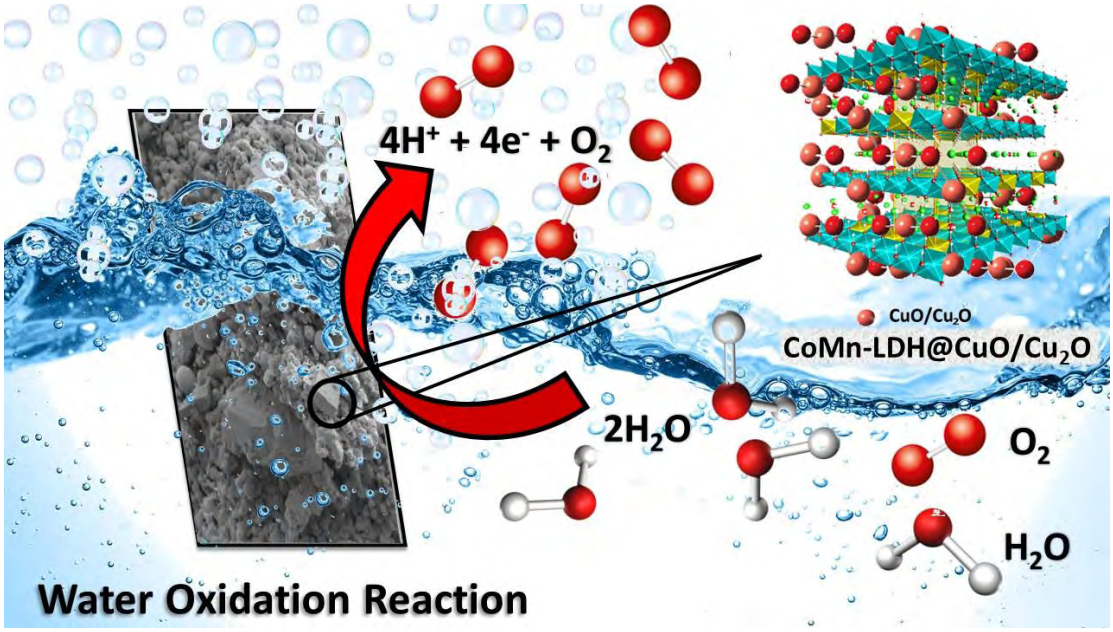

Figure 3.1: Graphical representation of the OER catalysis using CoMn-LDH@CuO/Cu_2O composite material.

3.1.1 Powder X-ray Diffraction Analysis

To investigate the lattice parameters of the synthesized catalysts, powder X-Ray Diffraction (pXRD) patterns were taken. Figure 3.2 showed the characteristic diffraction peaks at 11.54°, 23.76°, and 33.5°, which confirmed the layered morphology and could be indexed to the (003), (006) and (009) planes of LDHs (JCPDS # 01-089-0460) [302]. 2θ angles of 35.6°, 38.9°, 48.8°, 53.7°, 58.6°, 61.9°, 65.6°, 67.8°, correspond to the indices (002), (111), (-202), (020), (202), (-113), (-311) and (220) reflections of CuO lattice planes respectively (JCPDS # 00-002-1040).[303] Moreover, the diffraction peaks at 36.6°, 42.5° and 73.4° belong to the (111), (200) and (311) lattice planes of Cu_2O respectively (JCPDS # 00-001-1142). The intensity of the typical diffraction peaks of Cu_2O (111) and CuO (111) planes shows that CuO is the predominant specie produced, with traces of Cu_2O.[304-306] The pXRD pattern of CoMn-LDH@CuO/Cu_2O have all the characteristics peaks of CoMn-LDH and MOF derived CuO/Cu_2O which reveals that dispersion of CuO/Cu_2O does not change the chemical composition of the catalyst.

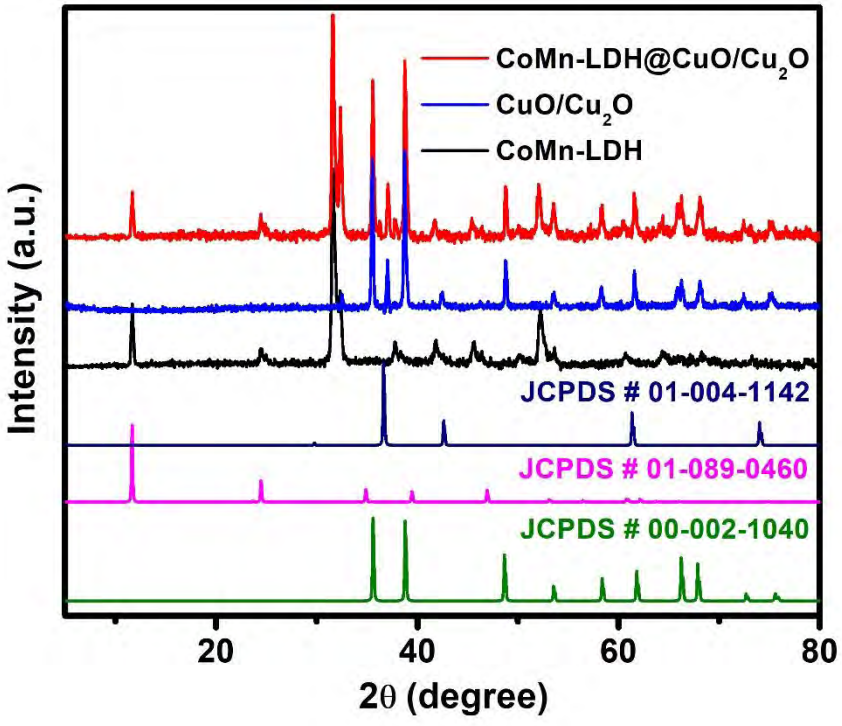

Figure 3.2: Comparison of powder XRD patterns of CoMn-LDH (black), CuO/Cu_2O (blue) and CoMn-LDH@CuO/Cu_2O (red)

3.1.2 X-ray Photoelectron Spectroscopy (XPS)

The surface elemental composition was thoroughly examined and confirmed through X-ray photoelectron spectroscopy (XPS) analysis. Figure 3.3(a) of the spectroscopic data reveals the presence of two prominent peaks at 781.6 eV and 798.2 eV, corresponding to the binding energies (BEs) of Co $2p_{3/2}$ and Co $2p_{1/2}$, respectively. Additionally, two satellite peaks were observed at slightly higher energies, measuring 786.8 eV and 803.4 eV. The measured BE of Co $2p_{3/2}$ falls within the range distinct from that of Co^0 (777.6 ± 0.8 eV) but shows proximity to the Co^{2+} state (780.9 ± 0.4 eV), indicating the prevalent valence state of cobalt as Co^{2+}.

Moreover, mixed oxidation states of manganese (Mn) were also detected within the analyzed sample. The XPS analysis revealed three distinct binding energy values: 641.4 eV, 642.8 eV, and 644.7 eV, which corresponded to Mn^{2+}, Mn^{3+}, and Mn^{4+}, respectively. Figure 3.3(b) displayed the Mn $2p_{1/2}$ peak at 647.3 eV, further supporting the existence of multiple states of oxidation of manganese. In Figure 3.3(c), the XPS analysis exhibited two main peaks in the Cu $2p_{3/2}$ and Cu $2p_{1/2}$ binding energy regions, measured at 933.8 eV and 953.5 eV, respectively. These peaks displayed a spin-orbit splitting of approximately 20.2 eV. Additionally, the appearance of two satellite peaks at higher binding energies, along with a shoulder peak in the Co $2p_{3/2}$ region, indicated the presence of both Cu^{2+} and Cu^{+} states within the sample. Furthermore, the deconvolution analysis of the O 1s peak resulted in the formation of two distinct subpeaks Figure 3.3(d). The first subpeak at 532.3 eV corresponded to 'O' in CuO, while the second subpeak at 533.5 eV represented 'O' present in chemisorbed hydroxyl groups. This analysis provided valuable insights into the chemical environment and bonding configurations of oxygen within the sample.

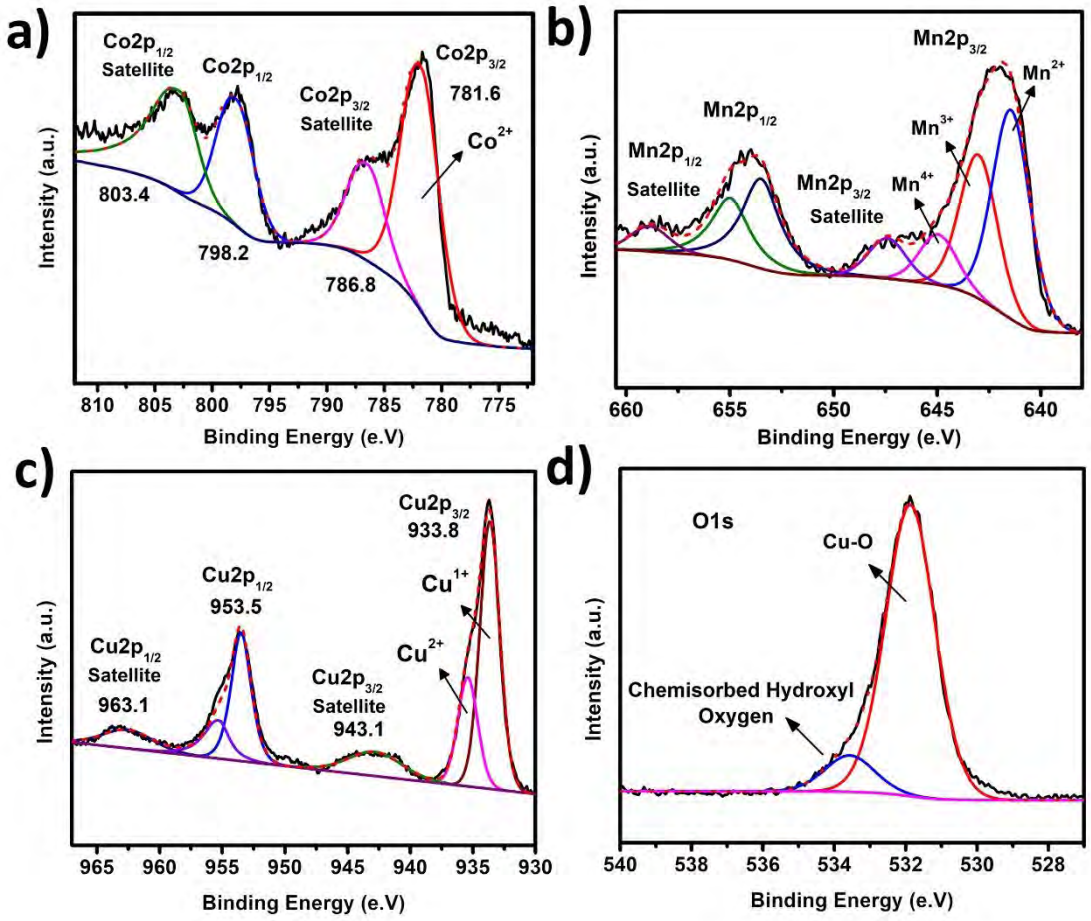

Figure 3.3: XPS spectra of CoMn-LDH@CuO/Cu_2O composite material, showing core-level binding energies for (a) Co 2p, (b) Mn 2p, (c) Cu 2p, and (d) O 1s orbitals.

3.1.3 SEM and TEM Analysis

The size, morphology, and structural characteristics of the synthesized materials were comprehensively examined by using scanning electron microscopy (SEM) and high-resolution transmission electron microscopy (HRTEM). The interior structure of both the as-synthesized CoMn-LDH and the composite CoMn-LDH@CuO/Cu_2O was specifically investigated using HRTEM, allowing for a detailed analysis at the atomic scale. SEM and TEM images of CoMn-LDH, as depicted in Figure 3.4 (a and c), exhibit the presence of hexagonal platelets, which provide further confirmation of the layered structure of CoMn-LDH. This observation aligns with the expected morphology based on the synthesis process. Moving on to the composite CoMn-LDH@CuO/Cu_2O, SEM and HRTEM images depicted in figure 3.4 (b and d) highlight the successful dispersion of Cu-BTC derived CuO/Cu_2O nanoparticles across the layers of LDH. The uniform

distribution of CuO/Cu_2O within the LDH structure facilitates effective mass and charge transfer, resulting in a high ECSA. The HRTEM images in Figure 3.4(d) also reveal lattice fringes within the composite material, indicating the crystalline nature of CuO/Cu_2O. The measured d-spacing values of 0.23 nm and 0.245 nm correspond to the (111) plane of CuO and the (111) plane of Cu_2O, respectively, further corroborated by X-ray diffraction (XRD) spectra. These lattice fringes provide direct evidence of the crystal structure and orientation of the CuO/Cu_2O nanoparticles within the composite.

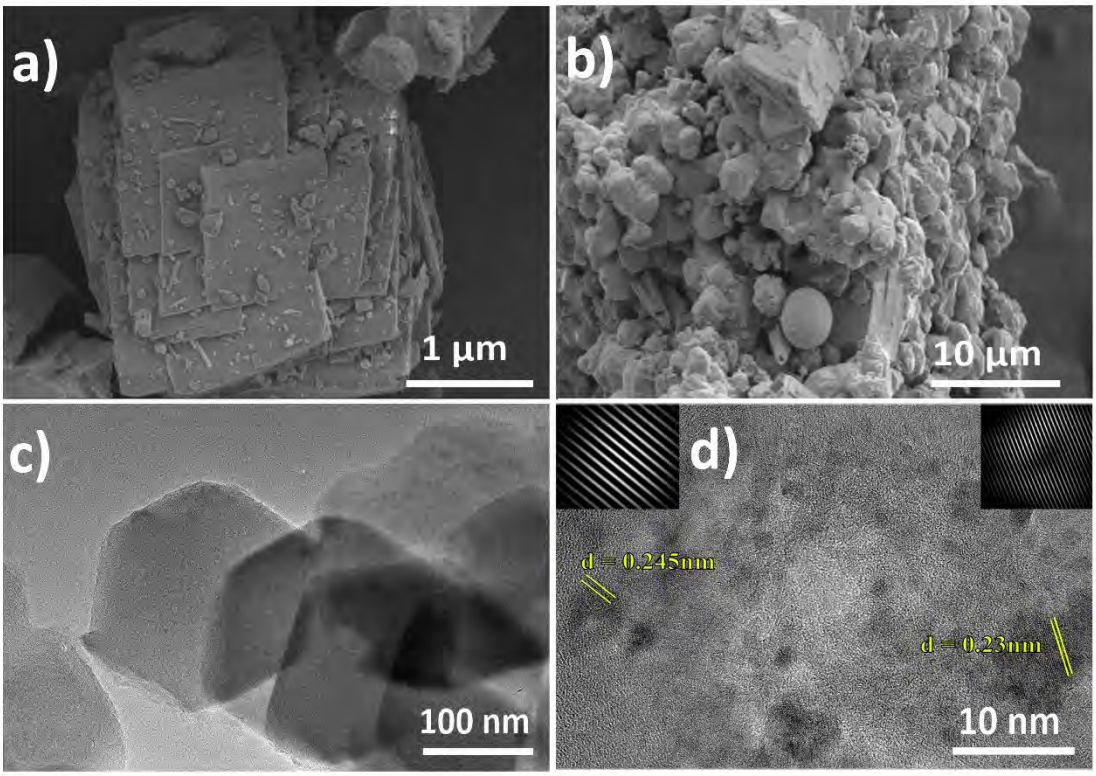

Figure 3.4: Scanning Electron Microscopy (SEM) and Transmission Electron Microscopy (TEM) images of (a and c) CoMn-LDH and (b and d) CoMn-LDH@CuO/Cu_2O nanocomposites.

3.1.4 Elemental Mapping

Elemental mapping was conducted to investigate the elemental composition and distribution within the CoMn-LDH@CuO/Cu_2O composite material in Figure 3.5 (a-d). The elemental mapping technique provides valuable insights into the spatial distribution of various elements present in the composite, allowing researchers to analyze and understand the composite's chemical composition and its homogeneity or

heterogeneity. The resulting maps offer a visual representation of the distribution of cobalt, manganese, copper, and oxygen elements, aiding in the characterization and optimization of the composite material for its intended application. The obtained results show the homogeneous distribution of elements, including Co, Mn, Cu, and O, across the entire sample. This further confirms the successful formation of the CoMn-LDH@CuO/Cu_2O composite material.

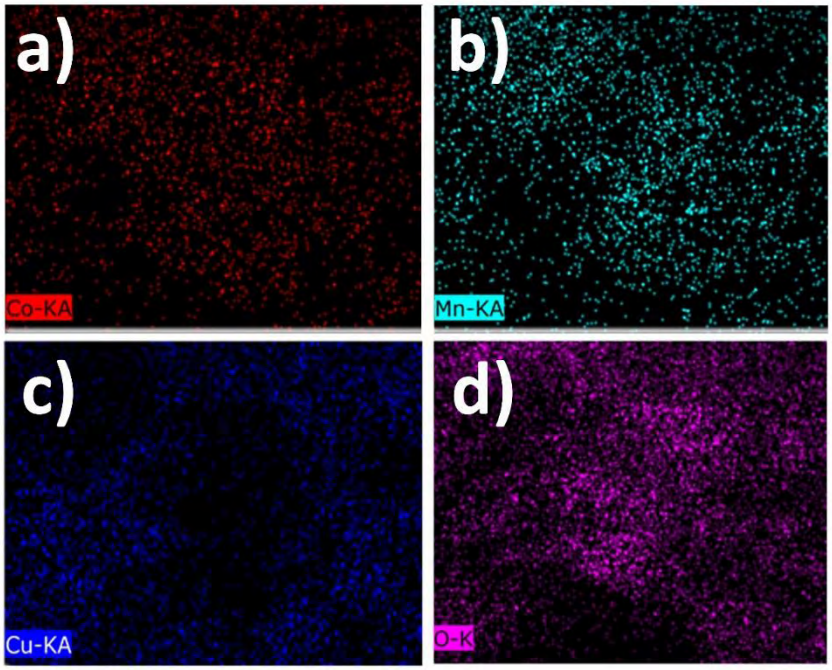

Figure 3.5: Elemental mapping images of CoMn-LDH@CuO/Cu_2O composite: (a) Co, (b) Mn, (c) Cu, and (d) O distributions.

3.1.5 Oxygen Evolution Performance

Electrochemical evaluation of different parameters was performed in 1 M N_2-saturated KOH solution, the catalytic performance of the CoMn-LDH@CuO/Cu_2O were investigated using a three-electrode system. First, we synthesized a series of CoMn-LDH with varying molar ratios of 1:1, 1:3, and 1:5. Through extensive experimentation, we discovered that the molar ratio of 1:1 resulted in optimized performance. This specific ratio depicted an overpotential of 332 mV at a current density of 10 mA/cm^2. In contrast, the molar ratios of 1:3 and 1:5 required a little bit higher potential of 390 mV, and 570 mV, accordingly. These findings highlight the significance of the 1:1 molar ratio in maximizing the electrocatalytic properties of CoMn-LDH. By using this

optimized ratio, we successfully synthesized CoMn-LDH@CuO/Cu_2O. To provide a fair comparison, the mass loading of the CoMn-LDH@CuO/Cu_2O catalyst was set to the same value as that of the CoMn-LDH and CuO/Cu_2O samples (1 mg/cm^2). The LSV curves of catalysts versus RHE for OER without IR correction are shown in Figure 3.6(a). As predicted, alkaline solution, the bare electrode exhibits negligible OER activity. Among all the three synthesized electrocatalysts, the CoMn-LDH@CuO/Cu_2O exhibits the lowest onset potential for OER and the highest catalytic current density at the similar overpotential, indicating the highest electrochemical activity towards water oxidation. The catalytic current density of 10 and 20 mA/cm^2 was attained by the CoMn-LDH@CuO/Cu_2O at low overpotential of 297 mV and 320 mV accordingly, which is far less than CoMn-LDH (380 mV) and CuO/Cu_2O (540 mV) at the same current density. For comparison OER activity of RuO_2 was also checked under same circumstances and it required overpotential of 320 mV@10 mA/cm^2. Indeed, when compared to previously reported electrocatalysts, CoMn-LDH@CuO/Cu_2O shows superior OER activity. As depicted in figure 3.6(b), the Tafel slopes were obtained to check the kinetics of the reaction and CoMn-LDH@CuO/Cu_2O exhibits low value of Tafel slope of 89 mV dec^{-1}, as compared to 97mV dec^{-1} for RuO_2, 190 mVdec^{-1} for CuO/Cu_2O and 160 mV dec^{-1} for CoMn-LDH. We computed turnover frequency (TOF), another essential parameter, to assess the intrinsic characteristic of the electrocatalyst. The TOF value of CoMn-LDH@CuO/Cu_2O is (0.012 s^{-1}) at onset overpotential.

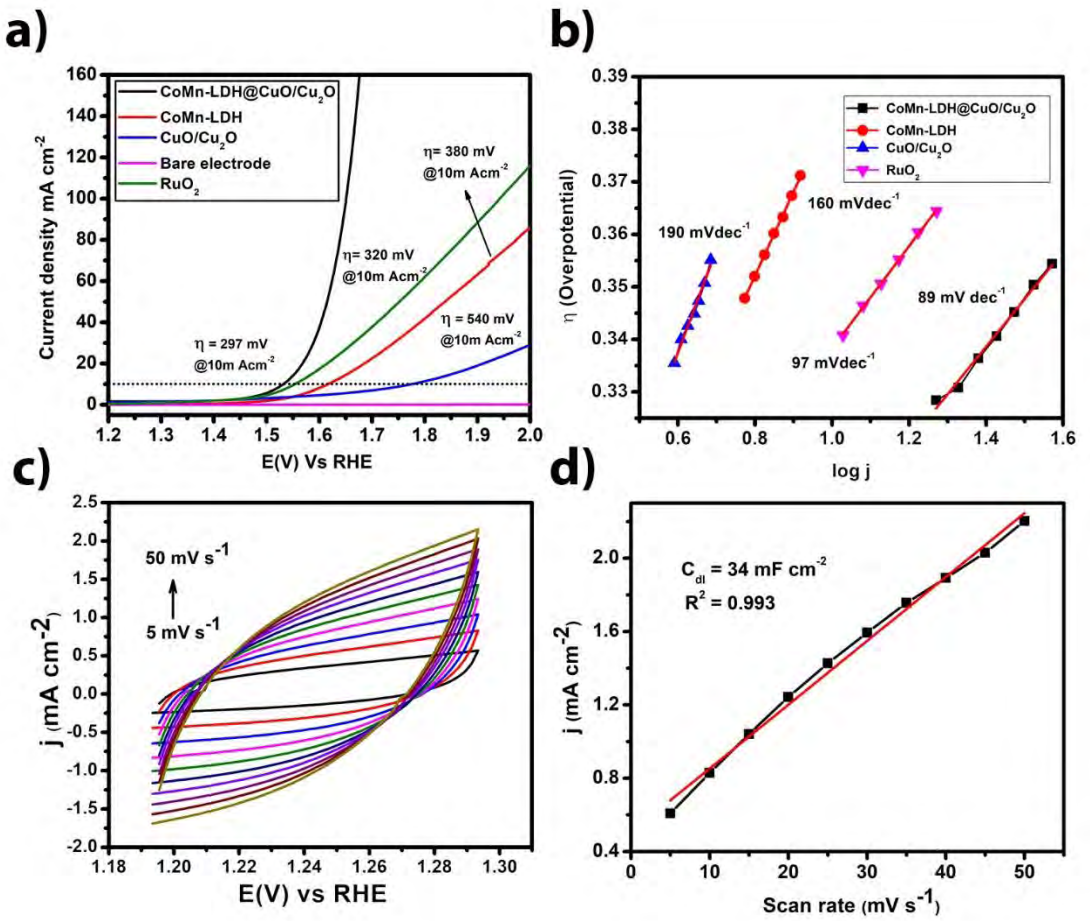

Figure 3.6: Linear sweep voltammograms of CoMn-LDH, CuO/Cu_2O, CoMn-LDH@CuO/Cu_2O, RuO_2 and Bare electrode b) Tafel Slopes of CoMn-LDH, CuO/Cu_2O, CoMn-LDH@CuO/Cu_2O and RuO_2 c) CV plots recorded across various scan rates within the non-faradaic zone d) Anodic current density plot Vs scan rate of CoMn-LDH@CuO/Cu_2O fabricated electrode in 1M KOH solution as an electrolyte.

The ECSA of an electrocatalyst holds significant importance, as it governs the degree to which active sites accessible to positive or negative ions become visible on the electrode surface. This visibility occurs specifically during the application of anodic or cathodic potentials within the non-faradaic region. The extent of exposed active sites correlates directly with the Cdl exhibited by the modified working electrode. To determine the capacitance of the double layer, we used cyclic voltammetry in the non-faradaic region at various scan rates. Cyclic voltammograms shown in Figure 3.6(c), demonstrate increase in current density with the increase in the scan rate. A single potential value was computed by detecting it in the capacitive potential window that is

non-Faradic. In the region of 5 to 50 mV s^{-1}, plotting anodic current versus scan rates yielded a straight line whose slope is equal to Cdl. Figure 3.6(d) shows the calculated Cdl values of CoMn-LDH@CuO/Cu_2O as 34 mF/cm². While in Figure 3.7(a-d), the Cdl values for CoMn-LDH, CuO/Cu_2O were determined to be 14.4 mF/cm², and 9.2 mF/cm², respectively. It was observed that CoMn-LDH@CuO/Cu_2O had Cdl slope value which indicates high electrochemical active surface area (ECSA). The double layer capacitance values of some reported materials also support our Cdl studies i.e. NiCo.P/C nanocubes (145 mF/cm^2), Ni.Co LDH nanocubes (9.16 mF/cm^2) and NiCo.P nanoboxes (28.94 mF/cm^2).[307] The ECSA has also been calculated from double layer capacitance. We noticed that CoMn-LDH@CuO/Cu_2O exhibits the highest electrochemical active surface area (425 cm^2) compared to CoMn-LDH (180 cm^2) and CuO/Cu_2O (115 cm^2) materials. The high value of Cdl and ECSA indicates that CoMn-LDH@CuO/Cu2O facilitate mass and charge transfer.

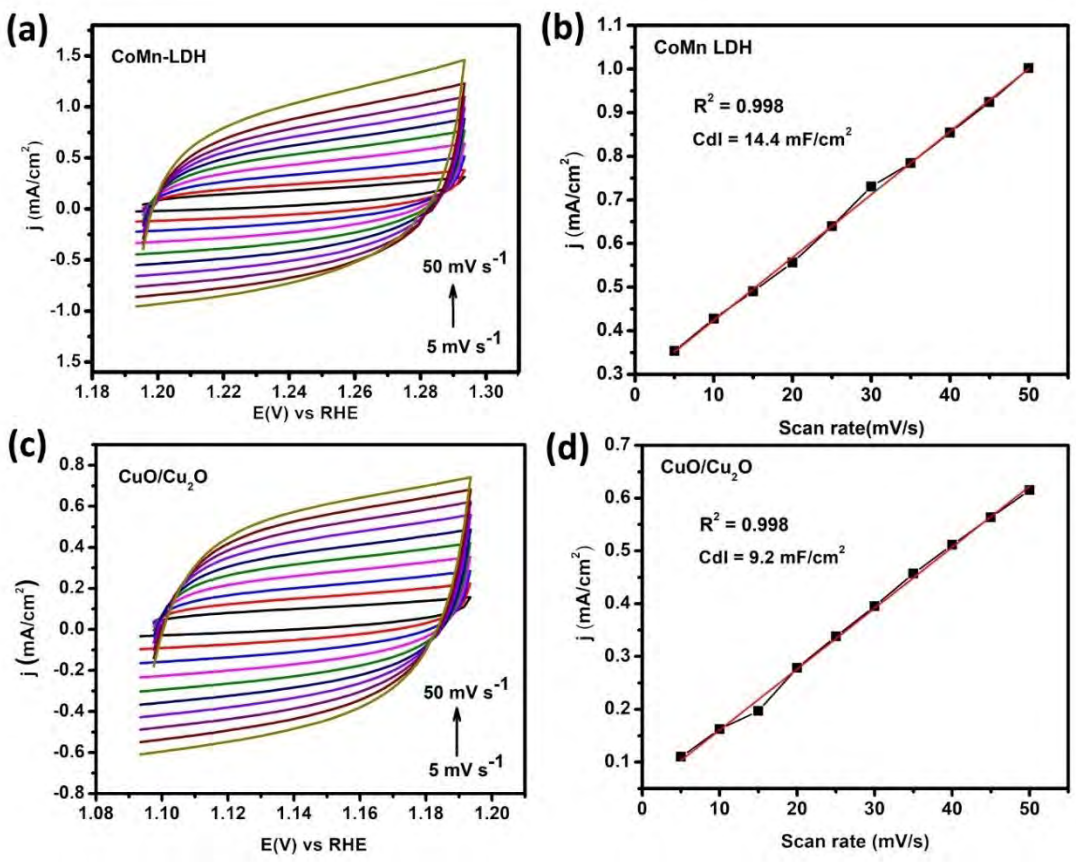

Figure 3.7: (a) non-faradaic region cyclic voltammograms of CoMn-LDH at various scan rates (mV/s) (b) plot of current density 'j' vs scan rates of CoMn-LDH fabricated

electrode in 1M KOH solution as an electrolyte. (c) non-faradaic region cyclic voltammograms of CuO/Cu_2O at various scan rates (b) Anodic current density plot Vs scan rate of CuO/Cu_2O fabricated electrode in 1M KOH solution as an electrolyte.

Conventionally, the electrochemical water oxidation process primarily entails three intermediate stages: (1) the physical adsorption of water molecules to the electrode surface, (2) the separation of water into O_2, and (3) the evolution of oxygen. The CoMn-LDH nanosheets have a distinct layered structure and the sheets are usually stacked over the other. Since LDH has a wide interlayer gap, the hydroxide units and molecules of water can diffuse across the layers and move randomly, enabling close contact among the catalyst and active species. The addition of CuO/Cu_2O in the catalyst not only helps in enhancing the ionic conductivity of the catalyst and enhance the exposure of the active sites via preventing LDH sheets from coagulation. Therefore, the ECSA increases, and reactions occur at accessible sites. In addition, the interlayer spacing will make it easier for O_2 to transit and to evolve from the surface, which is essential for the third phase of the OER process.

As predicted by the Pourbaix diagrams of Co[308] and Mn[309], the cations in higher oxidation states ($Co^{3+/4+}$, or $Mn^{3+/4+}$) are highly crucial for OER.[310] XAS[311], in situ Raman spectroscopy[312], and DFT calculations[313] have demonstrated that In alkaline conditions, Co hydroxide electrocatalysts can undergo in-situ oxidation, transforming into the catalytically active CoOOH, which has been recognized as the favored metal species for OER. On the other hand, 'Mn' cations also exchange oxygen atoms with electrolyte at corresponding potential.[314] This crucial feature of Mn may facilitate the OER process. In 1M KOH, OER often comprises PCET activities, the PCET transformation of Co^{3+}/OH to Co^{4+}/O, just before the production of oxygen molecule.[315] So, we can say that under given conditions, cobalt center is the actual active catalytic site, however, manganese center and copper oxide species are proposed to boost the OER ability of cobalt center via different mechanistic roles, as stated above.

3.1.6 Faradaic Efficiency (FE)

Determining the FE of a electrode material is a beneficial parameter for elucidating its oxygen generation ability (FE). To obtain the FE, the actual and predicted yields of evolved oxygen are compared by using chronoamperometry. To check the faradaic

efficiency of the catalyst, CPE was carried out utilizing comparable electrochemical reaction conditions at a static potential of 1.45 V versus RHE for a period of 1 h.[316] To establish a baseline, DO meter probe was immersed in an electrolyte of airtight anodic chamber and the concentration of dissolved oxygen was measured for an h. The expected yield of O_2 was estimated using Faraday's law and the charge stored during the electrochemical reaction. Figure 3.8 and Table 3.1 present the computed faradaic efficiency values for CoMn-LDH@CuO/Cu_2O, CoMn-LDH, and CuO/Cu_2O as 92.4%, 75.6%, and 62.3%, respectively. The current due to the redox reaction of metals is also involved along with water electrolysis.

Table 3.1: Theoretical and experimental faradaic efficiency of CoMn-LDH@CuO/Cu_2O, CoMn-LDH and CuO/Cu_2O.

Time (s)	**Micro moles of dissolved oxygen (Theoretical)**	**Experimental**		
		CoMn-LDH	**CuO/Cu_2O**	**CoMn-LDH@CuO/Cu_2O**
0	0	0	0	0
300	0.31155	0.24689	0.23366	0.19316
600	0.62061	0.49021	0.46546	0.38478
900	0.92346	0.81217	0.69259	0.57254
1200	1.2263	1.13843	0.91973	0.76031
1500	1.54221	1.41783	1.15666	0.95617
1800	1.84692	1.72447	1.38519	1.14509
2100	2.15256	2.01134	1.61442	1.33459
2400	2.47251	2.34766	1.85438	1.53296
2700	2.77318	2.63452	2.07988	1.71937
3000	3.0782	2.92468	2.30865	1.90848
Percentage Yield		**75.6%**	**62.3%**	**92.4 %**

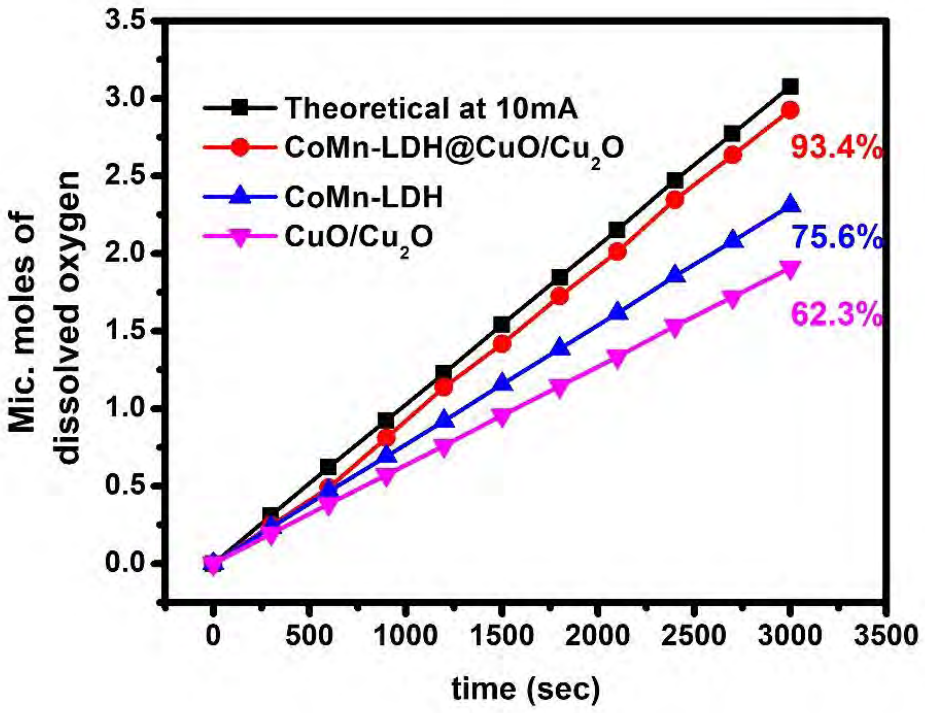

Figure 3.8: Faradaic Efficiency Curves for Oxygen Production of CoMn-LDH@CuO/Cu_2O, CoMn-LDH, and CuO/Cu_2O: Unveiling the Catalysts' Oxygen Evolution Abilities.

3.1.7 Electron Impedance Spectroscopy

EIS was employed to evaluate the conductance of CoMn-LDH, CuO/Cu_2O, and CoMn-LDH@CuO/Cu_2O composite within the range of 0.1 Hz to 100 kHz. The Rct correlates with the diameter of the semicircle in the high-frequency region of the Nyquist plot, and a low Rct value signifies a rapid reaction rate. In Figure 3.9, it can be clearly shown that CoMn-LDH@CuO/Cu_2O has small radii of its semi-circle and low Rct as compared to individual CoMn-LDH and CuO/Cu_2O, thus revealing its fast OER kinetics and low Rct. The low Rct, which facilitates efficient charge transport, is owing in part to the dispersion of CuO/Cu_2O and the synergistic impact of the presence of several transition metals, as well as other intrinsic factors.

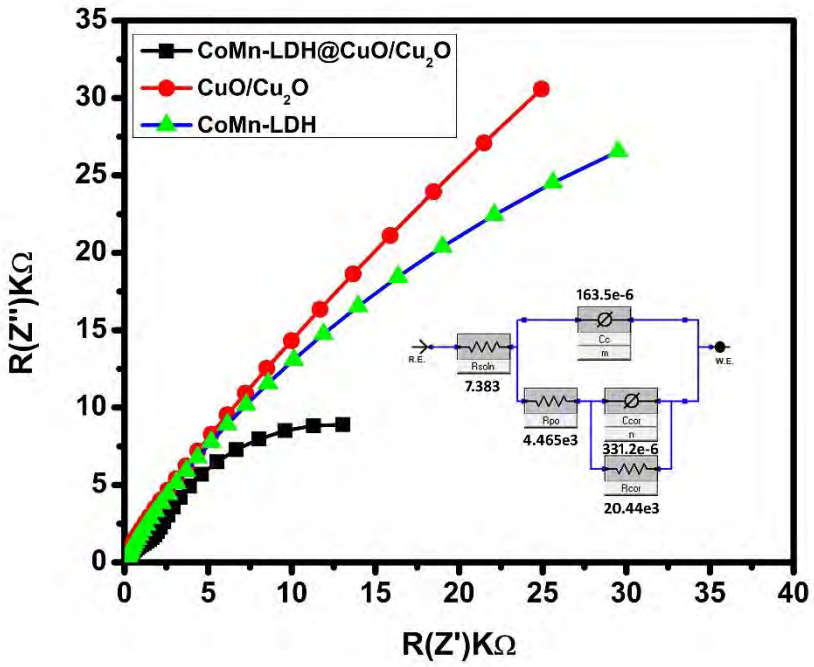

Figure 3.9: Electrochemical Impedance Spectroscopy (EIS) spectra of CoMn-LDH, CuO/Cu_2O, and CoMn-LDH@CuO/Cu_2O recorded over a frequency range spanning from 0.1 Hz to 100 kHz.

3.1.8 Stability

For commercial and industrial water electrolyzer, the stability of catalyst is a critical criterion. Since catalyst's catalytic activity and selectivity are the key parameters, its effectiveness is critical unless it exhibits adequate long-term stability. For this purpose, a 15 h CPE study was conducted under constant experimental conditions utilizing chronoamperometry at 1.42 V against RHE to determine the stability and durability of the catalyst CoMn-LDH@CuO/Cu_2O. A steady current of 10 mA was maintained by the catalyst until the last minute (Figure 3.10). LSV has been performed to check the durability of the catalyst. From the inset of Figure 3.10 it is cleared that the maximum current density values of the LSV of modified electrode (CoMn-LDH@CuO/Cu_2O) that has been coated (pristine and post-catalytic reactions) showed no significant change, indicating that structure of CoMn-LDH@CuO/Cu_2O remained the same throughout the catalytic phenomena.

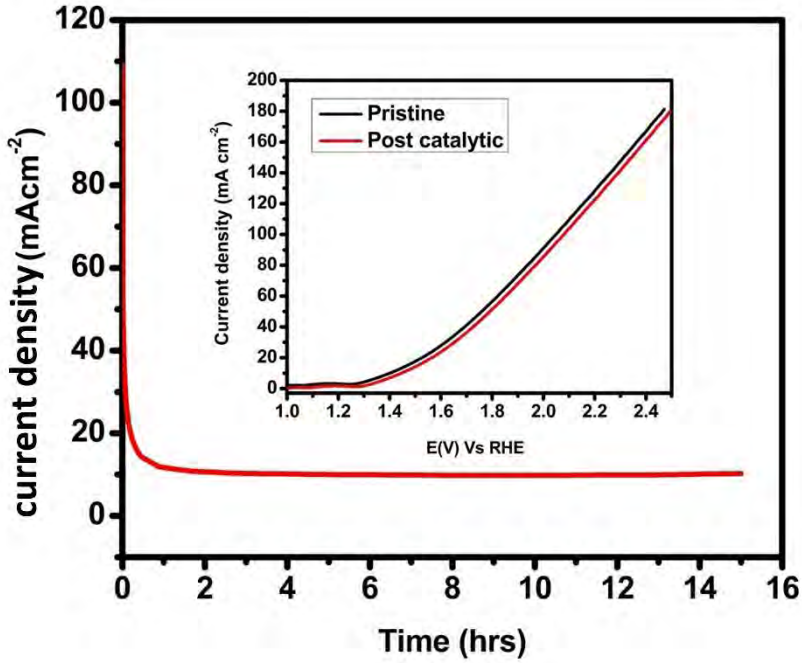

Figure 3.10: Controlled potential electrolysis of CoMn-LDH@CuO/Cu_2O for 15 h (inset) LSV curve of pristine and post catalytic CoMn-LDH@CuO/Cu_2O.

After subjecting the catalyst to a 15 h CPE test, XPS analysis of the post-catalytic sample was conducted (Figure 3.11(a-d)). The results revealed no significant changes, indicating that the catalyst's structure and physical properties were retained even after the extended test duration. This observation underscores the stability and durability of the catalyst under the studied catalytic conditions.

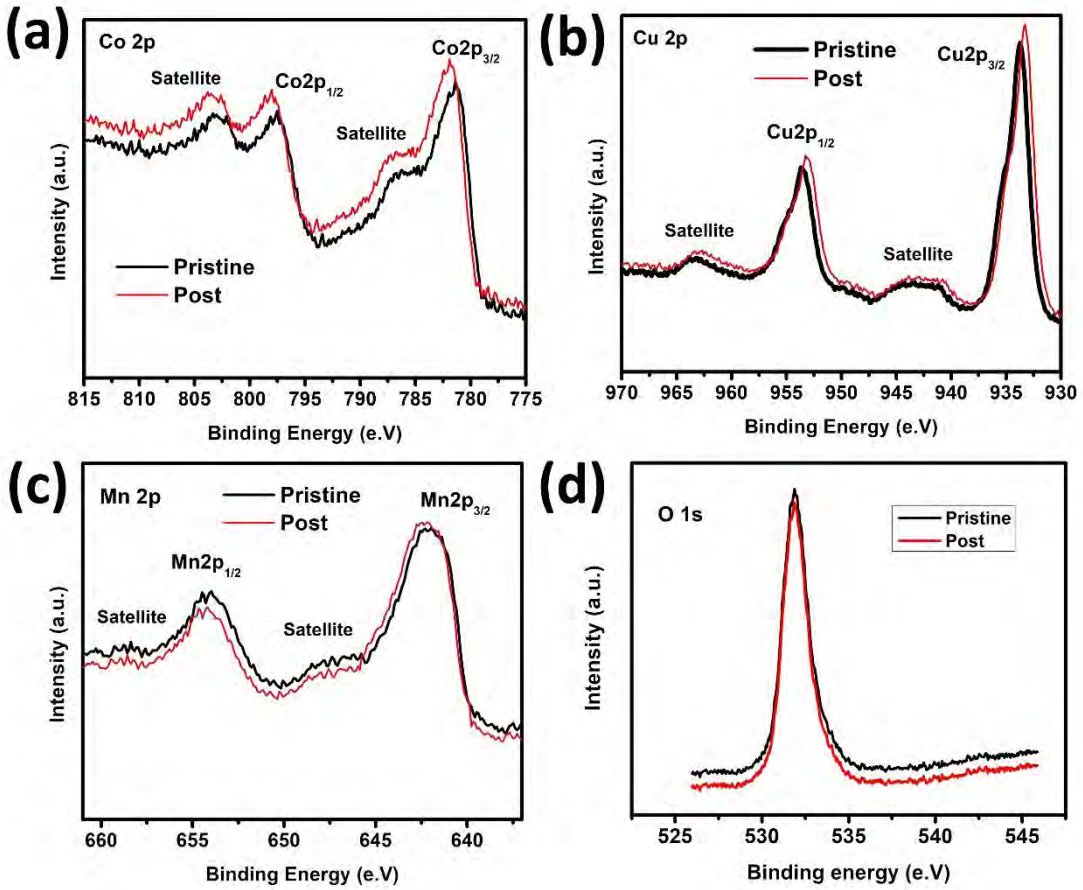

Figure 3.11: X-ray Photoelectron Spectroscopy (XPS) spectra of the post-catalytic samples CoMn-LDH@CuO/Cu_2O, showing the elemental compositions of (a) cobalt, (b) copper, (c) manganese, and (d) oxygen.

The proposed mechanism for OER in alkaline media is shown in figure 3.12. In the first step metal active site binds with OH- ion from water to form M-OH. Further oxidation leads to the formation of M-O species followed by M-OOH which is thermodynamically unfavorable intermediate because of the weak interaction between metal and -OOH. In the last step metal oxygen bond breaks leading to the formation of O_2.

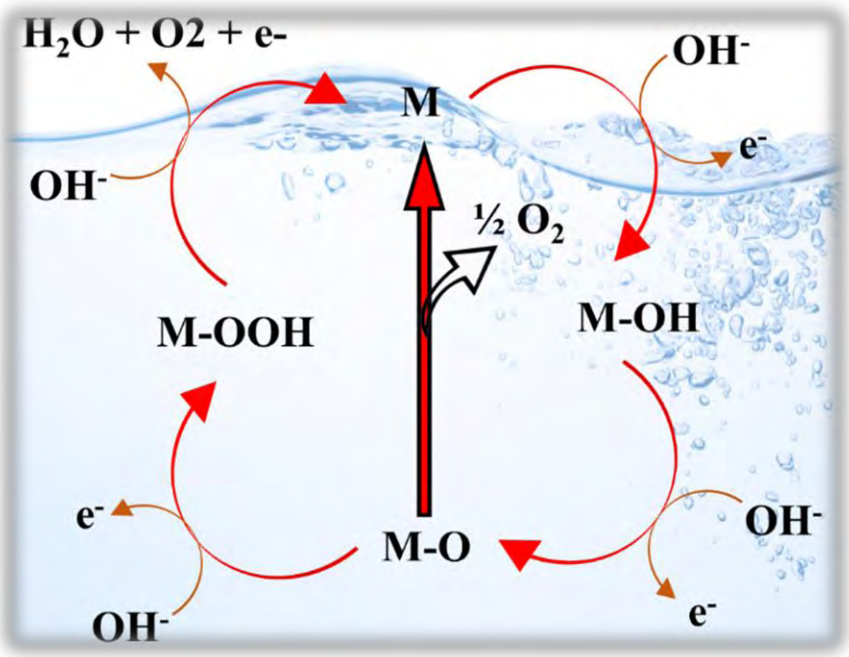

Figure 3.12: Proposed mechanism for the OER by the surface metals, depicted in a schematic diagram.

Table 3.2 presents a comparative study of various reported catalysts alongside the CoMn-LDH@CuO/Cu_2O composite. The table likely includes key performance metric for each catalyst under specific reaction conditions or applications. The purpose of this comparison is to assess and highlight the superior catalytic properties of the CoMn-LDH@CuO/Cu_2O composite material relative to other known catalysts, making it a promising candidate for specific catalytic reactions or processes.

Table 3.2: Comparative analysis of the OER efficiency of CoMn-LDH@CuO/Cu_2O in comparison with reported composites of layered double hydroxide.

Catalyst	Method	Overpotential at 10 mA/cm^2 (mV)	Ref
Fabrication of CoFe-LDH over graphitic nitrides	Co-precipitation	280	317
Al @ NiFe-LDH	Solvothermal	300	35
NiMn-LDH@MWCNT	Refluxing	350	318
Ni Fe-LDH on Cabon quantum	Solvothermal	235	319
CoFe-LDH @ Cu Foam	Electrodeposition	240	320

CoFe-LDH	Hydrothermal	266	[321]
Enriching vacancy CoFe-LDH	Acid Etching	302	[38]
CoFe-LDH@g-C_3N_4	Hydrothermal	322	[322]
CoMn-LDH@MWCNT	Refluxing	300	[318]
CoMn-LDH@CuO/Cu_2O	Hydrothermal	190	This work

3.1.9 Conclusions

In this study, we successfully synthesized CoMn-LDH@CuO/Cu_2O electrocatalyst through a simple and efficient process. First, CuO/Cu_2O nanoparticles were formed by calcining HKUST-1, and then they were incorporated during the growth of CoMn-LDH nanosheets. Remarkably, our designed electrocatalyst displayed exceptional performance in the OER. It only required 297 mV extra potential to drive 10 mA cm^{-2} current density with a minimal Tafel slope value of 89 mV dec^{-1}, which was significantly lower compared to the separate CoMn-LDH and CuO/Cu_2O catalysts. Moreover, the CoMn-LDH@CuO/Cu_2O catalyst exhibited excellent stability during a 15 h period, with negligible current loss. The remarkable OER performance of our catalyst can be attributed to two key factors. Firstly, the interaction between CoMn-LDH and CuO/Cu_2O led to enlarged electrochemical active surface area, providing more sites for the OER process to occur. Secondly, this interaction resulted in a decline in the resistance of charge transfer, which facilitated efficient flow of electron during the OER. The comprehensive characterization and understanding of the catalyst's performance pave the way for further advancements in the field of renewable energy and sustainable electrocatalysis.

3.2 Material-II (NiCo-Alloy@CeO_2 nanorods)

NiCo-Alloy@CeO_2 as a bifunctional electrode material, was successfully synthesized by hydrothermal approach followed by annealing. The composite electrode material exhibited exceptional electrocatalytic performance for OER and HER in alkaline environments, making it an up-and-coming candidate for electrocatalytic hydrolysis. NiCo-alloy@CeO_2 demonstrated high performance toward OER by demanding low overpotential value of 170 mV to acquire current density of 20 mA/cm^2. The material exhibited high durability for 14 h at 50 mA/cm^2 and accelerated kinetics with a 51.1 mV/dec Tafel slope. It also displayed excellent electrocatalytic performance toward HER, demanding overpotential of 221 mV at 50 mA/cm^2. Moreover, it exhibits small Tafel slope, least charge transfer resistance, high active electrochemical surface area and excellent durability for a period of 14 h. Detail of Complete characterization and electrochemical performance is discussed it this section. Figure 3.13 presents a Graphical Abstract depicting the utilization of a NiCo-Alloy@CeO_2 composite material for catalyzing the OER and HER. The graphical abstract likely illustrates the catalytic processes of water splitting into oxygen gas and hydrogen gas using the NiCo-Alloy@CeO_2 composite, showcasing its potential as an efficient catalyst for clean energy generation.

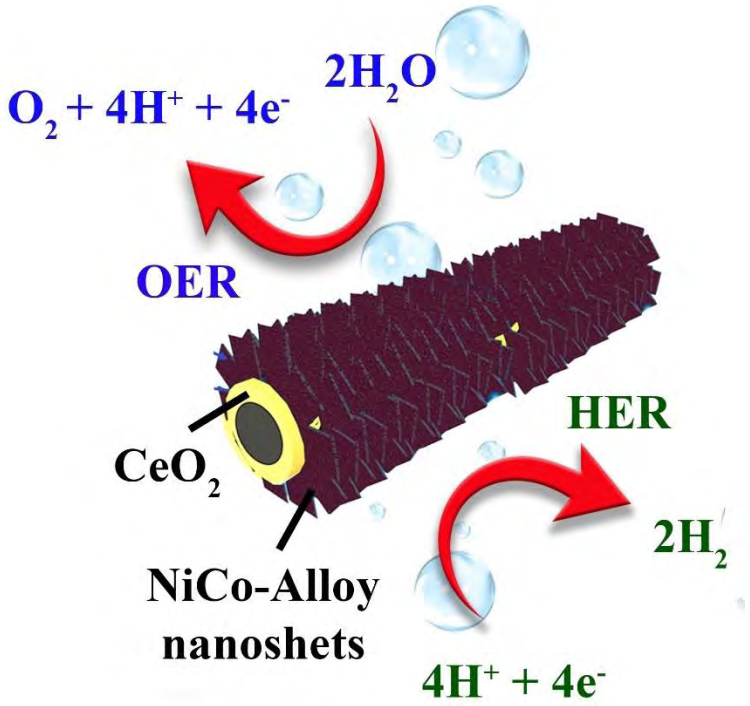

Figure 3.13: Graphical illustrating of the OER and HER catalysis utilizing a NiCo-Alloy@CeO_2 composite material.

3.2.1 Powder X-ray Diffraction analysis

To confirm the formation of a NiCo-alloy over CeO_2, we conducted powder X-ray diffraction (pXRD) analysis. Figure 3.14 illustrates the XRD patterns of CeO_2, NiCo-Alloy, and NiCo-Alloy@CeO2 nanomaterials. In the pure CeO_2 diffractogram, the strong diffraction peaks at 2θ of 28.23°, 33.31°, 47.56°, 56.94°, 76.77°, and 79.52° correspond to (111), (200), (220), (311), and (331) planes of CeO_2.These peaks indicate the presence of a cubic fluorite phase in the synthesized CeO_2, as confirmed by comparing the diffractogram with the standard reference (JCPDS No: 00-001-0800). The sharpness of the diffraction peaks indicates a high degree of crystallinity in the synthesized CeO_2.

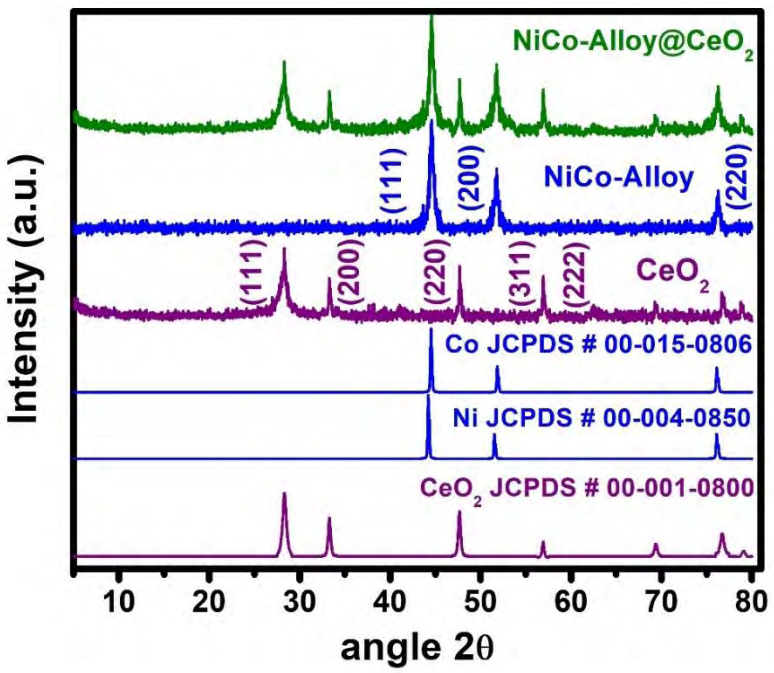

Figure 3.14: Diffractogram comparison of NiCo-Alloy@CeO2, NiCo-Alloy, and CeO2 with Corresponding JCPDS card patterns along with their respective card numbers.

In the XRD pattern of NiCo-Alloy@CeO_2, additional peaks are observed and attributed to metallic nickel (Ni) and cobalt (Co) at 2θ values of 44.50°, 51.84°, and 76.37°,

ascribed to the (111), (200), and (220) facets of the face-centered cubic (fcc) phases of Ni and Co. Due to partial overlap, it is challenging to differentiate between the diffraction peaks of Ni and Co. The respective standard references (JCPDS No. 00-004-0850) and (00-015-0806) confirm the presence of Ni and Co. Importantly, no significant shift is observed in the peak position of CeO_2 in the diffractogram of NiCo-Alloy@CeO_2 nanorods, indicating that the introduction of NiCo-Alloy nanosheets does not affect the fluorite-phase nanostructure of CeO_2 nanorods. However, the lattice parameter of CeO_2 differwhich indicate that the NiCo-alloy nanosheets are successfully impregnated into CeO_2. Table 3.3 represents the lattice parameters of pure CeO_2 and NiCo-Alloy@CeO_2. These findings suggest that crystal structure of CeO_2 is under strain which results in partial distortion of the crystal structure of CeO_2. indicating the interfacial effect. The small deviation of the lattice parametrs indicates the electronic interaction between NiCo-Alloy and CeO_2 which results in synergistic effect leading to efficient electrocatalytic behaviour.

Table 3.3: Calculation of lattice parameters from PXRD analysis

Material	Miller indices (hkl)	Position (2θ)	Cell parameter (a) (nm)	d-spacing (nm)
CeO_2	200	33.3	0.538	0.269
	220	47.56	0.539	0.1909
	331	76.77	0.54	0.124
NiCo-Alloy@CeO_2	200	33.17	0.54	0.270
	220	47.70	0.538	0.1904
	331	76.16	0.53	0.1238

3.2.2 Average Crystallite Size by Using Debye-Sherrer Equation

The crystallite size of crystalline materials was estimated from X-ray diffraction patterns using the Debye-Scherrer equation. The equation was utilized, in which the Scherrer constant, wavelength of the X-ray, full width at half maximum (FWHM) of

the diffraction peak, and Bragg angle were considered. The Scherrer constant was taken as 0.89, and the wavelength of the X-ray was determined by the X-ray source, which was Cu Kα radiation with a wavelength of 1.5406 Å. The FWHM (β) was measured by determining the diffraction peak width at half its maximum intensity, and the Bragg angle (θ) was obtained from the XRD pattern by locating the position of the diffraction peak.

$$D = K\lambda / \beta \cos\theta$$

The crystallite size was then computed using the above equation, which yields an average size of the crystallites rather than the size of individual crystallite. Average crystallite size has been calculated for CeO_2 (Table 3.4) and NiCo-Alloy (Table 3.5). The size of NiCo-Alloy crystallites decreases after the incorporation of CeO_2 nanorods. This size reduction can be attributed to the interaction between CeO_2 and NiCo-Alloy, which hinders agglomeration and promotes more dispersion of NiCo-Alloy over the surface of CeO_2 nanorods.

Table 3.4: The table presents the average crystallite sizes of CeO_2, determined through Debye Scherrer equation.

Material	Position (2θ)	FWHM (Deg)	Crystallite size (nm)	Average crystallite size
Pure CeO_2	28.23	1.0671	8.02	27.68
	33.317	0.24044	36.04	
	47.56	0.26081	34.78	
	56.94	0.22491	41.99	
	76.77	0.60275	17.57	
CeO_2 in NiCo-Alloy@CeO_2	28.23	1.0458	8.18	27.97
	33.17	0.23591	36.71	
	47.70	0.25579	35.48	
	56.94	0.22490	41.99	
	76.21	0.60275	17.50	

Table 3.5: Crystallite size calculation of NiCo-Alloy

Material	Position (2θ)	FWHM (Deg)	Crystallite size (nm)	Average crystallite size
Pure NiCo-Alloy	44.595	0.65719	13.64	16.2 nm
	51.743	0.68045	13.54	
	76.248	0.4921074	21.42	
NiCo-Alloy in NiCo-Alloy@CeO_2	44.595	0.7093	12.63	13.6 nm
	51.743	0.8206	11.23	
	76.248	0.62198	16.95	

3.2.3 Morphology of the Catalyst

The phase composition and internal morphology of NiCo-Alloy@CeO_2 was thoroughly investigated using high-resolution transmission electron microscopy (HRTEM). The HRTEM images shown in Figure 3.15 reveal distinct interfaces among several crystalline phases within the material. Figure 3.15(a) provides clear evidence of the presence of CeO_2 nanorods alongside nanosheets of NiCo-alloy. Moreover, Figures 3.15(b) demonstrate that the NiCo-alloy nanosheets completely cover the surface of CeO_2 nanorods, forming a well-integrated composite structure.

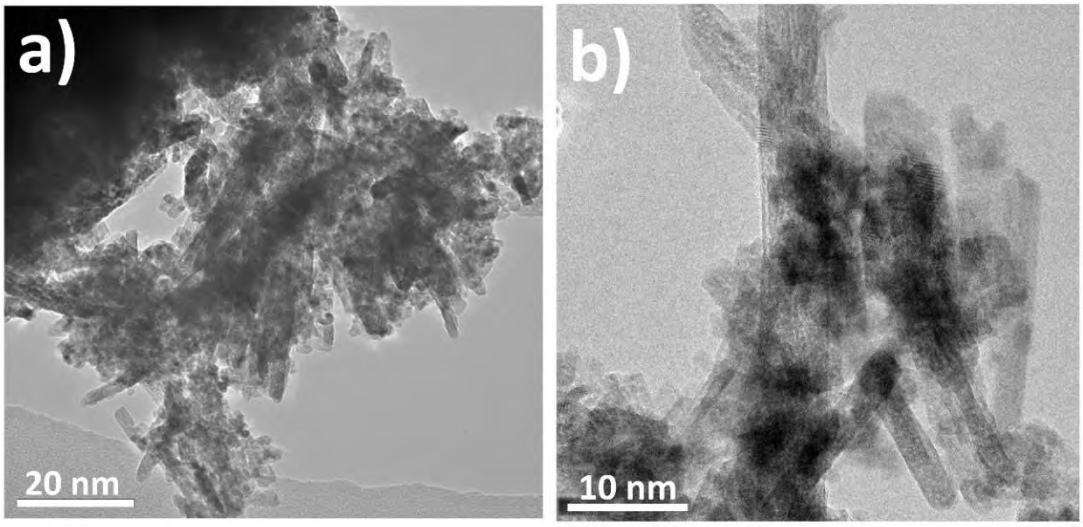

Figure 3.15: (a) HRTEM micrograph of NiCo-Alloy@CeO_2 at a magnification of 20 nm, revealing detailed structural features and crystal arrangement. (b) HRTEM micrograph of NiCo-Alloy@CeO_2 at a higher magnification of 10 nm, providing a closer view of the crystalline morphology and nanostructure.

Moreover, well-resolved lattice fringes with interlayer spacings of 0.311, 0.201, and 0.204 nm are observed in figure 3.16, which are correspond to crystal lattice (111) of CeO_2, Ni^0, and Co^0, respectively. These crystal lattice fringes confirm the crystalline nature of the different phases in the composite. The presence of such an interfacial region, as evident from HRTEM measurements, is of paramount significance in increasing the electrocatalytic efficiency of the materials, as it can furnish active sites for catalytic reactions.

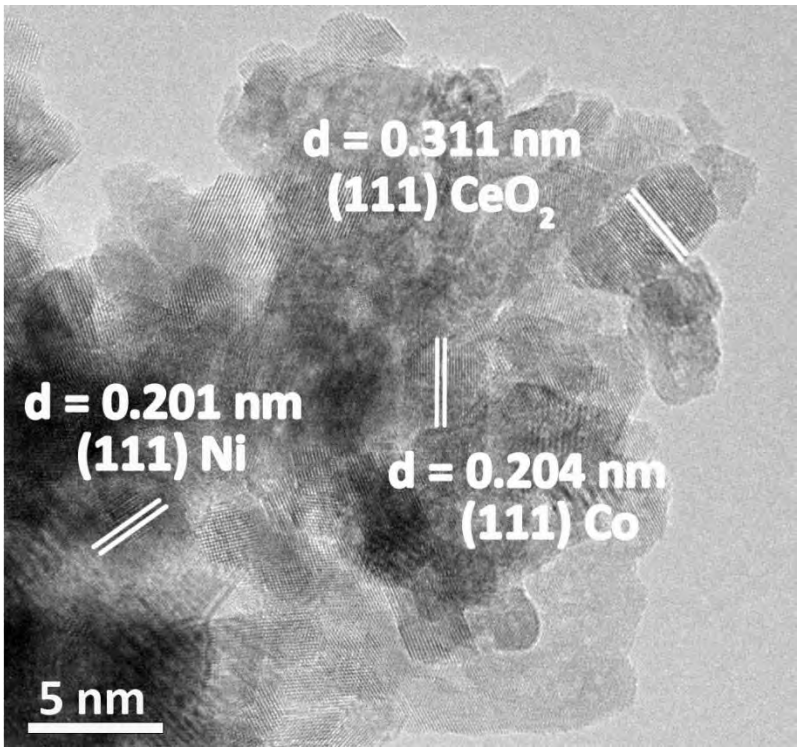

Figure 3.16: HRTEM analysis at 5 nm, displaying distinct and visible lattice fringes in the specimen.

The polycrystalline nature of NiCo-Alloy@CeO_2 is further corroborated by the SAED technique. Figure 3.17 illustrates a SAED pattern featuring well-defined diffraction rings, which can be attributed to the (111), (200), and (220) crystallographic planes of

NiCo-alloy, and the (111), (200), and (400) crystallographic planes of CeO_2. This pattern indicates that the synthesized material exhibits a polycrystalline structure, where multiple nanocrystals with different orientations coexist. Overall, the HRTEM and SAED analyses provide comprehensive insights into the phase distribution and crystallographic characteristics of NiCo-Alloy@CeO_2, confirming its well-defined morphology and crystalline nature, which are crucial factors influencing its electrocatalytic performance.

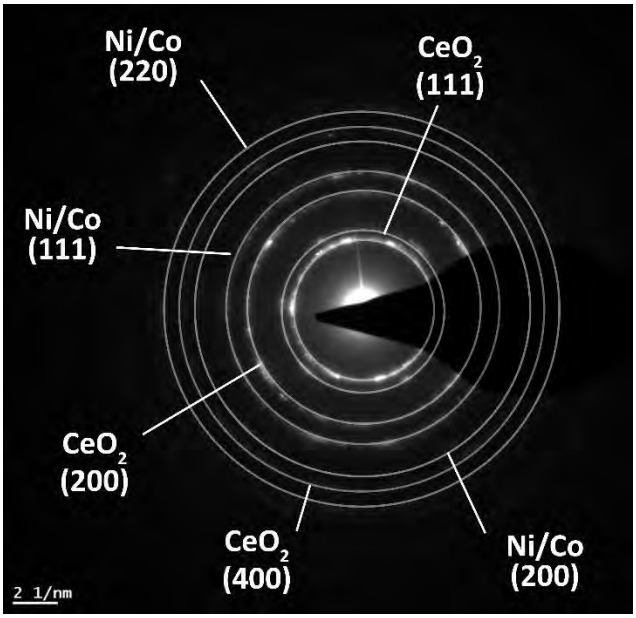

Figure 3.17: SAED analysis of the NiCo-Alloy@CeO_2, illustrating the crystallographic arrangement and phase information of the materials.

3.2.4 EDX and EELS Mapping

The presence and chemical composition of Ni, Co, and Ce in the NiCo-Alloy@CeO2 nanomaterial are further validated using energy dispersive X-ray spectrum (EDX) analysis, as shown in Figure 3.18. EDX provides elemental information by detecting characteristic X-rays emitted from the sample when it is bombarded with electrons. The EDX analysis reinforces the existence of elements Ni, Co, and Ce in the nanomaterial, corroborating the results obtained from other characterization techniques.

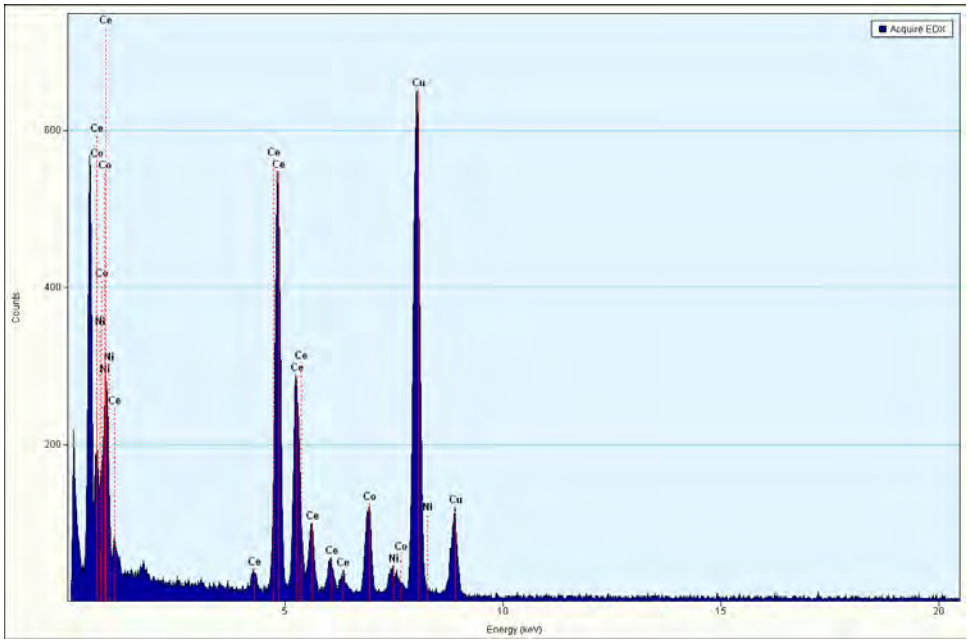

Figure 3.18: Energy Dispersive X-ray (EDX) Spectrum of the NiCo-Alloy@CeO_2 composite, providing elemental analysis and composition characterization of the material.

In addition to EDX, Electron Energy Loss Spectroscopy (EELS) mapping was used to investigate the distribution of NiCo-Alloy on the surface of Ceria (CeO_2) nanorods. EELS represents a potent analytical method applied within TEM that gives information about the elemental composition and chemical bonding within the material. Figures 3.19(a-e), present the EELS mapping images, revealing the homogenous distribution of NiCo-Alloy over the surface of Ceria nanorods. The EELS mapping clearly shows that NiCo-Alloy is uniformly dispersed on the CeO_2 nanorods, confirming the successful integration of these two components in the composite material. This homogeneous distribution is vital for enhancing the electrocatalytic performance of the catalyst, as it provides many active sites for catalytic reactions to occur.

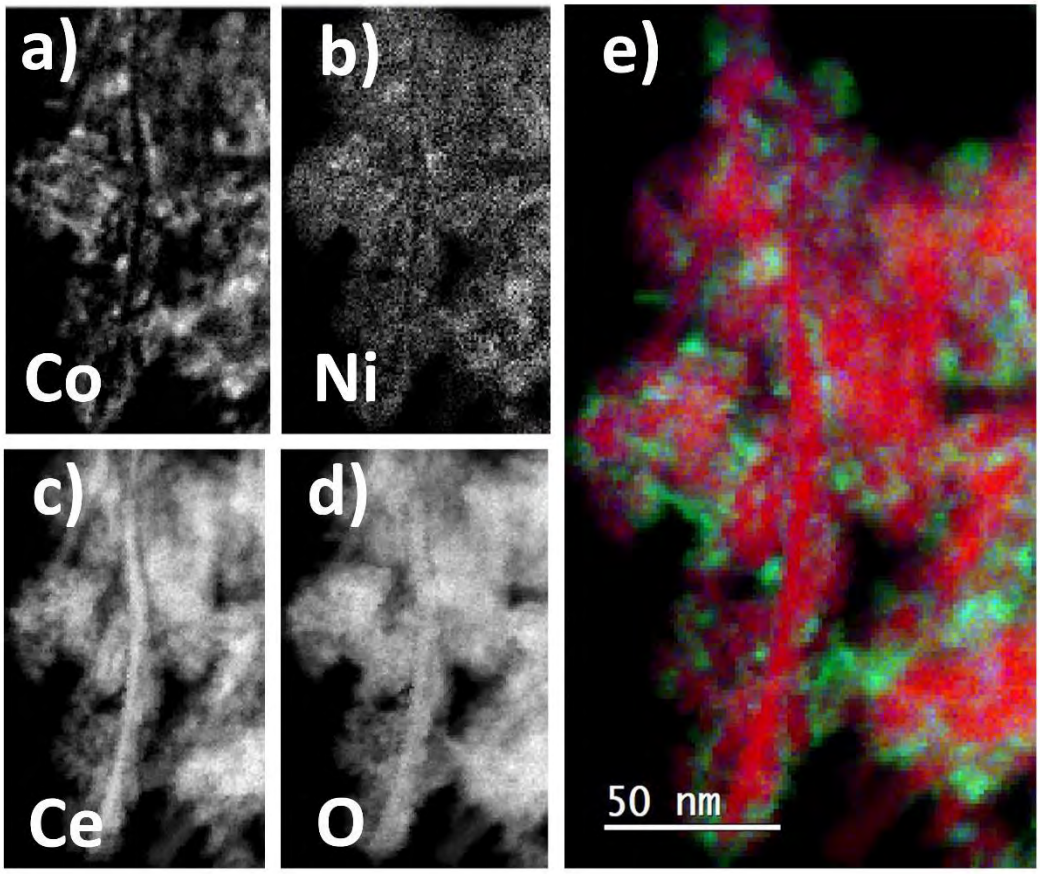

Figure 3.19: Electron Energy Loss Spectroscopy (EELS) Mapping of the NiCo-Alloy@CeO_2 composite at a spatial resolution of 50 nm. (a-e) showcase the elemental distribution and chemical composition of the material across the analyzed area.

3.2.5 X-ray Photon Spectroscopy

To further investigate the chemical composition of NiCo-Alloy@CeO_2, XPS was performed. The XPS analysis of NiCo-Alloy@CeO_2 illustrates the presence of nickel, cobalt, oxygen, and cerium constituents. All the orbitals except s orbital give rise to doublets known as spin orbit coupling with specific binding energy difference for each element. These peaks also have a specific area ratio based on the degeneracy of each spin state. In Figure 3.20(a), the doublet of Ni 2p XPS spectrum consists of Ni $2p_{3/2}$ and $2p_{1/2}$ (spin orbit coupling ~ 17.1 eV). The deconvoluted XPS spectrum of Ni 2p for NiCo-Alloy@CeO_2 shows the emergence of peak at 852.7 eV for Ni $2p_{3/2}$, corresponding to Ni^0, indicating the existence of Ni-Ni/Ni-Co bonds within the NiCo alloy. Additionally, the observed peak located at 855.2 eV is attributed to the Ni-O

moieties that arise due to the interaction between the nickel present in NiCo and the oxygen atoms in CeO_2, along with the surface oxidation of the material.[232, 323] In the high-resolution Ce 3d XPS spectra of NiCo-Alloy@CeO_2 (spin-orbit coupling ~ 15.8 eV), well observed peaks in $3d_{5/2}$ (881.9 eV and 883.3 eV) and $3d_{3/2}$ region (897.7 eV and 901.2 eV) reparents Ce^{+4} and Ce^{+3} moieties respectively (Figure 3.20(b)). The XPS spectrum of cobalt consists of doublets having $2p_{3/2}$ and $2p_{1/2}$ peaks with a binding energy difference of 15.5 eV. Figure 3.20(c) revealed two peaks at 777.8 and 779.2 eV in the Co $2p_{3/2}$ region of NiCo-Alloy@CeO_2 indicating the Co^0 in Co-Co/Co-Ni bond in NiCo alloy and the Co-O bond, respectively.[232] These results confirm the Co-O interaction between NiCo and CeO_2. In Figure 3.20(d), the O 1s spectrum of NiCo-Alloy@CeO_2 exhibited three peaks at 528.9, 530.2, and 531.7 eV, which were identified as Ce-O, Ni/Co-O, O vacancy and absorbed oxygen respectively.[324] The peak at 530.2 eV in the O 1s XPS spectrum signifies metal-oxygen bond, which could originate from the interaction of both Ni-O and Co-O with the oxygen atom of CeO_2. These outcomes propose that there is an electron transfer from NiCo to CeO_2, resulting in a shortage of electrons in NiCo and a surfeit of electrons in Ce in NiCo-Alloy@CeO_2.[232] The optimized electronic arrangement of CeO_2 could potentially played a crucial role in augmenting the catalytic proficiency of NiCo-Alloy@CeO_2.

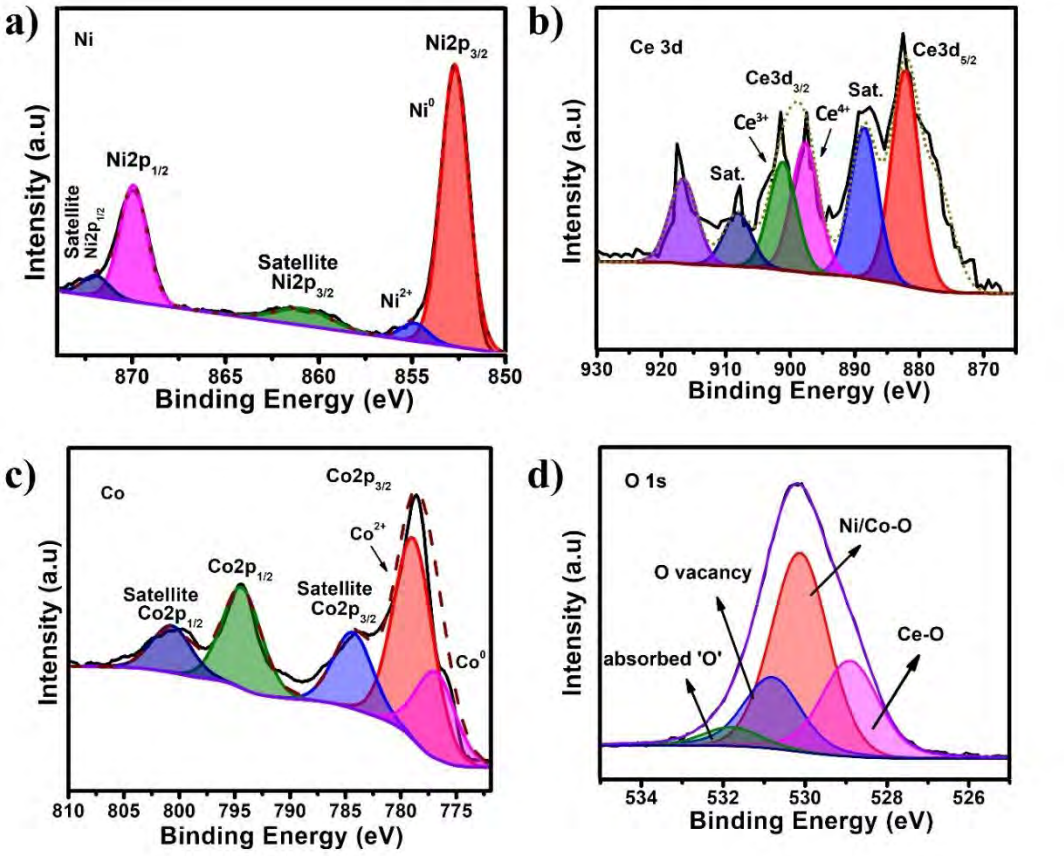

Figure 3.20: X-ray Photoelectron Spectroscopy (XPS) spectra of the NiCo-Alloy@CeO_2 composite, showing core-level peaks of key elements: (a) Ni 2p, (b) Ce 3d, (c) Co 2p, and (d) O 1s. The spectra provide valuable insights into the chemical states and bonding environments within the material.

3.2.6 OER Performance

The electrocatalytic efficiency of the synthesized materials, including NiCo-Alloy@CeO_2, NiCo-Alloy, NiCo-LDH, and CeO_2, was evaluated for the OER and the HER at room temperature. LSV curves were obtained at 10 mV/s to minimize the capacitive current and obtain accurate results (Figure 3.21(a)). All the materials displayed varying degrees of OER activity, but NiCo-Alloy@CeO_2 exhibited notably superior catalytic efficiency with a considerably lower overpotential (η), a critical parameter for OER performance. The overpotential at 20 mA/cm^2 of each synthesized material is indicated with a dotted line on the respective LSV curves. The comparison of LSV curves revealed that the onset potential (E_{onset}) of the NiCo-Alloy@CeO_2

electrode was significantly shifted to the cathodic side, indicating its improved electrocatalytic activity. Specifically, NiCo-Alloy@CeO_2 showed a low value of overpotential (η) ~ 170 mV at 20 mA/cm^2, that was much lower than that of the other synthesized materials. In fact, the electrocatalytic performance of NiCo-Alloy@CeO_2 was found to surpass that of reported ceria-based materials known to date (as summarized in Table 3.4). To obtain insight into kinetics of the electrocatalytic process, the Tafel slopes were calculated from the subsequent LSV curves. A lower Tafel slope indicates faster kinetics and enhanced catalytic performance. Figure 3.21(b) depicts the Tafel slope values for each material. Notably, NiCo-Alloy@CeO_2 exhibited a remarkably lower Tafel slope value of 51 mV/dec for OER performance compared to NiCo-Alloy, NiCo-LDH, and CeO_2, which had Tafel slopes of 69 mV/dec, 170 mV/dec, and 179 mV/dec, respectively. This further confirms the superior catalytic performance of NiCo-Alloy@CeO_2.

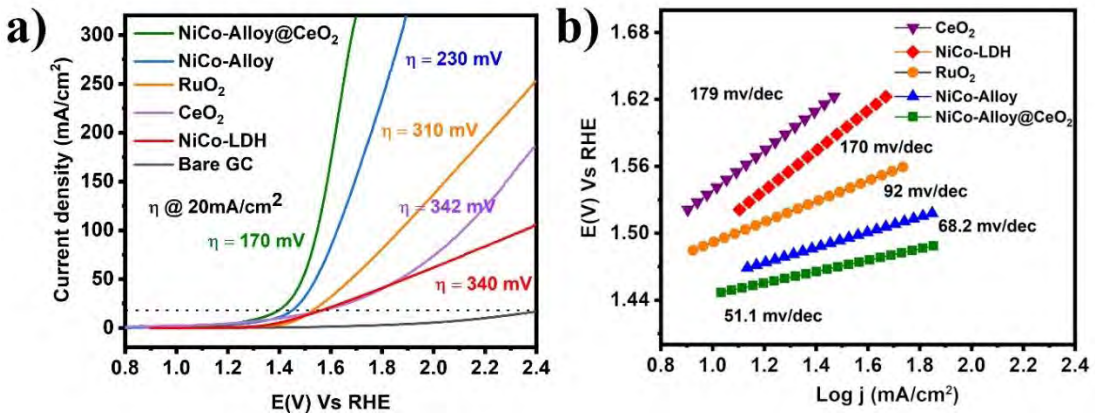

Figure 3.21: Assessment of the electrochemical performance of the synthesized electrocatalysts for OER: (a) Anodic LSV curves, and (b) conforming Tafel plots derived from the LSV data.

The remarkable improvements in catalytic performance towards OER can be attributed primarily to the heterostructure interface interaction between NiCo-alloy nanosheets and CeO_2 nanorods. This unique heterostructure enhances the catalytic activity by providing abundant active sites for the electrochemical reactions to take place, leading to the outstanding electrocatalytic performance observed in NiCo-Alloy@CeO_2.

Durability of the Catalyst

To assess the long-term stability of NiCo-Alloy@CeO_2 in 1M KOH, various stability tests were conducted. These tests include controlled potential electrolysis at constant potentials of 1.48 V_{RHE} and 1.54 V_{RHE} for a duration of 30 h as shown in Figure 3.22(a). Additionally, multistep chrono-potentiometry experiments were performed at different current densities ranging from 10 to 250 $mAcm^{-2}$, further confirming the durability of the catalyst Figure 3.22(b). This finding confirms the exceptional durability and stability of NiCo-Alloy@CeO_2, even under demanding conditions with high current densities.

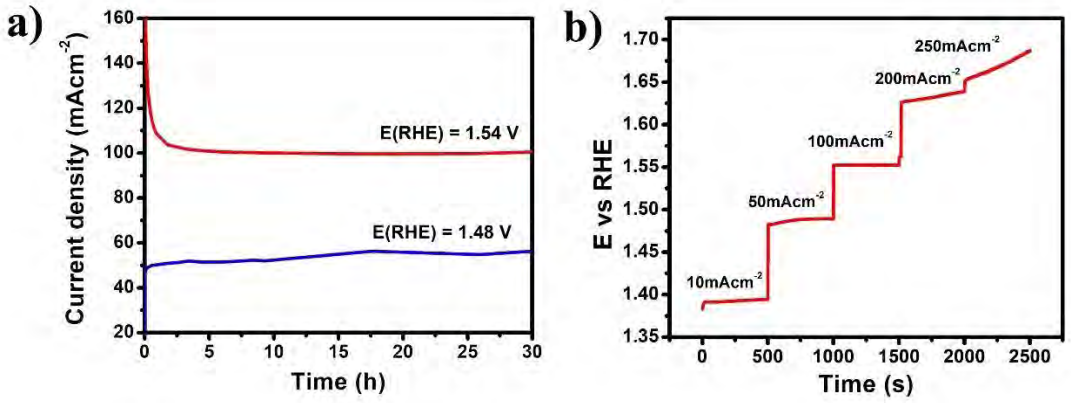

Figure 3.22: (a) Controlled potential electrolysis of NiCo-Alloy@CeO_2 at 1.48 V and 1.54 V vs. RHE (b) Multistep chronopotentiometry of NiCo-Alloy@CeO_2 at different current densities ranging from 10 mA cm^{-2} to 250 mA cm^{-2}.

The consistent and sustained performance of NiCo-Alloy@CeO_2 during the controlled potential electrolysis demonstrates its robustness and resistance to degradation, rendering it an exceedingly promising contender for real-world implementation in electrocatalytic processes, especially for OER. The material's ability to maintain its catalytic activity over prolonged periods at elevated current densities highlights its potential for long-term and efficient usage in various energy conversion and storage devices.

Electron Impedance Spectroscopy

To assess the electrocatalytic capabilities of the fabricated electrodes, Electrochemical Impedance Spectroscopy (EIS) was performed and analyzed (Figure 3.23). At an overpotential of 50 mA/cm^2, NiCo-Alloy@CeO_2 exhibited a charge-transfer resistance (Rct) of 5.5 Ω, which was significantly lower than those observed for NiCo-Alloy (14.5 Ω), NiCo-LDH (24.38 Ω), and CeO_2 (43.4 Ω). This finding indicates that NiCo-Alloy@CeO_2 possesses highly efficient charge transfer kinetics, contributing to its superior electrocatalytic performance for the OER.

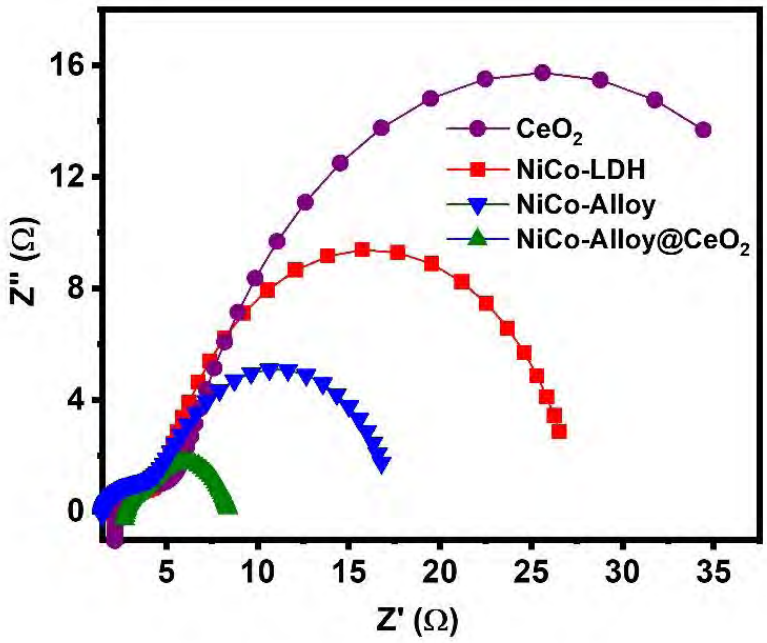

Figure 3.23: Nyquist diagrams of the synthesized electrocatalysts were obtained between frequency span ranging from 100 kHz down to 0.1 Hz.

Double Layer Capacitance and ECSA

To further examined the intrinsic activities of the fabricated electrocatalysts, the Electrochemical Active Surface Area (ECSA) of the electrodes was calculated by examining the double-layer capacitances (Cdl) (Figure 3.24). Cyclic voltammetry was conducted in the non-faradaic zone at various scan rates to calculate the Cdl of the electrode surface. The obtained cyclic voltammograms (Figures 3.24(a-c)) showed that the current density increased with increasing scan rate during the OER process. As

depicted in Figure 3.24(d), the NiCo-Alloy@CeO_2 electrocatalyst exhibited the largest Cdl, indicating the highest ECSA among all the synthesized materials, measuring 555 cm^2. In comparison, the ECSA values for NiCo-Alloy, NiCo-LDH, and CeO_2 were 355 cm^2, 245 cm^2, and 165 cm^2, respectively.

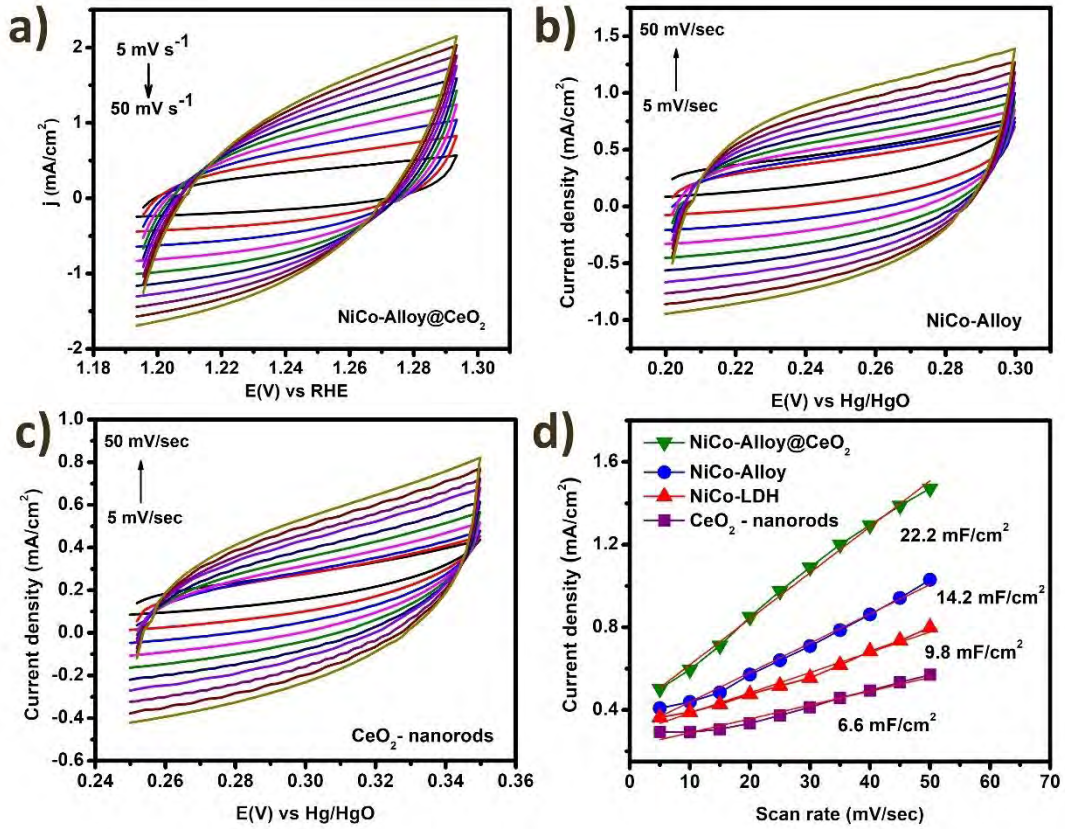

Figure 3.24: Cyclic voltammograms at different rates in the non-faradaic zone for (a) NiCo-Alloy@CeO_2, (b) NiCo-Alloy, and (c) CeO_2. (d) plot between current density vs different scan rates to calculate Double Layer Capacitance (Cdl) values of all the synthesized electrocatalysts.

The significant difference in ECSA values among the materials suggests that the integration of NiCo-alloy nanosheets with CeO_2 nanorods in NiCo-Alloy@CeO_2 contributes to a larger active surface area available for electrocatalytic reactions. The increased ECSA further supports the superior catalytic performance of NiCo-Alloy@CeO_2 in the OER compared to the other synthesized materials. This enhanced surface area facilitates a higher number of active sites, which is critical for enhancing

the electrocatalytic efficiency and durability during the OER process. Figure 3.25 displays a bar graph that compares the evaluating parameters of various electrocatalysts for the OER in a 1M KOH electrolyte. The bar graph likely includes performance metrics, such as overpotential, current density, Tafel slope, and other relevant parameters, for each electrocatalyst. This comparison allows for a comprehensive assessment of the efficiency and effectiveness of different catalysts in promoting the OER process in alkaline conditions.

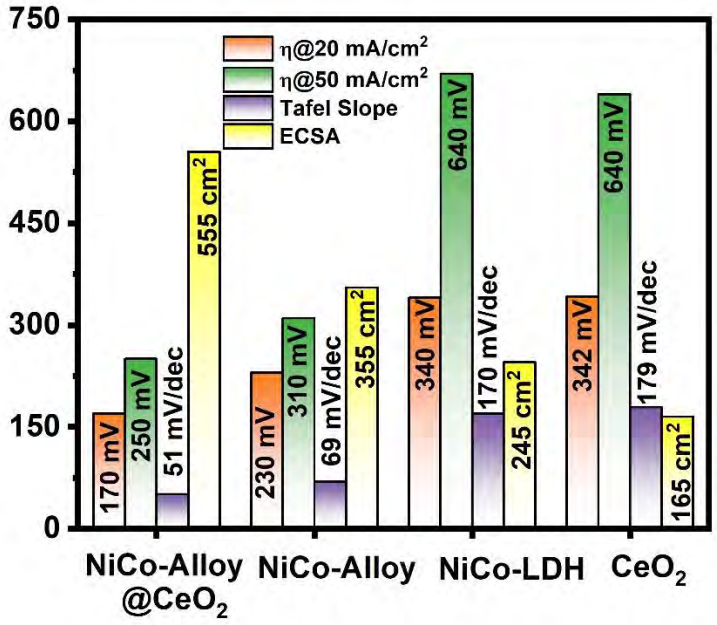

Figure 3.25: Bar-graph comparing the evaluating parameters of different electrocatalysts for the OER in 1M KOH electrolyte.

The superior catalytic performance of NiCo-Alloy@CeO_2 can be attributed to the synergistic effects resulting from the heterointerface formed between NiCo-alloy and CeO_2 nanorods. This heterointerface provides abundant active hotspot for the catalytic reactions, enhancing the efficiency of the OER. Additionally, the presence of oxygen deficiencies in the CeO_2 lattice creates unoccupied locations, facilitating the migration of adjacent oxygen anions. This leads to increased ionic conductivity, further improving the OER kinetics. [325, 326]

Reaction Mechanism

The Ce^{3+} species in CeO_2 play a crucial role in the OER mechanism. Ce^{3+} can adsorb additional hydroxyl groups and exhibits stronger interactions with OH*, promoting the water dissociation process. This, in turn, expedites the overall OER kinetics. [327-329] The proposed mechanism for oxygen evolution is depicted in figure 3.26. Reaction mechanism on active sites of Ce^{3+} - Ce^{4+} involves the raising of the oxidation state of Ce^{3+} by one unit when one H_2O molecule coordinatively binds to empty sites. [327, 330, 331]. This process involves the loss of one electron and one proton to form OH*. The intermediate O* is generated through the release of one proton and one electron from OH*. However, the O* species exists only as an O radical since Ce^{4+} is in its highest oxidation state. O* then continues to combine with water to produce OOH*, releasing an electron and a proton. Finally, OOH* creates an empty site after losing one electron and one proton, generating O_2 and completing the catalytic cycle.

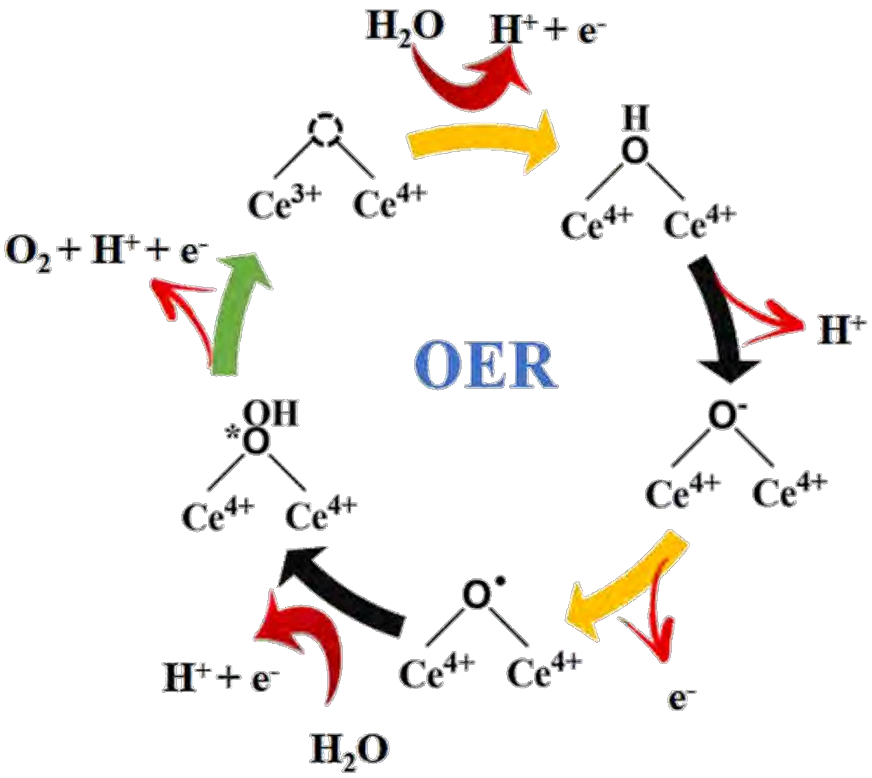

Figure 3.26: Proposed OER mechanism on the catalytic active site of CeO_2. The schematic diagram illustrates the step-by-step process of oxygen evolution at the CeO_2

surface, offering valuable perspective into the underlying catalytic mechanism and the role of active site in the OER process.

Comparative Analysis

In comparative studies of different parameters for OER, NiCo-Alloy@CeO_2 stands out as the most efficient electrocatalyst, showcasing its superior performance compared to NiCo-Alloy, NiCo-LDH, and CeO_2. In Table 3.6, a comprehensive comparison of the OER electrocatalytic activities between the synthesized materials and those reported in the literature is presented. The table serves to highlight and confirm the outstanding catalytic performance of the NiCo-Alloy@CeO_2 composite material. By comparing the OER performance metrics, such as overpotential, current density, Tafel slope, and other relevant parameters, with previously reported catalysts, the remarkable catalytic prowess of NiCo-Alloy@CeO_2 is evident. This confirms the composite's superiority and further supports its potential as a superior electrode material for clean energy applications.

Table 3.6: Comparison of OER performance of the synthesized electrocatalyst with reported materials.

Catalyst	Overpotential	Tafel slope (mV/dec)	Reference
$NiCo_{2.7}(OH)_x$	350 @ 10 mA/cm^2	65	[332]
NiCo-LDH	420 @ 10 mA/cm^2	113	[333]
O-NiCoFe-LDH	340 @ 10 mA/cm^2	93	[334]
$NiCo_2O_4$@MoS_2	305@ 10 mA/cm^2	80	[335]
FeCoNi-Alloy@N-dopped graphitic carbon	288 @ 10 mA/cm^2	60	[336]
$NiCo_2S_4$@NiFe-LDH/NF	201 @ 10 mA/cm^2	46.3	[337]
CeO_2/Co_3O_4	265 @ 10 mA/cm^2	68	[338]
Ce-NiO-E	382 @ 10 mA/cm^2	118	[339]
NiCo-Alloy@CeO_2	**170** @ 10 mA/cm^2	**51**	**This work**

3.2.7 HER Performance

The HER performance of as synthesized electrode was also evaluated in 1M KOH electrolyte. Figure 3.27(a), shows the linear sweep voltammogram of NiCo-Alloy@CeO_2, NiCo-Alloy, NiCo-LDH and CeO_2 with iR correction. The HER overpotential recorded for NiCo-Alloy@CeO_2 is 221 mV vs RHE to generate a current density of 50 mA/cm^2, which is significantly less than the overpotential measured for NiCo-Alloy (393 mV), NiCo-LDH (503 mV), and CeO_2 nanorods (727 mV) to attain the same catalytic current density. The high efficacy of NiCo-Alloy@CeO_2 towards HER is accredited to synergism of nickel and cobalt, also CeO_2 optimized the electronic structure of NiCo-Alloy by its high potency of undergoing exchangeable oxidation states (Ce^{4+}/Ce^{3+}).[340]

To uncover the inherent kinetics of electrocatalytic reaction, Tafel slopes were computed from the corresponding LSV curves. As depicted in figure 3.27(b), a minimal Tafel slope value of 89 mV/dec is executed by the NiCo-Alloy@CeO_2, which suggests its faster kinetics than the precursor NiCo-Alloy (110 mV/dec), NiCo-LDH (125 mV/dec) and CeO_2 (175 mV/dec). The HER in alkaline media is accompanied by three principle reaction steps: Volmer step (i), in which the adsorption of hydrogen via a dissociated water molecule proceeded by Heyrovsky (ii) or Tafel step (iii) that is detachment of hydrogen molecule by interaction of water with adsorbed hydrogen atom or by the combination of two hydrogen atoms.[341]

$$H_2O + M^+ e^- \rightarrow MH_{ads} + OH^- \quad \text{(i)}$$

$$MH_{ads} + H_2O + e^- \rightarrow M + OH^- + H_2 \quad \text{(ii)}$$

$$2MH_{ads} \rightarrow 2M + H_2 \quad \text{(iii)}$$

The Tafel slope value ~ 30 mV/dec predicts that the rate determining step could be Tafel step, while a Tafel slope of ~ 40 mV/dec and ~ 120 mV/dec suggest Heyrovsky and Volmer are the rate determining steps respectively. The catalyst (NiCo-Alloy@CeO_2), displays a Tafel value of 89 mV/dec indicating the rate determining step is Volmer-Heyrovsky reaction.[342-344]

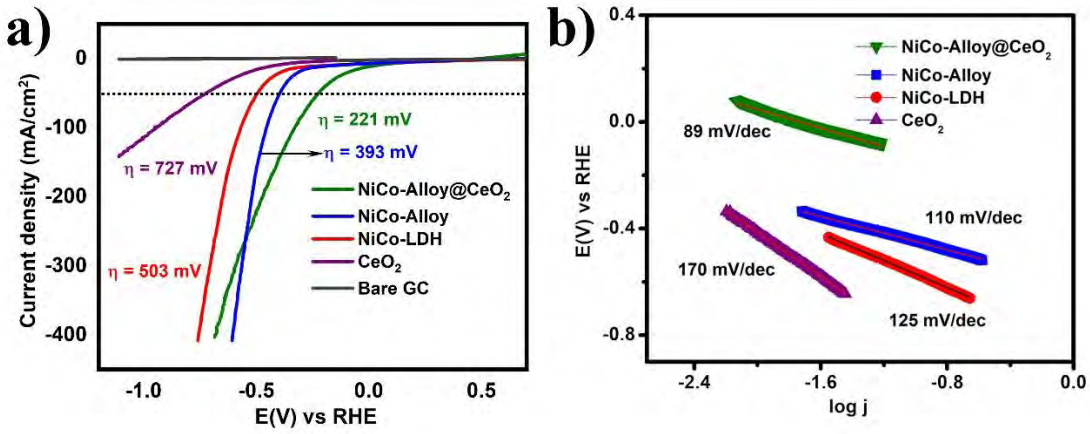

Figure 3.27: (a) Linear sweep voltammetry (LSV) curves comparing the performance of different catalysts, including NiCo-Alloy@CeO_2, NiCo-Alloy, NiCo-LDH, CeO_2, RuO_2, and Bare Glassy Carbon (GC), for the HER (b) Tafel plots obtained from corresponding LSV curve, illustrating the catalytic activity and electrochemical behavior of the investigated catalysts for the HER.

Stability

The stability of the catalyst is key parameter to quest its commercial applicability. Controlled potential electrolysis was performed in an alkaline media at an operation potential (-0.2 V) vs RHE to measure durability of the electrocatalyst. As illustrated in figure 3.28, that current density for NiCo-Alloy@CeO_2 is maintained even after 14 h, which evident the high robustness of the synthesized catalyst. Meanwhile, the LSV curves of pristine and post catalytic NiCo-Alloy@CeO_2 (figure 3.28 (inset) is not significantly different reveals excellent durability of catalyst.

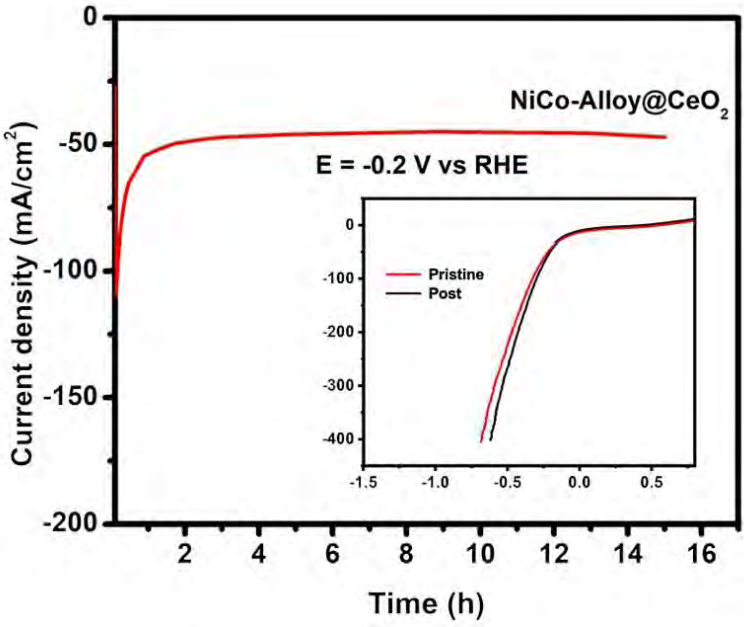

Figure 3.28: Controlled potential electrolysis conducted at a steady potential of -0.2V vs RHE, with an inset figure showing the pristine and post-catalytic Linear Sweep Voltammetry (LSV) curves of NiCo-Alloy@CeO_2 catalyst.

Electron Impedance Spectroscopy

To evaluate the charge transfer capabilities, electrochemical impedance spectroscopy was conducted. It is worth mentioning that NiCo-Alloy@CeO_2 demonstrated a least charge transfer resistance as depicted by a small semicircle in the Nyquist plot. As illustrated in figure 3.29(a), NiCo-Alloy@CeO_2 displays a small radius of its semicircle and low Rct (6.1 Ω) compared to individual NiCo-Alloy (10 Ω), NiCo-LDH (15.2 Ω), and CeO_2 nanorods (26.3 Ω) suggested the strong electronic coupling between NiCo-Alloy and CeO_2 which enhance electronic conductivity. Although, CeO_2 itself does not possess sufficient conductivity but its unique surface property resulting from the reversible reduction (Ce^{3+}/Ce^{4+}) potentially promotes the adsorption and desorption of reactants and products throughout the reaction.[345]

Double Layer Capacitance and ECSA

To investigate the intrinsic behavior of the active sites, cyclic voltammetry has been performed in the non-faradaic zone to calculate Cdl, spanning from 5-50 mV/s. This specific scan range allows for the evaluation of the capacitive response of the material

without involving any Faradaic reactions, providing insights into the electrochemical double layer behavior at the active hotspots. The obtained double layer capacitance data helps in understanding the charge storage capabilities and surface properties of the material. Electrochemical active surface area (ECSA) is evaluated by a relation C_{dl}/C_s, where C_s is specific capacitance. Value of Cs is 0.04 mF/cm^2 stated by McCrory in alkaline solution.[346] The results reveals that NiCo-Alloy@CeO_2 shows highest C_{dl} value of 25 mF/cm^2, this would result in a substantial quantity of catalytic sites, ultimately revealing a high electrochemically active surface area of 625 cm^2. The Cdl values are also computed for NiCo-Alloy, NiCo-LDH and CeO_2 nanorods which are 18.9 mF/cm^2, 14.9 mF/cm^2 13.9 mF/cm^2 and their corresponding ECSA are 625 cm^2, 472 cm^2, 372 cm^2 and 347 cm^2, respectively (Figure 3.29(b)). This might be attributed to the nanosized ceria particles which significantly reduces the particle size of NiCo-Alloy as calculated by PXRD.

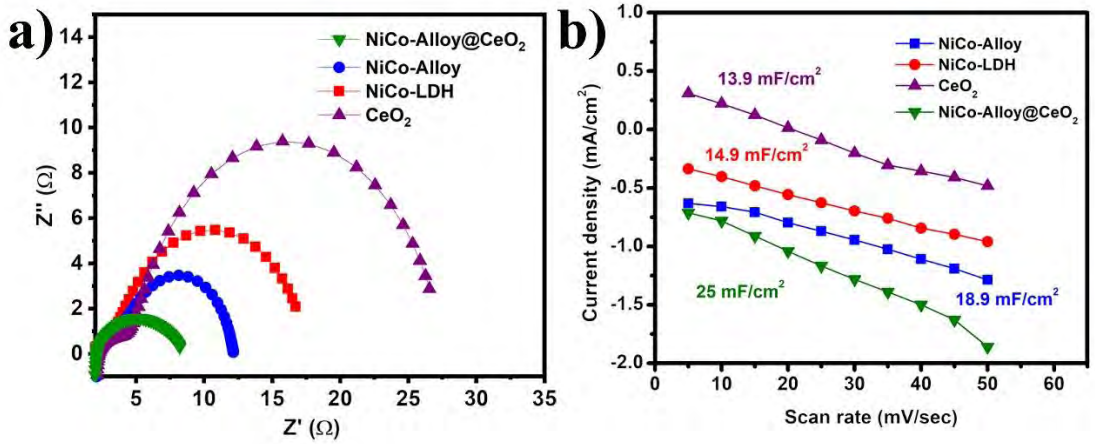

Figure 3.29: a) Nyquist plots obtained for a series of electrocatalysts, spanning a range of frequency from 100 kHz to 0.1 Hz b) Double layer capacitance (C_{dl}) values determined from the Nyquist plots for the different electrocatalysts.

The remarkable HER activity of NiCo-Alloy is explained by various factors such as synergistic effect of NiCo-Alloy and CeO_2. Addition of ceria to a metal catalyst beneficially modulate the electronic configuration of the catalyst, which as a result enhance the adsorption/desorption of reactants and products significantly enhance the electrocatalytic activity.[219,347] Moreover, easily transformable oxidation states Ce^{4+} to Ce^{3+} creates oxygen vacancies, particularly beneficial for oxidation reactions as the

binding energy of water is stronger particularly beneficial for oxidation of water during Volmer step.[228, 230] Figure 3.2.30, shows a comparative analysis for as fabricated electrodes.

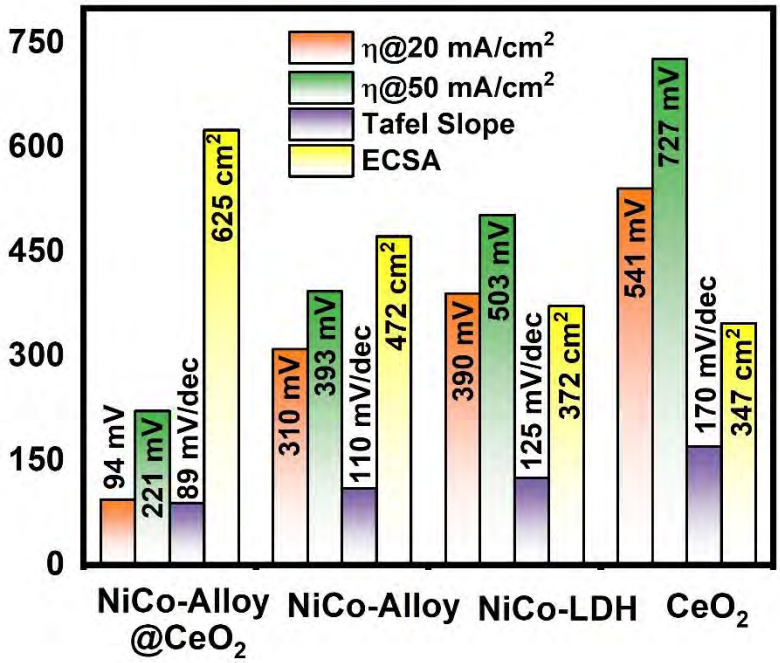

Figure 3.30: Bar-graph comparing various electrocatalysts for the OER in 1M KOH, highlighting their respective overpotentials at 20 and 50 mA/cm², Tafel slopes, and Electrochemical Active Surface Area (ECSA) for direct comparison and evaluation.

In Table 3.7, a comparison of the HER performance of the synthesized electrocatalyst is provided in relation to reported materials. This comparative analysis enables researchers to assess the efficiency and effectiveness of the synthesized electrocatalyst in promoting the HER process. By comparing the HER performance with existing materials, the table helps to validate and demonstrate the superiority of the synthesized electrocatalyst and its potential as an efficient HER catalyst. This information is valuable for understanding the electrocatalytic properties of the material and its potential applications in hydrogen generation and other clean energy technologies.

Table 3.7: Comparison of the HER performance of the synthesized electrocatalyst with respect to reported materials. The graph showcases key metrics such as catalytic activity, overpotential, and stability, enabling an assessment of the synthesized material's effectiveness as an HER catalyst in relation to existing literature.

Catalyst	Overpotential	Tafel Slope (mV/dec)	Reference
NiCoP/rGO	209 @10 mA/cm^2	65.3	[348]
$Ni_{0.71}Co_{0.29}P$	232 @10 mA/cm^2	93	[349]
SCFN	184 @10 mA/cm^2	126	[350]
$CoFeN_x$-500 HNAs/NF	200 @10 mA/cm^2	84.3	[179]
Ni_3FeN-NPs	158@10 mA/cm^2	42	[237]
NiFeMoS-400	210 @10 mA/cm^2	88	[276]
NiCo-Alloy@CeO_2	221 @50 mA/cm^2	89	**This Work**

3.2.8 Conclusions

A novel bifunctional electrode material, NiCo-Alloy@CeO_2, has been successfully synthesized through a hydrothermal approach followed by annealing. The synthesis process involving two steps, forming NiCo-Alloy by annealing LDHs-based precursors, and integrating it onto Ceria nanorods through impregnation, was confirmed successful by various analytical techniques. This composite material demonstrates exceptional performance toward both OER as well as HER under alkaline environments. The NiCo-Alloy@CeO_2 exhibits superior OER electrocatalytic efficiency at low overvoltage of 170 mV at 20 mA/cm^2, high durability for 14 h at 50 mA/cm^2, and accelerated kinetics with a 51.1 mV/dec Tafel slope. The NiCo-Alloy@CeO_2 catalyst also displays excellent electrocatalytic performance for HER, required minimal overpotential of 221 mV to obtain 50 mA/cm^2, just a very low Tafel slope, minimal Rct, high active electrochemical surface area, and excellent durability for 14 h. This remarkable efficiency can be accredited to several factors, including the synergism at interface between NiCo-Alloy and CeO_2, the oxygen vacancies enhancing ionic conductivity, and the absorption of hydroxyl groups by Ce^{3+} facilitating water dissociation. The integration of CeO_2 nanorods into NiCo-Alloy nanosheets expedites

the electro-coupled dissociation of water and facilitates the adsorption of intermediate hydrogen species, which caused enhanced OER efficiency. The open ends of ceria nanorods further boost catalytic performance by aiding the diffusion of active species. The unique electronic attributes of ceria, along with the active sites provided by nickel and cobalt, also contribute to the enhanced HER efficiency. Overall, the development of this bifunctional material presents a viable and cost-effective solution for clean and efficient energy conversion.

3.3 Material – III (NiFeSe@CoOx-NCNTs)

In this study, a novel and versatile strategy has been employed to synthesize a highly efficient and stable electrocatalyst, NiFeSe@CoOx-NCNTs, which shows exceptional activity for both the OER and the HER. The synthesis process involves a hydrothermal approach to create an LDH precursor, followed by a selenization process to produce bimetallic nickel-iron selenide (NiFeSe) modified with ZIF-derived CoOx-NCNTs. The resulting material exhibits a remarkably low OER overpotential of only 240 mV at 20 mA/cm^2, along with a small Tafel value of 59.2 mV/dec. For the HER process, it achieves a current density of 20 mA/cm^2 at 145 mV, with a Tafel slope of 169 mV/dec. Additionally, the composite demonstrates low charge transfer resistance, a high electrochemical active surface area, and impressive stability for 15 h, making NiFeSe@CoOx-NCNTs a highly attractive candidate for energy conversion systems. Transition metal selenides like this offer great potential as efficient and abundant electrocatalysts for clean hydrogen production through water splitting. Figure 3.31 illustrates graphical abstract for OER and HER catalysis utilizing a NiFeSe@CoOx-NCNTs composite material. A comprehensive analysis of the material's properties and electrochemical performance is elaborated in the following sections.

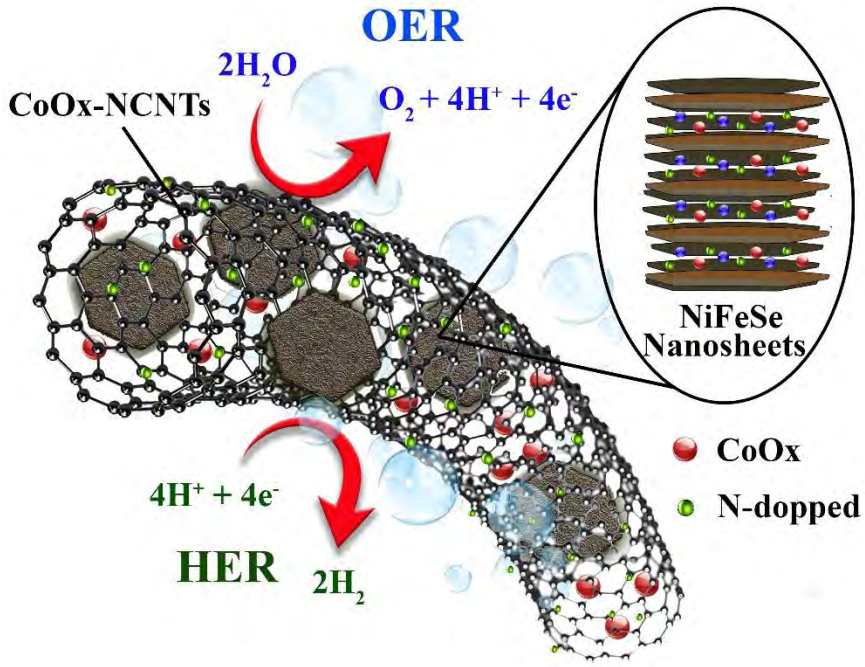

Figure 3.31: Graphical abstract illustrating the OER and HER catalysis utilizing a NiFeSe@CoOx-NCNTs composite material.

3.3.1 Characterization

Powder X-ray Diffraction

The characterization of the synthesized catalyst, NiFeSe@CoOx-NCNTs, was performed using Powdered X-ray Diffraction (PXRD) to investigate its crystalline features. The PXRD diffractogram of the composite material, as shown in Figure 3.32, revealed distinct peaks corresponding to different crystal planes. Specifically, peaks located at 29.7°, 33.4°, and 36.8° were identified as the (200), (210), and (211) planes of the cubic phases of NiSe, respectively. Another set of Bragg's reflections at 2θ angles of 24.1°, 40.9°, 44.2°, and 64.2° were attributed to the (110), (210), (121), and (122) indices of the orthorhombic phases of FeSe, respectively, confirming the presence of both nickel selenide and iron selenide in the composite. The PXRD pattern of CoOx-NCNTs exhibited a broad diffraction peak around 26°, which corresponds to the (002) facets of the graphitic carbon network, and a peak at 43°, indicative of the characteristic sp^2-hybridized graphitic structure. [351] However, upon analyzing the XRD pattern of the NiFeSe@CoOx-NCNTs composite, it was observed that the (002) peak from the graphitic carbon network was not clearly discernible. This was accredited to the

development of iron selenide nanosheets on the surface of CoOx-NCNTs, effectively concealing the exposed surface of the carbon nanotubes, including the (002) facets of the graphitic carbon network. Consequently, the peak became obscured, indicating successful integration of NiFeSe onto the CoOx-NCNTs support.

Furthermore, the XRD pattern of the composite material did not show any distinct diffraction peaks corresponding to cobalt oxide (CoOx) phases. This observation was explained by the encapsulation of the cobalt oxides within the carbon nanotubes, as confirmed by XPS spectra. The encapsulation process led to the cobalt oxides existing in a highly dispersed or amorphous state, hindering the formation of well-defined diffraction peaks. This encapsulation phenomenon further supported the successful integration of the NiFeSe and CoOx components in the composite. [352] Another notable finding from the XRD analysis was the absence of diffraction peaks corresponding to the starting material, NiFe-layered double hydroxide (NiFe-LDH). This indicated the complete conversion of NiFe-LDH into NiFeSe during the selenization process, demonstrating the effectiveness of the synthetic approach in producing the desired composite material.

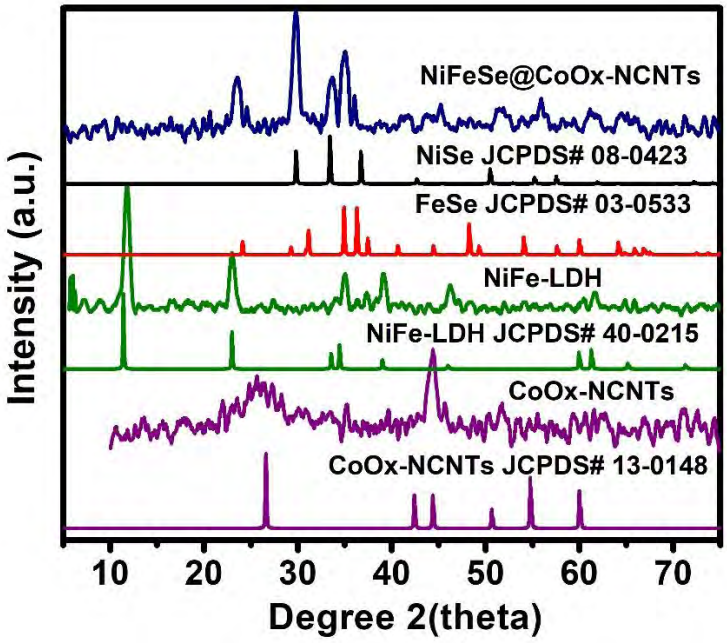

Figure 3.32: PXRD patterns of NiFeSe@CoOx-NCNTs, NiFe-LDH, and CoOx-NCNTs, along with their corresponding JCPDS cards.

X-ray Photoelectron Spectroscopy (XPS)

XPS was employed to gain a deeper understanding of the chemical states and surface elemental composition of both NiFeSe@CoOx-NCNTs (Figure 3.33) and CoOx-NCNTs (Figure 3.34). The XPS spectra of the composite material in figure 3.33 clearly showed the presence of Ni, Fe, Co, and Se. Specifically, the Ni 2p orbital exhibited several distinct peaks (Figure 3.33(a)) at BEs of 855.6 eV and 873.6 eV, which were attributed to Ni^{2+} ions present in the metal selenides. However, the presence of additional peak at 870.7 eV indicated the formation of nickel oxide species, likely due to surface oxidation. [353, 354] The appearance of satellite peaks at 862.4 and 878.5 eV serves as further evidence for the presence of Ni^{2+} in the selenide. This phenomenon could result in modifications of the electronic environment around nickel species. Analysis of the high-resolution Fe 2p spectrum (Figure 3.33(b)) revealed prominent peaks at 710.8 eV (Fe $2p_{3/2}$) and 723.6 eV (Fe $2p_{1/2}$), which correspond to Fe^{2+} in metal selenides. [355-357] These findings are in line with previous studies on similar systems and confirm the presence of iron species in the selenide phase.

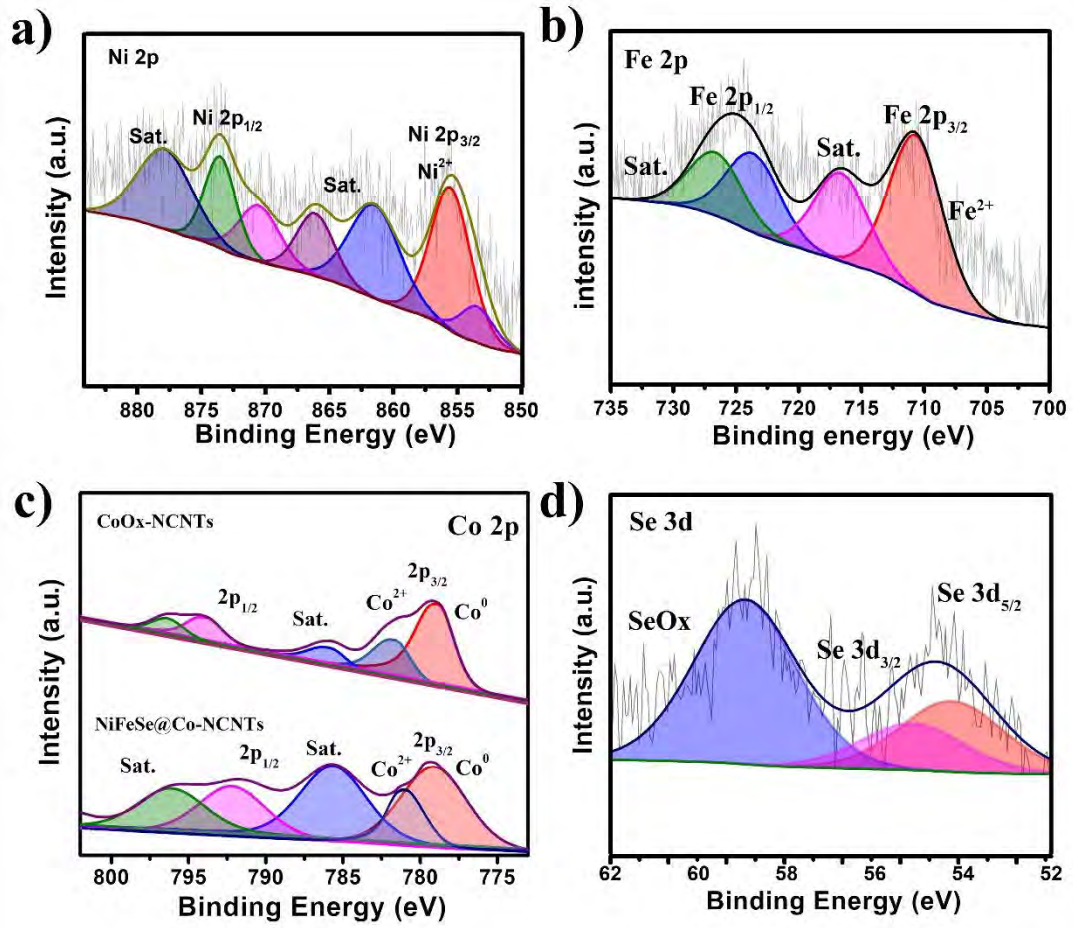

Figure 3.33: XPS spectra of NiFeSe@CoOx-NCNTs showing (a) Ni 2p, (b) Fe 2p, (c) Co 2p in both CoOx-NCNTs, and NiFeSe@CoOx-NCNTs, and (d) Se 3d.

In the XPS survey of CoOx-NCNTs (Figure 3.33(c)), the Co 2p spectrum displayed a complex profile, indicating the existence of multiple cobalt phases. A peak observed at 779.1 eV was attributed to metallic cobalt (Co^0), while the appearance of peaks at 781.7 eV (Co $2p_{3/2}$) and 793.9 eV (Co $2p_{1/2}$) corresponded to CoOx, confirming the existence of cobalt oxides in the material. [358, 359] Additionally, satellite peaks observed at 786.02 eV and 796.3 eV further confirmed the presence of mixed phases of cobalt oxides. [360] These results suggest that CoOx-NCNTs comprise a combination of different cobalt oxide species. The XPS spectra of Co 2p in NiFeSe@CoOx-NCNTs exhibited similar characteristics to those observed in CoOx-NCNTs, indicating that the oxidation states of cobalt remained unchanged in the composite material. However, slight shifts in the peak positions were observed, implying alterations in the local chemical surroundings of the cobalt species. These shifts suggested that the formation of NiFeSe@CoOx-

NCNTs involved interactions between CoOx-NCNTs and metal selenides (NiFeSe), resulting in a modified electronic configuration and the emergence of a synergism between the two components. This interaction likely contributed to the enhanced catalytic efficiency of the composite.

In the XPS spectrum of Se 3d (Figure 3.33(d)), two distinct peaks were observed at BEs of 54.4 eV and 55.3 eV, subsequent to the spin-orbit coupling of the $3d_{5/2}$ and $3d_{3/2}$ states, accordingly, of metal-selenium bonds. [284] These peaks indicated the presence of selenium in the material and confirmed its association with the metal elements in the composite. Additionally, there were additional peaks observed at a B.E of 58.8 eV, which belong to Se-O bonding structures. This observation suggested that there was a slight surface oxidation of the selenium species when exposed to air. The presence of Se-O bonds indicates that some selenium atoms at the surface of the material reacted with oxygen in the air, forming oxide species. This surface oxidation of selenium may have implications for the electrocatalytic properties of the material, as it could affect the surface reactivity and the interaction with reactant species during catalytic reactions. In Figure 3.34, XPS spectra of CoOx-NCNTs are presented, showcasing the elemental composition of the material. The graphs demonstrate that the composition of CoOx-NCNTs remained unchanged during the selenization process. This observation suggests that the selenization treatment did not significantly alter the elemental composition of the material.

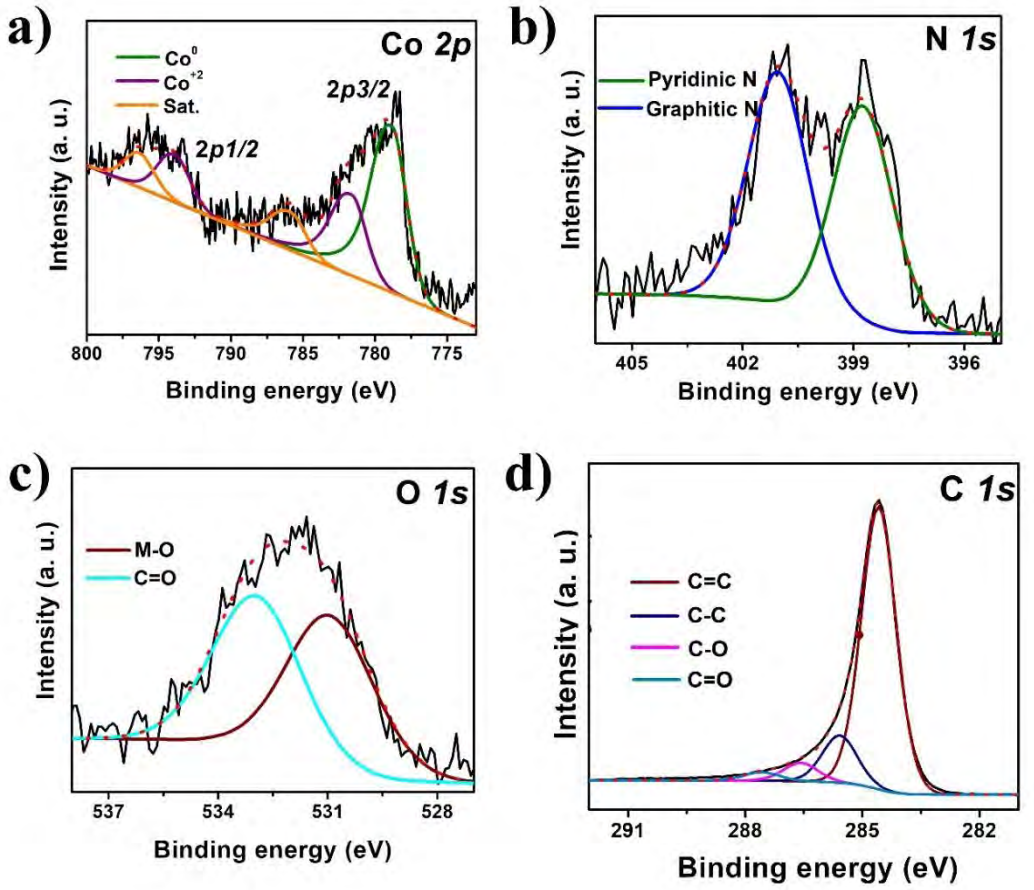

Figure 3.34: XPS spectra of CoOx-NCNTs demonstrating (a) Co 2p, (b) N 1s, (c) O 1s, and (d) C 1s regions.

Morphology of the Catalyst

The morphology of ZIF-12 derived CoOx-NCNTs and its composite with NiFeSe nanosheets was thoroughly investigated using HRTEM measurements (Figure 3.35). The HRTEM images of CoOx-NCNTs revealed a well-defined tubular structure (Figure 3.35(a)) with CoOx nanoparticles observed at the ends of the tubular nitrogen-doped carbon network, having a size distribution centered around 50 nm. These CoOx nanoparticles were intricately embedded within multiple layers of a nitrogen-doped carbon network. The HRTEM image of the composite (Figure 3.35(b and c)) clearly depicts the existence of nanosheets of NiFeSe over CoOx-NCNTs. This presence of nanosheets was found to foster greatly to the enhanced catalytic activity of the composite, as a synergistic effect resulted from the interaction between CoOx-NCNTs

and the NiFeSe nanosheets. Additionally, the nitrogen-doped carbon nanotubes (NCNTs) played a vital role in preventing the agglomeration of the NiFeSe nanosheets, thus exposing more active sites and promoting catalytic activity.

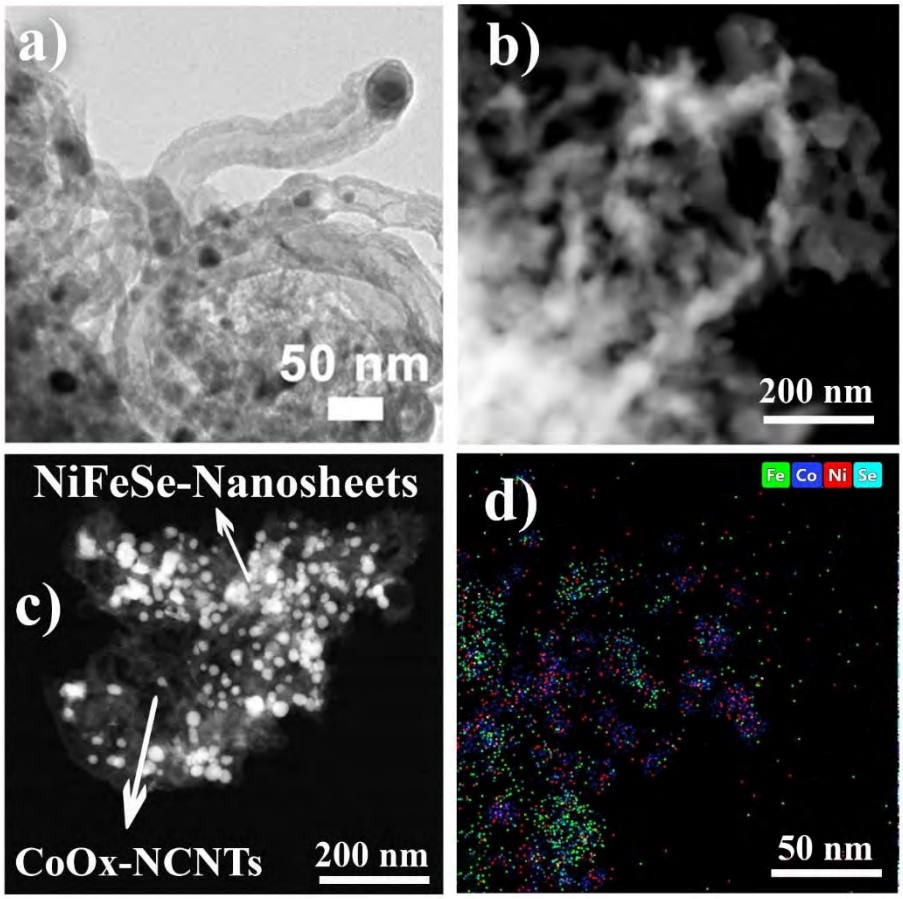

Figure 3.35: HRTEM images and elemental mapping analysis of ZIF-12 derived CoOx-NCNTs and its composite, (a) Tubular structure of CoOx-NCNTs, (b) Network of CoOx-nitrogen doped carbon tubes, (c) HRTEM image of the composite (NiFeSe@CoOx-NCNTs), and (d) Elemental mapping of NiFeSe@CoOx-NCNTs.

Elemental Mapping

Elemental mapping results provided strong evidence for the presence and effective distribution of nickel, iron, cobalt, and selenium elements in the composite (Figure 3.35(d). The HRTEM elemental mapping analysis confirmed the successful integration and dispersion of NiFeSe nanosheets over the cobalt oxide-encapsulated nitrogen-doped tubular carbon network (CoOx-NCNTs). These comprehensive HRTEM

observations and elemental mapping analyses provide valuable insights into the structural features and distribution of elements in the composite material, NiFeSe@CoOx-NCNTs. The well-designed nanoscale architecture and synergistic interactions between different components in the composite contribute to its outstanding catalytic performance for the OER and HER, making it a highly promising electrocatalyst for clean and efficient energy conversion.

3.3.2 Electrochemical Performance

OER Performance

The electrocatalytic performance of the as-synthesized samples for both the OER and HER was tested at room temperature, using 1M KOH as the electrolyte. For comparison, the bare glassy carbon electrode and benchmark material, RuO_2, were also evaluated under the same conditions. LSV curves were obtained at 10 mV/s to reduce capacitive current. Figure 3.36(a) shows the anodic LSV curves obtained for the synthesized samples and the reference samples between the potential window range of 1.1-1.8 V relative to the RHE. To eliminate potential confusion arising from overlapping regions of metal oxidation and oxygen evolution, Figure 3.36(b), presents zoomed-in LSV curves for a clear and distinct analysis of the individual electrochemical processes, ensuring accurate interpretation of the data. The bare glassy carbon electrode exhibited a negligible current density with the applied voltage, indicating that it had no contribution to the electrocatalytic performance. Among the prepared catalysts, NiFeSe@CoOx-NCNTs demonstrated the highest performance towards OER. It demands just 240 mV low overpotential to obtain catalytic current density of 20 mA/cm^2, which is nearly comparable to the overpotential recorded for the benchmark material, RuO_2. On the other hand, all the other materials showed some degree of OER activity, but their efficiency was far less than that of the NiFeSe@CoOx-NCNTs composite. Notably, the anodic peak shifted from 1.56 V to 1.47 V vs. RHE after the selenization of the precursor NiFe-LDH@CoOx-NCNTs. This shift in peak potential indicates the low polarization of the catalyst. [361-363] Electrodes with low polarization exhibit improved charge transfer kinetics, which is consistent with previous research findings. The enhanced electrocatalytic performance of NiFeSe@CoOx-NCNTs is majorly attributed to the synergism between NiFeSe

nanosheets and ZIF-12 derived CoOx-NCNTs support, as observed in the HRTEM images. Additionally, the nitrogen-doped carbon nanotubes (NCNTs) played a crucial role in preventing the agglomeration of NiFeSe nanosheets, exposing more active sites and promoting catalytic activity. Indeed, the observed shift in redox potential can be ascribed to the distinct electronic configuration of selenides. Se possesses unique electronic properties characterized by a small energy gap between its 3d, 3s, and 3p orbitals, which results in good electrical conductivity. [364] This small energy gap allows for efficient charge transport within the material, facilitating rapid electron transfer during the redox processes. The presence of selenide species, particularly in the NiFeSe@CoOx-NCNTs composite, introduces additional electronic states that can effectively participate in electrochemical reactions. The electronic configuration of the selenides effects the electronic environment of the composite material, which, in turn, affects its redox properties and catalytic performance. As a result, the selenization process of the precursor NiFe-LDH@CoOx-NCNTs leads to modifications in the local chemical surroundings of cobalt (Co) and other metal species, influencing the redox potential during electrocatalytic reactions. The good electrical conductivity arising from the small energy gap in Se 3d, 3s, and 3p orbitals plays role in enhancing the charge transfer kinetics at the electrode-electrolyte interface. This efficient charge transport contributes to the low polarization of the catalyst, as observed in the anodic LSV curves. The reduced polarization facilitates faster reaction kinetics, leading to enhanced electrocatalytic efficacy for both OER and HER.

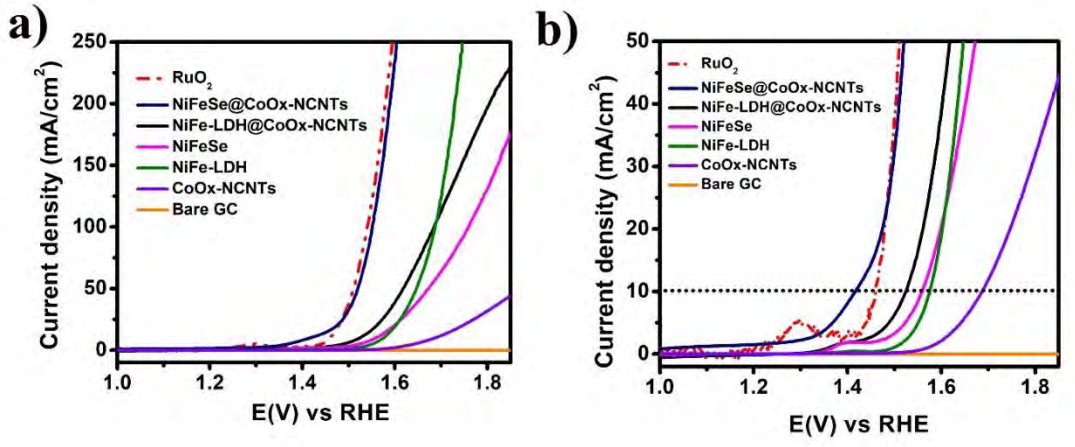

Figure 3.36: (a) Anodic Linear Sweep Voltammetry (LSV) curves of NiFeSe@CoOx-NCNTs compared with other synthesized materials (b) Zoomed-in LSV curves, highlighting the detailed electrochemical behavior and performance of NiFeSe@CoOx-NCNTs and the other synthesized materials at specific voltage regions. The zoomed curves allow for a more precise examination of the catalytic activity and reaction kinetics.

The Tafel slope, which provides insights into the kinetics of the electrocatalytic reaction, was calculated from the subsequent LSV curves, as shown in figure 3.37. The Tafel slope represents the change of rate in the logarithm of the current density with respect to the applied potential and is used to determine the mechanism of the reaction and reaction rate of the electrocatalytic process. A Tafel value of 59.5 mV/dec was observed for the NiFeSe@CoOx-NCNTs composite, indicating faster reaction kinetics. This low Tafel slope value is in line with the excellent electrocatalytic activity observed in the LSV data for this composite. Comparatively, the Tafel slopes determined for the other catalysts were higher: 126.3 mV/dec for NiFe-LDH@CoOx-NCNTs, 126.3 mV/dec for NiFeSe, 83.6 mV/dec for NiFe-LDH, and 108.6 mV/dec for CoOx-NCNTs. These higher Tafel slope values suggest slower reaction kinetics for these individual catalysts compared to the NiFeSe@CoOx-NCNTs composite. These results further corroborate the superior OER performance of the composite material, highlighting its efficient reaction kinetics and enhanced catalytic activity. The low Tafel slope value for the NiFeSe@CoOx-NCNTs composite indicates a favorable reaction mechanism, likely involving rapid electron transfer and efficient adsorption/desorption of intermediate species. The synergistic effect between NiFeSe nanosheets and the CoOx-NCNTs support, along with the good electrical conductivity of the selenides, likely contributes to the enhanced reaction kinetics and superior electrocatalytic efficacy of the composite material.

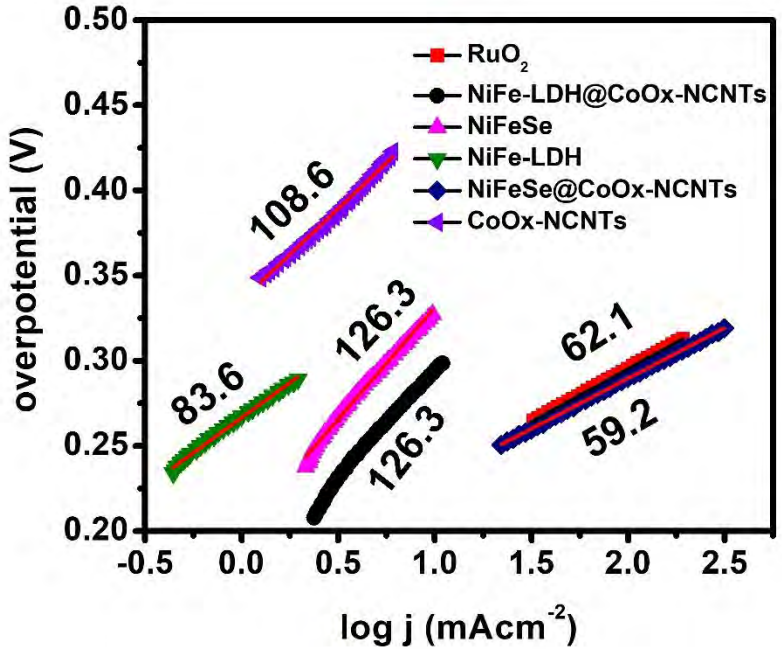

Figure 3.37: Tafel slopes derived from the corresponding LSV curves of the synthesized materials.

The remarkable OER performance of the NiFeSe@CoOx-NCNTs is majorly due to synergism resulting from the combination of NiFeSe nanosheets and the CoOx-NCNTs support. The NiFeSe nanosheets served as electroactive centers for catalytic reaction, facilitating the OER process. On the other hand, the CoOx-NCNTs act as a beneficial substrate that plays multiple roles in enhancing the overall electrocatalytic performance. Firstly, the CoOx-NCNTs notably enhanced conductance of the composite. This enhanced conductivity ensures efficient charge transport throughout the catalyst, reducing energy losses and leading to faster reaction kinetics during the OER. Secondly, the CoOx-NCNTs provide a well-structured support for the NiFeSe nanosheets, preventing their agglomeration and ensuring a uniform distribution of active sites. [365, 366] This efficient exposure of the active centers further improved catalytic efficacy, as it allows more reactants to interact with the active centers during the OER process. The combination of these factors, the active sites provided by NiFeSe nanosheets and the supportive role of CoOx-NCNTs, creates a synergistic effect that greatly enhanced catalytic performance of the composite.

To further investigate the electrochemical properties of the NiFeSe@CoOx-NCNTs composite, EIS experiments were conducted at a specific potential where the anodic

current density was upheld at 20 mA/cm². EIS is a powerful technique used to study the charge transfer processes and investigate the electrochemical behavior of catalysts. By analyzing the impedance data, information about the resistance to charge transfer and the effective electrochemical surface area of the catalyst can be obtained, providing valuable insights into its electrocatalytic performance. The Nyquist plots shown in figure 3.38 provide a comparative analysis of the charge transfer resistances (Rct) for different catalysts. In Nyquist plots, the semicircle diameter corresponds to Rct, where a reduced diameter of the semicircle signifies decreased resistance to charge transfer. Among the tested catalysts, the NiFeSe@CoOx-NCNTs composite displays the smallest semicircle arc in the Nyquist plot, indicating the least charge transfer resistance. The Rct value for the NiFeSe@CoOx-NCNTs composite is measured at 2.5 Ω, which is notably lower than the Rct values of the other individual catalysts: 5.2 Ω for NiFe-LDH@CoOx-NCNTs, 8.6 Ω for NiFeSe, 12.7 Ω for NiFe-LDH, and 35.3 Ω for CoOx-NCNTs.bThis observation further supports the excellent performance NiFeSe@CoOx-NCNTs composite. The low charge transfer resistance in the composite material indicates that it facilitates faster charge transfer kinetics during the OER. The efficient charge transfer is crucial for enhancing the overall electrocatalytic performance and contributes to the superior OER performance observed in the NiFeSe@CoOx-NCNTs composite. The reduced charge transfer resistance can be ascribed to the collaborative influence between NiFeSe nanosheets and CoOx-NCNTs, as discussed earlier. The combination of these components enhances the catalytic efficiency and promotes rapid electron transfer, leading to the lower Rct value and superior OER performance.

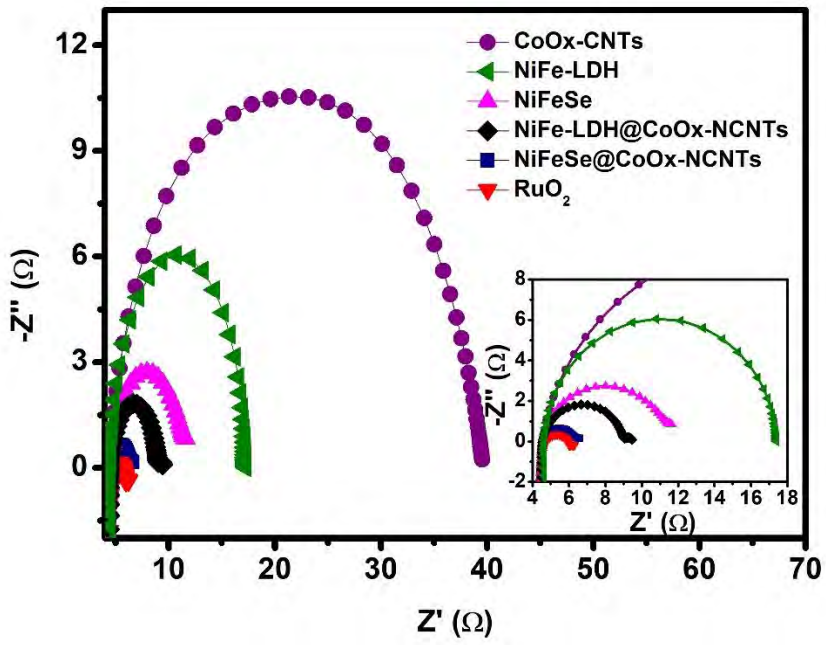

Figure 3.38: Nyquist plots obtained from Electron Impedance Spectroscopy (EIS) measurements for NiFeSe@CoOx-NCNTs and other synthesized materials.

To get insight into the intrinsic behavior of the active sites, the double-layer capacitance (Cdl) was estimated by cyclic voltammetry (CV) in the non-faradaic region, as shown in figure 3.39(a-e). The slope of the current density vs. various scan rates plots at constant potential (0.28 V vs. Hg/HgO) was determined by linear fitting. The results revealed that the NiFeSe@CoOx-NCNTs composite possesses the highest value of the Cdl slope, which is measured to be 19.5 mF/cm^2 (Figure 3.39(f)). The Cdl has direct correlation with ECSA of the electrocatalyst. [367] To evaluate the ECSA, the Cdl was divided by the specific capacitance (Cs), with Cs determined to be 0.04 mF/cm^2 according to McCrory under alkaline cicumstances. [346] The results show that the NiFeSe@CoOx-NCNTs composite exhibits the highest ECSA, measured to be 243.7 cm^2, surpassing the ECSA values of NiFe-LDH@CoOx-NCNTs (176 cm^2), NiFeSe (116.25 cm^2), NiFe-LDH (90 cm^2), and CoOx-NCNTs (102.5 cm^2). The high Cdl slope and ECSA of the NiFeSe@CoOx-NCNTs composite indicate a greater number of active sites available for the electrocatalytic reactions. The heightened concentration of active sites contributes to the improved catalytic performance toward OER by the composite. The synergistic effect between NiFeSe nanosheets and CoOx-NCNTs, along with the well-structured support provided by the nitrogen-doped carbon nanotubes, likely plays

a significant role in increasing the number of electrochemically active sites in the composite.

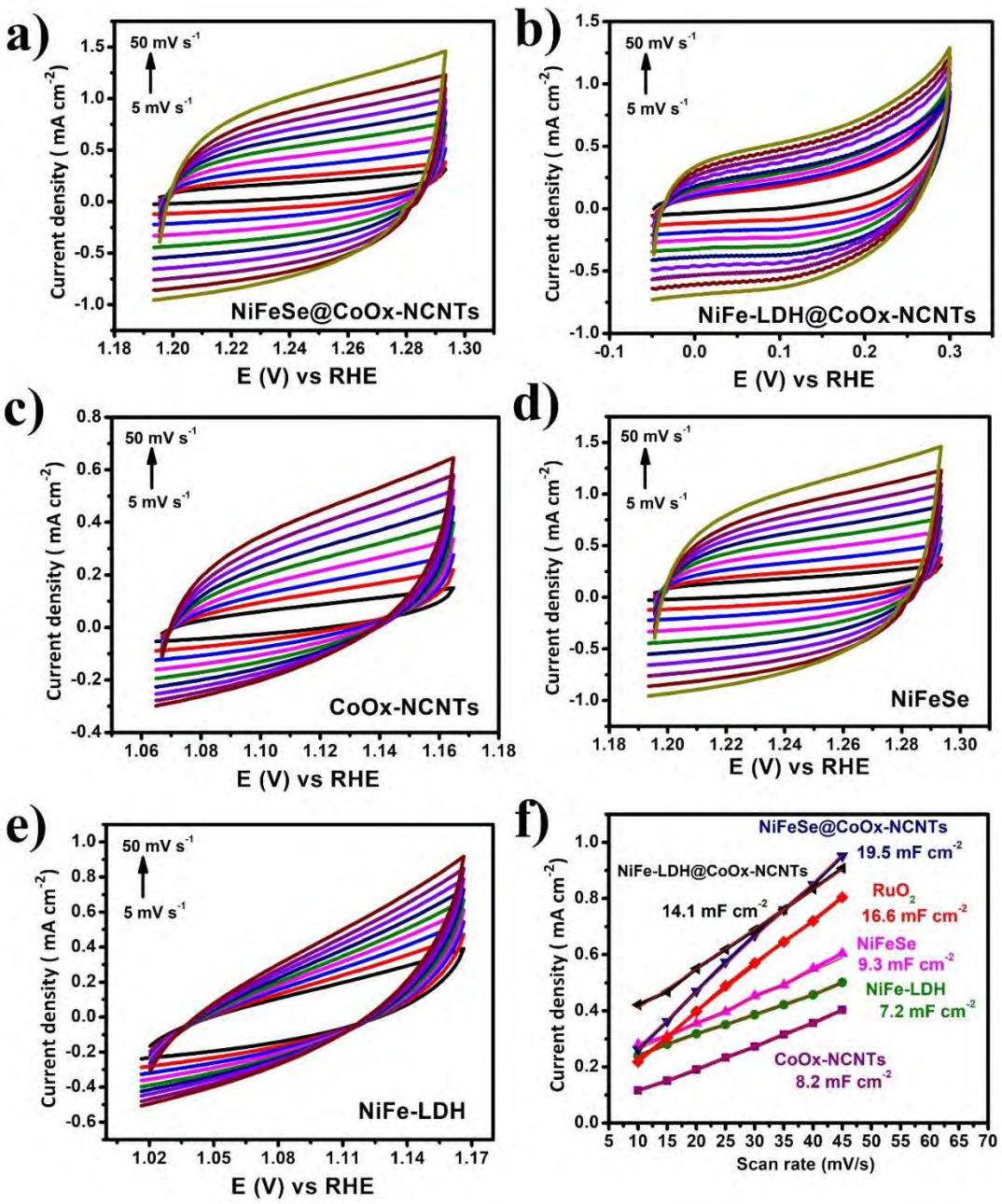

Figure 3.39: Cyclic voltammograms recorded in the non-faradaic window for (a) NiFeSe@CoOx-NCNTs, (b) NiFe-LDH@CoOx-NCNTs, (c) CoOx-NCNTs, (d) NiFeSe, (e) NiFe-LDH, and (f) Double layer capacitances of the synthesized materials derived from the cyclic voltammograms.

The stability of a catalyst is vital factor in assessing its suitability for practical applications. To evaluate the stability of the NiFeSe@CoOx-NCNTs composite, controlled potential electrolysis (CPE) was conducted at an operating potential of 1.47 V vs. RHE, which is the optimized potential for the catalyst in the OER. The CPE curve, shown in figure 3.40, demonstrates that the catalyst maintains a constant current density of 20 mA/cm^2 for an impressive period of 15 hour under the applied constant voltage. This exceptional stability over the extended duration of the test is a strong indicator of the catalyst's potential for long-term and reliable performance in practical applications. Additionally, the overlap between the pristine and post-LSV (Linear Sweep Voltammetry) curves (Figure 3.40) further confirms the high durability of the NiFeSe@CoOx-NCNTs catalyst under OER conditions. The fact that the post-LSV curve aligns closely with the initial pristine curve indicates minimal performance degradation and suggests that the catalyst retains its activity even after prolonged exposure to the electrocatalytic conditions.The excellent stability and durability of the NiFeSe@CoOx-NCNTs composite are essential characteristics for its commercial viability in clean energy conversion devices. A stable and durable catalyst ensures consistent and reliable performance over time, making it a promising candidate for practical usage in electrolyzers or other energy conversion systems. Overall, these findings provide strong evidence of the high stability and long-term performance of the NiFeSe@CoOx-NCNTs composite, highlighting its potential as an efficient and robust electrocatalyst for sustainable and clean energy production.

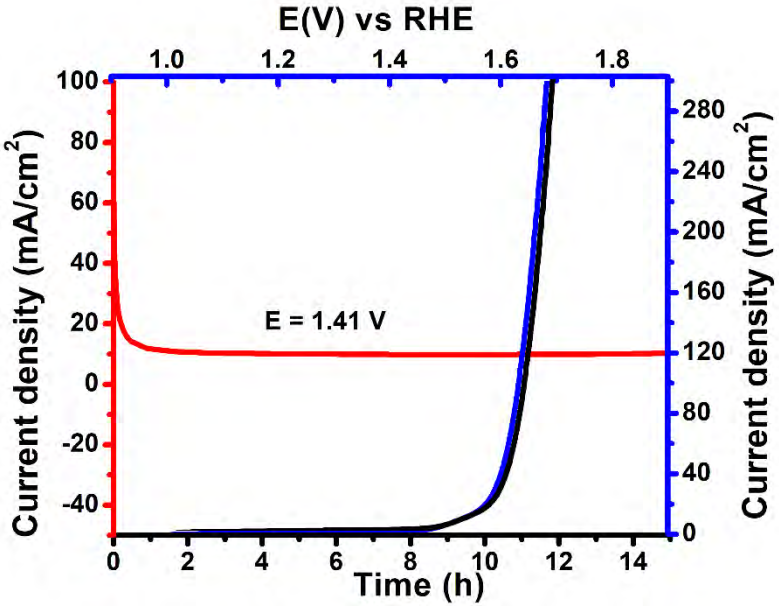

Figure 3.40: Controlled potential electrolysis of NiFeSe@CoOx-NCNTs for 15 h, Polarization curve comparing the pristine material with the post-catalytic material after 15 h of bulk electrolysis. The polarization curve allows the assessment of the electrocatalytic performance and stability of the NiFeSe@CoOx-NCNTs material over the electrolysis duration.

The impact of varying ratios of NiFeSe and CoOx-NCNTs on the electrocatalytic activity of NiFeSe@CoOx-NCNTs catalysts was also investigated (Figure 3.41). The difference in electrocatalytic activity observed among these ratios is attributed to the complex interplay between the two components and their synergistic effects. The 1:1 ratio was found to exhibit the optimum electrocatalytic performance due to well-balanced and efficient distribution of NiFeSe and CoOx-NCNTs on the surface of catalyst, maximizing the availability of active sites for the OER and enhancing catalytic efficiency. Conversely, the 1:2 ratio, with an excess of CoOx-NCNTs, displayed reduced activity, likely because the overwhelming presence of CoOx-NCNTs limited the exposure of active sites in NiFeSe, hindering OER kinetics. The 2:1 ratio, with an excess of NiFeSe, showed intermediate activity, benefiting from increased NiFeSe active sites and structural support from CoOx-NCNTs. However, an excess of NiFeSe may lead to overcrowding of active sites, potentially decreasing performance compared to the optimum 1:1 ratio.

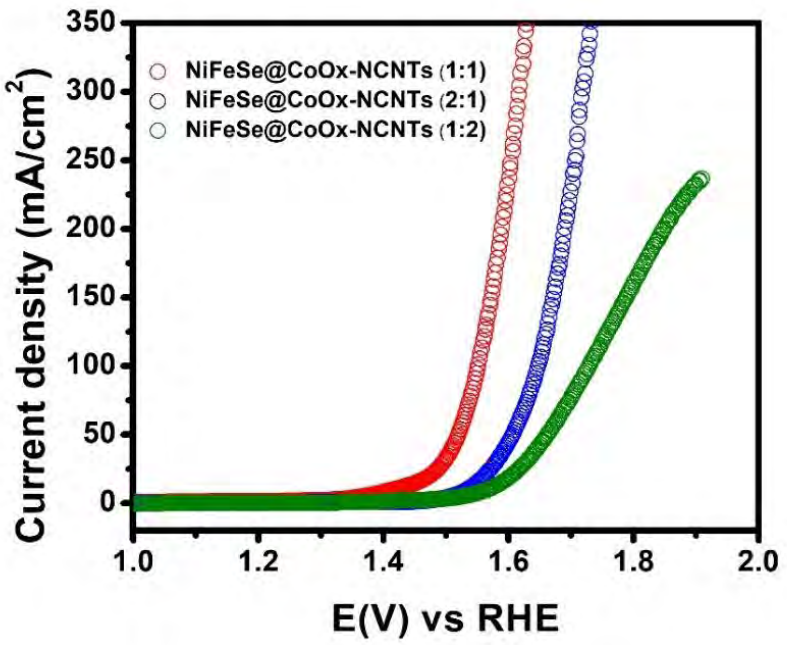

Figure 3.41: Anodic LSV plots of NiFeSe@CoOx-NCNTs employing various substrate ratios (1:1, 2:1, and 1:2)

The heightened activity of the synthesized NiFeSe@CoOx-NCNTs (1:1) catalyst can be attributed to several factors based on prior research insights. Firstly, the inherent electronic structure of transition metal chalcogenides, such as NiFeSe, is known to exhibit remarkable electrocatalytic activity. Chalcogenides, particularly selenides, have unique electronic properties with a small energy gap between their 3d, 3p, and 3s orbitals, resulting in good electrical conductivity. This high electrical conductivity in selenides, which arises from selenium's lower electronegativity compared to oxygen, is advantageous for charge transfer processes and enhances the overall catalytic activity. [368,369] Secondly, the existence of both nickel (Ni) and iron (Fe) in the NiFeSe@CoOx-NCNTs composite contributes to the synergistic effects that specifically boost the OER performance. [370] Nickel and iron have been associated with efficient OER catalysis in previous studies. The interaction between these transition metal elements and the selenide phases creates a favorable environment for charge transfer and promotes the exposure of active sites, further enhancing the catalyst's catalytic activity. Moreover, the unique heterostructures formed in the composite, which consist of distinct selenide phases, play a crucial role in accelerating electron flow and exposing greater active sites. The presence of negative charge centers on selenium (Se) sites and the repulsion

between the 3d-2p orbitals of Se and the metal-d orbitals facilitate the delivery of dioxygen molecules, thus enhancing the OER kinetics. [290, 371, 372]

To determine the composition of NiFeSe@CoOx-NCNTs after OER reaction, catalyst is characterized by XRD and XPS. XRD analysis in figure 3.42(a) revealed that the pristine and post-cycling patterns are nearly identical, indicating that the crystal structure of the material remains intact even after extended cycling. This observation strongly suggests the structural stability of our material throughout the cycling process, which is a critical aspect for understanding its performance. XPS analysis was employed to examine the composition of NiFeSe@CoOx-NCNTs after OER electrolysis. In Figure 3.42(b), the high-resolution Ni 2p XPS spectrum shows two distinct peaks at 855.28 and 872.28 eV, which correspond to the binding energies of Ni^{3+} $2p_{3/2}$ and Ni^{3+} $2p_{1/2}$, respectively. Furthermore, the presence of peak at 874.79 eV suggests the involvement of oxyhydroxide.[373, 374] This indicates that nickel undergoes a change in its valence state during the OER process. Similarly, in the high-resolution Fe 2p spectrum (figure 3.42(c)), two peaks are observed at 704.3 and 711.1 eV, corresponding to the binding energies of Fe^{2+} $2p_{3/2}$ and Fe^{3+} $2p_{3/2}$, respectively. Meanwhile, it becomes evident that the proportion of Fe^{3+} to Fe^{2+} increases following the OER process, implying the oxidation of Fe^{2+} species during OER electrolysis. Furthermore, Figure 3.42(d) illustrates an increase in the SeOx peak intensity, indicating surface oxidation of Se on the NiFeSe@CoOx-NCNTs during OER. Through XPS analysis, it is established that some hydroxide or oxyhydroxide phases become evident on the surface of NiFeSe@CoOx-NCNTs after electrochemical testing, revealing the authentic active sites for the OER. These findings are consistent with previous literature analyses. The cumulative evidence strongly suggests that a substantial portion of the NiFeSe@CoOx-NCNTs' surface undergoes oxidation, primarily resulting in the formation of oxyhydroxides. This likely leads to the generation of $Ni_{1-x}Fe_xOOH$ on the surface, in accordance with the reaction:

$$(Ni_{1-x}Fe_x)^{2+} + 3OH^- \rightarrow Ni_{1-x}Fe_xOOH + H_2O + e^-$$

This mechanism is consistent with the previous Ni-based catalysts reported.[375-377] The $Ni_{1-x}Fe_xOOH$/NiFeSe@CoOx-NCNTs complex emerges as the actual active sites during the electrolysis process. Additionally, the presence of selenide appears to

facilitate electron transfer between the electrode and the hydroxide or oxyhydroxide layer, thereby enhancing the OER activity. Meanwhile, the CoOx-NCNTs play a crucial role in preserving electronic conductivity between the electrode and the active oxyhydroxide layer, establishing an effective electron pathway that significantly contributes to the exceptional OER performance.

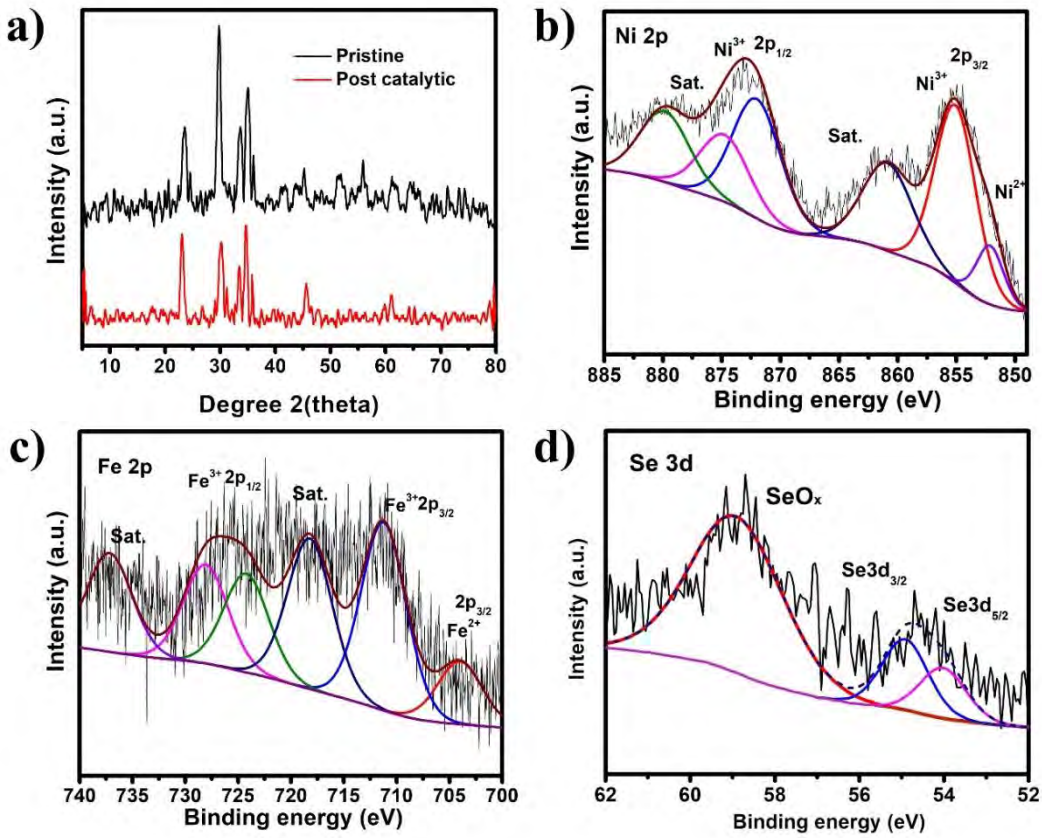

Figure 3.42: (a) XRD patterns of the pristine and post-catalytic NiFeSe@CoOx-NCNTs. The XPS spectra for the post-catalytic NiFeSe@CoOx-NCNTs, featuring (b) Ni 2p, (c) Fe 2p, and (d) Se 3d regions.

Proposed Mechanism of OER

The proposed mechanism of ORR on the surface of NiFeSe@CoOx-NCNTs is depicted in figure 3.43. The oxidation state of NiFe active site is raised by one unit when one H_2O molecule coordinatively binds to empty sites along with the loss of one electron and proton to form OH*. The intermediate O* is generated by releasing one proton and an electron from OH*. However, the O* only exists as an O radical. O* continued to combine with water to produce OOH*, producing an electron and proton. Finally,

OOH* creates an empty site after losing one electron and proton to generate O_2 and complete the catalytic cycle.

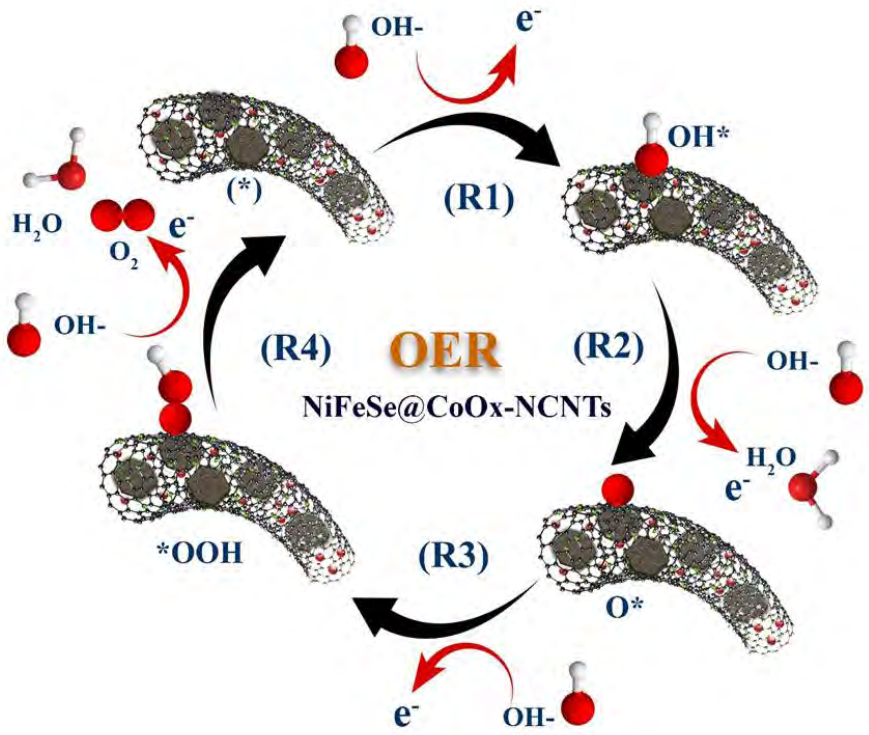

Figure 3.43: Proposed mechanism of OER on the surface of NiFeSe@CoOx-NCNTs

HER Performance

The electrochemical studies for the HER were conducted in 1M KOH at room temperature, and the comparative cathodic LSV curves of the synthesized materials are shown in figure 3.44(a). The LSV data clearly demonstrates the remarkable catalytic activities of the NiFeSe@CoOx-NCNTs electrode material towards HER. The NiFeSe@CoOx-NCNTs catalyst exhibits exceptional HER performance, achieving a current density of 20 mA/cm^2 with an overpotential of only 145 mV. This low overpotential indicates that the catalyst is highly efficient in promoting the HER process and requires less energy to drive the reaction. In comparison, the overpotentials required for other catalysts to reach the same catalytic current density are significantly higher. Specifically, NiFe-LDH@CoOx-NCNTs requires an overpotential of 340 mV, NiFe-LDH requires 370 mV, NiFeSe requires 434 mV, and CoOx-NCNTs requires 475 mV. The exceptional HER performance of the NiFeSe@CoOx-NCNTs catalyst can be attributed to its unique composition and structural characteristics. The synergistic

effects originate from the combination of NiFeSe nanosheets and CoOx-NCNTs provide efficient electron flow pathways and expose more electroactive sites, which greatly improved the catalytic activity towards HER. Additionally, the inherent electronic structure of transition metal chalcogenides, as discussed earlier, also contributes to the excellent HER performance of the composite.

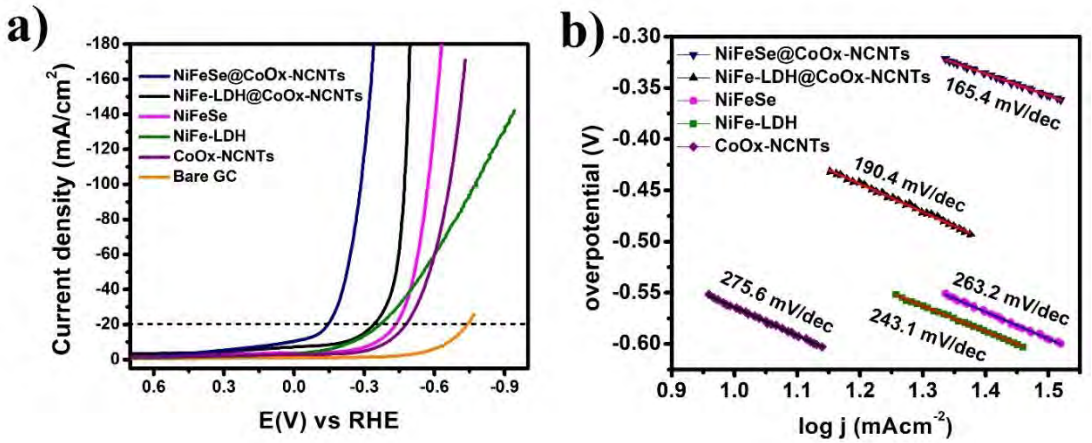

Figure 3.44: (a) Cathodic Linear Sweep Voltammetry (LSV) curves of NiFeSe@CoOx-NCNTs and other synthesized materials (b) Corresponding Tafel slopes derived from the cathodic LSV curves of the synthesized materials.

The Tafel analysis (Figure 3.44(b)) provides valuable insights into the efficiency of different electrodes for the HER. Remarkably, the NiFeSe@CoOx-NCNTs electrode demonstrates the most favorable outcome with the smallest Tafel slope value of 165.4 mV/dec, indicating its superior performance in promoting the HER process. In comparison, the other fabricated electrodes, namely NiFe-LDH@CoOx-CNTs, NiFe-LDH, NiFeSe, and CoOx-CNTs, exhibit Tafel slope values of 190.4, 243, 263, and 275.6 mV/dec, respectively.The Tafel slope values directly correlate with the rate of the HER process, where lower values indicate faster kinetics and more efficient hydrogen evolution. The significantly lower Tafel slope of the NiFeSe@CoOx-NCNTs electrode suggests that it facilitates the HER more effectively compared to the other fabricated electrodes. This enhanced efficacy can be ascribed to the synergism between the nanosheets of NiFeSe and CoOx-NCNTs, which offered great number of electroactive sites for the HER reaction and offer efficient charge transfer pathways.

The outstanding HER performance of the NiFeSe@CoOx-NCNTs electrode is crucial for practical applications in hydrogen production and clean energy conversion. Its ability to achieve a high current density with a minimal overpotential of only 145 mV highlights its potential as an competent and cost-economical electrocatalyst towards HER process in alkaline environments. Indeed, the remarkable performance of the NiFeSe@CoOx-NCNTs electrode in promoting the HER process, as demonstrated by its lower Tafel slope value of 165.4 mV/dec, compared to the other fabricated electrodes, highlights its superior efficiency. The HER mechanism in alkaline solutions involves three potential reaction steps: the Volmer step ($H_2O + M^+ e^- \rightarrow MH_{ads} + OH^-$), the Heyrovsky step ($MH_{ads} + H_2O + e^- \rightarrow M + OH^- + H_2$), and the Tafel step ($2MH_{ads} \rightarrow 2M + H_2$). [341] The Volmer step involves the initial adsorption of water molecules and metal species to form adsorbed intermediates, M-H_{ads} and OH. The Heyrovsky step includes the reaction between M-H_{ads} and water, resulting in the production of metal (M), hydroxide (OH), and hydrogen gas (H_2). The Tafel step involves the recombination of two adsorbed intermediates, 2 M-H_{ads}, to yield two metal species (M) and hydrogen gas (H_2).

Theoretically, a Tafel value of approximately 30 mV/dec indicates that the Tafel reaction is the rate-determining step, which means the overall HER rate is limited by the recombination of the adsorbed intermediates. However, in this investigation, the observed Tafel value exceeding 120 mV/dec suggests that the rate-determining step is the adsorption of hydrogen, specifically the Volmer step. [342] This implies that the HER performance is primarily influenced by the initial adsorption of hydrogen species on the catalyst surface, which is critical for the overall reaction rate. The high efficiency of the NiFeSe@CoOx-NCNTs electrode in the Volmer step can be attributed to its unique composition and structural characteristics, as previously discussed. The synergistic effects of NiFeSe nanosheets and CoOx-NCNTs provide more active centers and efficient charge transfer pathways, leading to enhanced adsorption of hydrogen species and promoting faster HER kinetics. [343, 344]

The estimation of the ECSA is crucial for understanding the catalytic activity of the electrodes. For ECSA calculation, the Cdl is assessed through CV, that was conducted within the cathodic range, employing various spanning from 5 to 50 mV/s. In figure

3.45, the Cdl value obtained for the NiFeSe@CoOx-NCNTs catalyst is measured to be 10.2 mF/cm², which corresponds to an ECSA of 255 cm². Notably, this ECSA value significantly exceeds the Cdl values measured for the precursor materials: NiFe-LDH@CoOx-NCNTs (7.1 mF/cm², ECSA 177.5 cm²), NiFeSe (5.3 mF/cm², ECSA 132.5 cm²), and NiFe-LDH (3.8 mF/cm², ECSA 95 cm²). The higher ECSA of the NiFeSe@CoOx-NCNTs catalyst is indicative of its larger ECSA, which implies a greater number of electroactive sites for HER. This enhanced ECSA is majorly due to synergism and structural characteristics of the NiFeSe@CoOx-NCNTs composite. The presence of NiFeSe nanosheets and CoOx-NCNTs contributes to the unveiling additional electroactive sites and efficient electron transport pathways, resulting in a significant enhanced surface area accessible for the HER. The greater ECSA of the NiFeSe@CoOx-NCNTs catalyst is a key factor contributing to its outstanding performance in promoting the HER process, as demonstrated by its lower Tafel slope value and lower overpotential compared to the other fabricated electrodes. The large ECSA ensures a higher catalytic activity, making the NiFeSe@CoOx-NCNTs catalyst a highly efficient and promising electrocatalyst for hydrogen evolution in alkaline solutions.

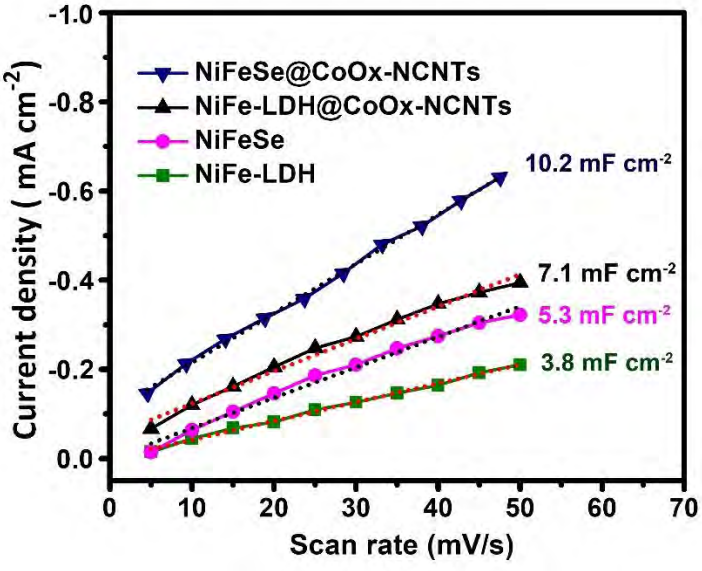

Figure 3.45: Double layer capacitances of synthesized materials obtained from cyclic voltammograms.

These findings further establish the superior performance and potential applications of the NiFeSe@CoOx-NCNTs catalyst in clean energy technologies, where hydrogen production via the HER is a crucial step towards achieving sustainable and renewable energy sources.

The electron transmission capability of the electrodes during the HER process was further evaluated through EIS measurements. The Nyquist plot (Figure 3.46) clearly illustrates that the NiFeSe@CoOx-NCNTs electrode exhibits a smaller Nyquist semicircle, indicating a significantly lower charge transfer resistance (Rct) value. This observation suggests that the NiFeSe@CoOx-NCNTs electrode possesses superior intrinsic electrical conductivity compared to the other electrodes.

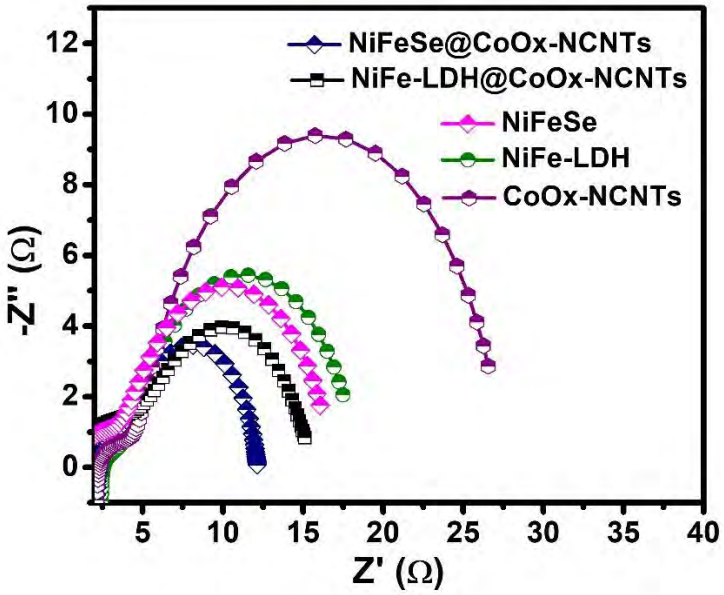

Figure 3.46: Nyquist plots obtained from Electron Impedance Spectroscopy (EIS) measurements for NiFeSe@CoOx-NCNTs and other synthesized materials.

The NiFeSe@CoOx-NCNTs catalyst demonstrates an Rct value of 9.8 Ω, which is considerably lower than the Rct values predicted for the corresponding precursor materials: NiFe-LDH@CoOx-NCNTs (14.5 Ω), NiFeSe (15.6 Ω), NiFe-LDH (16.7 Ω), and CoOx-NCNTs (25.3 Ω). The lower Rct value of the NiFeSe@CoOx-NCNTs electrode indicates efficient charge transfer kinetics, suggesting that the charge carriers, i.e., electrons, can move more freely and rapidly through the catalyst during the HER process. The enhanced intrinsic electrical conductivity of the NiFeSe@CoOx-NCNTs

electrode is mainly due to distinctive composition and structural features of the composite. The synergistic effects originating from the combination of NiFeSe nanosheets and CoOx-NCNTs contribute to improved charge transport properties, leading to a lower charge transfer resistance. Additionally, the nitrogen-doped carbon nanotubes (NCNTs) in the composite play significant role in enhancing electron transfer and preventing the agglomeration of electroactive sites, significantly enhancing the overall conductance. The superior intrinsic electrical conductivity of the NiFeSe@CoOx-NCNTs electrode is a critical factor that contributes to its excellent performance in the HER process, as demonstrated by the lower overpotential and Tafel slope values compared to the other electrodes.

The durability of the NiFeSe@CoOx-NCNTs catalyst was evaluated through chronoamperometry, a technique that measures current over time, specifically for the HER in alkaline conditions at -0.3 V vs. RHE (Figure 3.47(a)). The results show that the catalyst maintained a consistently steady current even after 15 h of continuous operation, demonstrating its high robustness and long-term stability as an electrocatalyst for HER. This extended stability is essential for practical applications in hydrogen production systems. To further assess the durability of the NiFeSe@CoOx-NCNTs catalyst, the pristine (before testing) and post-catalytic (after 15 h of HER) LSV curves were compared (Figure 3.47(b)). Importantly, no significant changes or deviations were observed in the LSV curves, indicating the excellent durability of the catalyst under HER conditions. The catalyst retains its initial high performance even after prolonged electrocatalytic testing, confirming its reliability and long-lasting efficiency.

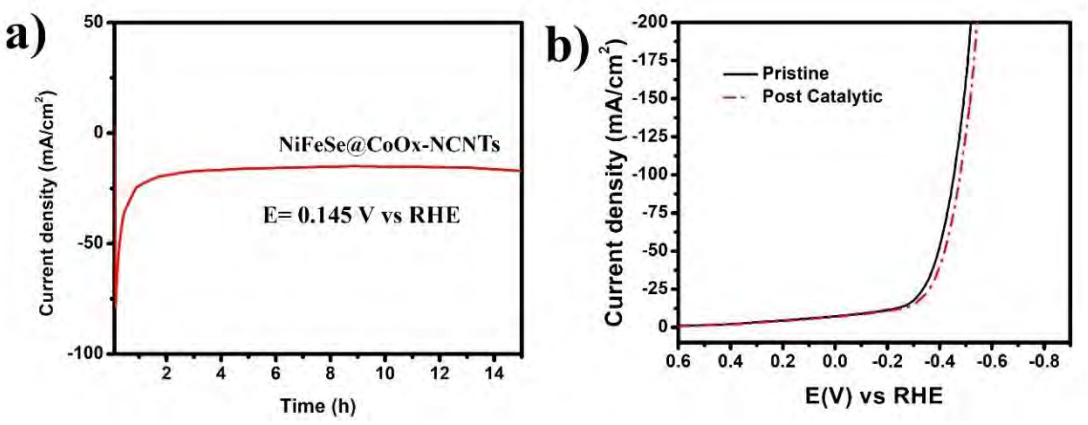

Figure 3.47: (a) Controlled potential electrolysis of NiFeSe@CoOx-NCNTs for 15 hs. The controlled potential electrolysis was performed to study the electrocatalytic performance and stability of NiFeSe@CoOx-NCNTs over the course of 15 hs (b) Polarization curve comparing the pristine material with the post-catalytic material after 15 hs of bulk electrolysis. The polarization curve allows the assessment of the electrocatalytic activity and efficiency of NiFeSe@CoOx-NCNTs before and after the electrolysis process.

We have also conducted tests to assess the HER catalytic activity in 0.5M H_2SO_4 electrolyte. We observed enhanced HER performance of the NiFeSe@CoOx-NCNTs catalyst under acidic condition in comparison to the alkaline environment of 1M KOH (figure 3.48(a)). The LSV data in Figure 3.48(b) demonstrates the impressive catalytic activity of NiFeSe@CoOx-NCNTs for the HER under acidic conditions, achieving a remarkable current density of 20 $mAcm^{-2}$ with low $\eta \sim 95$ mV. Notably, the η of NiFeSe@CoOx-NCNTs is significantly lower when compared to NiFe-LDH@CoOx-NCNTs (~ 228 mV), and NiFeSe (~ 288 mV) at the same catalytic current density. Additionally, the Tafel slope for NiFeSe@CoOx-NCNTs is notably smaller ~125.7 mV/dec, signifying its superior performance (Figure 3.48(c)). In contrast, NiFe-LDH@CoOx-CNTs and NiFeSe exhibit Tafel slopes of 162.3 mV/dec and 210.4 mV/dec, respectively. Furthermore, EIS measurements were performed to assess R_{ct}, as illustrated in Figure 3.48(d). It is evident that the NiFeSe@CoOx-NCNTs electrode displays a smaller Nyquist semicircle, indicating significantly lower R_{ct}. This observation suggests that the NiFeSe@CoOx-NCNTs electrode possesses superior intrinsic electrical conductivity in comparison to the other electrodes. This enhanced performance can be attributed to several key factors: In acidic conditions, the catalyst may benefit from the presence of protons (H^+) and a higher concentration of positively charged species, promoting the HER mechanism.[378] This results in faster proton reduction and improves overall catalytic activity. The increased concentration of protons in acidic solution compared to alkaline solution provides a more conducive environment for the proton reduction pathway of the HER. The higher proton concentration accelerates the reaction rate, contributing to improved performance. However, conducting both reactions (OER and HER) in alkaline conditions is often

more beneficial for the development of bifunctional electrocatalysts, particularly for practical applications like water electrolysis.[379, 380]

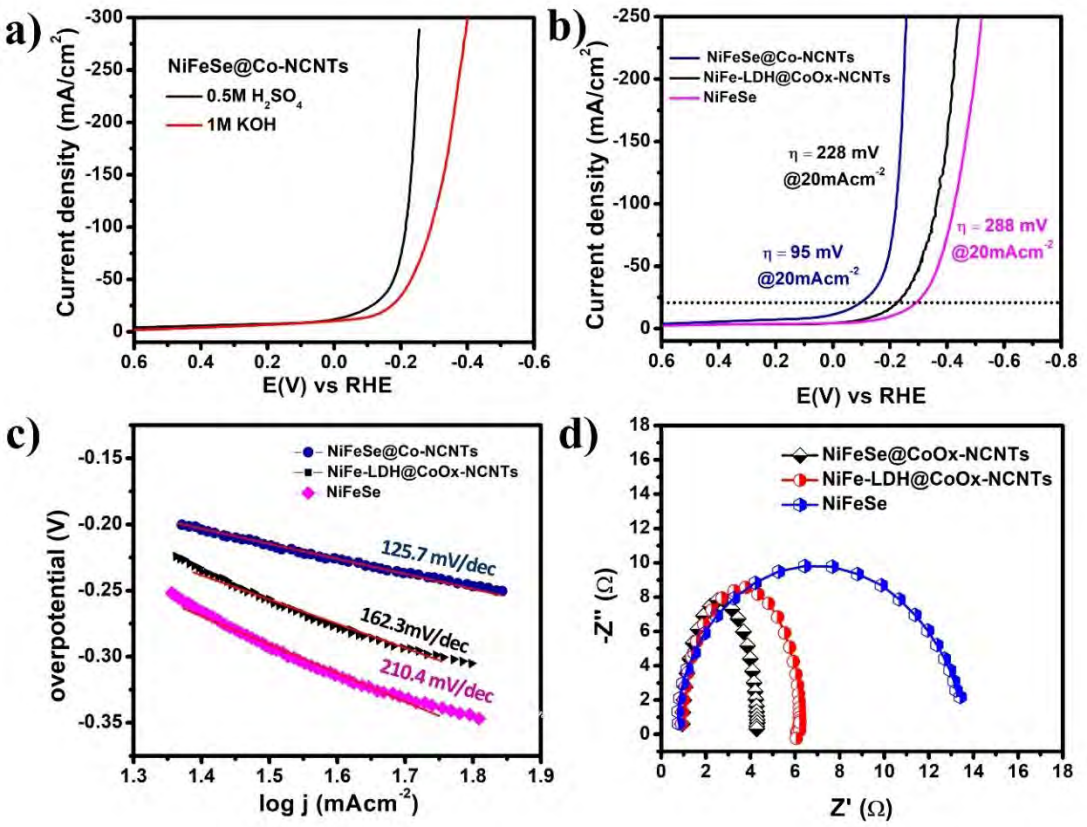

Figure 3.48: (a) Cathodic LSV profiles of NiFeSe@CoOx-NCNTs in 0.5M H_2SO_4 and 1M KOH electrolytes. (b) Cathodic LSV curves of NiFeSe@CoOx-NCNTs, NiFe-LDH@CoOx-NCNTs, and NiFeSe in 0.5M H_2SO_4. (c) Associated Tafel slopes. (d) Electrochemical impedance spectroscopy analysis conducted under acidic conditions.

The exceptional performance of the NiFeSe@CoOx-NCNTs catalyst can be attributed to several factors. One significant factor is the negative charge induced on the selenium atoms in the composite, which acts as a base and efficiently captures protons to promote HER activity. This electron-rich characteristic of the selenium sites enhances the adsorption and activation of hydrogen, leading to improved catalytic efficiency. Furthermore, the synergistic effect between the NiFeSe nanosheets and CoOx-NCNTs provides efficient charge transport and exposes more active sites, contributing to the overall enhanced catalytic performance and durability of the catalyst. The presence of nitrogen-doped carbon nanotubes (NCNTs) prevents aggregation of the active sites and

provides a favorable substrate for HER, further enhancing the catalyst's durability. [381] Figure 3.49 presents a comparative analysis of the electrocatalytic activities of NiFeSe@CoOx-NCNTs (from this work) with several other materials reported in the literature for both the OER and HER. The materials included in the comparison are Mo–Ni–Se@NF,[382] $NiCoSe_{2-x}$/NC,[383] Cu-(a-$NiSe_x$/c-$NiSe_2$)/TiO_2 NRs,[384] $Fe_{0.08}Ni_{0.77}Se$/CNT_3,[385] Fe-doped NiSeNSs/CNTs,[386] CoPSe–$CoSe_2$/CNTs,[387] $Ni_{0.85}Se$/RGO/CNTs,[388] NiCo(Sn)Se,[389] Co-Fe Selenide,[390] and Fe_2O_3-$CoSe_2$@Se/CC.[391]

The comparative analysis shows that NiFeSe@CoOx-NCNTs demonstrated remarkable electrocatalytic prowess for total water splitting, outperforming most of the other reported materials. For the OER, NiFeSe@CoOx-NCNTs display a significantly lower overpotential (240 mV at 20 mA/cm^2) compared to most of the other materials. This indicates its superior efficiency in promoting oxygen evolution. For the HER, NiFeSe@CoOx-NCNTs again demonstrate outstanding catalytic efficiency with just low overpotential 145 mV at 20 mA/cm^2, which is considerably lower than that of the other materials. The superior electrocatalytic performance of NiFeSe@CoOx-NCNTs mainly ascribed to its unique electronic configuration, synergistic effects, and intrinsic electronic properties. The presence of both NiFeSe nanosheets and CoOx-NCNTs in the composite provides a favorable platform for efficient charge transfer, while the negative charge on the selenium atoms enhances hydrogen adsorption and activation, leading to enhance HER activity. The combination of these factors contributes to the outstanding performance and stability of NiFeSe@CoOx-NCNTs as an electrocatalyst for both OER and HER, making it a highly promising material for clean and sustainable energy conversion applications.

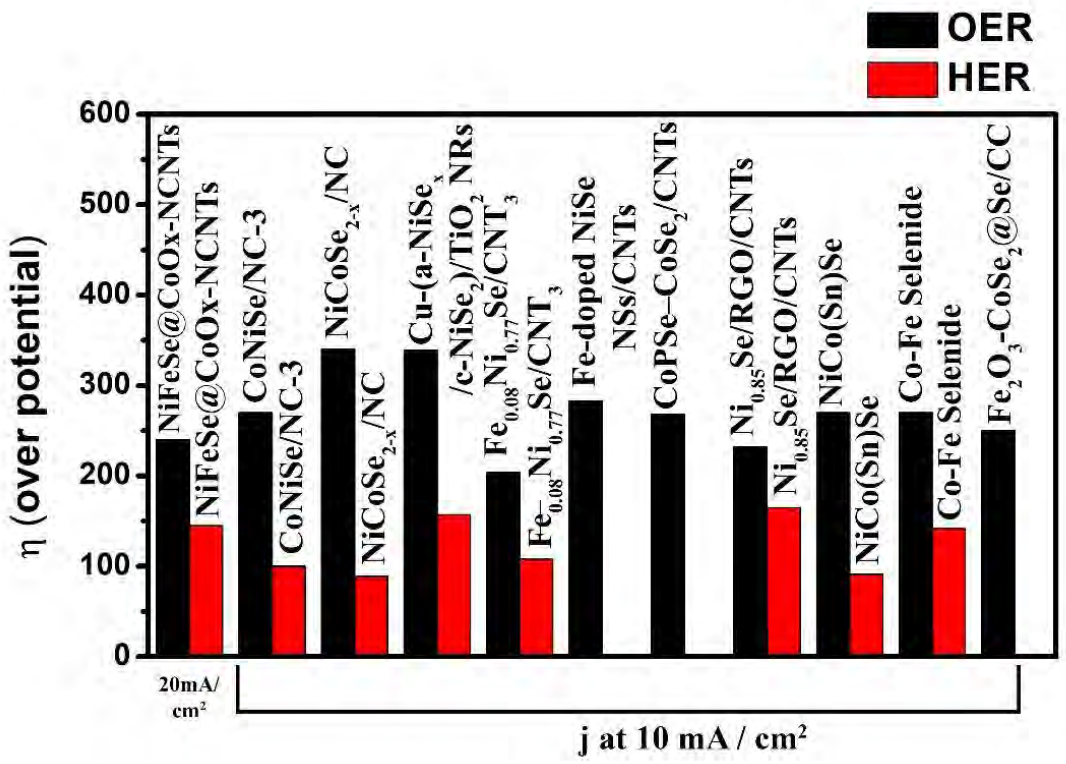

Figure 3.49: Comparative analysis of NiFeSe@CoOx-NCNTs for OER and HER activities against recently reported Transition Metal-based Electrocatalysts (TMSes). The graph presents a comprehensive evaluation of the catalytic performance of NiFeSe@CoOx-NCNTs in comparison to other recently reported TMSes for both OER and HER, showcasing its potential as a promising multifunctional electrocatalyst.

3.3.3 Conclusions

In conclusion, the NiFeSe@CoOx-NCNTs bifunctional electrocatalyst has been effectively synthesized using a two-step process consisting of hydrothermal synthesis of NiFe-LDH supported on ZIF-12 derived CoOx-NCNTs, followed by selenization. This catalyst demonstrates notable performance towards OER and HER in alkaline medium. The catalyst displays a low overpotential of 240 mV at 20 mA/cm^2 for OER, along with a reduced Tafel slope of 59.2 mV/dec. For HER, it achieves a high current density of 20 mA/cm^2 at an overpotential of 145 mV, with a Tafel slope of 169 mV/dec. Moreover, the catalyst displays a small Rct, a large ECSA, and exceptional stability over 15 h of continuous experiments.

Indeed, the exceptional performance of the NiFeSe@CoOx-NCNTs catalyst in both OER and HER provides significant advantages in designing efficient water electrolyzers. The reduced overpotentials observed for these electrochemical reactions are crucial as they directly impact the overall energy efficiency of the water splitting process. By minimizing the overpotentials, the catalyst enables a more efficient conversion of electrical energy into hydrogen, thereby promoting clean and sustainable hydrogen energy generation. The simplified electrolyzer design, facilitated by the catalyst's remarkable performance, can lead to cost reductions in hydrogen production systems, making them more economically viable for large-scale implementation. Additionally, the use of low-cost materials in the catalyst's synthesis further enhances its potential for practical applications and commercialization. However, to fully harness the catalyst's potential and improve its performance even further, continuous research efforts should be directed towards optimizing the synthesis process. Understanding the underlying mechanisms that govern the enhanced electrocatalytic activity of NiFeSe@CoOx-NCNTs is critical for tailoring the catalyst's properties and fine-tuning its performance. Exploring the application of the catalyst in various energy conversion systems beyond water splitting, such as fuel cells and other electrochemical devices, can unlock its versatility and potential in the broader field of energy storage and conversion. These future perspectives in research and development will collectively contribute to the advancement of sustainable and efficient hydrogen-based energy technologies. As hydrogen emerges as a key component in the transition towards a greener and cleaner energy landscape, catalysts like NiFeSe@CoOx-NCNTs play a pivotal role in realizing the full potential of hydrogen as a clean energy carrier.

3.4 Summary of the Work

This study mainly focusses on comprehensive exploration of LDHs, and their derived novel nanomaterials tailored for efficient water splitting, a fundamental process with profound implications for renewable energy generation. The study focuses on the synthesis, characterization, and evaluation of three distinct materials, each demonstrating remarkable electrocatalytic properties for OER and HER in alkaline electrolytes. The culmination of this research offers significant contributions to the advancement of sustainable energy conversion devices. In this study we have synthesized three distinct materials, each demonstrating remarkable electrocatalytic properties for OER and HER under alkaline conditions. All the synthesized materials were characterized by exploiting different characterization techniques that includes PXRD, XPS, SEM, TEM, EDX, EELS, SAED, and elemental mapping. All the electrochemical experiments were carried out under alkaline circumstances i.e 1M KOH. Electrochemical techniques including LSV, CV, CA, and EIS were employed for electrochemical evaluation

The first material, CoMn-LDH@CuO/Cu_2O was synthesized by using facile approach, aimed at advancing the field of water splitting for renewable energy production. The synthesis method involves the incorporation of HKUST-1 derived CuO/Cu_2O nanoparticles, into the growth process of CoMn-LDH nanosheets. The resultant electrocatalyst represents impressive towards OER, a crucial step in water splitting. Notably, the optimized electrode exhibits a remarkably small overpotential of only 297 mV to achieve a catalytic current density of 10 mA/cm^2, accompanied by an exceptionally low Tafel slope of 89 mV/dec. This performance significantly outperforms individual CoMn-LDH and CuO/Cu_2O catalysts. The synergistic integration of CoMN-LDH with CuO/Cu_2O derived from HKUST-1 drives enhanced catalytic activity and stability. This catalytic system demonstrates outstanding stability over a continuous 15 h experimental period, highlighting its practical viability. The remarkable OER performance is attributed to two key factors. Firstly, the interaction between CoMn-LDH and CuO/Cu_2O substantially increases the electrochemically active surface area, providing ample sites for the OER process. Secondly, this interaction reduces charge transfer resistance, facilitating efficient electron flow during OER. The comprehensive characterization and mechanistic insights garnered from this

study contribute to the broader advancement of renewable energy and sustainable electrocatalysis. By displaying the exceptional performance and stability of the CoMn-LDH@CuO/Cu_2O electrocatalyst, this research paves the way for innovative applications in water electrolysis for clean hydrogen production.

The second material, a novel bifunctional electrode material NiCo-Alloy@CeO_2, has been successfully synthesized using a sequential hydrothermal approach followed by annealing. The synthesis procedure involves two distinct stages: the creation of NiCo-Alloy through annealing LDHs-based precursors and the subsequent integration of this alloy onto Ceria nanorods via impregnation. Thorough validation through various analytical techniques confirms the successful execution of this composite synthesis process. This composite material exhibits remarkable catalytic efficiency towards both OER and HER within alkaline environments. Specifically, NiCo-Alloy@CeO_2 displays exceptional OER electrocatalytic activity, compelling a mere 170 mV overpotential generate a current density of 20 mA/cm^2. Additionally, it demonstrates impressive durability, maintaining its catalytic efficiency for a continuous 14 h operation at 50 mA/cm^2, along with an accelerated reaction rate characterized by a Tafel slope of 51.1 mV/dec. In parallel, the catalyst excels in HER, demanding a minimal overpotential of 221 mV to achieve a current density of 50 mA/cm^2. This achievement is accompanied by a notably low Tafel slope, negligible charge transfer resistance, a substantial active electrochemical surface area, and sustained performance over a 14 h period. These exceptional catalytic capabilities stem from several underlying factors. The orchestrated synergy at the interface between NiCo-Alloy and CeO_2, coupled with the presence of oxygen vacancies that enhance ionic conductivity, contribute to the overall efficiency of the material. Additionally, the absorption of hydroxyl groups by Ce^{3+} facilitates water dissociation, further boosting the catalytic performance. The integration of CeO_2 nanorods within the NiCo-Alloy nanosheets expedites the electro-coupled dissociation of water and enhances the adsorption of intermediate hydrogen species, consequently elevating OER efficiency. The open ends of ceria nanorods play a role in enhancing catalytic performance by facilitating the diffusion of active species. The distinctive electronic characteristics of ceria, combined with the active sites provided by nickel and cobalt, collectively contribute to the heightened efficiency in HER. This work offers valuable insights into the design of multifunctional materials for

sustainable energy conversion, paving the way for further exploration and application in the realm of clean energy generation and storage.

The third material, NiFeSe@CoOx-NCNTs was successfully synthesized as bifunctional electrocatalyst for OER and HER. The utilization of transition metal selenides, exemplified by NiFeSe@CoOx-NCNTs, holds significant promise as highly efficient and abundant electrocatalysts for clean hydrogen production via water splitting. The successful synthesis of the bifunctional electrocatalyst NiFeSe@CoOx-NCNTs has been achieved through a two-step process, encompassing the hydrothermal synthesis of NiFe-LDH supported on CoOx-NCNTs derived from ZIF-12, followed by selenization. This catalyst demonstrates noteworthy performance in both OER and HER within an alkaline electrolyte. Specifically, it boosts a low OER overpotential of 240 mV at 20 mA/cm^2, accompanied by a reduced Tafel slope of 59.2 mV/dec. For HER, it displays a high current density of 20 mA/cm^2 at a small overpotential of 145 mV, characterized by a Tafel slope of 169 mV/dec. Furthermore, the catalyst exhibits low charge transfer resistance, a large electrochemical active surface area, and exceptional stability over a continuous 15 h testing period. The remarkable performance of the NiFeSe@CoOx-NCNTs catalyst in both OER and HER holds significant implications for the design of efficient water electrolyzers. The observed reduction in overpotentials is pivotal, as it directly influences the overall energy efficiency of the water splitting process. By minimizing overpotentials, the catalyst enhances the conversion of electrical energy into clean and sustainable hydrogen, thereby promoting a greener energy landscape. The catalyst's impressive performance also simplifies electrolyzer design, potentially reducing costs in hydrogen production systems and facilitating large-scale implementation. Moreover, the integration of cost-effective materials in the catalyst's synthesis enhances its practical applicability and potential for commercialization. To fully harness the catalyst's potential and further enhance its performance, continuous research efforts should be directed towards refining the synthesis process. An understanding of the underlying mechanisms governing NiFeSe@CoOx-NCNTs' enhanced electrocatalytic activity is pivotal for tailoring its properties and optimizing its performance. Additionally, exploring the catalyst's applicability in diverse energy conversion systems beyond water splitting, such as fuel cells and other electrochemical devices, can unlock its versatility and broaden its impact

within the realm of energy storage and conversion. These future perspectives in research and development collectively contribute to advancing sustainable and efficient hydrogen-based energy technologies. As hydrogen takes center stage in the transition to a cleaner energy landscape, catalysts like NiFeSe@CoOx-NCNTs play a pivotal role in realizing hydrogen's full potential as a clean energy carrier.

The outcomes of this study not only serve as significant milestones in the field of electrocatalysis but also set a dynamic trajectory for future research and technological advancements. The synthesis methods and materials developed provide a platform for continuous optimization, enabling researchers to fine-tune catalyst properties for improved efficiency and stability. Exploring new compositions and structures has the potential to unlock previously untapped catalytic capabilities, offering a breadth of options for designing next-generation catalysts. Equally crucial is the practical implementation of these catalysts in real-world energy conversion applications, such as electrolyzers and fuel cells, driving the transition from laboratory success to tangible societal impact. Scaling up the synthesis processes and ensuring the commercial viability of these materials will play a pivotal role in integrating them into existing energy infrastructure. The concept of multifunctional materials that excel in multiple catalytic reactions concurrently is an exciting avenue to explore, potentially leading to more compact and efficient energy conversion systems. Collaborations across disciplines can infuse fresh perspectives, fostering interdisciplinary innovation and accelerating the development of practical solutions. As the world shifts towards sustainability, evaluating the entire life cycle and environmental impact of these catalysts becomes paramount, ensuring that the benefits they provide are achieved in an environmentally responsible manner. Ultimately, these catalysts stand at the forefront of advancing energy conversion technologies, driving progress towards cleaner and more efficient energy sources and thereby contributing to the global pursuit of a sustainable energy future.

References

1. Shan, J.; Ye, C.; Chen, S.; Sun, T.; Jiao, Y.; Liu, L.; Zhu, C.; Song, L.; Han, Y.; Jaroniec, M., Short-range ordered iridium single atoms integrated into cobalt oxide spinel structure for highly efficient electrocatalytic water oxidation. *J. Am. Chem. Soc.* **2021,** *143* (13), 5201-5211.
2. Yang, D.; Chen, Y.; Su, Z.; Zhang, X.; Zhang, W.; Srinivas, K., Organic carboxylate-based MOFs and derivatives for electrocatalytic water oxidation. *Coord. Chem. Rev.* **2021,** *428*, 213619.
3. Shi, Z.; Nie, K.; Shao, Z.-J.; Gao, B.; Lin, H.; Zhang, H.; Liu, B.; Wang, Y.; Zhang, Y.; Sun, X., Phosphorus-Mo_2C@carbon nanowires toward efficient electrochemical hydrogen evolution: composition, structural and electronic regulation. *Energy Environ. Sci.* **2017,** *10* (5), 1262-1271.
4. Anwar, S.; Khan, F.; Zhang, Y.; Djire, A., Recent development in electrocatalysts for hydrogen production through water electrolysis. *Int. J. Hydrog. Energy* **2021,** *46* (63), 32284-32317.
5. Huang, J.; Han, J.; Wu, T.; Feng, K.; Yao, T.; Wang, X.; Liu, S.; Zhong, J.; Zhang, Z.; Zhang, Y., Boosting hydrogen transfer during volmer reaction at oxides/metal nanocomposites for efficient alkaline hydrogen evolution. *ACS Energy Lett.* **2019,** *4* (12), 3002-3010.
6. Hu, C.; Lv, C.; Liu, S.; Shi, Y.; Song, J.; Zhang, Z.; Cai, J.; Watanabe, A., Nickel phosphide electrocatalysts for hydrogen evolution reaction. *Catal.* **2020,** *10* (2), 188.
7. Chen, Z.; Wei, W.; Ni, B.-J., Cost-effective catalysts for renewable hydrogen production via electrochemical water splitting: Recent advances. *Curr. Opin. Green Sustain. Chem.* **2021,** *27*, 100398.
8. Hameed, A.; Batool, M.; Iqbal, W.; Abbas, S.; Imran, M.; Khan, I. A.; Nadeem, M. A., ZIF-12/Fe-Cu LDH composite as a high performance electrocatalyst for water oxidation. *Front. Chem.* **2021,** *9*, 686968.
9. Garcés-Pineda, F. A.; Blasco-Ahicart, M.; Nieto-Castro, D.; López, N.; Galán-Mascarós, J. R., Direct magnetic enhancement of electrocatalytic water oxidation in alkaline media. *Nat. Energy* **2019,** *4* (6), 519-525.
10. Zhuang, Z.; Wang, Y.; Xu, C.-Q.; Liu, S.; Chen, C.; Peng, Q.; Zhuang, Z.; Xiao, H.; Pan, Y.; Lu, S., Three-dimensional open nano-netcage

electrocatalysts for efficient pH-universal overall water splitting. *Nat. Commun.* **2019,** *10* (1), 4875.

11. Iqbal, W.; Batool, M.; Hameed, A.; Abbas, S.; Nadeem, M. A., Boosting the activity of FeOOH via integration of ZIF-12 and graphene to efficiently catalyze the oxygen evolution reaction. *Int. J. Hydrog. Energy* **2021,** *46* (49), 25050-25059.
12. Zhu, J.; Hu, L.; Zhao, P.; Lee, L. Y. S.; Wong, K.-Y., Recent advances in electrocatalytic hydrogen evolution using nanoparticles. *Chem. Rev.* **2019,** *120* (2), 851-918.
13. Kang, Z.; Guo, H.; Wu, J.; Sun, X.; Zhang, Z.; Liao, Q.; Zhang, S.; Si, H.; Wu, P.; Wang, L., Engineering an Earth-Abundant Element-Based Bifunctional Electrocatalyst for Highly Efficient and Durable Overall Water Splitting. *Adv. Funct. Mater.* **2019,** *29* (9), 1807031.
14. Li, L.; Wang, P.; Shao, Q.; Huang, X., Metallic nanostructures with low dimensionality for electrochemical water splitting. *Chem. Soc. Rev.* **2020,** *49* (10), 3072-3106.
15. Joya, K. S.; Ahmad, Z.; Joya, Y. F.; Garcia-Esparza, A. T.; de Groot, H. J., Efficient electrochemical water oxidation in neutral and near-neutral systems with a nanoscale silver-oxide catalyst. *Nanoscale* **2016,** *8* (32), 15033-15040.
16. Okolie, J. A.; Patra, B. R.; Mukherjee, A.; Nanda, S.; Dalai, A. K.; Kozinski, J. A., Futuristic applications of hydrogen in energy, biorefining, aerospace, pharmaceuticals and metallurgy. *Int. J. Hydrog. Energy* **2021,** *46* (13), 8885-8905.
17. Liu, W.; Zuo, H.; Wang, J.; Xue, Q.; Ren, B.; Yang, F., The production and application of hydrogen in steel industry. *Int. J. Hydrog. Energy* **2021,** *46* (17), 10548-10569.
18. Cai, Z.; Bu, X.; Wang, P.; Ho, J. C.; Yang, J.; Wang, X., Recent advances in layered double hydroxide electrocatalysts for the oxygen evolution reaction. *J. Mater. Chem.* **2019,** *7* (10), 5069-5089.
19. Zhou, P.; Zhai, G.; Lv, X.; Liu, Y.; Wang, Z.; Wang, P.; Zheng, Z.; Cheng, H.; Dai, Y.; Huang, B., Boosting the electrocatalytic HER performance of Ni_3N-V_2O_3 via the interface coupling effect. *Appl. Catal. A* **2021,** *283*, 119590.

20. Yu, J.; Zhong, Y.; Wu, X.; Sunarso, J.; Ni, M.; Zhou, W.; Shao, Z., Bifunctionality from synergy: CoP nanoparticles embedded in amorphous CoOx nanoplates with heterostructures for highly efficient water electrolysis. *Adv. Sci.* **2018,** *5* (9), 1800514.
21. Warren, K. J.; Tran, J. T.; Weimer, A. W., A thermochemical study of iron aluminate-based materials: A preferred class for isothermal water splitting. *Energy Environ. Sci* **2022,** *15* (2), 806-821.
22. Zhao, G.; Kraglund, M. R.; Frandsen, H. L.; Wulff, A. C.; Jensen, S. H.; Chen, M.; Graves, C. R., Life cycle assessment of H_2O electrolysis technologies. *Int. J. Hydrog. Energy* **2020,** *45* (43), 23765-23781.
23. Wu, Q.; Wang, Y.; Zhang, K.; Xie, Z.; Sun, K.; An, W.; Liang, X.; Zou, X., Advances and status of anode catalysts for proton exchange membrane water electrolysis technology. *Mater. Chem. Front.* **2023**.
24. Shi, Q.; Zhu, C.; Du, D.; Lin, Y., Robust noble metal-based electrocatalysts for oxygen evolution reaction. *Chem. Soc. Rev.* **2019,** *48* (12), 3181-3192.
25. Yu, J.; Dai, Y.; Wu, X.; Zhang, Z.; He, Q.; Cheng, C.; Wu, Z.; Shao, Z.; Ni, M., Ultrafine ruthenium-iridium alloy nanoparticles well-dispersed on N-rich carbon frameworks as efficient hydrogen-generation electrocatalysts. *J. Chem. Eng.* **2021,** *417*, 128105.
26. Escalera-López, D.; Czioska, S.; Geppert, J.; Boubnov, A.; R.se , P.; Saraci, E.; Krewer, U.; Grunwaldt, J.-D.; Cherevko, S., Phase-and surface composition-dependent electrochemical stability of Ir-Ru nanoparticles during oxygen evolution reaction. *ACS Catal.* **2021,** *11* (15), 9300-9316.
27. Zhu, K.; Zhu, X.; Yang, W., Application of in situ techniques for the characterization of NiFe-based oxygen evolution reaction (OER) electrocatalysts. *Angew. Chem., Int. Ed.* **2019,** *58* (5), 1252-1265.
28. Tahir, M.; Pan, L.; Idrees, F.; Zhang, X.; Wang, L.; Zou, J.-J.; Wang, Z. L., Electrocatalytic oxygen evolution reaction for energy conversion and storage: a comprehensive review. *Nano Energy* **2017,** *37*, 136-157.
29. Xia, C.; Nguyen, T. H. C.; Nguyen, X. C.; Kim, S. Y.; Nguyen, D. L. T.; Raizada, P.; Singh, P.; Nguyen, V.-H.; Nguyen, C. C.; Van Le, Q., Emerging cocatalysts in TiO_2-based photocatalysts for light-driven catalytic hydrogen evolution: Progress and perspectives. *Fuel* **2022,** *307*, 121745.

30. Karmakar, A.; Karthick, K.; Sankar, S. S.; Kumaravel, S.; Madhu, R.; Kundu, S., A vast exploration of improvising synthetic strategies for enhancing the OER kinetics of LDH structures: a review. *J. Mater. Chem.* **2021,** *9* (3), 1314-1352.

31. Hameed, A.; Batool, M.; Liu, Z.; Nadeem, M. A.; Jin, R., Layered double hydroxide-derived nanomaterials for efficient electrocatalytic water splitting: Recent progress and future perspective. *ACS Energy Lett.* **2022,** *7* (10), 3311-3328.

32. Wang, Y.; Yan, D.; El Hankari, S.; Zou, Y.; Wang, S., Recent progress on layered double hydroxides and their derivatives for electrocatalytic water splitting. *Adv. Sci.* **2018,** *5* (8), 1800064.

33. Zhitova, E. S.; Krivovichev, S. V.; Pekov, I. V.; Yapaskurt, V. O., Crystal chemistry of chlormagaluminite, $Mg_4Al_2(OH)_{12}Cl_2$ $(H_2O)_2$, a natural layered double hydroxide. *Minerals* **2019,** *9* (4), 221.

34. Guan, X.; Yuan, X.; Zhao, Y.; Wang, H.; Wang, H.; Bai, J.; Li, Y., Application of functionalized layered double hydroxides for heavy metal removal: A review. *Sci. Total Environ.* **2022**, 155693.

35. Liu, H.; Wang, Y.; Lu, X.; Hu, Y.; Zhu, G.; Chen, R.; Ma, L.; Zhu, H.; Tie, Z.; Liu, J., The effects of Al substitution and partial dissolution on ultrathin NiFeAl trinary layered double hydroxide nanosheets for oxygen evolution reaction in alkaline solution. *Nano Energy* **2017,** *35*, 350-357.

36. Teixeira, A. C.; Morais, A. F.; Silva, I. G.; Breynaert, E.; Mustafa, D., Luminescent layered double hydroxides intercalated with an anionic photosensitizer via the memory effect. *Crystals* **2019,** *9* (3), 153.

37. Mohapatra, L.; Parida, K., A review on the recent progress, challenges and perspective of layered double hydroxides as promising photocatalysts. *J. Mater. Chem.* **2016,** *4* (28), 10744-10766.

38. Zhou, P.; Wang, Y.; Xie, C.; Chen, C.; Liu, H.; Chen, R.; Huo, J.; Wang, S., Acid-etched layered double hydroxides with rich defects for enhancing the oxygen evolution reaction. *Chemcomm.* **2017,** *53* (86), 11778-11781.

39. Gao, M.; Sheng, W.; Zhuang, Z.; Fang, Q.; Gu, S.; Jiang, J.; Yan, Y., Efficient water oxidation using nanostructured α-nickel-hydroxide as an electrocatalyst. *J. Am. Chem. Soc.* **2014,** *136* (19), 7077-7084.

40. Hu, Y.; Wang, Z.; Liu, W.; Xu, L.; Guan, M.; Huang, Y.; Zhao, Y.; Bao, J.; Li, H.-m.; Engineering, Novel cobalt–iron–vanadium layered double hydroxide nanosheet arrays for superior water oxidation performance. *ACS Sustain. Chem. Eng.* **2019,** *7* (19), 16828-16834.

41. Li, C.; Bao, Y.; Liu, E.; Zhao, B.; Sun, T., Recent Advances of Modified Ni (Co, Fe)-Based LDH 2D Materials for Water Splitting. *Molecules* **2023,** *28* (3), 1475.

42. Suntivich, J.; May, K. J.; Gasteiger, H. A.; Goodenough, J. B.; Shao-Horn, Y., A perovskite oxide optimized for oxygen evolution catalysis from molecular orbital principles. *Sci.* **2011,** *334* (6061), 1383-1385.

43. Pei, Y.; Ge, Y.; Chu, H.; Smith, W.; Dong, P.; Ajayan, P. M.; Ye, M.; Shen, J., Controlled synthesis of 3D porous structured cobalt-iron based nanosheets by electrodeposition as asymmetric electrodes for ultra-efficient water splitting. *Appl. Catal. B Environ* **2019,** *244*, 583-593.

44. Ye, Y.; Li, H.; Cao, J.; Liu, X.; Fan, H.; Wei, M.; Yang, L.; Yang, J.; Chen, Y., Constructing microstructures in nickel-iron layered double hydroxide electrocatalysts by cobalt doping for efficient overall water splitting. *Int. J. Hydrog. Energy* **2023,** *48* (45), 17026-17034.

45. KC; R, S.; D, T.; Chang, Strmcnik D. Paulikas AP Hirunsit P. Chan M. Greeley J. Stamenkovic V. Markovic NM Trends in activity for the water electrolyser reactions on 3d M (Ni, Co, Fe, Mn) hydr (oxy) oxide catalysts. *Nat. Mater.* **2012,** *11* (6), 550-557.

46. Zhan, T.; Zhang, Y.; Liu, X.; Lu, S.; Hou, W., NiFe layered double hydroxide/reduced graphene oxide nanohybrid as an efficient bifunctional electrocatalyst for oxygen evolution and reduction reactions. *J. Power Sources* **2016,** *333*, 53-60.

47. Yu, M.; Budiyanto, E.; Tüysüz, H., Principles of water electrolysis and recent progress in cobalt-, nickel-, and iron-based oxides for the oxygen evolution reaction. *Angew. Chem., Int. Ed.* **2022,** *61* (1), e202103824.

48. Han, L.; Dong, S.; Wang, E., Transition-metal (Co, Ni, and Fe)-based electrocatalysts for the water oxidation reaction. *Adv. Mater.* **2016,** *28* (42), 9266-9291.

49. Zhao, P.; Ma, L.; Guo, J., Vanadium doped nickel hydroxide nanosheets for efficient overall alkaline water splitting. *J. Phys. Chem. Solid* **2022,** *164*, 110634.
50. Casas-Cabanas, M.; Canales-Vázquez, J.; Rodríguez-Carvajal, J.; Palacín, M. R., Deciphering the structural transformations during nickel oxyhydroxide electrode operation. *J. Am. Chem. Soc.* **2007,** *129* (18), 5840-5842.
51. Zhang, X.; Fang, X.; Zhu, K.; Yuan, W.; Jiang, T.; Xue, H.; Tian, J., Fe-doping induced electronic structure reconstruction in Ni-based metal-organic framework for improved energy-saving hydrogen production via urea degradation. *J. Power Sources* **2022,** *520*, 230882.
52. Liu, S.; Gao, R.-T.; Liu, X.; Zhang, X.; Wu, L.; Wang, L., Active straining engineering on self-assembled stacked Ni-based hybrid electrode for ultra-low overpotential. *J. Energy Chem.* **2023,** *77*, 217-226.
53. Wang, R.; Wang, C.; Yin, S.; Peng, Y.; Chen, J.; Deng, Y.; Li, J., Hierarchically devising $NiFeO_xH_y$ catalyst with surface Fe active sites for efficient oxygen evolution reaction. *Catal. Today* **2021,** *364*, 140-147.
54. Zhang, J.; Huang, S.; Ning, P.; Xin, P.; Chen, Z.; Wang, Q.; Uvdal, K.; Hu, Z., Nested hollow architectures of nitrogen-doped carbon-decorated Fe, Co, Ni-based phosphides for boosting water and urea electrolysis. *Nano Res.* **2022,** *15* (3), 1916-1925.
55. Chang, J.; Chen, L.; Zang, S.; Wang, Y.; Wu, D.; Xu, F.; Jiang, K.; Gao, Z., The effect of Fe(III) cations in electrolyte on oxygen evolution catalytic activity of $Ni(OH)_2$ electrode. *J. Colloid Interface Sci.* **2020,** *569*, 50-56.
56. Gultom, N. S.; Abdullah, H.; Hsu, C.-N.; Kuo, D.-H., Activating nickel iron layer double hydroxide for alkaline hydrogen evolution reaction and overall water splitting by electrodepositing nickel hydroxide. *J. Chem. Eng.* **2021,** *419*, 129608.
57. Chen, S.; Yu, C.; Cao, Z.; Huang, X.; Wang, S.; Zhong, H., Trimetallic NiFeCr-LDH/MoS_2composites as novel electrocatalyst for OER. *Int. J. Hydrog. Energy* **2021,** *46* (10), 7037-7046.
58. Yang, Y.; Dang, L.; Shearer, M. J.; Sheng, H.; Li, W.; Chen, J.; Xiao, P.; Zhang, Y.; Hamers, R. J.; Jin, S., Highly active trimetallic NiFeCr layered

double hydroxide electrocatalysts for oxygen evolution reaction. *Adv. Energy. Mater.* **2018,** *8* (15), 1703189.

59. Han, P.; Hua, S.; Ji, J.; Wu, Y.; Ma, L.; Xu, H.; Sun, X.; Yu, S.; Chen, S.; Xiao, J., Hierarchical porous structured trimetallic non-oxides CoFeMo-A (A= P, Se) as electrocatalysts for oxygen evolution reaction. *J. Alloys Compd* **2023,** *932*, 167538.
60. Santos, R.; Tronto, J.; Briois, V.; Santilli, C., Thermal decomposition and recovery properties of ZnAl–CO_3 layered double hydroxide for anionic dye adsorption: insight into the aggregative nucleation and growth mechanism of the LDH memory effect. *J. Mater. Chem.* **2017,** *5* (20), 9998-10009.
61. Bates, M. K.; Jia, Q.; Doan, H.; Liang, W.; Mukerjee, S., Charge-transfer effects in Ni–Fe and Ni–Fe–Co mixed-metal oxides for the alkaline oxygen evolution reaction. *ACS Catal.* **2016,** *6* (1), 155-161.
62. Yang, Y.; Wei, S.; Li, Y.; Guo, D.; Liu, H.; Liu, L., Effect of cobalt doping-regulated crystallinity in nickel-iron layered double hydroxide catalyzing oxygen evolution. *Appl. Catal. B: Environ.* **2022,** *314*, 121491.
63. Jiang, J.; Sun, F.; Zhou, S.; Hu, W.; Zhang, H.; Dong, J.; Jiang, Z.; Zhao, J.; Li, J.; Yan, W., Atomic-level insight into super-efficient electrocatalytic oxygen evolution on iron and vanadium co-doped nickel (oxy) hydroxide. *Nat. Commun.* **2018,** *9* (1), 2885.
64. Liang, J.; Shen, H.; Ma, Y.; Liu, D.; Li, M.; Kong, J.; Tang, Y.; Ding, S., Autogenous growth of the hierarchical V-doped NiFe layer double metal hydroxide electrodes for an enhanced overall water splitting. *Dalton Trans.* **2020,** *49* (32), 11217-11225.
65. Karim, A. V.; Hassani, A.; Eghbali, P.; Nidheesh, P., Nanostructured modified layered double hydroxides (LDHs)-based catalysts: a review on synthesis, characterization, and applications in water remediation by advanced oxidation processes. *Curr. Opin. Solid State Mater. Sci* **2022,** *26* (1), 100965.
66. Zhang, F.; Xiang, X.; Li, F.; Duan, X., Layered double hydroxides as catalytic materials: recent development. *Catal. Surv. from Asia.* **2008,** *12*, 253-265.
67. Zhang, G.; Li, Y.; He, C.; Ren, X.; Zhang, P.; Mi, H., Recent progress in 2D catalysts for photocatalytic and electrocatalytic artificial nitrogen reduction to ammonia. *Adv. Energy. Mater.* **2021,** *11* (11), 2003294.

68. Mallakpour, S.; Hatami, M.; Hussain, C. M., Recent innovations in functionalized layered double hydroxides: Fabrication, characterization, and industrial applications. *Adv. colloid intrface Sci.* **2020,** *283*, 102216.

69. Xie, J.; Zhang, J.; Li, S.; Grote, F.; Zhang, X.; Zhang, H.; Wang, R.; Lei, Y.; Pan, B.; Xie, Y., Controllable disorder engineering in oxygen-incorporated MoS_2 ultrathin nanosheets for efficient hydrogen evolution. *J. Am. Chem. Soc.* **2013,** *135* (47), 17881-17888.

70. Li, Z.; Duan, H.; Shao, M.; Li, J.; O'Hare, D.; Wei, M.; Wang, Z. L., Ordered-vacancy-induced cation intercalation into layered double hydroxides: a general approach for high-performance supercapacitors. *Chem.* **2018,** *4* (9), 2168-2179.

71. Xu, M.; Wei, M., Layered double hydroxide-based catalysts: recent advances in preparation, structure, and applications. *Adv. Funct. Mater.* **2018,** *28* (47), 1802943.

72. Zeng, Y.; Wang, Y.; Huang, G.; Chen, C.; Huang, L.; Chen, R.; Wang, S., Porous CoP nanosheets converted from layered double hydroxides with superior electrochemical activity for hydrogen evolution reactions at wide pH ranges. *Chemcomm.* **2018,** *54* (12), 1465-1468.

73. Wang, Y.; Qiao, M.; Li, Y.; Wang, S., Tuning surface electronic configuration of NiFe LDHs nanosheets by introducing cation vacancies (Fe or Ni) as highly efficient electrocatalysts for oxygen evolution reaction. *Small.* **2018,** *14* (17), 1800136.

74. Wang, L.; Peng, C.; Lin, H.; Zhao, B., Unraveling the Role of Defects in Electrocatalysts for Water Splitting: Recent Advances and Perspectives. *Energy Fuels* **2022,** *36* (19), 11660-11690.

75. Zhang, X.; Yan, F.; Ma, X.; Zhu, C.; Wang, Y.; Xie, Y.; Chou, S. L.; Huang, Y.; Chen, Y., Regulation of morphology and electronic structure of FeCoNi layered double hydroxides for highly active and stable water oxidization catalysts. *Adv. Energy. Mater.* **2021,** *11* (48), 2102141.

76. Barwe, S.; Andronescu, C.; Masa, J.; Schuhmann, W., The two Janus faces in oxygen evolution electrocatalysis: activity versus stability of layered double hydroxides. *Curr. Opin. Solid State Mater. Sci* **2017,** *4* (1), 4-10.

77. Li, D.; Li, T.; Hao, G.; Guo, W.; Chen, S.; Liu, G.; Li, J.; Zhao, Q., IrO_2 nanoparticle-decorated single-layer NiFe LDHs nanosheets with oxygen vacancies for the oxygen evolution reaction. *J. Chem. Eng.* **2020,** *399*, 125738.

78. Hu, W.; Liu, Q.; Lv, T.; Zhou, F.; Zhong, Y., Impact of interfacial CoOOH on OER catalytic activities and electrochemical behaviors of bimetallic CoxNi-LDH nanosheet catalysts. *Electrochim. Acta* **2021,** *381*, 138276.

79. He, J.; Yang, Z.; Zhang, L.; Li, Y.; Pan, L., Cu supported on ZnAl-LDHs precursor prepared by in-situ synthesis method on γ-Al_2O_3 as catalytic material with high catalytic activity for methanol steam reforming. *Int. J. Hydrog. Energy* **2017,** *42* (15), 9930-9937.

80. Alobaid, A.; Wang, C.; Adomaitis, R. A., Mechanism and kinetics of HER and OER on NiFe LDH films in an alkaline electrolyte. *J. Electchem. Soc.* **2018,** *165* (15), J3395-J3404.

81. Meng, L.; Xuan, H.; Liang, X.; Li, Y.; Yang, J.; Han, P., Flower-like Co_3O_4@ NiFe-LDH nanosheets enable high-performance bifunctionality towards both electrocatalytic HER and OER in alkaline solution. *J. Alloys Compd* **2022,** *919*, 165877.

82. Karmakar, A.; Karthick, K.; Sankar, S. S.; Kumaravel, S.; Madhu, R.; Bera, K.; Dhandapani, H. N.; Nagappan, S.; Murugan, P.; Kundu, S., Stabilization of ruthenium nanoparticles over NiV-LDH surface for enhanced electrochemical water splitting: an oxygen vacancy approach. *J. Mater. Chem.* **2022,** *10* (7), 3618-3632.

83. Sahoo, D. P.; Das, K. K.; Mansingh, S.; Sultana, S.; Parida, K., Recent progress in first row transition metal Layered double hydroxide (LDH) based electrocatalysts towards water splitting: A review with insights on synthesis. *Coord. Chem. Rev.* **2022,** *469*, 214666.

84. Yao, L.; Li, R.; Zhang, H.; Humayun, M.; Xu, X.; Fu, Y.; Nikiforov, A.; Wang, C., Interface engineering of NiTe@ CoFe LDH for highly efficient overall water-splitting. *Int. J. Hydrog. Energy* **2022,** *47* (76), 32394-32404.

85. Bao, J.; Wang, Z.; Xie, J.; Xu, L.; Lei, F.; Guan, M.; Huang, Y.; Zhao, Y.; Xia, J.; Li, H., The CoMo-LDH ultrathin nanosheet as a highly active and bifunctional electrocatalyst for overall water splitting. *Inorg. Chem. Front.* **2018,** *5* (11), 2964-2970.

86. Tezuka, S.; Chitrakar, R.; Sonoda, A.; Ooi, K.; Tomida, T., Studies on selective adsorbents for oxo-anions. Nitrate ion-exchange properties of layered double hydroxides with different metal atoms. *Green Chem.* **2004,** *6* (2), 104-109.

87. Bai, X.; Liu, J.; Liu, Q.; Chen, R.; Jing, X.; Li, B.; Wang, J., In-Situ Fabrication of MOF-Derived Co− Co Layered Double Hydroxide Hollow Nanocages/Graphene Composite: A Novel Electrode Material with Superior Electrochemical Performance. *Eur. J. Chem.* **2017,** *23* (59), 14839-14847.

88. Bai, X.; Liu, Q.; Lu, Z.; Liu, J.; Chen, R.; Li, R.; Song, D.; Jing, X.; Liu, P.; Wang, J.; Engineering, Rational design of sandwiched Ni–Co layered double hydroxides hollow nanocages/graphene derived from metal–organic framework for sustainable energy storage. *ACS Sustain. Chem. Eng.* **2017,** *5* (11), 9923-9934.

89. Zhang, R.; Russo, P. A.; Buzanich, A. G.; Jeon, T.; Pinna, N., Hybrid Organic–Inorganic Transition-Metal Phosphonates as Precursors for Water Oxidation Electrocatalysts. *Adv. Funct. Mater.* **2017,** *27* (40), 1703158.

90. Su, X.; Wang, Y.; Zhou, J.; Gu, S.; Li, J.; Zhang, S., Operando spectroscopic identification of active sites in NiFe prussian blue analogues as electrocatalysts: activation of oxygen atoms for oxygen evolution reaction. *J. Am. Chem. Soc.* **2018,** *140* (36), 11286-11292.

91. Palin, L.; Milanesio, M.; van Beek, W.; Conterosito, E., Understanding the ion exchange process in LDH nanomaterials by fast in situ XRPD and PCA-assisted kinetic analysis. *J. Nanomater.* **2019,** *2019*.

92. Lv, H.; Rao, H.; Liu, Z.; Zhou, Z.; Zhao, Y.; Wei, H.; Chen, Z., NiAl layered double hydroxides with enhanced interlayer spacing via ion-exchange as ultra-high performance supercapacitors electrode materials. *J. Energy Storage* **2022,** *52*, 104940.

93. Khorshidi, M.; Asadpour, S.; Sarmast, N.; Dinari, M., A review of the synthesis methods, properties, and applications of layered double hydroxides/carbon nanocomposites. *J. Mol. Liq.* **2022,** *348*, 118399.

94. Zhong, H.; Cheng, X.; Xu, H.; Li, L.; Li, D.; Tang, P.; Alonso-Vante, N.; Feng, Y., Carbon fiber paper supported interlayer space enlarged Ni_2Fe-LDHs improved OER electrocatalytic activity. *Electrochim. Acta* **2017,** *258*, 554-560.

95. Li, C.-F.; Xie, L.-J.; Zhao, J.-W.; Gu, L.-F.; Wu, J.-Q.; Li, G.-R., Interfacial electronic modulation by Fe_2O_3/NiFe-LDHs heterostructures for efficient oxygen evolution at high current density. *Appl. Catal. B Environ* **2022,** *306*, 121097.

96. Cunha, V. R. R.; de Souza, R. B.; da Fonseca Martins, A. M. C. R. P.; Koh, I. H. J.; Constantino, V. R. L., Accessing the biocompatibility of layered double hydroxide by intramuscular implantation: Histological and microcirculation evaluation. *Sci. Rep.* **2016,** *6* (1), 30547.

97. Jin, W.; Lee, D.; Jeon, Y.; Park, D.-H., Biocompatible hydrotalcite nanohybrids for medical functions. *Minerals* **2020,** *10* (2), 172.

98. Shirin, V. A.; Sankar, R.; Johnson, A. P.; Gangadharappa, H.; Pramod, K., Advanced drug delivery applications of layered double hydroxide. *JCR.* **2021,** *330*, 398-426.

99. Figueiredo, M. P.; Cunha, V. R.; Leroux, F.; Taviot-Gueho, C.; Nakamae, M. N.; Kang, Y. R.; Souza, R. B.; Martins, A. M. C.; Koh, I. H. J.; Constantino, V. R., Iron-based layered double hydroxide implants: Potential drug delivery carriers with tissue biointegration promotion and blood microcirculation preservation. *ACS Omega* **2018,** *3* (12), 18263-18274.

100. Aziz, A.; Asif, M.; Ashraf, G.; Azeem, M.; Majeed, I.; Ajmal, M.; Wang, J.; Liu, H., Advancements in electrochemical sensing of hydrogen peroxide, glucose and dopamine by using 2D nanoarchitectures of layered double hydroxides or metal dichalcogenides. A review. *Microchim. Acta* **2019,** *186*, 1-16.

101. Choi, M.-J.; Eom, J.-H.; Shin, S.-H.; Nah, J.; Choi, J.-S.; Song, H.-A.; An, H.; Kim, H. Y.; Pammi, S.; Choi, G., Most facile synthesis of Zn-Al: LDHs nanosheets at room temperature via environmentally friendly process and their high power generation by flexoelectricity. *Mater. Today Energ.* **2018,** *10*, 254-263.

102. Ma, X.-R.; Wei, X.-Y.; Dang, R.; Guo, W.; Kang, Y.-H.; Li, X.; Gao, Y.; Bai, J.-J.; Zhang, Y.; Zhang, Z.-F., A simple, environmentally friendly synthesis of recyclable magnetic γ-Fe_2O_3/Cd^{2+}-Ni^{2+}-Fe^{3+}-CO_3^{2-} layered double hydroxides for the removal of fluoride and cadmium ions. adsorption capacity and the underlying mechanisms. *Appl. Clay Sci.* **2021,** *211*, 106191.

103. Gong, Y.; Yao, J.; Wang, P.; Li, Z.; Zhou, H.; Xu, C., Perspective of hydrogen energy and recent progress in electrocatalytic water splitting. *Chin. J. Chem. Eng.* **2022**.

104. Dresp, S.; Thanh, T. N.; Klingenhof, M.; Brückner, S.; Hauke, P.; Strasser, P., Efficient direct seawater electrolysers using selective alkaline NiFe-LDH as OER catalyst in asymmetric electrolyte feeds. *Energy Environ. Sci.* **2020,** *13* (6), 1725-1729.

105. Tu, Q.; Liu, W.; Jiang, M.; Wang, W.; Kang, Q.; Wang, P.; Zhou, W.; Zhou, F., Preferential adsorption of hydroxide ions onto partially crystalline NiFe-layered double hydroxides leads to efficient and selective OER in alkaline seawater. *ACS Appl. Energy Mater.* **2021,** *4* (5), 4630-4637.

106. Wang, Z.; Wang, C.; Ye, L.; Liu, X.; Xin, L.; Yang, Y.; Wang, L.; Hou, W.; Wen, Y.; Zhan, T., MnO_x Film-Coated NiFe-LDH Nanosheets on Ni Foam as Selective Oxygen Evolution Electrocatalysts for Alkaline Seawater Oxidation. *Inorg. Chem.* **2022,** *61* (38), 15256-15265.

107. Ma, L.; Zhou, H.; Xu, M.; Hao, P.; Kong, X.; Duan, H., Integrating hydrogen production with anodic selective oxidation of sulfides over a CoFe layered double hydroxide electrode. *Chem. Sci.* **2021,** *12* (3), 938-945.

108. Gao, R.; Zhu, J.; Yan, D., Transition metal-based layered double hydroxides for photo (electro) chemical water splitting: a mini review. *Nanoscale* **2021,** *13* (32), 13593-13603.

109. Zhou, D.; Cai, Z.; Jia, Y.; Xiong, X.; Xie, Q.; Wang, S.; Zhang, Y.; Liu, W.; Duan, H.; Sun, X., Activating basal plane in NiFe layered double hydroxide by Mn^{2+} doping for efficient and durable oxygen evolution reaction. *Nanoscale Hori.* **2018,** *3* (5), 532-537.

110. Johnston, A.-L.; Lester, E.; Williams, O.; Gomes, R. L., Understanding Layered Double Hydroxide properties as sorbent materials for removing organic pollutants from environmental waters. *J. Environ. Chem. Eng.* **2021,** *9* (4), 105197.

111. Zhou, D.; Li, P.; Lin, X.; McKinley, A.; Kuang, Y.; Liu, W.; Lin, W.-F.; Sun, X.; Duan, X., Layered double hydroxide-based electrocatalysts for the oxygen evolution reaction: identification and tailoring of active sites, and

superaerophobic nanoarray electrode assembly. *Chem. Soc. Rev.* **2021,** *50* (15), 8790-8817.

112. Richetta, M.; Digiamberardino, L.; Mattoccia, A.; Medaglia, P.; Montanari, R.; Pizzoferrato, R.; Scarpellini, D.; Varone, A.; Kaciulis, S.; Mezzi, A., Surface spectroscopy and structural analysis of nanostructured multifunctional (Zn, Al) layered double hydroxides. *Surf. Interface* **2016,** *48* (7), 514-518.
113. Gou, W.; Wang, X.; Zhu, M.; Guan, D.-X.; Mo, X.; Wang, H.; Li, W., Long-range and short-range structures of multimetallic layered double hydroxides. *J. Phys. Chem. C* **2022,** *126* (11), 5311-5322.
114. Xu, M.; Wei, M., Layered double hydroxide-based catalysts: recent advances in preparation, structure, and applications. *Adv. Funct. Mater.* **2018,** *28* (47), 1802943.
115. Bai, L.; Lee, S.; Hu, X., Spectroscopic and electrokinetic evidence for a bifunctional mechanism of the oxygen evolution reaction. *Angew. Chem., Int. Ed.* **2021,** *60* (6), 3095-3103.
116. Li, P.; Duan, X.; Kuang, Y.; Li, Y.; Zhang, G.; Liu, W.; Sun, X., Tuning electronic structure of NiFe layered double hydroxides with vanadium doping toward high efficient electrocatalytic water oxidation. *Adv. Funct. Mater.* **2018,** *8* (15), 1703341.
117. Zhang, F.-S.; Wang, J.-W.; Luo, J.; Liu, R.-R.; Zhang, Z.-M.; He, C.-T.; Lu, T.-B., Extraction of nickel from NiFe-LDH into Ni_2P@NiFe hydroxide as a bifunctional electrocatalyst for efficient overall water splitting. *Chem. Sci.* **2018,** *9* (5), 1375-1384.
118. Cao, S.; Huang, H.; Shi, K.; Wei, L.; You, N.; Fan, X.; Yang, Z.; Zhang, W., Engineering superhydrophilic/superaerophobic hierarchical structures of Co-CH@ NiFe-LDH/NF to boost the oxygen evolution reaction. *J. Chem. Eng.* **2021,** *422*, 130123.
119. Feng, C.; Faheem, M. B.; Fu, J.; Xiao, Y.; Li, C.; Li, Y., Fe-based electrocatalysts for oxygen evolution reaction: progress and perspectives. *ACS Catal.* **2020,** *10* (7), 4019-4047.
120. Zhao, J.; Wang, X.-r.; Chen, F.-w.; He, C.; Wang, X.-j.; Li, Y.-p.; Liu, R.-h.; Chen, X.-m.; Hao, Y.-j.; Yang, M., A one-step synthesis of hierarchical porous CoFe-layered double hydroxide nanosheets with optimized

composition for enhanced oxygen evolution electrocatalysis. *Inorg. Chem. Front.* **2020,** *7* (3), 737-745.

121. Gicha, B. B.; Tufa, L. T.; Kang, S.; Goddati, M.; Bekele, E. T.; Lee, J., Transition metal-based 2D layered double hydroxide nanosheets: design strategies and applications in oxygen evolution reaction. *Nano Mater.* **2021,** *11* (6), 1388.
122. Kuang, M.; Han, P.; Huang, L.; Cao, N.; Qian, L.; Zheng, G., Electronic Tuning of Co, Ni-Based Nanostructured (Hydr) oxides for Aqueous Electrocatalysis. *Adv. Funct. Mater.* **2018,** *28* (52), 1804886.
123. Arif, M.; Yasin, G.; Luo, L.; Ye, W.; Mushtaq, M. A.; Fang, X.; Xiang, X.; Ji, S.; Yan, D., Hierarchical hollow nanotubes of NiFeV-layered double hydroxides@CoVP heterostructures towards efficient, pH-universal electrocatalytical nitrogen reduction reaction to ammonia. *Appl. Catal. B Environ* **2020,** *265*, 118559.
124. Liang, Q.; Brocks, G.; Bieberle-Hütter, A., Oxygen evolution reaction (OER) mechanism under alkaline and acidic conditions. *J. Phys. Energy* **2021,** *3* (2), 026001.
125. Lu, F.; Zhou, M.; Zhou, Y.; Zeng, X., First-row transition metal based catalysts for the oxygen evolution reaction under alkaline conditions: basic principles and recent advances. *Small* **2017,** *13* (45), 1701931.
126. He, T.; Matta, S. K.; Will, G.; Du, A., Transition-metal single atoms anchored on graphdiyne as high-efficiency electrocatalysts for water splitting and oxygen reduction. *Small Methods* **2019,** *3* (9), 1800419.
127. Kurtz, D. A.; Hunter, B. M., Forming O–O bonds. *Joule* **2022**.
128. Wan, X.; Song, Y.; Zhou, H.; Shao, M., Layered double hydroxides for oxygen evolution reaction towards efficient hydrogen generation. *Adv. Energy. Mater.* **2022,** *2022*.
129. Li, Y.; Sun, Y.; Qin, Y.; Zhang, W.; Wang, L.; Luo, M.; Yang, H.; Guo, S., Recent advances on water-splitting electrocatalysis mediated by noble-metal-based nanostructured materials. *Adv. Energy. Mater.* **2020,** *10* (11), 1903120.
130. Yu, M.; Budiyanto, E.; Tüysüz, H., Principles of water electrolysis and recent progress in cobalt-, nickel-, and iron-based oxides for the oxygen evolution reaction. *Angew. Chem. Intl. Ed.* **2022,** *61* (1), e202103824.

131. Zhou, B.; Gao, R.; Zou, J. J.; Yang, H., Surface design strategy of catalysts for water electrolysis. *Small* **2022,** *18* (27), 2202336.

132. Chen, Q.; Yu, Y.; Li, J.; Nan, H.; Luo, S.; Jia, C.; Deng, P.; Zhong, S.; Tian, X., Recent Progress in Layered Double Hydroxide-Based Electrocatalyst for Hydrogen Evolution Reaction. *ChemElectroChem* **2022,** *9* (9), e202101387.

133. Lasia, A., Mechanism and kinetics of the hydrogen evolution reaction. *Int. J. Hydrog. Energy* **2019,** *44* (36), 19484-19518.

134. Kronberg, R.; Lappalainen, H.; Laasonen, K., Revisiting the Volmer–Heyrovský mechanism of hydrogen evolution on a nitrogen doped carbon nanotube: constrained molecular dynamics versus the nudged elastic band method. *PCCP* **2020,** *22* (19), 10536-10549.

135. Alobaid, A.; Wang, C.; Adomaitis, R. A., Mechanism and kinetics of HER and OER on NiFe LDH films in an alkaline electrolyte. *Journal of The Electrochemical Society* **2018,** *165* (15), J3395-J3404.

136. Wei, J.; Zhou, M.; Long, A.; Xue, Y.; Liao, H.; Wei, C.; Xu, Z. J., Heterostructured electrocatalysts for hydrogen evolution reaction under alkaline conditions. *Nanomicro Lett.* **2018,** *10*, 1-15.

137. Liu, L.; Liu, Y.; Liu, C., Enhancing the understanding of hydrogen evolution and oxidation reactions on Pt (111) through ab initio simulation of electrode/electrolyte kinetics. *J. Am. Chem. Soc.* **2020,** *142* (11), 4985-4989.

138. Zhang, J.; Yu, L.; Chen, Y.; Lu, X. F.; Gao, S.; Lou, X. W., Designed formation of double-shelled Ni–Fe layered-double-hydroxide nanocages for efficient oxygen evolution reaction. *Adv. Mater.* **2020,** *32* (16), 1906432.

139. Liu, M.; He, Q.; Huang, S.; Zou, W.; Cong, J.; Xiao, X.; Li, P.; Cai, J.; Hou, L., NiCo-layered double hydroxide-derived B-doped CoP/Ni_2P hollow nanoprisms as high-efficiency electrocatalysts for hydrogen evolution reaction. *ACS Appl. Mater. Interfaces* **2021,** *13* (8), 9932-9941.

140. Guo, J.; Wang, K.; Zhang, H.; Zhang, H., Enhanced Electrocatalytic Activity of Mo-Doped NiFe Layered Double Hydroxide Nanosheet Arrays for the Hydrogen Evolution Reaction. *ACS Appl. Nano Mater.* **2022**.

141. Hu, J.; Zhang, C.; Jiang, L.; Lin, H.; An, Y.; Zhou, D.; Leung, M. K.; Yang, S., Nanohybridization of MoS_2 with layered double hydroxides efficiently

synergizes the hydrogen evolution in alkaline media. *Joule* **2017,** *1* (2), 383-393.

142. Liu, Z.; He, T.; Jiang, Q.; Wang, W.; Tang, J., A review of heteroatomic doped two-dimensional materials as electrocatalysts for hydrogen evolution reaction. *Int. J. Hydrog. Energy* **2022**.

143. Zhang, L.; Zheng, Y.; Wang, J.; Geng, Y.; Zhang, B.; He, J.; Xue, J.; Frauenheim, T.; Li, M., Ni/Mo Bimetallic-Oxide-Derived Heterointerface-Rich Sulfide Nanosheets with Co-Doping for Efficient Alkaline Hydrogen Evolution by Boosting Volmer Reaction. *Small* **2021,** *17* (10), 2006730.

144. Dubouis, N.; Grimaud, A., The hydrogen evolution reaction: from material to interfacial descriptors. *Chem. Sci.* **2019,** *10* (40), 9165-9181.

145. Zheng, Y.; Jiao, Y.; Vasileff, A.; Qiao, S. Z., The hydrogen evolution reaction in alkaline solution: from theory, single crystal models, to practical electrocatalysts. *Angew. Chem., Int. Ed.* **2018,** *57* (26), 7568-7579.

146. Hu, K.; Wu, M.; Hinokuma, S.; Ohto, T.; Wakisaka, M.; Fujita, J.-i.; Ito, Y., Boosting electrochemical water splitting via ternary NiMoCo hybrid nanowire arrays. *J. Mater. Chem. A* **2019,** *7* (5), 2156-2164.

147. Luo, X.; Ji, P.; Wang, P.; Cheng, R.; Chen, D.; Lin, C.; Zhang, J.; He, J.; Shi, Z.; Li, N., Interface engineering of hierarchical branched Mo-doped Ni_3S_2/Ni_xPy hollow heterostructure nanorods for efficient overall water splitting. *Adv. Energy. Mater.* **2020,** *10* (17), 1903891.

148. Yasin, G.; Ibraheem, S.; Ali, S.; Arif, M.; Ibrahim, S.; Iqbal, R.; Kumar, A.; Tabish, M.; Mushtaq, M.; Saad, A., Defects-engineered tailoring of tri-doped interlinked metal-free bifunctional catalyst with lower gibbs free energy of OER/HER intermediates for overall water splitting. *Mater. Chem. Today* **2022,** *23*, 100634.

149. Huang, G.; Shao, L.; He, X.; Jiang, L., Treatment of simulated liquid radioactive waste containing cobalt by in-situ co-precipitation of Zn/Al layered double hydroxides. *J. Radioanal. Nucl. Chem.* **2019,** *319*, 847-854.

150. Bukhtiyarova, M., A review on effect of synthesis conditions on the formation of layered double hydroxides. *J. Solid State Chem.* **2019,** *269*, 494-506.

151. Theiss, F. L.; Ayoko, G. A.; Frost, R. L., Synthesis of layered double hydroxides containing Mg^{2+}, Zn^{2+}, Ca^{2+} and Al^{3+} layer cations by co-precipitation methods—A review. *Appl. Surf. Sci.* **2016,** *383*, 200-213.

152. Pang, H.; Wu, Y.; Wang, X.; Hu, B.; Wang, X., Recent advances in composites of graphene and layered double hydroxides for water remediation: a review. *Chem. Asian J.* **2019,** *14* (15), 2542-2552.

153. Wijitwongwan, R.; Intasa-ard, S.; Ogawa, M., Preparation of layered double hydroxides toward precisely designed hierarchical organization. *ChemEng* **2019,** *3* (3), 68.

154. Guzmán-Vargas, A.; Vazquez-Samperio, J.; Oliver-Tolentino, M. A.; Nava, N.; Castillo, N.; Macías-Hernández, M. J.; Reguera, E., Influence of cobalt on electrocatalytic water splitting in NiCoFe layered double hydroxides. *J. Mater. Sci.* **2018,** *53* (6), 4515-4526.

155. Zhuang, L.; Ge, L.; Yang, Y.; Li, M.; Jia, Y.; Yao, X.; Zhu, Z., Ultrathin iron-cobalt oxide nanosheets with abundant oxygen vacancies for the oxygen evolution reaction. *Adv. Mater.* **2017,** *29* (17), 1606793.

156. Jeon, C.-W.; Lee, S.-S.; Park, I.-K., Structural evolution of NiAl-based layered nanostructures grown by a low-temperature hydrothermal method. *Appl. Surf. Sci.* **2019,** *473*, 65-69.

157. Anantharaj, S.; Karthick, K.; Venkatesh, M.; Simha, T. V.; Salunke, A. S.; Ma, L.; Liang, H.; Kundu, S., Enhancing electrocatalytic total water splitting at few layer Pt-NiFe layered double hydroxide interfaces. *Nano Energy* **2017,** *39*, 30-43.

158. Janani, F.; Taoufik, N.; Khiar, H.; Boumya, W.; Elhalil, A.; Sadiq, M.; Puga, A.; Barka, N., Nanostructured layered double hydroxides based photocatalysts: Insight on synthesis methods, application in water decontamination/splitting and antibacterial activity. *Surf. Interface* **2021,** *25*, 101263.

159. Wilhelm, M.; Bastos, A.; Neves, C.; Martins, R.; Tedim, J., Ni-Fe layered double hydroxides for oxygen evolution Reaction: Impact of Ni/Fe ratio and crystallinity. *Mater. Des.* **2021,** *212*, 110188.

160. Hou, Y.; Lohe, M. R.; Zhang, J.; Liu, S.; Zhuang, X.; Feng, X., Vertically oriented cobalt selenide/NiFe layered-double-hydroxide nanosheets supported

on exfoliated graphene foil: an efficient 3D electrode for overall water splitting. *Energ. Environ. Sci.* **2016,** *9* (2), 478-483.

161. Zhao, L.; Guo, Z.; Liu, Z., Facile synthesis and efficient electrochemical water splitting of bifunctional nanostructured Ni-based layered double hydroxide/sulfide composite. *J. Alloys Compd.* **2022,** *910*, 164880.
162. Wang, Q.; O'Hare, D., Recent advances in the synthesis and application of layered double hydroxide (LDH) nanosheets. *Chem. Rev.* **2012,** *112* (7), 4124-4155.
163. Feng, J.; He, Y.; Liu, Y.; Du, Y.; Li, D., Supported catalysts based on layered double hydroxides for catalytic oxidation and hydrogenation: general functionality and promising application prospects. *Chem. Soc. Rev.* **2015,** *44* (15), 5291-5319.
164. Hou, C.; Cui, Z.; Zhang, S.; Yang, W.; Gao, H.; Luo, X., Rapid large-scale synthesis of ultrathin NiFe-layered double hydroxide nanosheets with tunable structures as robust oxygen evolution electrocatalysts. *RSC Adv.* **2021,** *11* (59), 37624-37630.
165. Li, C.; Wei, M.; Evans, D. G.; Duan, X., Layered double hydroxide-based nanomaterials as highly efficient catalysts and adsorbents. *Small* **2014,** *10* (22), 4469-4486.
166. Li, C.; Wei, M.; Evans, D. G.; Duan, X., Recent advances for layered double hydroxides (LDHs) materials as catalysts applied in green aqueous media. *Catal. Today* **2015,** *247*, 163-169.
167. Xie, W.; Song, Y.; Li, S.; Shao, M.; Wei, M., Integrated nanostructural electrodes based on layered double hydroxides. *Energ. Environ. Sci.* **2019,** *2* (3), 158-171.
168. Wang, T.; Wang, W.; Shao, W.; Bai, M.; Zhou, M.; Li, S.; Ma, T.; Ma, L.; Cheng, C.; Liu, X., Synthesis and electronic modulation of nanostructured layered double hydroxides for efficient electrochemical oxygen evolution. *ChemSusChem* **2021,** *14* (23), 5112-5134.
169. Zhang, X.; Yan, F.; Ma, X.; Zhu, C.; Wang, Y.; Xie, Y.; Chou, S. L.; Huang, Y.; Chen, Y., Regulation of morphology and electronic structure of FeCoNi layered double hydroxides for highly active and stable water oxidization catalysts. *Adv. Energy Mater.* **2021,** *11* (48), 2102141.

170. Long, X.; Wang, Z.; Xiao, S.; An, Y.; Yang, S., Transition metal based layered double hydroxides tailored for energy conversion and storage. *Mater. Today* **2016,** *19* (4), 213-226.

171. Wang, Y.; Yan, D.; El Hankari, S.; Zou, Y.; Wang, S., Recent progress on layered double hydroxides and their derivatives for electrocatalytic water splitting. *Adv. Sci.* **2018,** *5* (8), 1800064.

172. Yang, R.; Zhou, Y.; Xing, Y.; Li, D.; Jiang, D.; Chen, M.; Shi, W.; Yuan, S., Synergistic coupling of CoFe-LDH arrays with NiFe-LDH nanosheet for highly efficient overall water splitting in alkaline media. *Appl. Catal. B: Environ.* **2019,** *253*, 131-139.

173. Gong, Y.; Huang, J.; Cao, L.; Kajiyoshi, K.; Yang, D.; Feng, Y.; Kou, L.; Feng, L., Methanol-assisted synthesis of Ni^{3+}-doped ultrathin NiZn-LDH nanomeshes for boosted alkaline water splitting. *Dalton Trans.* **2020,** *49* (4), 1325-1333.

174. Zhang, Y.; Cheng, C.-Q.; Kuai, C.-G.; Sokaras, D.; Zheng, X.-L.; Sainio, S.; Lin, F.; Dong, C.-K.; Nordlund, D.; Du, X.-W., Unveiling the critical role of the Mn dopant in a $NiFe(OH)_2$ catalyst for water oxidation. *J. Mater. Chem. A* **2020,** *8* (34), 17471-17476.

175. Qian, L.; Chen, W.; Liu, M.; Jia, Q.; Xiao, D., One-Step Electrodeposition of S-Doped Cobalt–Nickel Layered Double Hydroxides on Conductive Substrates and their Electrocatalytic Activity in Alkaline Media. *ChemElectroChem* **2016,** *3* (6), 950-958.

176. Zeng, Y.-T.; Xu, M.-Y.; Wang, T.; Wu, S.-Y.; Zhang, J.; Mu, S.-C.; Yu, J., Ru-decorated cobalt-iron oxide nanosheet arrays derived from MOF and LDH double-precursors for overall water splitting in alkali and seawater. *Electrochim. Acta* **2023,** *444*, 142004.

177. Han, X.; Yu, C.; Niu, Y.; Wang, Z.; Kang, Y.; Ren, Y.; Wang, H.; Park, H. S.; Qiu, J., Full Bulk-Structure Reconstruction into Amorphorized Cobalt–Iron Oxyhydroxide Nanosheet Electrocatalysts for Greatly Improved Electrocatalytic Activity. *Small Methods* **2020,** *4* (10), 2000546.

178. Jiang, D.; Ma, W.; Yang, R.; Quan, B.; Li, D.; Meng, S.; Chen, M., Nickel–manganese bimetallic phosphides porous nanosheet arrays as highly active

bifunctional hydrogen and oxygen evolution electrocatalysts for overall water splitting. *Electrochim. Acta* **2020,** *329*, 135121.

179. Li, D.; Xing, Y.; Yang, R.; Wen, T.; Jiang, D.; Shi, W.; Yuan, S., Holey cobalt–iron nitride nanosheet arrays as high-performance bifunctional electrocatalysts for overall water splitting. *ACS Appl. Mater. Interfaces* **2020,** *12* (26), 29253-29263.
180. Suo, N.; Dou, Z.; Cui, L., Interface and composition engineering of vanadium doped cobalt nickel sulfide/phosphide heterostructure for efficient water splitting. *Electrochim. Acta* **2021,** *368*, 137602.
181. Dutta, S.; Indra, A.; Feng, Y.; Song, T.; Paik, U., Self-supported nickel iron layered double hydroxide-nickel selenide electrocatalyst for superior water splitting activity. *ACS Appl. Mater. Interfaces* **2017,** *9* (39), 33766-33774.
182. Yu, J.; Yu, F.; Yuen, M.-F.; Wang, C., Two-dimensional layered double hydroxides as a platform for electrocatalytic oxygen evolution. *J. Mater. Chem.* **2021,** *9* (15), 9389-9430.
183. Li, X.; Hao, X.; Wang, Z.; Abudula, A.; Guan, G., In-situ intercalation of NiFe LDH materials: an efficient approach to improve electrocatalytic activity and stability for water splitting. *J. Power Sources* **2017,** *347*, 193-200.
184. Li, L.; Dai, Y.; Xu, Q.; Zhang, B.; Zhang, F.; You, Y.; Ma, D.; Li, S.-S.; Zhang, Y.-X., Interlayer expanded nickel-iron layered double hydroxide by intercalation with sodium dodecyl sulfate for enhanced oxygen evolution reaction. *J. Alloys Compd.* **2021,** *882*, 160752.
185. Nejati, K.; Akbari, A. R.; Davari, S.; Asadpour-Zeynali, K.; Rezvani, Z., Zn–Fe-layered double hydroxide intercalated with vanadate and molybdate anions for electrocatalytic water oxidation. *New J. Chem.* **2018,** *42* (4), 2889-2895.
186. Peng, L.; Yang, N.; Yang, Y.; Wang, Q.; Xie, X.; Sun-Waterhouse, D.; Shang, L.; Zhang, T.; Waterhouse, G. I., Atomic Cation-Vacancy Engineering of NiFe-Layered Double Hydroxides for Improved Activity and Stability towards the Oxygen Evolution Reaction. *Angew. Chem., Int. Ed.* **2021,** *60* (46), 24612-24619.
187. Fang, M.; Dong, G.; Wei, R.; Ho, J. C., Hierarchical nanostructures: design for sustainable water splitting. *Adv. Energy. Mater.* **2017,** *7* (23), 1700559.

188. Bodhankar, P. M.; Sarawade, P. B.; Singh, G.; Vinu, A.; Dhawale, D. S., Recent advances in highly active nanostructured NiFe LDH catalyst for electrochemical water splitting. *J. Mater. Chem. A* **2021,** *9* (6), 3180-3208.

189. Zhang, X.; Marianov, A. N.; Jiang, Y.; Cazorla, C.; Chu, D., Hierarchically constructed silver nanowire@ nickel–iron layered double hydroxide nanostructures for electrocatalytic water splitting. *ACS Appl. Nano Mater.* **2019,** *3* (1), 887-895.

190. Bhowmik, T.; Kundu, M. K.; Barman, S., CoFe layered double hydroxide supported on graphitic carbon nitrides: an efficient and durable bifunctional electrocatalyst for oxygen evolution and hydrogen evolution reactions. *ACS Appl. Energy Mater.* **2018,** *1* (3), 1200-1209.

191. Liu, J.; Wang, J.; Zhang, B.; Ruan, Y.; Lv, L.; Ji, X.; Xu, K.; Miao, L.; Jiang, J., Hierarchical NiCo2S4@ NiFe LDH heterostructures supported on nickel foam for enhanced overall-water-splitting activity. *ACS Appl. Mater. Interfaces* **2017,** *9* (18), 15364-15372.

192. Xu, H.; Wang, B.; Shan, C.; Xi, P.; Liu, W.; Tang, Y., Ce-doped NiFe-layered double hydroxide ultrathin nanosheets/nanocarbon hierarchical nanocomposite as an efficient oxygen evolution catalyst. *ACS Appl. Mater. Interfaces* **2018,** *10* (7), 6336-6345.

193. Liu, P. F.; Yang, S.; Zhang, B.; Yang, H. G., Defect-rich ultrathin cobalt–iron layered double hydroxide for electrochemical overall water splitting. *ACS Appl. Mater. Interfaces* **2016,** *8* (50), 34474-34481.

194. Bulmer, J. S.; Kaniyoor, A.; Elliott, J. A., A Meta-Analysis of Conductive and Strong Carbon Nanotube Materials. *Adv. Mater.* **2021,** *33* (36), 2008432.

195. Salah, L. S.; Ouslimani, N.; Bousba, D.; Huynen, I.; Danlée, Y.; Aksas, H., Carbon nanotubes (CNTs) from synthesis to functionalized (CNTs) using conventional and new chemical approaches. *J. Nanomater.* **2021,** *2021*, 1-31.

196. Rathinavel, S.; Priyadharshini, K.; Panda, D., A review on carbon nanotube: An overview of synthesis, properties, functionalization, characterization, and the application. *Mater. Sci. Eng. B.* **2021,** *268*, 115095.

197. Tang, J.; Salunkhe, R. R.; Liu, J.; Torad, N. L.; Imura, M.; Furukawa, S.; Yamauchi, Y., Thermal conversion of core–shell metal–organic frameworks: a

new method for selectively functionalized nanoporous hybrid carbon. *J. Am. Chem. Soc.* **2015,** *137* (4), 1572-1580.

198. Chai, L.; Zhang, L.; Wang, X.; Xu, L.; Han, C.; Li, T.-T.; Hu, Y.; Qian, J.; Huang, S., Bottom-up synthesis of MOF-derived hollow N-doped carbon materials for enhanced ORR performance. *Carbon* **2019,** *146*, 248-256.
199. Ji, K.; Xia, X.; Yue, Y.; Yang, P., Nanoarchitectonics with NiFe-layered double hydroxide decorated Co/Ni-carbon nanotubes for efficient oxygen evolution reaction electrocatalysis. *J. Electroanal. Chem.* **2022,** *920*, 116573.
200. Wang, H.; Yuan, Y.; Gu, J.; Jia, Z.; Lu, Z.; Bai, Z.; Yang, L.; Yang, X., Facile one-pot synthesis of layered double hydroxides nanosheets with oxygen vacancies grown on carbon nanotubes for efficient oxygen evolution reaction. *J. Power Sources.* **2020,** *467*, 228354.
201. Aulia, S.; Chen, K.-Y.; Chang, L.-Y.; Wang, Y.-X.; Rinawati, M.; Lin, M.-H.; Ho, K.-C.; Yeh, M.-H., Designing bifunctional ZIF-67 derivatives decorated N-doped carbon nanotubes as an electrocatalyst for oxygen conversion reaction in rechargeable zinc-air battery. *J. Taiwan Inst. Chem.* **2022,** *141*, 104598.
202. Dinari, M.; Allami, H.; Momeni, M. M., A high-performance electrode based on Ce-doped nickel-cobalt layered double hydroxide growth on carbon nanotubes for efficient oxygen evolution. *J. Electroanal. Chem.* **2020,** *877*, 114643.
203. Liu, H.; Zhou, J.; Wu, C.; Wang, C.; Zhang, Y.; Liu, D.; Lin, Y.; Jiang, H.; Song, L., Integrated flexible electrode for oxygen evolution reaction: layered double hydroxide coupled with single-walled carbon nanotubes film. *ACS Sustain. Chem. Eng.* **2018,** *6* (3), 2911-2915.
204. Chen, R.; Sun, G.; Yang, C.; Zhang, L.; Miao, J.; Tao, H.; Yang, H.; Chen, J.; Chen, P.; Liu, B., Achieving stable and efficient water oxidation by incorporating NiFe layered double hydroxide nanoparticles into aligned carbon nanotubes. *Nanoscale.* **2016,** *1* (2), 156-160.
205. Jia, G.; Hu, Y.; Qian, Q.; Yao, Y.; Zhang, S.; Li, Z.; Zou, Z., Formation of hierarchical structure composed of (Co/Ni) Mn-LDH nanosheets on MWCNT backbones for efficient electrocatalytic water oxidation. *ACS Appl. Mater. Interfaces.* **2016,** *8* (23), 14527-14534.

206. Wang, L.; Cao, J.; Cheng, X.; Lei, C.; Dai, Q.; Yang, B.; Li, Z.; Younis, M. A.; Lei, L.; Hou, Y., ZIF-derived carbon nanoarchitecture as a bifunctional pH-universal electrocatalyst for energy-efficient hydrogen evolution. *ACS Sustain. Chem. Eng.* **2019,** *7* (11), 10044-10051.

207. Shen, X. Q.; Xiang, K.; Fu, X.-Z.; Luo, J.-L., High active and ultra-stable bifunctional FeNi/CNT electrocatalyst for overall water splitting. *Int. J. Hydrog. Energy* **2021,** *46* (7), 5398-5402.

208. Gao, T.; Li, X.; Chen, X.; Zhou, C.; Yue, Q.; Yuan, H.; Xiao, D., Ultra-fast preparing carbon nanotube-supported trimetallic Ni, Ru, Fe heterostructures as robust bifunctional electrocatalysts for overall water splitting. *J. Chem. Eng.* **2021,** *424*, 130416.

209. Cossar, E.; Agarwal, K.; Nguyen, V. B.; Safari, R.; Botton, G. A.; Baranova, E. A., Highly active nickel–iron nanoparticles with and without ceria for the oxygen evolution reaction. *Electrocatalysis* **2021,** *12* (5), 605-618.

210. Yu, J.; Du, X.; Liu, H.; Qiu, C.; Yu, R.; Li, S.; Ren, J.; Yang, S., Mini review on active sites in Ce-based electrocatalysts for alkaline water splitting. *Energy & Fuels* **2021,** *35* (23), 19000-19011.

211. Shaghaghi, Z.; Jafari, S.; Mohammad-Rezaei, R., The heterostructure of ceria and hybrid transition metal oxides with high electrocatalytic performance for water splitting and enzyme-free glucose detection. *J. Electroanal. Chem.* **2022,** *915*, 116369.

212. Song, X. Z.; Zhu, W. Y.; Wang, X. F.; Tan, Z., Recent Advances of CeO_2-Based Electrocatalysts for Oxygen and Hydrogen Evolution as well as Nitrogen Reduction. *ChemElectroChem* **2021,** *8* (6), 996-1020.

213. Chen, H.; Hu, M.; Jing, P.; Liu, B.; Gao, R.; Zhang, J., Constructing heterostructure of CeO_2/WS_2 to enhance catalytic activity and stability toward hydrogen generation. *J. Power Sources* **2022,** *521*, 230948.

214. Li, S.; Xu, Z.; Zhou, L.; Li, D.; Nan, B.; Dou, X.; Zhang, J.; Zeng, J.; Yu, L., Porous CeO_2/Ni-Cu composite catalyst for electrocatalytic hydrogen evolution in alkaline medium. *J. Electroanal. Chem.* **2021,** *898*, 115640.

215. Sha, W.; Song, Y.; Liu, P.; Wang, J.; Xu, B.; Feng, X.; Guo, J., Constructing multiple heterostructures on nickel oxide using rare-earth oxide and nickel as

efficient bifunctional electrocatalysts for overall water splitting. *ChemCatChem* **2022,** *14* (13), e202101975.

216. Zhao, M.; Dong, H.; Chen, Z.; Ma, Z.; Wang, L.; Wang, G.; Yang, W.; Shao, G., Study of Ni–S/CeO_2 composite material for hydrogen evolution reaction in alkaline solution. *Int. J. Hydrog. Energy* **2016,** *41* (45), 20485-20493.
217. Sung, M.-C.; Lee, G.-H.; Kim, D.-W., CeO_2/$Co(OH)_2$ hybrid electrocatalysts for efficient hydrogen and oxygen evolution reaction. *J. Alloys Compd.* **2019,** *800*, 450-455.
218. Wang, X.; Yang, Y.; Diao, L.; Tang, Y.; He, F.; Liu, E.; He, C.; Shi, C.; Li, J.; Sha, J., CeO x-decorated NiFe-layered double hydroxide for efficient alkaline hydrogen evolution by oxygen vacancy engineering. *ACS Appl. Mater. Interfaces.* **2018,** *10* (41), 35145-35153.
219. Mathew, S.; Hosseinirad, E.; Kim, K. C.; Chung, W. S.; Li, O. L.; Cho, Y.-R., Enhanced electrocatalytic water splitting by Sm and Gd-doped ceria electrocatalysts on Ni foam substrate. *Electrochim. Acta* **2022,** *435*, 141382.
220. Zhao, M.; Li, Y.; Dong, H.; Wang, L.; Chen, Z.; Wang, Y.; Li, Z.; Xia, M.; Shao, G., The effects of CeO_2 nanorods and CeO_2 nanoflakes on Ni–S alloys in hydrogen evolution reactions in alkaline solutions. *Catalysts* **2017,** *7* (7), 197.
221. Hu, Y.; Liu, W.; Jiang, K.; Xu, L.; Guan, M.; Bao, J.; Ji, H.; Li, H., Constructing a CeO_{2-x}@ CoFe-layered double hydroxide heterostructure as an improved electrocatalyst for highly efficient water oxidationsss. *Inorg. Chem. Front.* **2020,** *7* (22), 4461-4468.
222. Wang, B.; Xi, P.; Shan, C.; Chen, H.; Xu, H.; Iqbal, K.; Liu, W.; Tang, Y., In situ growth of ceria on cerium–nitrogen–carbon as promoter for oxygen evolution reaction. *Adv. Mater. Interfaces* **2017,** *4* (13), 1700272.
223. Zhang, X.; Qiu, Y.; Li, Q.; Liu, F.; Ji, X.; Liu, J., Facile construction of heterostructural Ni_3 $(NO_3)_2$ $(OH)_4$/CeO_2 bifunctional catalysts for boosted overall water splitting. *Int. J. Hydrog. Energy* **2022,** *47* (55), 23221-23229.
224. Zhao, D.; Pi, Y.; Shao, Q.; Feng, Y.; Zhang, Y.; Huang, X., Enhancing oxygen evolution electrocatalysis via the intimate hydroxide–oxide interface. *ACS Nano* **2018,** *12* (6), 6245-6251.

225. Li, J.; Xia, Z.; Xue, Q.; Zhang, M.; Zhang, S.; Xiao, H.; Ma, Y.; Qu, Y., Insights into the Interfacial Lewis Acid–Base Pairs in CeO_2-Loaded CoS_2 Electrocatalysts for Alkaline Hydrogen Evolution. *Small* **2021,** *17* (39), 2103018.

226. Wang, Z.; Du, H.; Liu, Z.; Wang, H.; Asiri, A. M.; Sun, X., Interface engineering of a CeO_2–Cu_3P nanoarray for efficient alkaline hydrogen evolution. *Nanoscale* **2018,** *10* (5), 2213-2217.

227. Wang, C.; Lv, X.; Zhou, P.; Liang, X.; Wang, Z.; Liu, Y.; Wang, P.; Zheng, Z.; Dai, Y.; Li, Y., Molybdenum nitride electrocatalysts for hydrogen evolution more efficient than platinum/carbon: Mo_2N/CeO_2@ nickel foam. *ACS Appl. Energy Mater.* **2020,** *12* (26), 29153-29161.

228. Long, X.; Lin, H.; Zhou, D.; An, Y.; Yang, S., Enhancing full water-splitting performance of transition metal bifunctional electrocatalysts in alkaline solutions by tailoring CeO_2–transition metal oxides–Ni nanointerfaces. *ACS Energy Lett.* **2018,** *3* (2), 290-296.

229. Yang, L.; Liu, R.; Jiao, L., Electronic redistribution: construction and modulation of interface engineering on CoP for enhancing overall water splitting. *Adv. Funct. Mater.* **2020,** *30* (14), 1909618.

230. Trovarelli, A.; Llorca, J., Ceria catalysts at nanoscale: how do crystal shapes shape catalysis? *ACS Catal.* **2017,** *7* (7), 4716-4735.

231. Li, S.; Xu, Z.; Zhou, L.; Li, D.; Nan, B.; Dou, X.; Zhang, J.; Zeng, J.; Yu, L., Porous CeO2/Ni-Cu composite catalyst for electrocatalytic hydrogen evolution in alkaline medium. *J. Electroanal. Chem.* **2021,** *898*, 115640.

232. Sun, H.; Tian, C.; Li, Y.; Wu, J.; Wang, Q.; Yan, Z.; Li, C. P.; Cheng, F.; Du, M., Coupling NiCo alloy and CeO_2 to enhance electrocatalytic hydrogen evolution in alkaline solution. *Adv. Sustain. Syst.* **2020,** *4* (11), 2000122.

233. Long, X.; Wang, Z.; Xiao, S.; An, Y.; Yang, S., Transition metal based layered double hydroxides tailored for energy conversion and storage. *Mater. Today.* **2016,** *19* (4), 213-226.

234. Shi, R.; Wang, J.; Wang, Z.; Li, T.; Song, Y.-F., Unique $NiFeNiCoO_2$ hollow polyhedron as bifunctional electrocatalysts for water splitting. *J. Energy Chem.* **2019,** *33*, 74-80.

235. Li, S.; Wang, L.; Su, H.; Hong, A. N.; Wang, Y.; Yang, H.; Ge, L.; Song, W.; Liu, J.; Ma, T., Electron Redistributed S-Doped Nickel Iron Phosphides Derived from One-Step Phosphatization of MOFs for Significantly Boosting Electrochemical Water Splitting. *Adv. Funct. Mater.* **2022**, 2200733.

236. Li, L.; Guo, Y.; Wang, X.; Liu, X.; Lu, Y., Ultraeven Mo-Doped CoP Nanocrystals as Bifunctional Electrocatalyst for Efficient Overall Water Splitting. *Langmuir* **2021,** *37* (19), 5986-5992.

237. Jia, X.; Zhao, Y.; Chen, G.; Shang, L.; Shi, R.; Kang, X.; Waterhouse, G. I.; Wu, L. Z.; Tung, C. H.; Zhang, T., Ni_3FeN nanoparticles derived from ultrathin NiFe-layered double hydroxide nanosheets: an efficient overall water splitting electrocatalyst. *Adv. Energy. Mater.* **2016,** *6* (10), 1502585.

238. Xiao, K.; Zhou, L.; Shao, M.; Wei, M., Fabrication of $(Ni, Co)_{0.85}Se$ nanosheet arrays derived from layered double hydroxides toward largely enhanced overall water splitting. *J. Mater. Chem. A* **2018,** *6* (17), 7585-7591.

239. Du, J.; Zou, Z.; Liu, C.; Xu, C., Hierarchical Fe-doped Ni 3 Se 4 ultrathin nanosheets as an efficient electrocatalyst for oxygen evolution reaction. *Nanoscale* **2018,** *10* (11), 5163-5170.

240. Karmakar, A.; Krishnan, A. V.; Jayan, R.; Madhu, R.; Islam, M. M.; Kundu, S., Structural modulation of low-valent iron in LDH-derived Ni_3Se_4 nanosheets: a breakthrough electrocatalyst for the overall water splitting reaction. *J. Mater. Chem. A* . **2023,** *11* (20), 10684-10698.

241. Zhou, H.; Zhang, D.; Dong, W.; Zhou, C.; Jiang, T.; Liu, Y.; Tian, C.; Liu, Y.; Liu, Y.; Mao, B., Stainless steel mesh-based $CoSe/Ni_3Se_4$ heterostructure for efficient electrocatalytic overall water splitting. *Int. J. Hydrog. Energy* **2023,** *48* (39), 14554-14564.

242. Zhao, X.; Li, X.; Yan, Y.; Xing, Y.; Lu, S.; Zhao, L.; Zhou, S.; Peng, Z.; Zeng, J., Electrical and structural engineering of cobalt selenide nanosheets by Mn modulation for efficient oxygen evolution. *Appl. Catal. B: Environ.* **2018,** *236*, 569-575.

243. Zhang, M.; Ma, X.; Zhong, H.; Yang, J.; Cao, Z., Morphology reconstruction and electronic optimization: Nickel-iron selenide nanospheres with Mo-doping as an efficient bifunctional electrocatalyst for overall water splitting. *J. Alloys Compd.* **2023,** *935*, 168135.

244. Huang, Y.; Jiang, L.-W.; Liu, X.-L.; Tan, T.; Liu, H.; Wang, J.-J., Precisely engineering the electronic structure of active sites boosts the activity of iron-nickel selenide on nickel foam for highly efficient and stable overall water splitting. *Appl. Catal. B: Environ.* **2021,** *299*, 120678.

245. Ali, Z.; Mehmood, M.; Aslam, M.; Haider, M. A., In-situ grown nickel-cobalt (NiCo) alloy nanoparticles decorated on petal-like nitrogen-doped carbon spheres for efficient OER activity. *ChemistrySelect* **2022,** *7* (11), e202200196.

246. Lei, Y.; Zhang, L.; Zhou, D.; Xiong, C.; Zhao, Y.; Chen, W.; Xiang, X.; Shang, H.; Zhang, B., Construction of interconnected NiO/CoFe alloy nanosheets for overall water splitting. *Renew. Energy* **2022,** *194*, 459-468.

247. Patil, R.; Rajput, A.; Kumar, N.; Agrawal, O.; Ujihara, M.; Salunkhe, R. R.; Chakraborty, B.; Dutta, S., Ultrafine Bimetallic Nickel–Cobalt Alloy from a Layered Hydroxide for Oxygen Evolution Reaction and Capacitors. *ACS Appl. Eng. Mater.* **2023**.

248. Gao, W.; Zhao, Y.; Chen, H.; Chen, H.; Li, Y.; He, S.; Zhang, Y.; Wei, M.; Evans, D. G.; Duan, X., Core–shell Cu@(CuCo-alloy)/Al_2O_3 catalysts for the synthesis of higher alcohols from syngas. *Green Chem.* **2015,** *17* (3), 1525-1534.

249. Liu, C.; Guo, Y.; Yu, Z.; Wang, H.; Yao, H.; Li, J.; Shi, K.; Ma, S., Hierarchical microsphere assembled by nanoplates embedded with MoS2 and (NiFe) Sx nanoparticles as low-cost electrocatalyst for hydrogen evolution reaction. *Nanotechnology* **2019,** *31* (3), 035403.

250. Long, X.; Li, G.; Wang, Z.; Zhu, H.; Zhang, T.; Xiao, S.; Guo, W.; Yang, S., Metallic iron–nickel sulfide ultrathin nanosheets as a highly active electrocatalyst for hydrogen evolution reaction in acidic media. *J. Am. Chem. Soc.* **2015,** *137* (37), 11900-11903.

251. Barton, B. E.; Whaley, C. M.; Rauchfuss, T. B.; Gray, D. L., Nickel− iron dithiolato hydrides relevant to the [NiFe]-hydrogenase active site. *J. Am. Chem. Soc.* **2009,** *131* (20), 6942-6943.

252. Li, S.; Gao, Y.; Li, N.; Ge, L.; Bu, X.; Feng, P., Transition metal-based bimetallic MOFs and MOF-derived catalysts for electrochemical oxygen evolution reaction. *Energ. Environ. Sci.* **2021,** *14* (4), 1897-1927.

253. Cai, M.; Liu, Q.; Xue, Z.; Li, Y.; Fan, Y.; Huang, A.; Li, M.-R.; Croft, M.; Tyson, T. A.; Ke, Z., Constructing 2D MOFs from 2D LDHs: a highly efficient and durable electrocatalyst for water oxidation. *J. Mater. Chem.* **2020,** *8* (1), 190-195.

254. Yang, L.; Zhu, G.; Wen, H.; Guan, X.; Sun, X.; Feng, H.; Tian, W.; Zheng, D.; Cheng, X.; Yao, Y., Constructing a highly oriented layered MOF nanoarray from a layered double hydroxide for efficient and long-lasting alkaline water oxidation electrocatalysis. *J. Mater. Chem. A* **2019,** *7* (15), 8771-8776.

255. Li, Z.; Niu, W.; Zhou, L.; Yang, Y., Phosphorus and aluminum codoped porous NiO nanosheets as highly efficient electrocatalysts for overall water splitting. *ACS Energy Lett.* **2018,** *3* (4), 892-898.

256. Xie, J.; Zhang, X.; Zhang, H.; Zhang, J.; Li, S.; Wang, R.; Pan, B.; Xie, Y., Intralayered Ostwald Ripening to Ultrathin Nanomesh Catalyst with Robust Oxygen-Evolving Performance. *Adv. Mater.* **2017,** *29* (10).

257. Liang, H.; Li, L.; Meng, F.; Dang, L.; Zhuo, J.; Forticaux, A.; Wang, Z.; Jin, S., Porous two-dimensional nanosheets converted from layered double hydroxides and their applications in electrocatalytic water splitting. *Chem. Mater.* **2015,** *27* (16), 5702-5711.

258. Long, X.; Ma, Z.; Yu, H.; Gao, X.; Pan, X.; Chen, X.; Yang, S.; Yi, Z., Porous FeNi oxide nanosheets as advanced electrochemical catalysts for sustained water oxidation. *J. Mater. Chem.* **2016,** *4* (39), 14939-14943.

259. Zhao, Y.; Jia, X.; Chen, G.; Shang, L.; Waterhouse, G. I.; Wu, L.-Z.; Tung, C.-H.; O'Hare, D.; Zhang, T., Ultrafine NiO nanosheets stabilized by TiO_2 from monolayer NiTi-LDH precursors: an active water oxidation electrocatalyst. *J. Am. Chem. Soc.* **2016,** *138* (20), 6517-6524.

260. Li, Y.; He, H.; Fu, W.; Mu, C.; Tang, X.-Z.; Liu, Z.; Chi, D.; Hu, X., In-grown structure of NiFe mixed metal oxides and CNT hybrid catalysts for oxygen evolution reaction. *Chemcomm.* **2016,** *52* (7), 1439-1442.

261. Han, X.; Yu, C.; Zhou, S.; Zhao, C.; Huang, H.; Yang, J.; Liu, Z.; Zhao, J.; Qiu, J., Ultrasensitive iron-triggered nanosized Fe–CoOOH integrated with graphene for highly efficient oxygen evolution. *Adv. Energy. Mater.* **2017,** *7* (14), 1602148.

262. Zhou, P.; Zhai, G.; Lv, X.; Liu, Y.; Wang, Z.; Wang, P.; Zheng, Z.; Cheng, H.; Dai, Y.; Huang, B., Boosting the electrocatalytic HER performance of Ni_3N-V_2O_3 via the interface coupling effect. *Appl. Catal. B Environ* **2021,** *283*, 119590.

263. Wang, Y.; Xie, C.; Liu, D.; Huang, X.; Huo, J.; Wang, S., Nanoparticle-stacked porous nickel–iron nitride nanosheet: a highly efficient bifunctional electrocatalyst for overall water splitting. *ACS Appl. Mater. Interfaces* **2016,** *8* (29), 18652-18657.

264. Liu, Y.; Li, Y.; Wu, Q.; Su, Z.; Wang, B.; Chen, Y.; Wang, S., Hollow CoP/FeP_4 Heterostructural nanorods interwoven by CNT as a highly efficient electrocatalyst for oxygen evolution reactions. *Nanomater.* **2021,** *11* (6), 1450.

265. Li, H.; Xu, S.-M.; Li, Y.; Yan, H.; Xu, S., An in situ phosphorization strategy towards doped Co_2P scaffolded within echinus-like carbon for overall water splitting. *Nanoscale* **2020,** *12* (37), 19253-19258.

266. Wang, J.; Chen, C.; Cai, N.; Wang, M.; Li, H.; Yu, F., High topological tri-metal phosphide of CoP@ FeNiP toward enhanced activities in oxygen evolution reaction. *Nanoscale* **2021,** *13* (2), 1354-1363.

267. Zhou, L.; Jiang, S.; Liu, Y.; Shao, M.; Wei, M.; Duan, X., Ultrathin CoNiP@ layered double hydroxides core–shell nanosheets arrays for largely enhanced overall water splitting. *ACS Appl. Energy Mater.* **2018,** *1* (2), 623-631.

268. He, K.; Tadesse Tsega, T.; Liu, X.; Zai, J.; Li, X. H.; Liu, X.; Li, W.; Ali, N.; Qian, X., Utilizing the Space-Charge Region of the FeNi-LDH/CoP P-n Junction to Promote Performance in Oxygen Evolution Electrocatalysis. *Angew. Chem., Int. Ed.* **2019,** *58* (34), 11903-11909.

269. Tang, C.; Zhang, R.; Lu, W.; He, L.; Jiang, X.; Asiri, A. M.; Sun, X., Fe-doped CoP nanoarray: a monolithic multifunctional catalyst for highly efficient hydrogen generation. *Adv. Mater.* **2017,** *29* (2), 1602441.

270. Zhang, B.; Lui, Y. H.; Ni, H.; Hu, S., Bimetallic (Fe_xNi_{1-x}) 2P nanoarrays as exceptionally efficient electrocatalysts for oxygen evolution in alkaline and neutral media. *Nano Energy* **2017,** *38*, 553-560.

271. Liang, H.; Gandi, A. N.; Anjum, D. H.; Wang, X.; Schwingenschlögl, U.; Alshareef, H. N., Plasma-assisted synthesis of NiCoP for efficient overall water splitting. *Nano Lett.* **2016,** *16* (12), 7718-7725.

272. Li, P.; Zeng, H. C., Bimetallic Ni–Fe phosphide nanocomposites with a controlled architecture and composition enabling highly efficient electrochemical water oxidation. *J. Mater. Chem.* **2018,** *6* (5), 2231-2238.

273. Wang, J.; Ma, X.; Qu, F.; Asiri, A. M.; Sun, X., Fe-doped Ni_2P nanosheet array for high-efficiency electrochemical water oxidation. *Inorg. Chem.* **2017,** *56* (3), 1041-1044.

274. Li, X.; Li, S.; Yoshida, A.; Sirisomboonchai, S.; Tang, K.; Zuo, Z.; Hao, X.; Abudula, A.; Guan, G., Mn doped CoP nanoparticle clusters: an efficient electrocatalyst for hydrogen evolution reaction. *Catal. Sci. Tech.* **2018,** *8* (17), 4407-4412.

275. Zhou, L.; Shao, M.; Li, J.; Jiang, S.; Wei, M.; Duan, X., Two-dimensional ultrathin arrays of CoP: electronic modulation toward high performance overall water splitting. *Nano Energy* **2017,** *41*, 583-590.

276. Liu, C.; Guo, Y.; Yu, Z.; Wang, H.; Yao, H.; Li, J.; Shi, K.; Ma, S., Hierarchical microsphere assembled by nanoplates embedded with MoS_2 and (NiFe) Sx nanoparticles as low-cost electrocatalyst for hydrogen evolution reaction. *Nanotechnol.* **2019,** *31* (3), 035403.

277. Li, D.; Liu, Z.; Wang, J.; Liu, B.; Qin, Y.; Yang, W.; Liu, J., Hierarchical trimetallic sulfide $FeCo_2S_4$–$NiCo_2S_4$ nanosheet arrays supported on a Ti mesh: An efficient 3D bifunctional electrocatalyst for full water splitting. *Electrochim. Acta* **2020,** *340*, 135957.

278. Xu, X.; Zhong, W.; Yan, S.; Zhang, L.; Liu, G.; Du, Y., Advanced catalysts for hydrogen evolution reaction based on MoS_2/$NiCo_2S_4$ heterostructures in Alkaline Media. *Int. J. Hydrog. Energy* **2020,** *45* (3), 1759-1768.

279. Luan, X.; Du, H.; Kong, Y.; Qu, F.; Lu, L., A novel FeS–NiS hybrid nanoarray: an efficient and durable electrocatalyst for alkaline water oxidation. *Chemcomm.* **2019,** *55* (51), 7335-7338.

280. Qin, K.; Wang, L.; Wen, S.; Diao, L.; Liu, P.; Li, J.; Ma, L.; Shi, C.; Zhong, C.; Hu, W., Designed synthesis of NiCo-LDH and derived sulfide on heteroatom-doped edge-enriched 3D rivet graphene films for high-performance asymmetric supercapacitor and efficient OER. *J. Mater. Chem.* **2018,** *6* (17), 8109-8119.

281. Zeng, Y.; Chen, L.; Chen, R.; Wang, Y.; Xie, C.; Tao, L.; Huang, L.; Wang, S., One-step, room temperature generation of porous and amorphous cobalt hydroxysulfides from layered double hydroxides for superior oxygen evolution reactions. *J. Mater. Chem.* **2018,** *6* (47), 24311-24316.

282. Xiao, K.; Zhou, L.; Shao, M.; Wei, M., Fabrication of $(Ni, Co)_{0.85}Se$ nanosheet arrays derived from layered double hydroxides toward largely enhanced overall water splitting. *J. Mater. Chem.* **2018,** *6* (17), 7585-7591.

283. Du, J.; Zou, Z.; Liu, C.; Xu, C., Hierarchical Fe-doped Ni_3Se_4 ultrathin nanosheets as an efficient electrocatalyst for oxygen evolution reaction. *Nanoscale* **2018,** *10* (11), 5163-5170.

284. Xu, X.; Song, F.; Hu, X., A nickel iron diselenide-derived efficient oxygen-evolution catalyst. *Nat. Commun.* **2016,** *7* (1), 12324.

285. Wang, Z.; Li, J.; Tian, X.; Wang, X.; Yu, Y.; Owusu, K. A.; He, L.; Mai, L., Porous nickel–iron selenide nanosheets as highly efficient electrocatalysts for oxygen evolution reaction. *ACS Appl. Mater. Interfaces* **2016,** *8* (30), 19386-19392.

286. Yu, J.; Cheng, G.; Luo, W., 3D mesoporous rose-like nickel-iron selenide microspheres as advanced electrocatalysts for the oxygen evolution reaction. *Nano Research* **2018,** *11*, 2149-2158.

287. Yang, L.; Zhu, G.; Wen, H.; Guan, X.; Sun, X.; Feng, H.; Tian, W.; Zheng, D.; Cheng, X.; Yao, Y., Constructing a highly oriented layered MOF nanoarray from a layered double hydroxide for efficient and long-lasting alkaline water oxidation electrocatalysis. *J. Mater. Chem.* **2019,** *7* (15), 8771-8776.

288. Xiang, M.-H.; Lu, C.; Xia, L.; Zhang, W.; Jiang, J.-H.; Qu, F.; Lu, L., In situ conversion of layered double hydroxide arrays into nanoflowers of Ni_xV_{1-x}-MOF as a highly efficient and stable electrocatalyst for the oxygen evolution reaction. *Catal. Sci. Technol.* **2020,** *10* (14), 4509-4512.

289. Anantharaj, S.; Karthick, K.; Kundu, S., Evolution of layered double hydroxides (LDH) as high performance water oxidation electrocatalysts: A review with insights on structure, activity and mechanism. *Mater. Today Energy.* **2017,** *6*, 1-26.

290. Anantharaj, S.; Ede, S. R.; Sakthikumar, K.; Karthick, K.; Mishra, S.; Kundu, S., Recent trends and perspectives in electrochemical water splitting with an

emphasis on sulfide, selenide, and phosphide catalysts of Fe, Co, and Ni: a review. *ACS Catal.* **2016,** *6* (12), 8069-8097.

291. Anantharaj, S.; Ede, S.; Karthick, K.; Sankar, S. S.; Sangeetha, K.; Karthik, P.; Kundu, S., Precision and correctness in the evaluation of electrocatalytic water splitting: revisiting activity parameters with a critical assessment. *Energy Environ. Sci.* **2018,** *11* (4), 744-771.
292. Raveendran, A.; Chandran, M.; Dhanusuraman, R., A comprehensive review on the electrochemical parameters and recent material development of electrochemical water splitting electrocatalysts. *RSC Adv.* **2023,** *13* (6), 3843-3876.
293. Li, S.; Li, E.; An, X.; Hao, X.; Jiang, Z.; Guan, G., Transition metal-based catalysts for electrochemical water splitting at high current density: current status and perspectives. *Nanoscale* **2021,** *13* (30), 12788-12817.
294. Wu, J.; Yu, Z.; Zhang, Y.; Niu, S.; Zhao, J.; Li, S.; Xu, P., Understanding the effect of second metal on CoM (M= Ni, Cu, Zn) metal–organic frameworks for electrocatalytic oxygen evolution reaction. *Small* **2021,** *17* (51), 2105150.
295. Karmakar, A.; Karthick, K.; Sankar, S. S.; Kumaravel, S.; Madhu, R.; Kundu, S., A vast exploration of improvising synthetic strategies for enhancing the OER kinetics of LDH structures: a review. *J. Mater. Chem. A* . **2021,** *9* (3), 1314-1352.
296. Wei, C.; Xu, Z. J., The comprehensive understanding of as an evaluation parameter for electrochemical water splitting. Wiley Online Library: 2018; Vol. 2, p 1800168.
297. Wang, Q. M.; Shen, D.; Bülow, M.; Lau, M. L.; Deng, S.; Fitch, F. R.; Lemcoff, N. O.; Semanscin, J., Metallo-organic molecular sieve for gas separation and purification. *MICROPOR MESOPOR MAT.* **2002,** *55* (2), 217-230.
298. Shaghaghi, Z.; Jafari, S.; Mohammad-Rezaei, R., The heterostructure of ceria and hybrid transition metal oxides with high electrocatalytic performance for water splitting and enzyme-free glucose detection. *J. Electroanal. Chem* **2022,** *915*, 116369.

299. Dey, S.; Dhal, G. C., Catalytic conversion of carbon monoxide into carbon dioxide over spinel catalysts: an overview. *Mater. Sci. Technol.* **2019,** *2* (3), 575-588.

300. He, M.; Yao, J.; Liu, Q.; Zhong, Z.; Wang, H., Toluene-assisted synthesis of RHO-type zeolitic imidazolate frameworks: synthesis and formation mechanism of ZIF-11 and ZIF-12. *Dalton Trans.* **2013,** *42* (47), 16608-16613.

301. Nasim, F.; Ali, H.; Waseem, A.; Nadeem, M. A.; Nadeem, M. A., Confinement of CoOx-CoP nanoparticles inside nitrogen doped CNTs: A low-cost ORR electrocatalyst. *Int. J. Hydrog. Energy* **2022,** *47* (94), 39898-39907.

302. Valente, J. S.; Lima, E.; Toledo-Antonio, J. A.; Cortes-Jacome, M. A.; Lartundo-Rojas, L.; Montiel, R.; Prince, J., Comprehending the thermal decomposition and reconstruction process of sol− gel MgAl layered double hydroxides. *J. Phys. Chem. A* **2010,** *114* (5), 2089-2099.

303. Tuncel, D.; Ökte, A., ZnO@ CuO derived from Cu-BTC for efficient UV-induced photocatalytic applications. *Catal. Today* **2019,** *328*, 149-156.

304. Zhang, R.; Hu, L.; Bao, S.; Li, R.; Gao, L.; Li, R.; Chen, Q., Surface polarization enhancement: high catalytic performance of $Cu/CuO_x/C$ nanocomposites derived from Cu-BTC for CO oxidation. *J. Mater. Chem. A* **2016,** *4* (21), 8412-8420.

305. Hu, L.; Huang, Y.; Zhang, F.; Chen, Q., CuO/Cu_2O composite hollow polyhedrons fabricated from metal–organic framework templates for lithium-ion battery anodes with a long cycling life. *Nanoscale* **2013,** *5* (10), 4186-4190.

306. Yang, Y.; Dong, H.; Wang, Y.; He, C.; Wang, Y.; Zhang, X., Synthesis of octahedral like Cu-BTC derivatives derived from MOF calcined under different atmosphere for application in CO oxidation. *J. Solid Stat. Chem.* **2018,** *258*, 582-587.

307. He, P.; Fang, Y.; Yu, X. Y.; Lou, X. W., Hierarchical nanotubes constructed by carbon-coated ultrathin SnS nanosheets for fast capacitive sodium storage. *Angew. Chem., Int. Ed.* **2017,** *56* (40), 12202-12205.

308. Bloor, L. G.; Molina, P. I.; Symes, M. D.; Cronin, L., Low pH electrolytic water splitting using earth-abundant metastable catalysts that self-assemble in situ. *J. Am. Chem. Soc.* **2014,** *136* (8), 3304-3311.

309. Zeng, Z.; Chan, M. K.; Zhao, Z.-J.; Kubal, J.; Fan, D.; Greeley, J., Towards first principles-based prediction of highly accurate electrochemical Pourbaix diagrams. *J. Phys. Chem. C* **2015,** *119* (32), 18177-18187.

310. Gao, M.-R.; Xu, Y.-F.; Jiang, J.; Zheng, Y.-R.; Yu, S.-H., Water oxidation electrocatalyzed by an efficient Mn_3O_4/$CoSe_2$ nanocomposite. *J. Am. Chem. Soc.* **2012,** *134* (6), 2930-2933.

311. Kanan, M. W.; Yano, J.; Surendranath, Y.; Dinca, M.; Yachandra, V. K.; Nocera, D. G., Structure and valency of a cobalt− phosphate water oxidation catalyst determined by in situ X-ray spectroscopy. *J. Am. Chem. Soc.* **2010,** *132* (39), 13692-13701.

312. Yeo, B. S.; Bell, A. T., Enhanced activity of gold-supported cobalt oxide for the electrochemical evolution of oxygen. *J. Am. Chem. Soc.* **2011,** *133* (14), 5587-5593.

313. Chen, J.; Selloni, A., First principles study of cobalt (hydr) oxides under electrochemical conditions. *J. Phys. Chem. C* **2013,** *117* (39), 20002-20006.

314. Su, H.-Y.; Gorlin, Y.; Man, I. C.; Calle-Vallejo, F.; Nørskov, J. K.; Jaramillo, T. F.; Rossmeisl, J., Identifying active surface phases for metal oxide electrocatalysts: a study of manganese oxide bi-functional catalysts for oxygen reduction and water oxidation catalysis. *Phys. Chem. Chem. Phys.* **2012,** *14* (40), 14010-14022.

315. Mattioli, G.; Giannozzi, P.; Amore Bonapasta, A.; Guidoni, L., Reaction pathways for oxygen evolution promoted by cobalt catalyst. *J. Am. Chem. Soc.* **2013,** *135* (41), 15353-15363.

316. Agote-Arán, M.; Lezcano-González, I.; Greenaway, A. G.; Hayama, S.; Díaz-Moreno, S.; Kroner, A. B.; Beale, A. M., Operando HERFD-XANES/XES studies reveal differences in the activity of Fe-species in MFI and CHA structures for the standard selective catalytic reduction of NO with NH_3. *Appl. Catal. A* **2019,** *570*, 283-291.

317. Kundu, M. K.; Mishra, R.; Bhowmik, T.; Kanrar, S.; Barman, S., Three-dimensional hierarchically porous iridium oxide-nitrogen doped carbon hybrid: An efficient bifunctional catalyst for oxygen evolution and hydrogen evolution reaction in acid. *Int. J. Hydrog. Energy* **2020,** *45* (11), 6036-6046.

318. Jia, G.; Hu, Y.; Qian, Q.; Yao, Y.; Zhang, S.; Li, Z.; Zou, Z., Formation of hierarchical structure composed of (Co/Ni) Mn-LDH nanosheets on MWCNT backbones for efficient electrocatalytic water oxidation. *ACS Appl. Mater. Interfaces* **2016,** *8* (23), 14527-14534.

319. Tang, D.; Liu, J.; Wu, X.; Liu, R.; Han, X.; Han, Y.; Huang, H.; Liu, Y.; Kang, Z., Carbon quantum dot/NiFe layered double-hydroxide composite as a highly efficient electrocatalyst for water oxidation. *ACS Appl. Mater. Interfaces* **2014,** *6* (10), 7918-7925.

320. Yu, L.; Zhou, H.; Sun, J.; Qin, F.; Luo, D.; Xie, L.; Yu, F.; Bao, J.; Li, Y.; Yu, Y., Hierarchical Cu@ CoFe layered double hydroxide core-shell nanoarchitectures as bifunctional electrocatalysts for efficient overall water splitting. *Nano Energy* **2017,** *41*, 327-336.

321. Wang, Y.; Zhang, Y.; Liu, Z.; Xie, C.; Feng, S.; Liu, D.; Shao, M.; Wang, S., Layered double hydroxide nanosheets with multiple vacancies obtained by dry exfoliation as highly efficient oxygen evolution electrocatalysts. *Angew. Chem., Int. Ed.* **2017,** *56* (21), 5867-5871.

322. Arif, M.; Yasin, G.; Shakeel, M.; Mushtaq, M. A.; Ye, W.; Fang, X.; Ji, S.; Yan, D., Hierarchical CoFe-layered double hydroxide and gC_3N_4 heterostructures with enhanced bifunctional photo/electrocatalytic activity towards overall water splitting. *Mater. Chem. Front.* **2019,** *3* (3), 520-531.

323. Yan, Z.; Liu, H.; Hao, Z.; Yu, M.; Chen, X.; Chen, J., Electrodeposition of (hydro) oxides for an oxygen evolution electrode. *Chem. Sci.* **2020,** *11* (39), 10614-10625.

324. Liu, B.; Cheng, J.; Peng, H.-Q.; Chen, D.; Cui, X.; Shen, D.; Zhang, K.; Jiao, T.; Li, M.; Lee, C.-S., In situ nitridated porous nanosheet networked Co_3O_4–Co_4 N heteronanostructures supported on hydrophilic carbon cloth for highly efficient electrochemical hydrogen evolution. *J. Mater. Chem.* **2019,** *7* (2), 775-782.

325. AlKhoori, A. A.; Polychronopoulou, K.; Belabbes, A.; Abi Jaoude, M.; Vega, L. F.; Sebastian, V.; Hinder, S.; Baker, M. A.; Zedan, A. F., Cu, Sm co-doping effect on the CO oxidation activity of CeO_2. A combined experimental and density functional study. *Appl. Surf. Sci.* **2020,** *521*, 146305.

326. Malavasi, L.; Fisher, C. A.; Islam, M. S., Oxide-ion and proton conducting electrolyte materials for clean energy applications: structural and mechanistic features. *Chem. Soc. Rev.* **2010,** *39* (11), 4370-4387.

327. Yu, J.; Wang, Z.; Wang, J.; Zhong, W.; Ju, M.; Cai, R.; Qiu, C.; Long, X.; Yang, S., The Role of Ceria in a Hybrid Catalyst toward Alkaline Water Oxidation. *ChemSusChem* **2020,** *13* (19), 5273-5279.

328. Zhang, Q.; Bu, J.; Wang, J.; Sun, C.; Zhao, D.; Sheng, G.; Xie, X.; Sun, M.; Yu, L., Highly efficient hydrogenation of nitrobenzene to aniline over Pt/CeO_2 catalysts: the shape effect of the support and key role of additional Ce^{3+} sites. *ACS Catal.* **2020,** *10* (18), 10350-10363.

329. Li, Q.; Song, L.; Liang, Z.; Sun, M.; Wu, T.; Huang, B.; Luo, F.; Du, Y.; Yan, C.-H., A review on CeO_2-based electrocatalyst and photocatalyst in energy conversion. *Adv. Energy. Sust. Research* **2021,** *2* (2), 2000063.

330. Li, P.-H.; Song, Z.-Y.; Yang, M.; Chen, S.-H.; Xiao, X.-Y.; Duan, W.; Li, L.-N.; Huang, X.-J., Electrons in oxygen vacancies and oxygen atoms activated by Ce^{3+}/Ce^{4+} promote high-sensitive electrochemical detection of Pb(II) over Ce-doped α-MoO_3 catalysts. *Anal. Chem.* **2020,** *92* (24), 16089-16096.

331. Yu, J.; Du, X.; Liu, H.; Qiu, C.; Yu, R.; Li, S.; Ren, J.; Yang, S., Mini review on active sites in Ce-based electrocatalysts for alkaline water splitting. *Energ. Fuel* **2021,** *35* (23), 19000-19011.

332. Nai, J.; Yin, H.; You, T.; Zheng, L.; Zhang, J.; Wang, P.; Jin, Z.; Tian, Y.; Liu, J.; Tang, Z., Efficient electrocatalytic water oxidation by using amorphous Ni–Co double hydroxides nanocages. *Adv. Energy. Mater.* **2015,** *5* (10), 1401880.

333. Jiang, J.; Zhang, A.; Li, L.; Ai, L., Nickel–cobalt layered double hydroxide nanosheets as high-performance electrocatalyst for oxygen evolution reaction. *J. Power Sources* **2015,** *278*, 445-451.

334. Qian, L.; Lu, Z.; Xu, T.; Wu, X.; Tian, Y.; Li, Y.; Huo, Z.; Sun, X.; Duan, X., Trinary layered double hydroxides as high-performance bifunctional materials for oxygen electrocatalysis. *Adv. Energy. Mater.* **2015,** *5* (13), 1500245.

335. Li, J.; Chu, D.; Baker, D. R.; Dong, H.; Jiang, R.; Tran, D. T., Distorted inverse spinel nickel cobaltite grown on a MoS_2 plate for significantly improved water splitting activity. *Chem. Mater.* **2019,** *31* (18), 7590-7600.

336. Yang, Y.; Lin, Z.; Gao, S.; Su, J.; Lun, Z.; Xia, G.; Chen, J.; Zhang, R.; Chen, Q., Tuning electronic structures of nonprecious ternary alloys encapsulated in graphene layers for optimizing overall water splitting activity. *ACS Catal.* **2017,** *7* (1), 469-479.

337. Liu, J.; Wang, J.; Zhang, B.; Ruan, Y.; Lv, L.; Ji, X.; Xu, K.; Miao, L.; Jiang, J., Hierarchical $NiCo_2S_4$@ NiFe LDH heterostructures supported on nickel foam for enhanced overall-water-splitting activity. *ACS Appl. Mater. Interfaces* **2017,** *9* (18), 15364-15372.

338. Qiu, B.; Wang, C.; Zhang, N.; Cai, L.; Xiong, Y.; Chai, Y., CeO_2-induced interfacial Co^{2+} octahedral sites and oxygen vacancies for water oxidation. *ACS Catal.* **2019,** *9* (7), 6484-6490.

339. Gao, W.; Xia, Z.; Cao, F.; Ho, J. C.; Jiang, Z.; Qu, Y., Comprehensive understanding of the spatial configurations of CeO_2 in NiO for the electrocatalytic oxygen evolution reaction: embedded or surface-loaded. *Adv. Funct. Mater.* **2018,** *28* (11), 1706056.

340. Cossar, E.; Agarwal, K.; Nguyen, V. B.; Safari, R.; Botton, G. A.; Baranova, E. A., Highly active nickel–iron nanoparticles with and without ceria for the oxygen evolution reaction. *Electrocatal.* **2021,** *12* (5), 605-618.

341. Shi, Y.; Feng, X.; Guan, H.; Zhang, J.; Hu, Z., Porous sunflower plate-like $NiFe_2O_4$/CoNi–S heterostructure as efficient electrocatalyst for overall water splitting. *Int. J. Hydrog. Energy* **2021,** *46* (12), 8557-8566.

342. Liu, W.; Tan, W.; He, H.; Peng, Y.; Chen, Y.; Yang, Y., One–step electrodeposition of Ni–Ce–Pr–Ho/NF as an efficient electrocatalyst for hydrogen evolution reaction in alkaline medium. *Energy* **2022,** *250*, 123831.

343. Wu, Z.; Wang, Z.; Geng, F., Radially aligned hierarchical nickel/nickel–iron (oxy) hydroxide nanotubes for efficient electrocatalytic water splitting. *ACS Appl. Mater. Interfaces* . **2018,** *10* (10), 8585-8593.

344. He, B.; Chen, L.; Jing, M.; Zhou, M.; Hou, Z.; Chen, X., 3D MoS_2-rGO@ Mo nanohybrids for enhanced hydrogen evolution: The importance of the synergy on the Volmer reaction. *Electrochim. Acta* **2018,** *283*, 357-365.

345. Gao, X.; Yu, G.; Zheng, L.; Zhang, C.; Li, H.; Wang, T.; An, P.; Liu, M.; Qiu, X.; Chen, W., Strong electron coupling from the sub-nanometer Pd clusters confined in porous ceria nanorods for highly efficient electrochemical hydrogen evolution reaction. *ACS Appl. Energy Mater.* **2019,** *2* (2), 966-973.

346. Njoku, C. B.; Kriek, R. J., Application of $Sm_{0.8}Sr_{0.2}Fe_{1-x}Co_xO_3$-δ (x= 0.2, 0.5, 0.8) Perovskite for the Oxygen Evolution Reaction in Alkaline Media. *Electrocatal.* **2019,** *10*, 305-313.

347. Zhao, M.; Li, Y.; Dong, H.; Wang, L.; Chen, Z.; Wang, Y.; Li, Z.; Xia, M.; Shao, G., The effects of CeO_2 nanorods and CeO_2 nanoflakes on Ni–S alloys in hydrogen evolution reactions in alkaline solutions. *Catal.* **2017,** *7* (7), 197.

348. Li, J.; Yan, M.; Zhou, X.; Huang, Z. Q.; Xia, Z.; Chang, C. R.; Ma, Y.; Qu, Y., Mechanistic insights on ternary $Ni_{2-x}Co_xP$ for hydrogen evolution and their hybrids with graphene as highly efficient and robust catalysts for overall water splitting. *Adv. Funct. Mater.* **2016,** *26* (37), 6785-6796.

349. Yu, J.; Li, Q.; Li, Y.; Xu, C. Y.; Zhen, L.; Dravid, V. P.; Wu, J., Ternary metal phosphide with triple-layered structure as a low-cost and efficient electrocatalyst for bifunctional water splitting. *Adv. Funct. Mater.* **2016,** *26* (42), 7644-7651.

350. Surendran, S.; Shanmugapriya, S.; Zhu, P.; Yan, C.; Vignesh, R. H.; Lee, Y. S.; Zhang, X.; Selvan, R. K., Hydrothermally synthesised NiCoP nanostructures and electrospun N-doped carbon nanofiber as multifunctional potential electrode for hybrid water electrolyser and supercapatteries. *Electrochim. Acta* **2019,** *296*, 1083-1094.

351. Wu, Y.; Wang, Y.; Xiao, Z.; Li, M.; Ding, Y.; Qi, M.-l., Electrocatalytic oxygen reduction by a Co/Co_3O_4@ N-doped carbon composite material derived from the pyrolysis of ZIF-67/poplar flowers. *RSC Adv.* **2021,** *11* (5), 2693-2700.

352. Khan, I.; Nasim, F.; Choucair, M.; Ullah, S.; Badshah, A.; Nadeem, M., Cobalt oxide nanoparticle embedded N-CNTs: lithium ion battery applications. *RSC Adv.* **2016,** *6* (2), 1129-1135.

353. Xuan, C.; Xia, K.; Lei, W.; Xia, W.; Xiao, W.; Chen, L.; Xin, H. L.; Wang, D., Composition-dependent electrocatalytic activities of NiFe-based selenides for the oxygen evolution reaction. *Electrochim. Acta* **2018,** *291*, 64-72.

354. Li, X.; Han, G.-Q.; Liu, Y.-R.; Dong, B.; Shang, X.; Hu, W.-H.; Chai, Y.-M.; Liu, Y.-Q.; Liu, C.-G., In situ grown pyramid structures of nickel diselenides dependent on oxidized nickel foam as efficient electrocatalyst for oxygen evolution reaction. *Electrochim. Acta* **2016,** *205*, 77-84.

355. Zhang, J.; Shang, X.; Ren, H.; Chi, J.; Fu, H.; Dong, B.; Liu, C.; Chai, Y., Modulation of inverse spinel Fe_3O_4 by phosphorus doping as an industrially promising electrocatalyst for hydrogen evolution. *Adv. Mater.* **2019,** *31* (52), 1905107.

356. Huang, Y.; Wang, J.-J.; Zou, Y.; Jiang, L.-W.; Liu, X.-L.; Jiang, W.-J.; Liu, H.; Hu, J.-S., Selective Se doping of $NiFe_2O_4$ on an active NiOOH scaffold for efficient and robust water oxidation. *Chinese J. Catal.* **2021,** *42* (8), 1395-1403.

357. Wu, Z.; Zou, Z.; Huang, J.; Gao, F., $NiFe_2O_4$ nanoparticles/NiFe layered double-hydroxide nanosheet heterostructure array for efficient overall water splitting at large current densities. *ACS Appl. Mater. Interfaces* **2018,** *10* (31), 26283-26292.

358. Singh, S. K.; Takeyasu, K.; Paul, B.; Sharma, S. K.; Nakamura, J., CoOx electro-catalysts anchored on nitrogen-doped carbon nanotubes for the oxygen evolution reaction. *Sustain. Energy Fuels* . **2021,** *5* (3), 820-827.

359. Poorahong, S.; Harding, D. J.; Keawmorakot, S.; Siaj, M., Free standing bimetallic nickel cobalt selenide nanosheets as three-dimensional electrocatalyst for water splitting. *J. Electroanal. Chem.* **2021,** *897*, 115568.

360. Ji, H.; Ma, Y.; Cai, Z.; Yun, M.; Han, J.; Tong, Z.; Wang, M.; Suhr, J.; Xiao, L.; Jia, S., Mesoporous Cobalt Oxide (CoOx) Nanowires with Different Aspect Ratios for High Performance Hybrid Supercapacitors. *Nanomaterials* **2023,** *13* (4), 749.

361. Tang, C.; Cheng, N.; Pu, Z.; Xing, W.; Sun, X., NiSe nanowire film supported on nickel foam: an efficient and stable 3D bifunctional electrode for full water splitting. *Angew. Chem.* **2015,** *127* (32), 9483-9487.

362. Shi, Y.; Wen, L.; Li, F.; Cheng, H.-M., Nanosized $Li_4Ti_5O_{12}$/graphene hybrid materials with low polarization for high rate lithium ion batteries. *J. Power Sources* **2011,** *196* (20), 8610-8617.

363. Wang, Z.; Li, J.; Tian, X.; Wang, X.; Yu, Y.; Owusu, K. A.; He, L.; Mai, L., Porous nickel–iron selenide nanosheets as highly efficient electrocatalysts for

oxygen evolution reaction. *ACS Appl. Mater. Interfaces* . **2016,** *8* (30), 19386-19392.

364. Chen, Z.; Zhou, T.; Liu, Q.; Wang, Z.; Gu, R.; Guo, L.; Liu, Y., Three-Dimensional Flower-Like Bimetallic Nickel–Iron Selenide for Efficient Oxygen Evolution Reaction. *J. Phys. Chem. C* **2022,** *126* (11), 5131-5137.
365. Li, Z.; Cai, L.; Song, M.; Shen, Y.; Wang, X.; Li, J.; Wang, J.; Wang, P.; Tian, L., Ternary FeCoNi alloy nanoparticles embedded in N-doped carbon nanotubes for efficient oxygen evolution reaction electrocatalysis. *Electrochim. Acta* **2020,** *339*, 135886.
366. Chen, Y. M.; Yu, L.; Lou, X. W., Hierarchical tubular structures composed of Co_3O_4 hollow nanoparticles and carbon nanotubes for lithium storage. *Angew. Chem., Int. Ed. Engl.* **2016,** *55* (20), 5990-5993.
367. Zhang, X.-Y.; Guo, B.-Y.; Lin, Z.-Y.; Dong, B.; Chen, Q.-W.; Dong, Y.-W.; Yang, M.; Wang, L.; Liu, C.-G.; Chai, Y.-M., In situ electro-reduction to modulate the surface electronic structure of Fe_3O_4 for enhancing oxygen evolution reaction. *Int. J. Hydrog. Energy* **2020,** *45* (31), 15476-15482.
368. Xu, K.; Ding, H.; Lv, H.; Tao, S.; Chen, P.; Wu, X.; Chu, W.; Wu, C.; Xie, Y., Understanding structure-dependent catalytic performance of nickel selenides for electrochemical water oxidation. *ACS Catal.* **2017,** *7* (1), 310-315.
369. Tan, L.; Yu, J.; Wang, H.; Gao, H.; Liu, X.; Wang, L.; She, X.; Zhan, T., Controllable synthesis and phase-dependent catalytic performance of dual-phase nickel selenides on Ni foam for overall water splitting. *Appl. Catal. B: Environ.* **2022,** *303*, 120915.
370. Hu, X.; Zhou, Q.; Cheng, P.; Su, S.; Wang, X.; Gao, X.; Zhou, G.; Zhang, Z.; Liu, J., Nickel-iron selenide polyhedral nanocrystal with optimized surface morphology as a high-performance bifunctional electrocatalyst for overall water splitting. *Appl. Surf. Sci.* **2019,** *488*, 326-334.
371. Zhu, J.; Lu, Y.; Zheng, X.; Xu, S.; Sun, S.; Liu, Y.; Li, D.; Jiang, D., Heterostructure arrays of (Ni, Co)Se_2 nanowires integrated with MOFs-derived $CoSe_2$ dodecahedra for synergistically high-efficiency and stable overall water splitting. *Appl. Surf. Sci.* **2022,** *592*, 153352.

372. Chen, S.; Mi, J.-L.; Zhang, P.; Feng, Y.-H.; Yong, Y.-C.; Shi, W.-D., Control synthesis of nickel selenides and their multiwalled carbon nanotubes composites as electrocatalysts for enhanced water oxidation. *J. Phys. Chem. C* **2018,** *122* (45), 26096-26104.

373. Wang, Z.; Li, J.; Tian, X.; Wang, X.; Yu, Y.; Owusu, K. A.; He, L.; Mai, L., Porous nickel–iron selenide nanosheets as highly efficient electrocatalysts for oxygen evolution reaction. *ACS Appl. Mater. Interfaces.* **2016,** *8* (30), 19386-19392.

374. Tang, C.; Cheng, N.; Pu, Z.; Xing, W.; Sun, X., NiSe nanowire film supported on nickel foam: an efficient and stable 3D bifunctional electrode for full water splitting. *Angew. Chemie* **2015,** *127* (32), 9483-9487.

375. Louie, M. W.; Bell, A. T., An investigation of thin-film Ni–Fe oxide catalysts for the electrochemical evolution of oxygen. *J. Am. Chem. Soc.* **2013,** *135* (33), 12329-12337.

376. Fominykh, K.; Chernev, P.; Zaharieva, I.; Sicklinger, J.; Stefanic, G.; Döblinger, M.; Müller, A.; Pokharel, A.; Böcklein, S.; Scheu, C., Iron-doped nickel oxide nanocrystals as highly efficient electrocatalysts for alkaline water splitting. *ACS Nano* **2015,** *9* (5), 5180-5188.

377. Trotochaud, L.; Young, S. L.; Ranney, J. K.; Boettcher, S. W., Nickel–iron oxyhydroxide oxygen-evolution electrocatalysts: the role of intentional and incidental iron incorporation. *J. Am. Chem. Soc.* **2014,** *136* (18), 6744-6753.

378. Wang, H.-Y.; Ren, J.-T.; Wang, L.; Sun, M.-L.; Yang, H.-M.; Lv, X.-W.; Yuan, Z.-Y., Synergistically enhanced activity and stability of bifunctional nickel phosphide/sulfide heterointerface electrodes for direct alkaline seawater electrolysis. *J. Energ. Chem.* **2022,** *75*, 66-73.

379. Ren, J.-T.; Chen, L.; Wang, H.-Y.; Tian, W.-W.; Song, X.-L.; Kong, Q.-H.; Yuan, Z.-Y., Synergistic Activation of Crystalline Ni2P and Amorphous NiMoO x for Efficient Water Splitting at High Current Densities. *ACS Catal.* **2023,** *13* (14), 9792-9805.

380. Ren, J.-T.; Yao, Y.; Yuan, Z.-Y., Fabrication strategies of porous precious-metal-free bifunctional electrocatalysts for overall water splitting: Recent advances. *Green Energ. Environ.* **2021,** *6* (5), 620-643.

381. Feng, W.; Pang, W.; Xu, Y.; Guo, A.; Gao, X.; Qiu, X.; Chen, W., Transition metal selenides for electrocatalytic hydrogen evolution reaction. *ChemElectroChem* **2020,** *7* (1), 31-54.

382. Yang, H.; Huang, Y.; Teoh, W. Y.; Jiang, L.; Chen, W.; Zhang, L.; Yan, J., Molybdenum selenide nanosheets surrounding nickel selenides sub-microislands on nickel foam as high-performance bifunctional electrocatalysts for water splitting. *Electrochim. Acta* **2020,** *349*, 136336.

383. Li, J.; Wan, M.; Li, T.; Zhu, H.; Zhao, Z.; Wang, Z.; Wu, W.; Du, M., $NiCoSe_{2-x}$/N-doped C mushroom-like core/shell nanorods on N-doped carbon fiber for efficiently electrocatalyzed overall water splitting. *Electrochim. Acta* **2018,** *272*, 161-168.

384. Park, K. R.; Tran, D. T.; Nguyen, T. T.; Kim, N. H.; Lee, J. H., Copper-Incorporated heterostructures of amorphous $NiSe_x$/Crystalline $NiSe_2$ as an efficient electrocatalyst for overall water splitting. *Chem. Eng. J.* **2021,** *422*, 130048.

385. Liu, G.; Shuai, C.; Mo, Z.; Guo, R.; Liu, N.; Dong, Q.; Wang, J.; Pei, H.; Liu, W.; Guo, X., Fe-doped $Ni_{0.85}Se$ nanospheres interspersed into carbon nanotubes as efficient and stable electrocatalyst for overall water splitting. *Electrochim. Acta* **2021,** *385*, 138452.

386. Chang, K.; Tran, D. T.; Wang, J.; Kim, N. H.; Lee, J. H., A 3D hierarchical network derived from 2D Fe-doped NiSe nanosheets/carbon nanotubes with enhanced OER performance for overall water splitting. *J. Mater. Chem. A* . **2022,** *10* (6), 3102-3111.

387. Huang, L.; Wu, H.; Zhang, Y., One-step synthesis of CoPSe–$CoSe_2$/CNTs as efficient electrocatalyst for oxygen evolution reaction. *Electrochim. Acta* **2020,** *331*, 135362.

388. Pei, H.; Liu, G.; Guo, R.; Liu, N.; Mo, Z., A novel efficient dual-functional electrocatalyst for overall water splitting based on $Ni_{0.85}Se$/RGO/CNTs nanocomposite synthesized via different nickel precursors. *Int. J. Hydrog. Energy* **2022,** *47* (83), 35227-35240.

389. Salarvand, V.; Mohammadi, M. A.; Ahmadian, F.; Kouchi, F. R.; Yazdi, M. S.; Mostafaei, A., In-situ hydrothermal synthesis of $NiCo_{(X)}Se$ compound on

nickel foam for efficient performance of water splitting reaction in alkaline media. *J. Electroanal. Chem.* **2022,** *926*, 116929.

390. Boakye, F. O.; Li, Y.; Owusu, K. A.; Amiinu, I. S.; Cheng, Y.; Zhang, H., One-step synthesis of heterostructured cobalt-iron selenide as bifunctional catalyst for overall water splitting. *Mater. Chem. Phys.* **2022,** *275*, 125201.

391. Wan, Z.; He, Q.; Qu, Y.; Dong, J.; Shoko, E.; Yan, P.; Isimjan, T. T.; Yang, X., Designing coral-like Fe_2O_3-regulated Se-rich $CoSe_2$ heterostructure as a highly active and stable oxygen evolution electrocatalyst for overall water splitting. *J. Electroanal. Chem.* **2022,** *904*, 115928.